# Asteroid touring by electric sail technology

Pekka Janhunen, Petri Toivanen, Jouni Envall & Jouni Polkko

*Finnish Meteorological Institute*

11th November 2019

**Abstract**

The electric solar wind sail (E-sail) uses the solar wind to generate propellantless propulsion. We analyse asteroid-related E-sail mission architectures. We find that the E-sail enables a portfolio of advanced mission scenarios. A large number of asteroids can be surveyed at low cost per asteroid in flyby mode. Sample return is possible with moderate mass. Asteroid mining can become economical because the propellantless nature and low mass of the E-sail enable a high mass ratio. A systematic study of the options and a detailed analysis of the most promising ones are included in this report.

# Contents

# Executive summary

The electric solar wind sail (E-sail, Chapter 1) uses the solar wind to generate propel-
lantless propulsion. The system consists of one or more long and thin metallic tethers
that are kept at high positive potential. To maintain the bias voltage, an electron gun is
used which pumps out negative charge from the system. This is needed to compensate
for the thermal electron current gathered by the tethers from the solar wind plasma.
The electric power requirement is low compared to typical electric propulsion, only of
order 0.7 W/mN.

A multi-tether E-sail with the so-called TI configuration can control its spinrate
and spinplane orientation using the E-sail effect itself (1.4). A single-tether E-sail can
also do this for the spinplane orientation, but for the spinrate magnitude, the orbital
Coriolis acceleration cannot be cancelled by the E-sail effect in this case. Therefore a
single-tether E-sail needs a traditional thruster placed in the remote unit at the tip of
the tether (1.5.1). The single-tether E-sail has the benefit of enabling platform pointing
without moving parts.

Candidate mission ideas were critically surveyed for suitability with E-sail propulsion
(Chapter 2). For asteroids, gravity assist manoeuvres are typically not available and
so low-thrust propulsion methods such as electric propulsion and E-sail often have an
advantage over chemical propulsion. The E-sail is the most efficient low-thrust method
known, so it suits well for asteroid missions. The main limitation of the E-sail is that
it is not possible to land or even go close to an asteroid with the opened tether rig, and
the tethers cannot be reliably retracted and re-opened. For flyby missions this is not
a limitation. For rendezvous, orbiting, landing and sample return missions, however,
other solutions must be sought. A secondary limitation is that the E-sail dictates the
platform's orientation, so pointing of antennas and instruments cannot be done by
turning the platform.

A fleet of 50 single-tether E-sails performing flybys of more than 300 main-belt
asteroids was proposed with name "Multi-Asteroid Touring" (MAT) in response to the
'Call for new ideas' in 2016 (Appendix D). To keep the telemetry costs down, automatic
optical navigation based on planets and known asteroids was envisioned, similar to that
demonstrated by Deep Space 1 in 1998–2001. Optical images and near-infrared spectra
of the flown-by asteroids would be stored in memory throughout the nominally 3.2
year mission for each member of the fleet, and downlinked at a final Earth flyby to a
16 m ground antenna in a 3-hour telemetry session transferring 10 gigabytes of data
from flash memory, for each 50 spacecraft. An engineering design of the spacecraft was
carried out where the mass came out to be 6 kg without launchpod structure (Slavinskis
et al., 2018).

In spring 2018, the MAT proposal was looked at in a CDF study "Small Planetary
Platform". The main criticisms raised were the need for autonavigation software (which,
although demonstrated 20 years ago by Deep Space 1, would need to be developed again
in Europe) and the mass-constrained nature of the design (in order to accomplish its

5

main-belt tour in a single orbit, it needs 1.0 mm/s$^2$ characteristic acceleration and scaling the thrust up is nontrivial because the single tether cannot be made arbitrarily long due to material tensile strength constraints). To address these criticism, a NEO version of MAT was developed (Chapter 5). Surveying NEOs instead of main-belt asteroids relaxes the characteristic acceleration requirement and so removes the mass-constrained nature of the design. It also enables ordinary navigation methods based on telemetry sessions to be used. As a bonus, it also removes the need to perform spinrate management by a thruster at the tether tip because the mission can be accomplished by fully radial propulsion in which case the orbital Coriolis effect is known to vanish.

In the multi-tether mission category, asteroid sample return was analysed in detail (Chapter 4). A two-spacecraft mission architecture is used where E-sail mothership is parked at the edge of the asteroid's Hill's sphere to avoid risk of tethers colliding with potential unseen minimoons of the asteroid. A separate science spacecraft lands, takes the sample and re-docks with the mothership. The entry capsule is part of the mothership and the sample canister is transferred from the science spacecraft at the re-docking. The telecommunication subsystem is part of the science spacecraft. The science spacecraft can be turned freely because it has no tethers, so pointing of the antennas and the science instruments is possible to do without moving parts. The mothership has 18 tethers, each of length 15 km and the total wet mass of the two spacecraft is 142 kg including 20 % margin. A simple scheme for docking and attachment was sketched and analysed.

The missions thus far analysed are scientific, although they also have some features that can benefit asteroid mining and resource prospecting. For economically profitable asteroid mining, however, the mass ratio (the ratio of the mass returned in the target orbit, versus the initial launch mass) should be high. To check how high mass ratio can be feasible, we analysed a single-tether mission architecture for returning regolith from NEO to LEO (Chapter 6). Reaching LEO is requires aerobraking, but it was selected as the target orbit because it is more likely to have near-term customers e.g. for regolith-extracted LOX than higher orbits. The spacecraft is a 6-U cubesat weighing 8 kg. After launch to marginal or other escape orbit, it deploys a single-tether E-sail to go the asteroid. At the asteroid the tether is abandoned and the spacecraft maps the asteroid for regolith pools and lands. It crawls on the surface, filling a lightweight plastic snail-shaped container with regolith as it goes. When up to 300 kg has been collected, it lifts off using gas propulsion and deploys a second E-sail tether for flying back to Earth. Near Earth, the tether is jettison so that it burns in the atmosphere, while the spacecraft itself deploys an aerobrake to lower the apogee gradually to LEO altitude. The maximum mass of 300 kg originates from the requirement that the achieved nominal acceleration is 1 km/s/year, which allows a triptime from a typical NEO of less than four years. The corresponding mass ratio is 37.5 which should be high enough for economical retrieval of NEO regolith to LEO for the purposes of LOX extraction.

The E-sail enables a portfolio of advanced mission scenarios. A large number of asteroids can be surveyed at low cost per asteroid in flyby mode. Application to NEOs is easier, but with some investment in autonavigation software and some risk-taking in miniaturisation, also main-belt asteroids can be surveyed. Sample return is possible with 140 kg total mass. Asteroid mining can become economical because the propellantless nature and low mass of the E-sail enable high mass ratio when returning from material from NEO to LEO, for example.

# Chapter 1

# WP1: E-sail designs

## 1.1 Objectives and background

The objective of WP1 is to review the E-sail and its development status, present main E-sail design options, analyse requirements posed by the E-sail on the spacecraft platform and recommend E-sail architecture(s) suitable for asteroid missions.

### 1.1.1 Asteroids as mission targets

Among solar system objects, asteroids are scientifically and practically very important targets for space missions. Asteroids contain also material from the period when the solar system was young, because unlike on planets where material has been typically heavily processed by melting, differentiation, erosion etc., on asteroids the primordial material is still partly intact. Asteroids are also literally a quite manyfold target, no two asteroids are exactly alike. On the other hand, many main belt asteroids belong to some asteroid family, i.e., they are collisional fragments of some parent body.

Asteroids are important objects to study not only for scientific reasons, but also because they are a threat to Earth in the form of asteroid impacts. The asteroid threat stands apart from other natural disasters such as earthquakes and volcanic eruptions because asteroid collisions would be in principle preventable by orbit deflection. Also, it would be possible to mine asteroid material and process it into rocket fuel, precious platinum group metals and large space constructions. The products could be transported by E-sails to various solar system orbits and destinations, including the Earth.

Both addressing the impact threat and asteroid mining need basic research and mapping of asteroids. Mining needs mineral prospecting while orbit deflection by low-thrust propulsion needs knowledge about the asteroid's rotational state and basic data of its mechanical properties for harpooning or other form of attachment. As an alternative to gradual deflection by low-thrust propulsion, one can deflect an asteroid by impactors that could also be E-sail propelled. Impact deflection needs information about the object's fragility, because one does not want to break the body apart.

Besides space missions, our knowledge of asteroids stems from mainly three traditional sources. *Meteorites* are typically modified asteroid fragments; for example from the study of meteorites we know that platinum group metals are much more common on asteroids than in Earth's crust. *Optical and infrared astronomy* yields reflectance spectra and lightcurves; the spectra tell about surface minerals and are the basis for asteroid classification while lightcurves tell about rotation state and shape. Finally, large *radars* have been used successfully to reveal detailed shape of some of those NEO

**Table 1.1:** Asteroid missions. Missions written in *italic* are planetary or lunar missions that made asteroid flybys as bonuses.

| Asteroid(-Family) | au | ∅/km | Type | Flyby dist etc. | Mission |
|---|---|---|---|---|---|
| 951 Gaspra-Flora | 1.8-2.6 | 12 | S | 1600 km | *Galileo 1991* |
| 243 Ida-Koronis | 2.7-3.0 | 30 | S | 2400 km | *Galileo 1993* |
| 253 Mathilde | 1.9-3.4 | 50 | C | 1200 km | NEAR 1997 |
| 9969 Braille | 1.3-3.4 | 1.5 | Q | 26 km | DeepSpace-1 1999 |
| 2685 Masursky-Eunomia | 2.3-2.9 | 15 | S | 1.6e6 km | *Cassini 2000* |
| 433 Eros | 1.1-1.8 | 17 | S | lander | NEAR 2001 |
| 5535 Annefrank-Augusta | 2.0-2.4 | 5 | S | 3000 km | Stardust 2002 |
| 25143 Itokawa | 0.95-1.7 | 0.4 | S | lander(+samp) | Hayabusa 2005 |
| Comet Tempel 1 | 1.5-4.7 | 6 | C | impactor | DeepImpact 2005 |
| 132524 APL | 1.9-3.3 | 2.3 | S | 1e5 km | *NewHorizons 2006* |
| 2867 Steins | 2.0-2.7 | 4.6 | E | 800 km | Rosetta 2008 |
| 21 Lutetia | 2.0-2.8 | 100 | M | 3000 km | Rosetta 2010 |
| 4 Vesta-Vesta | 2.2-2.6 | 500 | V | orbiter | Dawn 2011 |
| 4179 Toutatis | 0.94-4.0 | 3 | S | 3 km | *Chang'e-2 2012* |
| 67-P C-G | 1.2-5.7 | 4 | C | lander | Rosetta 2014 |
| 1 Ceres-interloper | 2.6-3.0 | 1000 | C | orbiter | Dawn 2015 |
| 1999 JU3 | 0.96-1.4 | 1 | C | sample return | Hayabusa-2 2018 |
| 101955 Bennu | 0.9-1.36 | 0.5 | B | sample return | OsirisRex 2022 |

asteroids that have come to Earth's vicinity.

Space missions can yield much better data than the traditional sources. Table 1.1 lists missions that have been made or are planned to make flyby, orbiting, landing or sample return studies of asteroids or comets (comet flybys are however excluded). As seen from the table, a lot has been done, but a lot also remains to be done. For example, many of the main belt's important asteroid families have not yet been targeted for missions and same holds for Jupiter Trojans.

Table 1.2 summarises the scientific instrumentation used on the missions. Optical and near infrared (NIR) imaging and some form of spectral capability has been employed in all missions. These instruments can reveal the morphology, main geologic units and surface mineralogy of the body. More accurate mapping of the asteroid's geometric shape can be done by laser altimetry. X-ray and UV imaging and spectrography can further improve the recognition of surface minerals.

To learn what lies below the topmost atomic layer, one needs additional instruments. Most missions have used precise monitoring of the Earth radio link to constrain the mass distribution of the body (not listed in Table 1.2 because it incurs almost no mass or power penalty). Imaging the body in thermal infrared allows for mapping the surface temperature which yields information about the surface layer's thermal inertia and thereby constrains its physical properties typically a few centimetres deep. Measuring the energy spectrum of cosmic ray spallated neutrons yields information about the degree of neutron thermalisation which is a measure of light element abundance in a $\sim 1$ m surface layer. Measuring cosmic ray triggered gammas can also be used to recognise elemental composition of a surface layer. Measuring the magnetic field, if any, can also constrain the asteroid's internal composition. A radar can be used to measure the conductivity and permittivity distribution of the interior of the body. Rosetta

**Table 1.2:** Instrumentation of dedicated asteroid missions. DI=DeepImpact, HB=Hayabusa, ORex=OsirisRex, MP-R=MarcoPolo-R. Not yet accomplished experiments are denoted in greyscale: HB-2 has been launched, ORex is planned and MP-R has been proposed.

| Mission: | NEAR | Rosetta | DI | Dawn | HB-1 | HB-2 | ORex | MP-R |
| --- | --- | --- | --- | --- | --- | --- | --- | --- |
| Launch: | 1996 | 2004 | 2005 | 2007 | 2003 | 2014 | 2016 | |
| optical+NIR imager | × | × | × | × | × | × | × | × |
| IR spectrograph | × | × | × | × | × | × | × | × |
| UV | | × | | | | | | |
| mm-wave | | × | | | | × | | |
| X-ray | × | × | | | × | | × | |
| gamma ray/neutron | × | | | × | | | | |
| laser altimeter | × | | | | × | × | × | |
| magnetometer | × | × | | | | × | | |
| radar | | × | | | | | | |
| dust | | × | | | | | | |
| neutral part./gas | | × | | | | | | × |
| plasma | | × | | | | | | |
| surface in situ | | × | | | | × | | |
| minilander | | | | | × | ×× | | |
| impactor | | | × | | | × | | |
| sample return | | | | | (×) | × | × | × |

employs the radar in a power efficient transmission geometry where the body is located between the transmitter (orbiter) and the receiver (lander).

To learn in more detail what lies below the surface, more elaborate strategies are needed. A lander can employ a drill to take samples of the subsurface (Rosetta), or a high speed impactor (DeepImpact, Hayabusa-2) can be used to create an impact plume and impact crater which can be studied from a distance by the usual imaging and spectral instruments. Sample return is the ultimate way of making detailed studies of limited amount of material. Hayabusa-2 will also attempt to take subsurface samples from the created impact crater.

As an example, Figure 1.1 shows the Itokawa asteroid.



**Figure 1.1:** Asteroid 25143 Itokawa is a 0.5 km long S-type (i.e., stony) NEO asteroid visited by JAXA's Hayabusa mission in 2005.

**Table 1.3:** Some interesting asteroids.

| Asteroid(-Family) | au | $i/°$ | $\emptyset$/km | Type | Interest |
|---|---|---|---|---|---|
| 1998 KY26 | 1.0-1.5 | 1.5 | 0.03 | C | Small, water? |
| 434 Hungaria | 1.8-2.1 | 23 | 20 | E | Hungaria family parent |
| 8 Flora-Flora | 1.9-2.5 | 6 | 130 | S | Flora family parent |
| 15 Eunomia-Eunomia | 2.1-3.1 | 12 | 270 | S | Eunomia family parent, largest S-type |
| 2 Pallas-Pallas | 2.1-3.4 | 35 | 500 | B | Pallas family parent, largest B-type |
| 16 Psyche | 2.5-3.3 | 3 | 200 | M | Largest M-type |
| 158 Koronis-Koronis | 2.7-3.0 | 1 | 35 | S | Koronis family parent |
| 221 Eos-Eos | 2.7-3.3 | 11 | 100 | K | Eos family largest member |
| 704 Interamnia | 2.6-3.5 | 17 | 350 | F | Large, high density |
| 24 Themis-Themis | 2.7-3.5 | 1 | 200 | C | Themis family parent, surface ice |
| 10 Hygiea-Hygiea | 2.8-3.5 | 4 | 430 | C | Hygiea family parent, largest C-type |
| 31 Euphrosyne-Euphr. | 2.4-3.9 | 26 | 250 | C | Euphrosyne family parent |
| 52 Europa | 2.8-3.4 | 7 | 320 | C | Large interloper in Hygiea family |
| 65 Cybele-Cybele | 3.1-3.8 | 3.5 | 270 | C | A parent of Cybele family |
| 87 Sylvia-Cybele | 3.2-3.8 | 11 | 290 | X | A parent of Cybele fam., 2 moons |
| 511 Davida | 2.6-3.8 | 16 | 230 | C | Large |
| 3 Juno | 2.0-3.6 | 13 | 230 | S | Parent of Juno clump |
| 2207 Antenor | 5.0-5.2 | 7 | 85 | D | 'Accessible' large Trojan |

Table 1.3 lists some examples of interesting mostly main belt asteroids. Any Jupiter Trojan asteroid is interesting because none has been studied and their origin and composition are largely unknown; in Table 1.3 we list an exemplary Trojan which is among the more accessible ones in terms of orbital characteristics. All NEOs are interesting and practically important (many are potential future Earth impact hazards and many would be potential targets for asteroid mining as well), but for brevity we list only one, KY-26, in Table 1.3. Figure 1.2 shows the locations of the main asteroid groups and the masses of largest main belt asteroids.



**Figure 1.2:** Asteroid groups (left) and the largest main belt asteroid masses (right).

## 1.1.2 The E-sail propulsion concept

The theoretical concept of the E-sail (Fig. 1.3) was discovered by Janhunen (2004) and a more practical design was conceptualised a couple of years later (Janhunen, 2006). The concept evolved and its applications to various solar wind missions were later studied; for a review, see Janhunen et al. (2010).
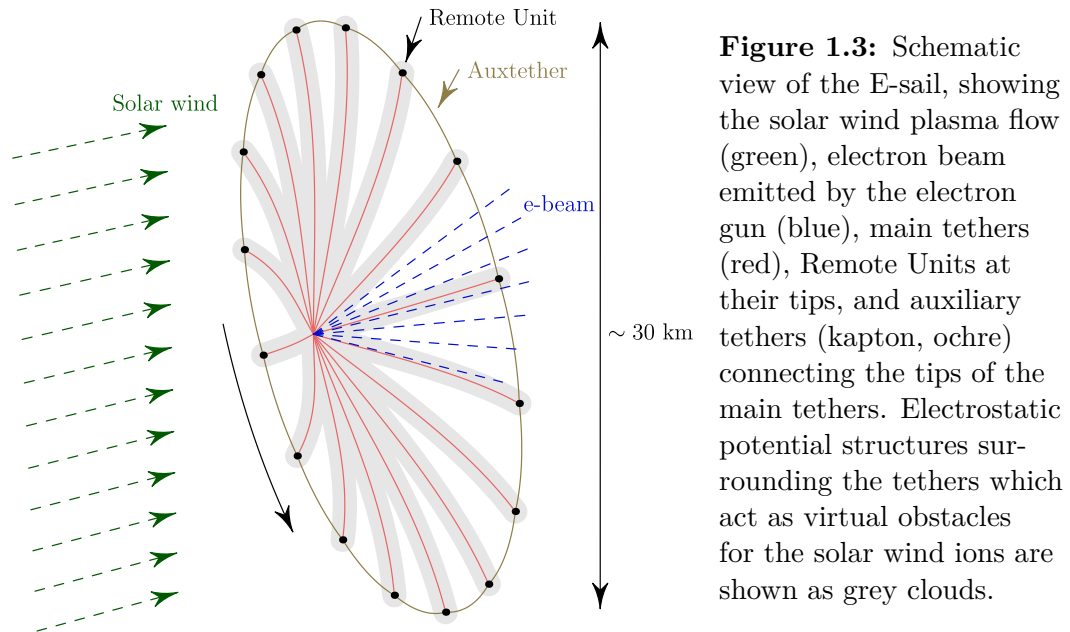


**Figure 1.3:** Schematic view of the E-sail, showing the solar wind plasma flow (green), electron beam emitted by the electron gun (blue), main tethers (red), Remote Units at their tips, and auxiliary tethers (kapton, ochre) connecting the tips of the main tethers. Electrostatic potential structures surrounding the tethers which act as virtual obstacles for the solar wind ions are shown as grey clouds.

Figure 1.3 shows a schematic of the spin-stabilised E-sail with auxtethers to keep the tethers apart and with Remote Units to host the auxtether reels. Radial main tethers are charged to high voltage to repel the solar wind ions and thereby to tap momentum flux from them. The electrostatic potential barrier generates an electron sheath with effective sail area of a few hundred metres around each tether. The main tethers themselves are very lightweight to enable a low-mass propulsion system. The tether charge state is maintained by a solar-powered electron gun whose current compensates the thermal electron current that the positively charged tethers draw from the surrounding solar wind plasma. The E-sail allows thrust magnitude to be throttled arbitrarily at any time by reducing the current and voltage of the electron gun. Thrust vectoring is possible by tilting the sail with respect to the solar wind direction. Tilting can be accomplished by differential spin-synchronised modulation of the tether voltages: the phase of the modulation determines the direction into which the spin axis turns.

The E-sail tether (Fig. 1.4) is made of one 50 $\mu$m diameter aluminium base wire to which three 25 $\mu$m diameter loop wires are bonded ultrasonically at a few centimetre intervals to create a redundant, micrometeoroid-resistant tether structure. The base wire is thicker than the loop wires to ease the ultrasonic bonding process.

Figure 1.5 shows the setup of the tether factory where ultrasonic tether production is made at Electronics Research Laboratory of the University of Helsinki, Finland. The figure also shows a scanning electron microscope (SEM) image of a single ultrasonic bond between base and loop wires. Each kilometre of E-sail tether contains about 100 000 ultrasonic bonds (Seppänen et al., 2011).

The technical readiness level (TRL) of the E-sail key component was increased to TRL 4-5 by the "ESAIL" project (ESAIL, 2011-2013) which was funded by the EU's
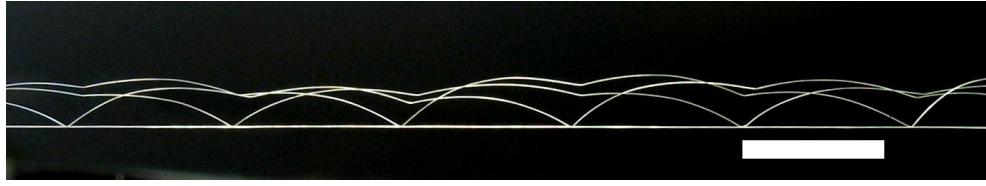
**Figure 1.4:** Four-wire micrometeoroid resistant E-sail tether. The white bar length is 1 cm.
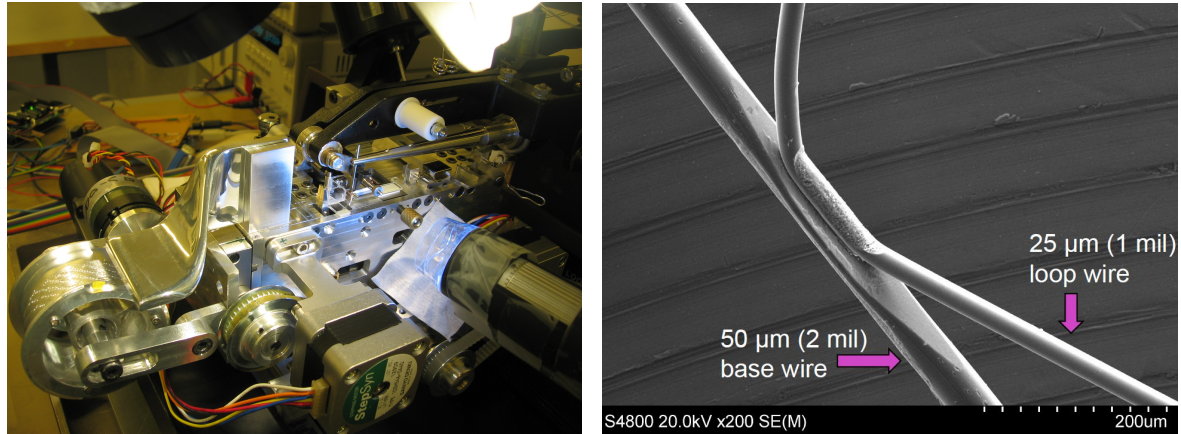


**Figure 1.5:** E-sail tether factory (left), SEM image of a single ultrasonic bond (right).

Seventh Framework Programme (FP7). The project's total EU contribution was 1.753 M€. Nine institutes from five countries (Finland, Sweden, Estonia, Germany and Italy) participated in ESAIL. A 1 km sample of final-type four-wire E-sail tether was produced, Fig. 1.6 top left, (Seppänen et al., 2013), as well as a TRL 4-5 Remote Unit prototype in cold gas and IL-FEEP versions, Fig. 1.6 top right, (Wagner et al., 2012; Thornell, 2013). Also, first principles time domain computer simulation software for analysing dynamical E-sail deployment, flight and stability with elastic tethers in realistic solar wind conditions was developed, Fig. 1.6 bottom left, (Janhunen, 2013b). Comprehensive, optimised orbital calculations to solar system targets were carried out, including for example optimised travel times to all Potentially Hazardous Asteroids i.e. asteroids that cross Earth's orbit, Fig. 1.6 bottom right, (Mengali et al., 2013).

The first planned E-sail space experiment flies onboard ESTCube-1 nanosatellite. The Estonian ESTCube-1 (Lätt et al., 2014) is a 1-U CubeSat (Fig. 1.7) that was launched in May 2013 as a piggyback payload of Vega. ESTCube-1 carries a 10 m long E-sail tether experiment (Envall et al., 2014). The satellite bus was a technical success, but the piezo motorised tether reel failed to rotate which prevented tether deployment. Post-launch testing revealed that launch vibrations might have caused mechanical damage at the slipring contact of the tether reel which may have caused enough extra friction to prevent the reel from rotating. To enable high voltage positive tether mode +500 V, ESTCube-1 has two redundant nanographite based cold cathode electron guns developed at Accelerator Laboratory of University of Jyväskylä, Finland (Kleshch et al., 2015). An electron gun worked in orbit and the details of the current measurements are undergoing analysis.

The second E-sail space experiment will fly in 2017. Aalto-1 (Kestilä et al., 2013) is a Finnish 3-U CubeSat which will be launched in January 2017 onboard Space-X's Falcon-
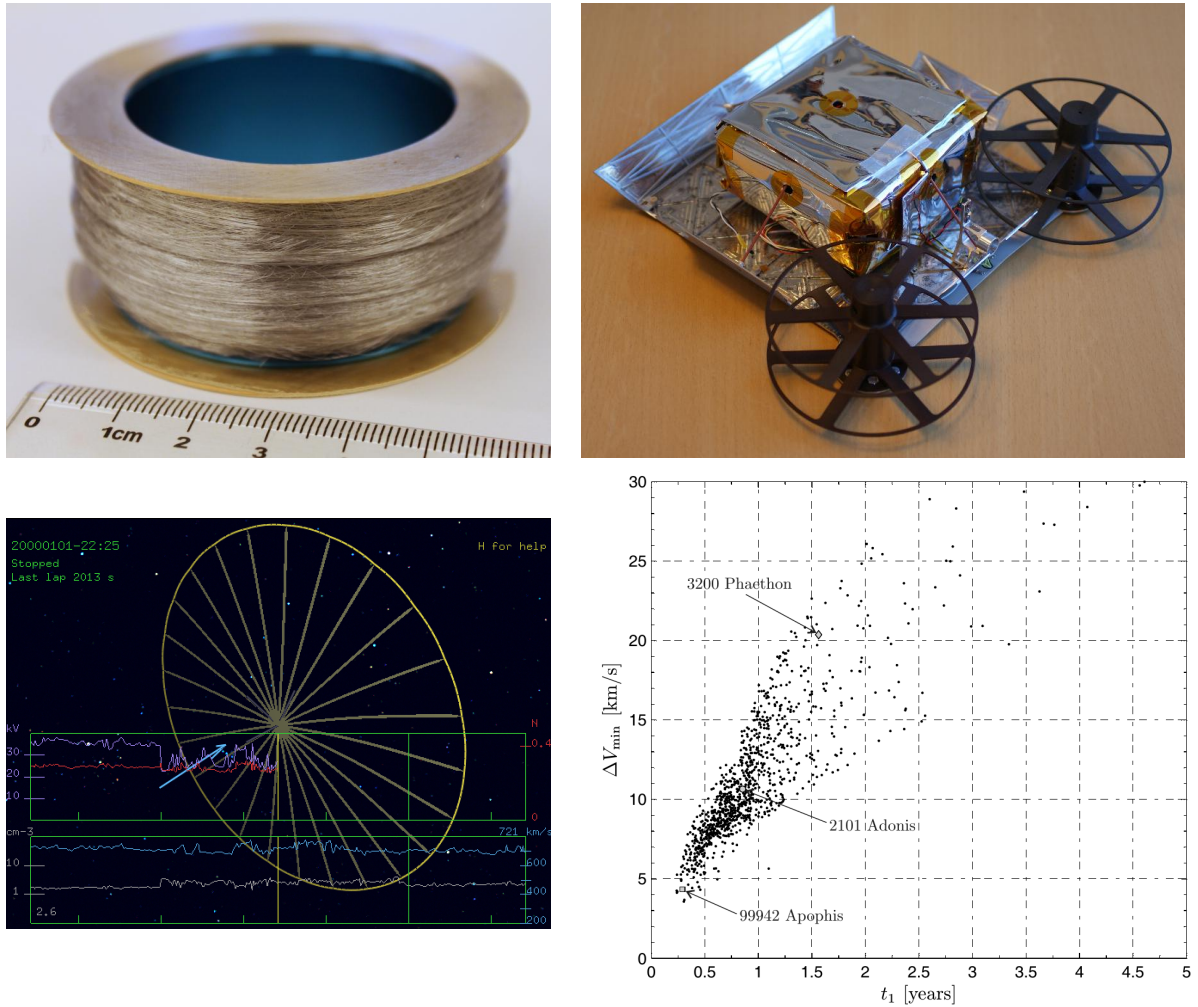
**Figure 1.6:** Results of ESAIL FP7 project. 1 km four-wire E-sail tether ($m = 11$ g) (top left); Remote Unit ($m = 0.56$ kg, allowed solar distance 0.9-4 au), the solar panel is attached to the sunshield plate and facing down and the two prominent reels are for storing the auxtether (top right); "flight simulator" software (bottom left); chemical delta-v versus E-sail rendezvous access time for all currently known Potentially Hazardous Asteroids assuming E-sail with 1 mm/s$^2$ characteristic acceleration (bottom right).
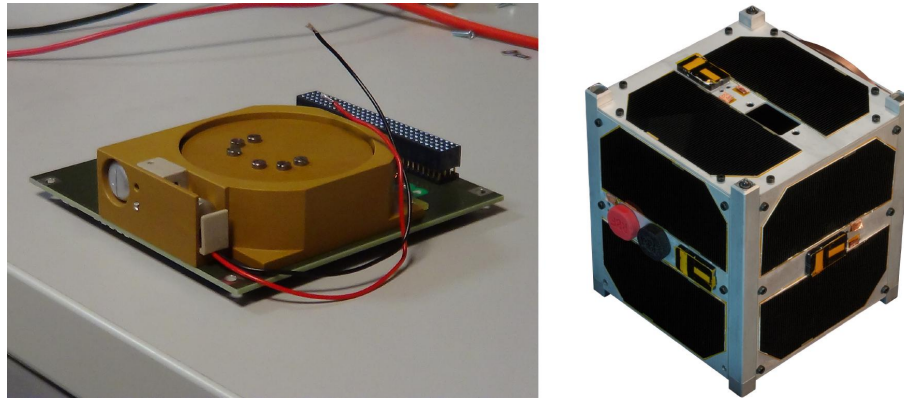
**Figure 1.7:** ESTCube-1 E-sail experiment payload (left) and the 1-U CubeSat itself ($m = 1$ kg, size $10{\times}10{\times}10$ cm, right).

9 launcher (Fig. 1.8). Aalto-1 carries an improved version of the E-sail experiment, this time with a 100 m tether and the mechanical problem encountered in ESTCube-1's reel now hopefully fixed.
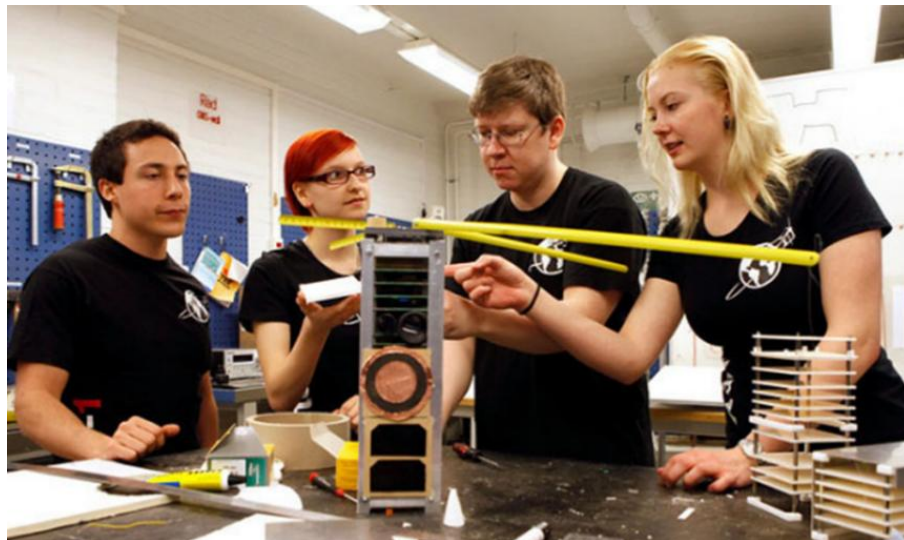


**Figure 1.8:** The Finnish Aalto-1 3-U CubeSat is going to be launched in August 2015.

## 1.2   Review of E-sail and its development status

The E-sail (Janhunen et al., 2010) can be applied to many types of solar system missions (Janhunen et al., 2014). The key components of E-sail technology were developed by the ESAIL FP7 project (2011-2013) to TRL 4-5. In particular, a 1 km sample of 4-wire ultrasonically bonded aluminium "Heytether" was produced, successful tether reel-out after launch vibrations was demonstrated and a prototype about 0.56 kg Remote Unit was built and tested in space environment conditions. A new tether technology is under development, which is intended to supersede the ultrasonically bonded Heytether technology.

    The main properties of the E-sail are summarised in Table 1.4. The mass budget data were taken from Janhunen et al. (2013) by selecting an exemplary 100 kg science payload and 1.0 mm/s$^2$ characteristic acceleration at 1 au. Characteristic acceleration of 1 mm/s$^2$ corresponds to 32 km/s of delta-v per year.

**Table 1.4:** Main properties of 1 mm/s$^2$ E-sail mission carrying exemplary 100 kg, 125 W science payload in 0.9-4 au solar distance range according to (Janhunen et al., 2013).

| | | | |
|---|---|---|---|
| Science payload mass | 100 | kg | |
| Characteristic acceleration at 1 au | 1.0 | mm/s$^2$ | (32 km/s of $\Delta$v/year) |
| Mission solar distance range | 0.9-4.0 | au | |
| Payload power consumption at 4 au | 125 | W | |
| Tether length | 15.3 | km | |
| Number of tethers | 44 | | |
| Tether voltage, nominal | 20 | kV | |
| E-sail thrust at 1 au | 0.39 | N | |
| E-sail thrust scaling | $\sim 1/r$ | | ($r$ is solar distance) |
| E-sail power requirement at 1 au | 409 | W | |
| E-sail power requirement scaling | $\sim 1/r^2$ | | |
| Mass of main tethers | 7.8 | kg | (without margin) |
| E-sail effective mass | 143 | kg | (includes 20 % margin) |
| Spacecraft total mass | 391 | kg | (includes 20 % margin) |

    Below we shall refine the numbers presented in Table 1.4 to reflect the present state of the art.

## 1.3   E-sail design options

The E-sail consists of thin, highly charged metallic wires or tethers which produce Coulomb drag when interacting with the solar wind. The tethers must be kept stretched and more or less perpendicular with respect to the solar wind because if they would be parallel to the wind, the propulsive effect would vanish. Because the tethers are very long (even 20 km), putting the tether rig to spin and using the resulting centrifugal force is the only currently known practically feasible way of keeping them stretched.

    In this section we go through various E-sail designs options. One of the options, the TI-model (a specific type of electric auxtether model) we shall select as the new baseline and it is treated in its own section below.
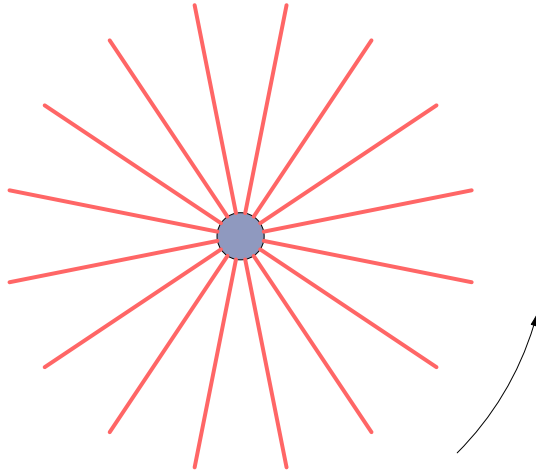
**Figure 1.9:** "Naïve" E-sail.

### 1.3.1 "Naïve" E-sail

Figure 1.9 shows a "naïve" E-sail which has only the rotating tethers. When tether voltages are on, the mutual Coulomb repulsion between tethers can be hoped to prevent tethers from colliding with each other. Checking whether or not this hope is realistic or not is not trivial because Coulomb repulsion between tethers is challenging to model accurately. A further complication is that Coulomb repulsion depends not only on tether voltages, but also on the instantaneous value of the solar wind plasma density which undergoes significant natural variations. Many missions also require coasting phases where propulsion is turned off. In pure coasting (voltages turned off completely) there is no Coulomb repulsion between tethers so it would be hard to guarantee that tethers do not collide. We cannot exclude the possibility, however, that some low level propulsion might be enough to exclude tether collisions and still approximate propulsion-free coasting in a useful way.

Our opinion is that although the "naïve" E-sail might potentially work (i.e., we currently cannot exclude the possibility that it could be made to work), there are many good reasons to concentrate on other, safer E-sail designs in this study. The "naïve" E-sail is an interesting theoretical concept, but a rigorous study of its feasibility would require either advances in numerical simulation tools or experiments in space. Even if the concept would turn out to be dynamically stable in some solar wind conditions, we think that it is unlikely that stability would extend to all relevant usage regimes and solar wind conditions.

### 1.3.2 E-sails with auxiliary tethers

The requirement to keep tethers apart from each other can be satisfied by connecting the tips of the tethers mechanically together by auxiliary tethers (Fig. 1.10). There are two variants: stretched auxtethers and centrifugally stabilising auxtethers. The stretched auxtether is like a flexible string (for example, a polyimide tape which is punched with holes to increase its elastic coefficient) which is constantly under tension (Polkko, 2012). The centrifugally stabilising auxtether is tensioned only by the centrifugal force acting on its own mass. In case of stretched auxtether, the mass of the auxtether plays no functional role so that the auxtether can be as lightweight as possible, as long as its micrometeoroid endurance and tensile strength requirements are met. In case of
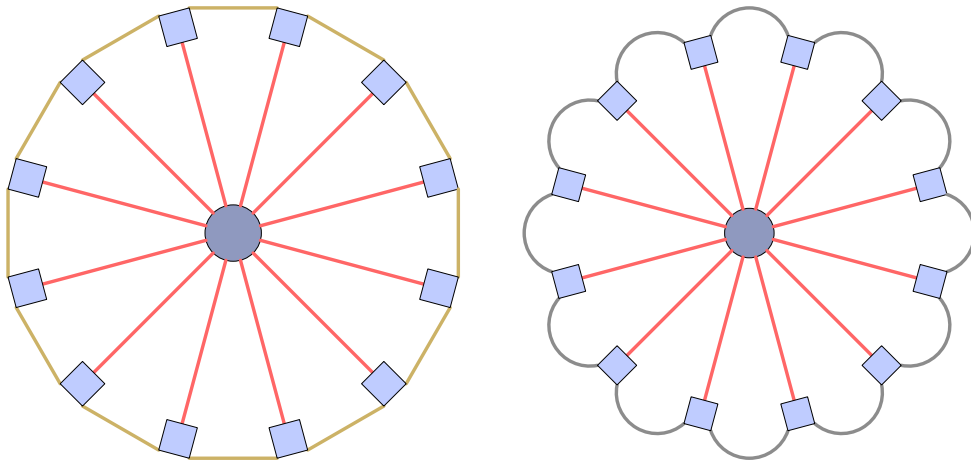
**Figure 1.10:** E-sail with Remote Units and auxiliary tethers. The auxtethers can be stretched (left) or centrifugally stabilising (right) or something in-between. In the stretched model, elasticity of the auxtether provides restoring force which tends to equalise maintether spacings. In the centrifugally stabilising version, restoring force is provided by the inertia of the auxtether.

centrifugally stabilising auxtether, the restoring force is provided by the auxtether's own mass so the mass cannot be made too small. The required mass depends on the number of tethers and other parameters.

Real tethers have, of course, both elasticity and mass so they have both stretched and centrifugally stablising character. Thus there is an engineering continuum of possibilities between the two idealised end cases.

### 1.3.2.1   Remote Units with cold gas or IL-FEEP thrusters

Adding auxtethers to the design (Fig. 1.10) solves the problem of eliminating the risk of tether collisions, but it does not yet address the issue how to generate the angular momentum for spinup and how to control the spinrate later during flight. Such need can arise from the orbital Coriolis effect in missions that orbit the Sun with an inclined E-sail (Toivanen and Janhunen, 2013). However, once auxtethers are added to the design, one must have some devices (called Remote Units) sitting at the tip of each main tether and hosting at least the auxtether reels.

Once the Remote Units exist, they are also a natural place where to add an auxiliary propulsion system for generating the spinup angular momentum and for controlling the spinrate later on. In the ESAIL FP7 project, two concepts were prototyped: Nanospace's a miniaturised microelectromechanical system (MEMS) technology cold gas thruster, and Alta's (nowadays Sitael's) ionic liquid field effect electric propulsion (IL-FEEP) thruster. Both concepts were found to fulfil their purpose; the cold gas thruster is lighter (Remote Unit dry mass 0.56 kg) and has higher TRL, while the IL-FEEP (Remote Unit dry mass 0.81 kg) has much higher total impulse capability so that it could perform spinrate management also in large (1 N, 100 tethers) E-sail missions. Besides Sitael's IL-FEEP thruster, there is no reason why also the Austrian indium FEEP thruster technology could not be similarly used.
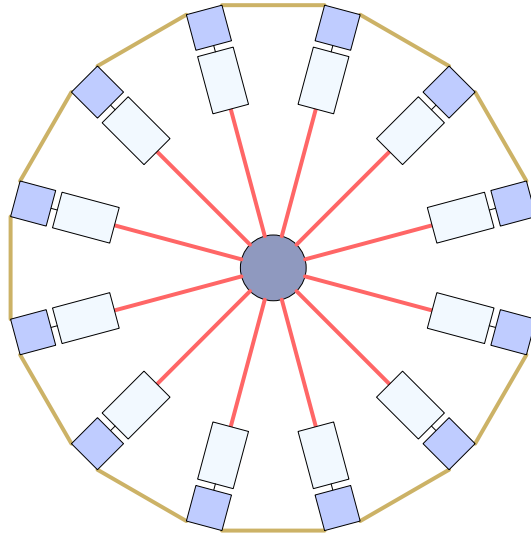
**Figure 1.11:** E-sail with photonic blade equipped Remote Units.

#### 1.3.2.2 Remote Units with photonic blades

While the cold gas and IL-FEEP thruster are possible solutions to the spinup and spin control problems, the total impulse capability of the cold gas option does not quite scale up to certain types of large missions. The IL-FEEP system has enough impulse capability, but is heavier and is not yet long-term flight proven. To address these issues, propellantless photonic sail spin control was explored by Janhunen (2013a), Fig. 1.11. A photonic blade made of aluminised kapton or mylar is deployed between the main tether end and the Remote Unit. The blade is kept stretched by the centrifugal force acting on the auxtether and the Remote Unit. The blade can be tilted about the main tether direction by a rotary actuator placed on the Remote Unit. Significant counter-rotation of the Remote Unit is prevented by the auxtethers.

To increase the reliability of deployment, one may want to be able to reel tethers from both ends with spare capacity so that a tether can be deployed in its desiged length even in case of one of the reel units getting stuck. The mass overhead of doing this is not very high because the tethers are lightweight. Tether doubling is, however, not straightforwardly compatible with the photonic blade concept of Fig. 1.11, because one would need a second remote unit located between the main tether and the blade. The second remote unit would only contain the tether reel. Another solution would be to put the blade on the outward side of the Remote Unit, but dynamical stability of this concept is not self-evident. Thus, the photonic blade and auxtether solution is otherwise promising, but its compatibility with the duplicated tether reliability engineering approach has some issues.

#### 1.3.2.3 Electric auxiliary tethers

If the auxiliary tethers also have controllable voltage, it turns out that one can regulate the spin rate (Janhunen and Toivanen, 2014). Intuitively the reason is that because auxtethers are orthogonal to maintethers, they produce thrust in different directions when the sail is inclined with respect to solar wind. Then, when the sail is inclined, a "watermill" modulation of maintethers can be used to speed up or slow down the

spin, while a suitable modulation of auxtether voltages can prevent the spinplane from turning.

We have developed a particularly simple and promising variant of this concept which we call the TI-model and which we select as our new baseline E-sail concept. The TI-model is treated in section 1.4.
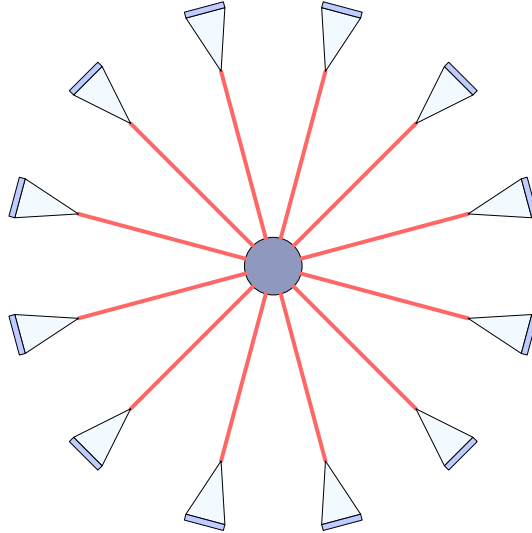


**Figure 1.12:** E-sail with freely guided photonic blade (FGPB) at each tether tip. No auxtethers are used. The one-dimensional attitude of each FGPB is controlled actively all the time e.g. by changing the blade's optical properties electrically or by moving the blade's centre of mass sideways.

### 1.3.3 Freely guided photonic blades and no auxtethers

Another approach is to get rid of the auxtethers completely and to control the flight of each tether separately using some auxiliary propulsion system. To this end, triangular freely guided photonic blades (FGPBs) were investigated by Janhunen (2014a), Fig. 1.12. The idea is that each tether tip contains a triangular photonic blade whose orientation is all the time actively controlled by some mechanism. The mechanism could be e.g. changed centre of mass or changed optical property of the blade. A benefit is that both number and length of the tethers can be easily scaled independently of each other. A drawback is the need for continuous active control of every tether and a control algorithm which would need to be developed and which might become to some extent complicated.

A benefit of the freely guided photonic blade solution is that it does not require tether doubling to achieve reliable deployment. If a reel jams during deployment, the tether in question can be allowed to remain shorter because it is all the time flown actively anyway, or it can be cut from the main spacecraft end if one first manoeuvres the other tethers to a different spin plane so that the outmoving tether does not hit the other ones. If a Remote Unit fails during flight, a similar procedure can be used to get rid of the failed tether.

We do not, however, adopt the FGPB as the baseline concept. One reason is the need of all Remote Units to sense their location and attitude and to perform active photopropulsive flight. The other reason is that the required area of the photonic blade needed is relatively large especially in the outer solar system.

## 1.4  The TI-model
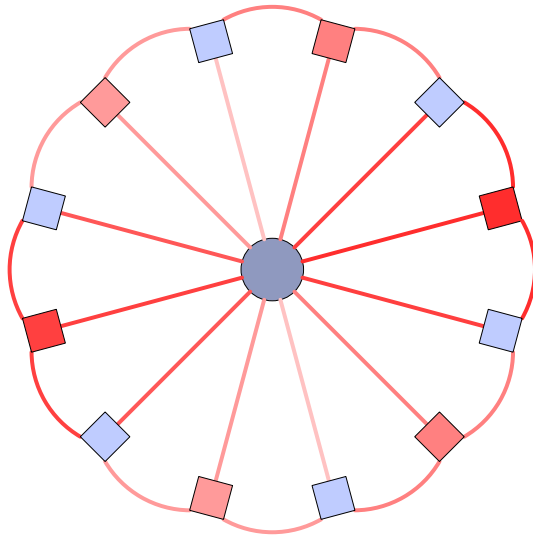


**Figure 1.13:** E-sail with electric auxtethers for spin control. Even-numbered Remote Unit (red) connect galvanically the maintether with its two adjoining auxtethers, while odd-numbered units (blue) act as insulators. In a given angular sector, the biasing of the auxtethers versus maintethers can be changed by biasing more the even or odd-numbered maintethers from the main spacecraft. Different hues of red symbolise bodies in different voltages.

Figure 1.13 shows a novel concept where the auxtethers are made of similar conducting material as the main tethers and also carry high voltage similar to the main tethers so that the auxtethers also contribute to E-sail thrust. Even-numbered Remote Units act as galvanic connectors between the maintether and the two adjacent auxtethers, hence making a T-shaped equipotential domain. Odd-numbered Remote Units are insulators, hence making up I-shaped equipotential domains (only maintethers). If the auxtether voltages can be controlled independently from the main tether voltages, even slightly, it enables one to control the spin rate of the system by using only E-sail propulsion (Janhunen and Toivanen, 2014). This is possible in the average sense, because the main spacecraft can control even-numbered T-tether voltages and odd-numbered I-tether voltages separately. By increasing T-tether voltage compared to I-tether voltages in some angular sector is equivalent to biasing more the auxtethers in that sector, which enables one to perform both spinrate control and spin axis orientation control by just modifying the maintether voltages.

The Remote Units are only needed during deployment. During flight they remain passive components which only provide fixed mechanical and fixed electrical connection and insulation between the maintether and the auxtethers.

We call this model the TI-model (referring to interleaved T-tethers and I-tethers). Because of its many benefits we select it as the new baseline E-sail configuration. Recently, a paper analysing its dynamics was submitted (Janhunen and Toivanen, 2016). The paper is appended in this report as Appendix A. The Lua source code used in the simulations of the paper is listed in Appendix B. In Appendix C we include another recently submitted paper which studies an analytical model of realistic tether shape and studies its implications to the control algorithm.

Figure 1.14 shows an examplary simulation with 14 days duration. The used solar wind is data taken starting from January 1, 2000, 00:00 UT. The thrust goal is set to 90 mN and the solar distance is 2.5 au. Average and maximum maintether and auxtether tensions are shown in panels e and f of Fig. 1.14. The tether tensions are relevant because they set the thickness requirement of the tether wire and therefore

affect the mass of the tether rig. The auxtether tension is typically more volatile than the maintether tension. Because the auxtethers are shorter than maintethers, one can make them of slightly thicker wire without increasing the mass of the tether rig much.

Figure 1.15 shows a typical case of how the control algorithm commands a single tether voltage as the tether rig rotates. Different tethers experience similar modulation with different time lags. The starting time in Fig. 1.15 corresponds to 6 days from the start of the simulation in Fig. 1.14. During this time the solar wind had relatively low density and the voltage was therefore higher than the nominal 20 kV. The hardware limit for the voltage was assumed to be 40 kV in the simulation. The tether angle $\alpha$ (angle between tether rig spin axis and solar wind direction) was 35°.

### 1.4.1   Coulomb repulsion and damping between tethers

Positively charged tethers generally repel each other. One might therefore hope that even in the naïve configuration (Fig. 1.9) tether collisions might be naturally prevented. Testing this hypothesis by modelling is computationally challenging because in response to geometric changes of the tether rig, charges continuously redistribute themselves along the tethers to minimise the energy of the electrostatic interaction. In fact, the effects of charge redistribution are so profound that if tethers biased at the same voltage approach each other close enough at some point, their local interaction can even turn from repulsive to attractive.

We have made some rough analytical estimates as well as incorporated Coulomb repulsion approximately in some of our dynamical models simulating tether behaviour. These studies suggest that Coulomb repulsion might not be in general enough to keep the tethers apart form each other, but it seems to contribute significantly to damping of tether oscillations at least in some cases. If the tethers oscillate and therefore periodically approach each other, their charges move back and forth in response, to maintain the same potential. This causes ohmic heating of the tethers. The energy comes from the kinetic and potential energy of the oscillating tethers.

In general, tether oscillations are driven by solar wind variations and they can occur in all types of E-sail. We like to minimise the oscillations because they cause periodic increases in the tensile stress of the tethers. Oscillations are damped by roughly three mechanisms: 1) material damping (loss modulus) of the tether wires, 2) active damping by the E-sail control algorithm, 3) ohmic heating due to tether-mutual Coulomb repulsion as described above.

## 1.5   Miniaturised few-tether E-sails

Instead of flying a traditional monolithic mission to asteroids, one can also consider flying a swarm of smaller spacecraft, each equipped with its own E-sail and studying different asteroids. The main benefits of a swarm mission are that a larger number of asteroids can be reached and that failure of a single spacecraft is not mission critical. The latter property also implies that since the spacecraft needs less internal redundancy, its performance (science output per mass ratio or cost) can be higher.

The main drawbacks of the swarm mission architecture are that the science payload must be small in each spacecraft and that the amount of data that can be returned
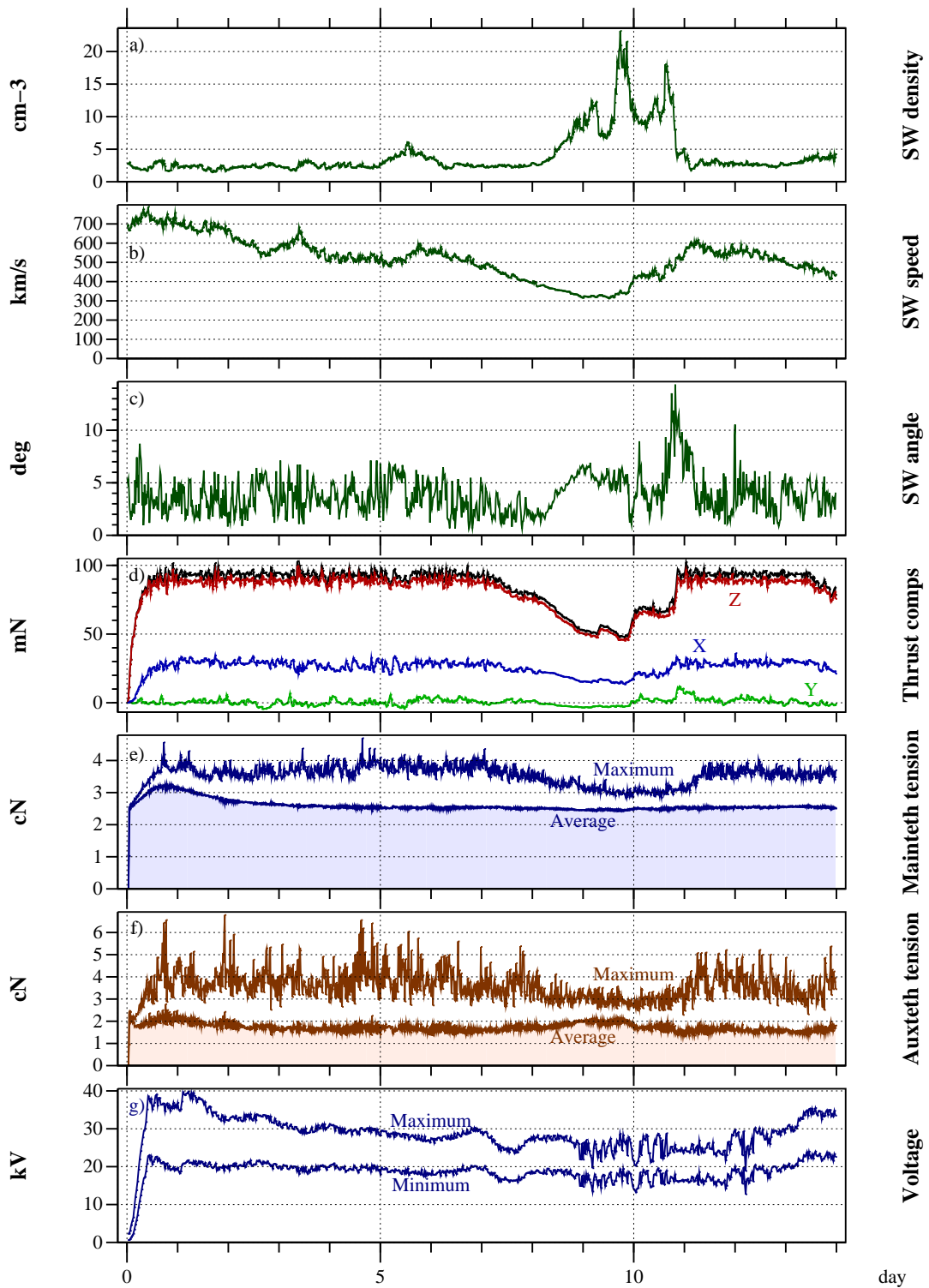
**Figure 1.14:** (a) Solar wind density, (b) solar wind speed, (c) solar wind angle, (d) E-sail thrust components, (e) average and maximum maintether tension, (f) average and maximum auxtether tension, (g) minimum and maximum voltage across tethers.
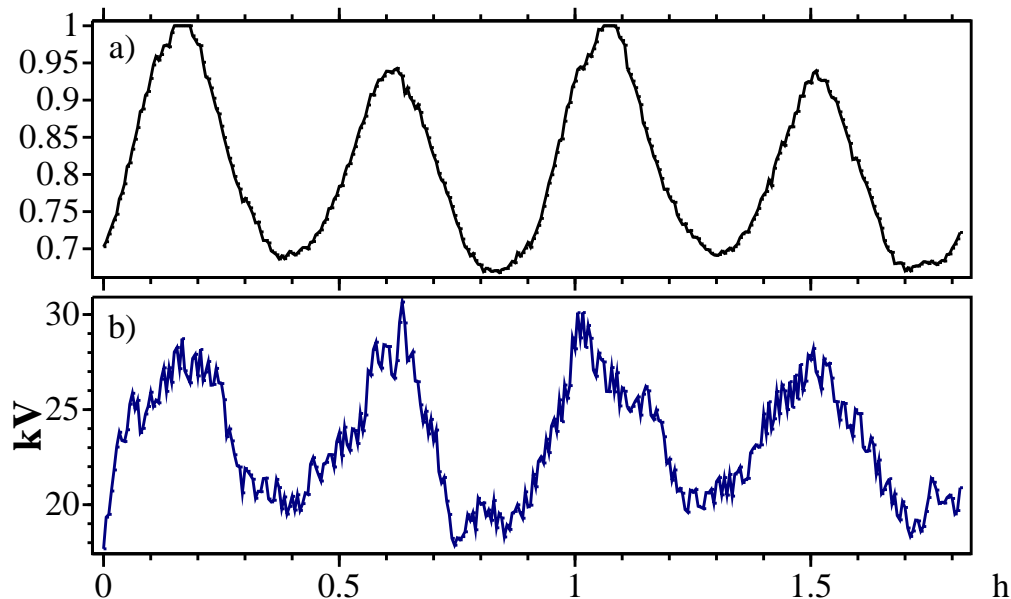
**Figure 1.15:** (a) Single tether throttling factor, (b) corresponding voltage. Approximately two spin periods are shown. Time zero corresponds to $t = 6$ days in Fig. 1.14. The controller implemented in Lua in Appendix B generated this signal from simulated accelerometer and remote unit angular position imager data.

is smaller. To consider the latter point, the data rate that a spacecraft can beam to Earth is proportional to the product of the area of the antenna aperture $A$ and the radio power $P$:

$$\text{datarate} \propto AP. \tag{1.1}$$

The aperture mass scales as $m \propto A^{3/2}$ so that for given mass budget $m$, the aperture area is $A \propto m^{2/3}$. For the radiating power, we have simply $P \propto m$. Then the data rate is

$$\text{datarate} \propto m^{2/3}P \propto m^{5/3}. \tag{1.2}$$

Because the exponent of $m$ in Eq. (1.2) is larger than unity, a monolithic spacecraft can return more data than a swarm of smaller spacecraft of the same total mass, if one assumes that everything else like the employed transmitter band is equal. For example, if one has a swarm of ten satellites, the total amount of returned data is according to Eq. (1.2) smaller by factor $10 \times 0.1^{5/3} = 0.22$, and each spacecraft transmits at a data rate which is $\sim 2\%$ of the monolithic case. Also the operations costs tend to be increased because there are 10 spacecraft to be tracked instead of one. Nevertheless, there are possible strategies to overcome or mitigate these issues, such as using a more advanced communication channel (higher radio frequency or optical) or by making every now and then a near-Earth pass by each spacecraft in the swarm, during which data can be downloaded quickly and at low cost.

A swarm mission is thus one of the options, and if selected, it calls for miniaturisation of the E-sail. Thus we ask the question what is the minimum number of tethers of an E-sail that can still fly well. Our answer to this question is – somewhat preliminarily – that

a single tether is enough, but then one cannot counteract the secular spinrate change due to orbital Coriolis effect by the E-sail effect itself. If one wants a design where the Coriolis effect is counteracted by the E-sail effect, the minimum configuration is a triangular tether rig consisting of three equal-mass spacecraft at the corners, connected by three equal-mass tethers. Next we consider these two options in some more detail.

### 1.5.1 Single tether E-sail

Our single-tether E-sail is composed of a main spacecraft which hosts the payload, the tether reel and the electron gun, and a remote unit at the tip of the tether which hosts only a one-axis attitude control system and two or more cold gas (CG) thrusters. The CG thrusters are used during spin-up phase to provide the angular momentum, and they are also used later during the mission for keeping the spinrate of the tether between acceptable limits.

The secular spinrate evolution due to the orbital Coriolis effect is approximately described by (Toivanen and Janhunen, 2013),

$$\omega(t) = \omega_0 \exp\left(2\pi \frac{t}{\tau_{\text{orb}}} \tan\alpha\right) = \omega_0 \exp\left(\Delta\varphi \tan\alpha\right) \tag{1.3}$$

where $\omega_0$ is the initial spinrate, $\tau_{\text{orb}}$ is the heliocentric orbiting period, $\alpha$ is the sail inclination angle with respect to the solar wind and $\Delta\varphi$ is the angle that the spacecraft has revolved around the sun. Because the centrifugal tether tension is proportional to $\omega(t)^2$, the effect gets large fairly quickly. For example if $\alpha = 35°$, the doubling time of the tether tension corresponds to 28°.5 motion around the sun which in 1 au circular orbit is equivalent to about one month. Hence, implementation of some kind of spin rate control seems important in many mission scenarios.

We make the following additional remarks regarding this spacecraft architecture:

1. To minimise CG propellant consumption, the remote unit should be kept as lightweight as possible. Thus, for example, we place the tether reel in the main spacecraft, not in the remote unit.

2. A typical value for CG delta-v requirement for the remote unit is 10 m/s per each full stop or full start of the spin. Enough cold gas fuel capacity for $\sim 20$ full stops or starts of spin can be expected, which is equivalent to about three revolutions around the Sun (each revolution effectively produces about $2\pi$ spin restarts) if one adjusts the spin continuously. These numbers are only rough guidelines and they depend on many parameters.

3. In asteroid touring, phases of positive and negative sail tilting typically follow each other. If the sequence is quick enough, it might not be necessary not fix the spinrate using CG thrusting before it already gets restored naturally when the sail is oppositely tilted.

### 1.5.2 Triangular E-sail

The triangular E-sail consists of three spacecraft with identical masses and connected together by three tethers of identical length and mass. Thus, the system is geometrically and equilateral triangle. A special property of such symmetrical polygonal E-sail

configurations is that their spinrate does not change [1] when one tilts them by modulating the tether voltages. By modulating the voltages in different ways it is only possible to tilt the spinplane in different directions, but voluntary or involuntary modification of the spinrate is not possible.

A triangular E-sail mission would use CG or other conventional propulsion to deploy the tethers and to set the proper spinrate. After that the E-sail effect would be used to produce propulsion and to incline the spinplane as needed. Despite such manoeuvres the original spinrate would be maintained for a long time. However, *if the spinrate* does get modified for some reason, there is no way to restore it using the E-sail force. The only way of restoration is to use conventional propulsion.

### 1.5.3 Conclusion for miniaturised E-sails

For miniaturised spacecraft, the single-tether configuration is our baseline option because it is simple and does not require splitting the payload into two or more spacecraft. Its drawback is that CG propellant is used to manage the spinrate, but the mission lifetime can nevertheless be rather long.

Reliability concerns are smaller for miniaturised than for full-scale E-sails, since there is a smaller number of subsystems that could potentially fail. In addition, a miniaturised E-sail would be typically part of a swarm mission which provides intrinsic redundancy by the number of spacecraft. This boosts mission reliability further. The biggest question is probably if enough scientific data can be returned at moderate operations cost from a fleet of miniaturised spacecraft operating miniaturised instruments.

Naturally, the CG thruster of the single-tether configuration could also be replaced by a more advanced alternative such as ionic liquid FEEP thruster (subsubsection 1.3.2.1) or a photonic blade (subsection 1.3.3), to provide higher specific impulse and therefore a longer mission.

## 1.6 Reliability and failure modes

In this section we treat reliability engineering of the TI-model E-sail and discuss different failure modes.

### 1.6.1 Reliable reel-out

The tethers are released from spinning reels. The reel is a cylindrical surface on which the tether is wound and which is rotated slowly. Because the tether is under some low centrifugal tension all the time, a passively rotating reel with controlled braking or stopping mechanism is in principle enough and a motor is not strictly necessary. The braking or stopping mechanism could use e.g. a solenoid which is normally off and needs electric power to stop or brake reeling. Duplication of the braking or stopping mechanism is possible. For controlling the mechanism, a sensor which senses reel rotation is needed. It can be e.g. an optical sensor that watches a reel which has black and white stripes. A separate launch lock for the reel is also needed which is released once in the beginning.

---

[1]Assuming straight tethers, i.e. neglecting tether oscillations

In addition to or in place of braking/stopping mechanisms, one can have a number of redundant motor units that are normally kept away from the reel by spring force, but which can be pressed against the reel e.g. by a solenoid so that the motor can turn the reel.

By these design concepts it should be possible to make a reel which rotates reliably and in a controlled way during tether deployment.

Deployment could also go wrong if the tether somehow gets stuck into itself. However, this can be made unlikely by proper choice of the tether geometry.

## 1.6.2    Bidirectional reeling and duplication of tethers

If the main tethers are opened from both ends, a reel failure causes a shortening of all tethers by an amount which is $50\%$ in the worst case and $0\%$ in the best case, the expected value being $75\%$. No mass asymmetry between remote units is induced by a reel failure. This approach enables the mission to succeed and fly despite reeling failure, just with moderately reduced propulsive performance. This is our recommended strategy for the main tethers.

It would also be possible to fully double all tethers, which would ensure full tether rig size even in case of reeling failure. However, a mass asymmetry between remote units would then arise which would probably dictate us to reduce the propulsion anyway. Since also the mass overhead of doubling all tethers is significant, full doubling of maintethers is not our baseline choice.

The flight-time dynamics is rather sensitive to the correct length of the auxtethers. For this reason we recommend bidirectional reeling and full dupling of the auxtethers. The mass overhead and mass asymmetry in case of reeling failure are smaller than in case of maintethers because the auxtethers are shorter.

## 1.6.3    Micrometeoroid tolerant tethers

The auxtether ring must not be broken or else the tether rig collapses. A maintether breakage event, although less dramatic, is also highly undesirable. A straightforward solution to ensure that tether never breaks is to simply add enough subwires to the tethers. Addition of each subwire increases the tether's expected lifetime exponentially. Four subwires is normally enough, and adding a fifth subwire should remove any chance of tether breakage.

Let us estimate the probability of tether breakage using a simple analytical model. Assume that a tether (total length $L = 2000\,\text{km}$) is made of $N = 4$ parallel wires where each subwire has length $L_1 = 5\,\text{cm}$ and the subwires are distance $h = 2.5\,\text{cm}$ apart. If the wire diameter is $d_w = 25\,\mu\text{m}$ and if one assumes that a colliding particle of diameter $d/3$ can cut the wire, then the relevant quantity is the flux $\Phi_1$ of micrometeoroids of diameter $8.3\,\mu\text{m}$ of larger. According to the widely used (Grün et al., 1985) micrometeoroid model, this flux is $\Phi_1 = 112\ \text{m}^{-2}\ \text{a}^{-1}$ at 1 au (without Earth's gravitational focussing, i.e. far from Earth). The probability $P_1$ that a single wire segment (length $L_1$, diameter $d_w$) breaks in mission time $\tau = 5\,\text{a}$ due to impact is proportional to the wire segment's surface area:

$$P_1 = \pi d_w L_1 \Phi_1 \tau = 2.20 \cdot 10^{-3}. \qquad (1.4)$$

The probability that all $N$ wires break at the same unit cell so that the tether is cut is $P_1^N$. The tether as a whole has $L/L_1 = 4 \cdot 10^7$ unit cells and the tether breaks if any of the unit cells breaks. So the probability that the tether is cut over 5 years is by cutting of the subwires (sw) is

$$P_{\text{sw}} = P_1^N \left( \frac{L}{L_1} \right) = 0.095\,\%. \tag{1.5}$$

If the mission time is increased, the probability increases faster than linearly. For example if the mission length is 10 years, then $P_1 = 4.41 \cdot 10^{-3}$ and $P_{\text{sw}} = 1.5\,\%$. If the mission time is 15 years, $P_1 = 6.61 \cdot 10^{-3}$ and $P_{\text{sw}} = 7.7\,\%$.

The tether can also be cut by a single large meteoroid which cuts all subwires at once. This probability depends on the flux of 2.5 cm meteoroid which is $\Phi_2 = 1.8 \cdot 10^{-9}$ m$^{-2}$ a$^{-1}$. The relevant area is now the area of the whole tether $\pi h L$ so that the cutting probability of the single blow (SB) mode is

$$P_{\text{SB}} = \pi h L \Phi_2 \tau = 0.14\,\% \tag{1.6}$$

in 5-year mission. The single blow probability grows linearly with time. For 5-year mission, the overall probability for tether breaking is the sum of the subwire and single blow modes,

$$P = P_{\text{sw}} + P_{\text{SB}} = 0.24\,\% \tag{1.7}$$

for a 5-year mission.

If the tether is made wider (narrower), the single blow risk decreases (increases) and the subwire cutting risk increases (decreases). For a given mission length, given $N$ and given micrometeoroid environment, there is an optimal tether width which minimises the total probablity.

It is thought that in the asteroid belt, larger micrometeoroids are somewhat more common and smaller micrometeoroids less common than at 1 au, relatively speaking. Therefore, the optimum tether is likely to be somewhat wider in the asteroid belt than at 1 au.

It should be possible in theory and also in practice to make the tether essentially non-breakable, if not by other means but by adding the fifth subwire while increasing the width of the tether somewhat. Adding a fifth wire would increase the mass of the tether by only 25 %.

One should also take care that the tether is not planar after deploying it in space. A planar tether would be more vulnerable to small micrometeoroids flying in the tether's plane than what the above calculations indicate. Also, when one subwire is cut, the geometry of the tether changes locally. If this change is such that it brings the wires closer together, the tether is then locally more vulnerable to single blow cutting mode than the intact tether.

### 1.6.4 Flight algorithm and sensors

The flight algorithm tracks the remote unit positions with 20 s time resolution and 0.17° angular resolution. The required imaged domain is 360° in azimuth and about 30° in latitude. To tolerate exceptional situations where the main spacecraft's attitude

is for any reason not be aligned with the tether rig, the latitudinal width of the imaged domain can be made larger. Pixels are cheap so doing this produces negligible mass overhead. The remote units are seen in the imager as magnitude $\sim 4$ stars if the solar distance is 2.5 au. Here we assumed that the remote unit's optical signature corresponds to a $4 \times 4$ cm sun-illuminated white square.

The flight algorithm also uses a vector accelerometer to measure the instantaneous thrust produced by the tether rig. The assumed accelerometer noise is $1.5 \cdot 10^{-5}\mathrm{m}/(\mathrm{s}^2\sqrt{\mathrm{Hz}})$. For example, the Colibrys SF-1500 accelerometer has 5 times better noise characteristic than this.

The algorithm takes as inputs the wanted thrust magnitude, the wanted orientation of the spin axis (which determines thrust direction) and the wanted rotation speed of the tethers. The actuating mechanism is modulation of the individual tether voltages. Spinplane turning takes typically $\sim 10$ hours and 5% spinrate modification takes typically a few days. Spinrate control is required to overcome the natural Coriolis acceleration which is due to the orbiting around the sun with an inclined spinning sail. The provided spinrate control authority exceeds the requirement manyfold.

The imaging system sees the remote units as starlike points. The remote units can be distinguished from stars because unlike the more or less pointlike remote units, stars are seen by the spinning platform as $\sim 2°$ (13 pixels) long line segments. The flight algorithm also needs to identify the remote unit, i.e., to recognise which is which. A straightforward method is to paint one or more remote unit with different colour than the other ones and to use colour imaging. An alternative approach is to ensure that the units are tracked continuously so that one never loses the knowledge which is which. Short breaks in tracking are not harmful because the units move relatively slowly. Furthermore, according to simulations, during flight the units typically do not drift far from their equilibrium points. Thus during flight the units can also be recognised simply based on their observed location.

### 1.6.5 Failure mechamisms

#### 1.6.5.1 A reel stops deploying the tether

A tether reel could theoretically stop deploying the tether for two reasons:

1. The reel stops turning because the bearing is mechanically damaged. We think that this can be made unlikely.

2. The reel stops turning because the motor which rotates the reel fails. This can be made unlikely by duplicating the mechanism that rotates the reel.

3. The reeled itself gets stuck with itself. This is probably also very unlikely, although it has not yet been demonstrated in practice because very long tethers have not yet been manufactured.

Our baseline approach is to use full doubling for auxtethers and bidirectional reeling for maintethers. Then a reeling failure with an auxtether is not harmful (except causing a small mass asymmetry) and a reeling failure with maintether causes 0-50 % reduction in total tether length and hence in propulsive performance. However, it may be possible to recover some of the lost performance by increasing the tether voltages in most solar wind conditions. This depends mainly on the hardware limit of the electron gun voltage.

### 1.6.6 Remote Unit fails during deployment

If a Remote Unit fails during deployment, deployment should be stopped at that point. The sail can still be used, but with reduced performance depending on how much of the tethers were deployed before the failure.

### 1.6.7 One of the Remote Units fails to detach from main spacecraft

If a Remote Unit fails to detach from the main spacecraft, it means total failure of the E-sail propulsion system.

### 1.6.8 Tether is cut by meteoroid

1. A main tether is cut by a meteoroid. If the broken tether piece collides and breaks other tethers on its way out, the outcome is hard to predict and is possibly fatal. A propulsive evasive manoeuvre ($\sim 2$ m/s chemical burn) might help the situation by pulling the other tethers away from the dangerous area. The broken piece(s) should also be jettisoned. However, the probability of tether getting severed is already quite small if four wires are used, and adding a fifth wire should make such risk negligible.

2. An auxtether is cut by a meteoroid. This is always a fatal condition because the tether rig then collapses to one side of the spacecraft and essentially loses its propulsive capability. In FGPB designs this failure mode does not exist because there are no auxtethers.

Our current baseline thinking is that if we use an auxtethered design, we use tether doubling to guard ourselves against reeling failures and use enough multiplicity and spatial separation in tether wire geometry so that tether cuts are unlikely. If we use an FGPB design, reeling failures are not very problematic, tether cuts can be made unlikely as in auxtethered designs, Remote Unit failures can be made unlikely by redundant engineering, and as a last resort we can invoke a predefined recovery procedure where other tethers are moved to different spinplane and the failed tether is jettisoned.

## 1.7 E-sail posed platform requirements

The E-sail poses some requirements on the platform that it is propelling:

1. The E-sail equipped spacecraft is a slow spinner (spin period typically tens of minutes) instead of being a three-axis stabilised spacecraft as most solar system missions. Spinning has implications especially to pointing of science instruments and telemetry antennas. Some instruments also benefit from spinning, and spinning may also decrease the use of ACS propellant and make implementation of the safe mode easier.

2. In E-sail designs having auxiliary tether (Section 1.3.2), the auxiliary tether must be stored somewhere between the Remote Units in launch configuration. In the FGPB design, this requirement does not exist.

3. There must be enough clearances to prevent the tethers from touching any parts of the spacecraft, including deployed solar panels, under any conditions. Plumes of attitude and orbit control system (AOCS) thrusters of the main spacecraft, if any, must be directed so that they do not damage the tethers.

4. High voltage parts are generally sensitive to outgassing, because strong enough outgassing may produce intermediate density gas which promotes arcing. By intermediate density gas we mean gas where the mean free path of electrons colliding with neutrals is shorter than the system size but also long enough that electrons can gain enough energy from the imposed electric field to cause ionisation and thereby successive electron multiplication. Therefore, possible outgassing from the payload must not have access to the E-sail's high voltage parts including the electron gun and its voltage source.

5. If flying through eclipse, E-sail tethers undergo rapid temperature changes because the tethers are thin and therefore they reach the environmental radiative equilibrium temperature quickly. Because the tethers are long, their thermal expansion is significant. Preliminary analysis has indicated that in extreme cases and depending on many parameters, eclipsing might cause harmful oscillations of the tethers. If eclipsing would be needed by a mission (fortunately probably not the case with asteroid missions), then these effects should be looked at in more detail.

6. The gravity gradient of a planet or asteroid may disturb the dynamics of the rotating tether rig. The gravity gradient is proportional to $M/r^3$ where $M$ is the mass of the body and $r$ is the distance from its centre of mass. Because $M$ scales as $\sim \rho R^3$ where $R$ is the body radius, the gravity gradient scales as $\sim \rho(R/r)^3$, that is, it is independent of the mass of the body but only depends on the *relative* distance $r/R$ and on the material density $\rho$. Our preliminary calculations indicate that in case of Earth, gravity gradient might be a problem below about 5000 km altitude, that is, at $r/R \approx 2$.

7. When manoeuvring in an asteroid's vicinity, one must keep a safety distance which ensures that the tethers do not collide with the body.

## 1.8 Preferred design and validation roadmap

In short, various pros and cons of different E-sail design options are the following.

− The ESAIL FP7 project recommended the stretched auxtether model (Fig. 1.10a) with cold gas or IL-FEEP thrusters. The total impulse provided by cold gas option is generally not sufficient for an asteroid touring mission because the mission orbits the sun at least once and therefore needs significant spinrate management to counter the orbital Coriolis effect. The IL-FEEP thruster remains in principle a viable alternative, but its TRL is lower.

− The photonic blade option (Fig. 1.11, Section 1.3.2.2) is more attractive than a thruster because it is propellantless as the E-sail itself and hence does not limit the mission time. Long-life, tribology-free twisting actuation of the blade could

use e.g. a low torque thread, a permanent magnet and an electromagnet. The blade is also low tech and low cost. The main issue with the photonic blade is that *if* duplication of the main tethers is considered to be necessary for reliability reasons, then for geometric reasons the spare reel must be located in a separate unit between the blade and the main tether. The extra unit hosting the spare reel only needs to function during sail deployment, however.

− The electric auxtether option (Section 1.3.2.3) is a simple, low cost and lightweight solution and is also compatible with redundant, bidirectional reeling. A drawback is that according to simulations made in ESAIL project, centrifugally stabilising auxtethers do not stabilise the system quite as efficiently as stretched auxtethers, for a given ratio of tether's centrifugal tension versus the E-sail thrust that it generates. To scale the electric auxtether option up towards 1 N thrust at 1 au, one might need to increase the tether length beyond 20 km in order to limit the number of tethers to be clearly less than 100. The electric auxtether option is the newest E-sail concept; it looks promising, but more work is needed.

− Using the freely guided photonic blades (FGPBs, Fig. 1.12, Section 1.3.3) is in principle an elegant solution. The needed area of the blade is bigger than in the auxtethered photonic blade case. For 20 km tethers at 1 au, 3-4 m$^2$ is enough in the auxtethered case while 16-20 m$^2$ must be used in the FGPB case. Because the photonic thrust decays as $1/r^2$ while the E-sail thrust only as $1/r$, the photonic blade area in principle scales linearly with the maximum solar distance of the mission. Hence for an asteroid mission going to 3 au the blades would be 3 times bigger than the numbers listed. An unattractive feature of FGPB is the fact that it requires continuous active control of all blades. In case of reeling failure or Remote Unit failure, the other tethers must be manoeuvred so that cutting the offending tether from the main spacecraft end can be done without risk of collision with other tethers. A financial benefit of FGPB is that a validation mission would need only one tether and could be smaller and cheaper than in the auxtether approach where the minimum number of tethers is about eight.

Our target is to point out at least one E-sail model which is able to meet the requirements of a relevant asteroid mission considered in later work packages, looks technically attractive to implement and is compatible with the M-class financial constraints.

We will also develop a validation roadmap for the selected design(s) with rough cost estimation.

# Chapter 2

# WP2: Candidate missions

## 2.1 Objectives and background

The objective of WP2 is to come up with a number of scientifically promising multi-asteroid mission concepts that can be expected to be implementable with the E-sail and be compatible with the M-class cost cap.

The objective of WP3 is to select one mission for a more detailed study in WP4 and to motivate the selection by scientific and technical reasons.

In this document, we do not present the options comprehensively, but instead concentrate on their relevant differences to make comparisons and to make the selection of the concept to be analysed in more detail in WP4.

### 2.1.1 Asteroids as mission targets

Among solar system objects, asteroids are scientifically and practically very important targets for space missions. Asteroids contain also material from the period when the solar system was young, because unlike on planets where material has been typically heavily processed by melting, differentiation, erosion etc., on asteroids the primordial material is still partly intact. Asteroids are also literally a quite manyfold target, no two asteroids are exactly alike. On the other hand, many main belt asteroids belong to some asteroid family, i.e., they are collisional fragments of some parent body.

Asteroids are important objects to study not only for scientific reasons, but also because they are a threat to Earth in the form of asteroid impacts. The asteroid threat stands apart from other natural disasters such as earthquakes and volcanic eruptions because asteroid collisions would be in principle preventable by orbit deflection. Also, it would be possible to mine asteroid material and process it into rocket fuel, precious platinum group metals and large space constructions. The products could be transported by E-sails to various solar system orbits and destinations, including the Earth.

Both addressing the impact threat and asteroid mining need basic research and mapping of asteroids. Mining needs mineral prospecting while orbit deflection by low-thrust propulsion needs knowledge about the asteroid's rotational state and basic data of its mechanical properties for harpooning or other form of attachment. As an alternative to gradual deflection by low-thrust propulsion, one can deflect an asteroid by impactors that could also be E-sail propelled. Impact deflection needs information about the object's fragility, because one does not want to break the body apart.

Besides space missions, our knowledge of asteroids stems from mainly three traditional sources. *Meteorites* are typically modified asteroid fragments; for example from

the study of meteorites we know that platinum group metals are much more common on asteroids than in Earth's crust. *Optical and infrared astronomy* yields reflectance spectra and lightcurves; the spectra tell about surface minerals and are the basis for asteroid classification while lightcurves tell about rotation state and shape. Finally, large *radars* have been used successfully to reveal detailed shape of some of those NEO asteroids that have come to Earth's vicinity.

Space missions can yield much better data than the traditional sources. Table 2.1 lists missions that have been made or are planned to make flyby, orbiting, landing or sample return studies of asteroids or comets (comet flybys are however excluded). As seen from the table, a lot has been done, but a lot also remains to be done. For example, many of the main belt's important asteroid families have not yet been targeted for missions and the same holds for Jupiter Trojans.

**Table 2.1:** Asteroid missions. Missions written in *italic* are planetary or lunar missions that made asteroid flybys as bonuses.

| Asteroid(-Family) | au | ∅/km | Type | Flyby dist. etc. | Mission |
|---|---|---|---|---|---|
| 951 Gaspra-Flora | 1.8-2.6 | 12 | S | 1600 km | *Galileo 1991* |
| 243 Ida-Koronis | 2.7-3.0 | 30 | S | 2400 km | *Galileo 1993* |
| 253 Mathilde | 1.9-3.4 | 50 | C | 1200 km | NEAR 1997 |
| 9969 Braille | 1.3-3.4 | 1.5 | Q | 26 km | DeepSpace-1 1999 |
| 2685 Masursky-Eunomia | 2.3-2.9 | 15 | S | 1.6e6 km | *Cassini 2000* |
| 433 Eros | 1.1-1.8 | 17 | S | lander | NEAR 2001 |
| 5535 Annefrank-Augusta | 2.0-2.4 | 5 | S | 3000 km | Stardust 2002 |
| 25143 Itokawa | 0.95-1.7 | 0.4 | S | lander(+samp) | Hayabusa 2005 |
| Comet Tempel 1 | 1.5-4.7 | 6 | C | impactor | DeepImpact 2005 |
| 132524 APL | 1.9-3.3 | 2.3 | S | 1e5 km | *NewHorizons 2006* |
| 2867 Steins | 2.0-2.7 | 4.6 | E | 800 km | Rosetta 2008 |
| 21 Lutetia | 2.0-2.8 | 100 | M | 3000 km | Rosetta 2010 |
| 4 Vesta-Vesta | 2.2-2.6 | 500 | V | orbiter | Dawn 2011 |
| 4179 Toutatis | 0.94-4.0 | 3 | S | 3 km | *Chang'e-2 2012* |
| 67-P C-G | 1.2-5.7 | 4 | C | lander | Rosetta 2014 |
| 1 Ceres-interloper | 2.6-3.0 | 1000 | C | orbiter | Dawn 2015 |
| 1999 JU3 | 0.96-1.4 | 1 | C | sample return | Hayabusa-2 2018 |
| 101955 Bennu | 0.9-1.36 | 0.5 | B | sample return | OsirisRex 2022 |

Table 2.2 summarises the scientific instrumentation used on the missions. Optical and near infrared (NIR) imaging and some form of spectral capability has been employed in all missions. These instruments can reveal the morphology, main geologic units and surface mineralogy of the body. Mapping of the asteroid's geometric shape can also be done by laser altimetry. X-ray and UV imaging and spectroscopy can further improve the recognition of surface minerals.

To learn what lies below the topmost atomic layer, one needs additional instruments. Most missions have used precise monitoring of the Earth radio link to constrain the mass distribution of the body (not listed in Table 2.2 because it incurs almost no mass or power penalty). Imaging the body in thermal infrared allows for mapping the surface temperature which yields information about the surface layer's thermal inertia and thereby constrains its physical properties typically a few centimetres deep. Measuring the energy spectrum of cosmic ray spallated neutrons yields information about the

**Table 2.2:** Instrumentation of dedicated asteroid missions. DI=DeepImpact, HB=Hayabusa, ORex=OsirisRex, MP-R=MarcoPolo-R. Not yet accomplished experiments are denoted in greyscale: HB-2 has been launched, ORex is planned and MP-R has been proposed.

| Mission: | NEAR | Rosetta | DI | Dawn | HB-1 | HB-2 | ORex | MP-R |
|---|---|---|---|---|---|---|---|---|
| Launch: | 1996 | 2004 | 2005 | 2007 | 2003 | 2014 | 2016 | |
| optical+NIR imager | × | × | × | × | × | × | × | × |
| IR spectrograph | × | × | × | × | × | × | × | × |
| UV | | × | | | | | | |
| mm-wave | | × | | | | × | | |
| X-ray | × | × | | | × | | × | |
| gamma ray/neutron | × | | | × | | | | |
| laser altimeter | × | | | | × | × | × | |
| magnetometer | × | × | | | | × | | |
| radar | | × | | | | | | |
| dust | | × | | | | | | |
| neutral part./gas | | × | | | | | | × |
| plasma | | × | | | | | | |
| surface in situ | | × | | | | × | | |
| minilander | | | | | × | ×× | | |
| impactor | | | × | | | × | | |
| sample return | | | | | (×) | × | × | × |

degree of neutron thermalisation which is a measure of light element abundance in a ∼ 1 m surface layer. Measuring cosmic ray triggered gammas can also be used to recognise elemental composition of a surface layer. Measuring the magnetic field, if any, can also constrain the asteroid's internal composition. A radar can be used to measure the conductivity and permittivity distribution of the interior of the body. Rosetta employs the radar in a power efficient transmission geometry where the body is located between the transmitter (orbiter) and the receiver (lander).

To learn in more detail what lies below the surface, more elaborate strategies are needed. A lander can employ a drill to take samples of the subsurface (Rosetta), or a high speed impactor (DeepImpact, Hayabusa-2) can be used to create an impact plume and impact crater which can be studied from a distance by the usual imaging and spectral instruments. Sample return is the ultimate way of making detailed studies of limited amount of material. Hayabusa-2 will also attempt to take subsurface samples from the created impact crater.

Table 2.3 lists some examples of interesting mostly main belt asteroids. Any Jupiter Trojan asteroid is interesting because none has been studied and their origin and composition are largely unknown; in Table 2.3 we list an exemplary Trojan which is among the more accessible ones in terms of orbital characteristics. All NEOs are interesting and practically important (many are potential future Earth impact hazards and many would be potential targets for asteroid mining as well), but for brevity we list only one, KY-26, in Table 2.3.

**Table 2.3:** Some interesting asteroids.

| Asteroid(-Family) | au | $i/°$ | $\emptyset$/km | Type | Interest |
|---|---|---|---|---|---|
| 1998 KY26 | 1.0-1.5 | 1.5 | 0.03 | C | Small, water? |
| 434 Hungaria | 1.8-2.1 | 23 | 20 | E | Hungaria family parent |
| 8 Flora-Flora | 1.9-2.5 | 6 | 130 | S | Flora family parent |
| 15 Eunomia-Eunomia | 2.1-3.1 | 12 | 270 | S | Eunomia family parent, largest S-type |
| 2 Pallas-Pallas | 2.1-3.4 | 35 | 500 | B | Pallas family parent, largest B-type |
| 16 Psyche | 2.5-3.3 | 3 | 200 | M | Largest M-type |
| 158 Koronis-Koronis | 2.7-3.0 | 1 | 35 | S | Koronis family parent |
| 221 Eos-Eos | 2.7-3.3 | 11 | 100 | K | Eos family largest member |
| 704 Interamnia | 2.6-3.5 | 17 | 350 | F | Large, high density |
| 24 Themis-Themis | 2.7-3.5 | 1 | 200 | C | Themis family parent, surface ice |
| 10 Hygiea-Hygiea | 2.8-3.5 | 4 | 430 | C | Hygiea family parent, largest C-type |
| 31 Euphrosyne-Euphr. | 2.4-3.9 | 26 | 250 | C | Euphrosyne family parent |
| 52 Europa | 2.8-3.4 | 7 | 320 | C | Large interloper in Hygiea family |
| 65 Cybele-Cybele | 3.1-3.8 | 3.5 | 270 | C | A parent of Cybele family |
| 87 Sylvia-Cybele | 3.2-3.8 | 11 | 290 | X | A parent of Cybele fam., 2 moons |
| 511 Davida | 2.6-3.8 | 16 | 230 | C | Large |
| 3 Juno | 2.0-3.6 | 13 | 230 | S | Parent of Juno clump |
| 2207 Antenor | 5.0-5.2 | 7 | 85 | D | 'Accessible' large Trojan |

## 2.2   E-sail posed platform requirements

The E-sail poses some requirements on the platform that it is propelling:

1. **Slow spinning platform**. The E-sail equipped spacecraft is a slow spinner (spin period typically tens of minutes) instead of being a three-axis stabilised spacecraft as most solar system missions. Spinning has implications especially to pointing of science instruments and telemetry antennas. Some instruments also benefit from spinning, and spinning may also decrease the use of ACS propellant and make implementation of the safe mode easier.

2. **Geometric constraint**. In E-sail designs having auxiliary tether, the auxiliary tether must be stored somewhere between the Remote Units in launch configuration. In the FGPB design, this requirement does not exist.

3. **Geometric constraint**. There must be enough clearances to prevent the tethers from touching any parts of the spacecraft, including deployed solar panels, under any conditions. Plumes of attitude and orbit control system (AOCS) thrusters of the main spacecraft, if any, must be directed so that they do not damage the tethers.

4. **Outgassing**. High voltage parts are generally sensitive to outgassing, because strong enough outgassing may produce intermediate density gas which promotes arcing. By intermediate density gas we mean gas where the mean free path of electrons colliding with neutrals is shorter than the system size but also long enough that electrons can gain enough energy from the imposed electric field to cause ionisation and thereby successive electron multiplication. Therefore, possible outgassing from the payload must not have access to the E-sail's high voltage parts including the electron gun and its voltage source.

5. **Eclipses**. If flying through eclipse, E-sail tethers undergo rapid temperature changes because the tethers are thin and therefore they reach the environmental radiative equilibrium temperature quickly. Because the tethers are long, their thermal expansion is significant. Preliminary analysis has indicated that in extreme cases and depending on many parameters, eclipsing might cause harmful oscillations of the tethers. If eclipsing would be needed by a mission (fortunately probably not the case with asteroid missions), then these effects should be looked at in more detail.

6. **Operating near massive body**. The gravity gradient of a planet or asteroid may disturb the dynamics of the rotating tether rig. The gravity gradient is proportional to $M/r^3$ where $M$ is the mass of the body and $r$ is the distance from its centre of mass. Because $M$ scales as $\sim \rho R^3$ where $R$ is the body radius, the gravity gradient scales as $\sim \rho(R/r)^3$, that is, it is independent of the mass of the body but only depends on the *relative* distance $r/R$ and on the material density $\rho$. Our preliminary calculations indicate that in case of Earth, gravity gradient might be a problem below about 5000 km altitude, that is, at $r/R \approx 2$.

7. **Orbital constraint**. When manoeuvring in an asteroid's vicinity, one must keep a safety distance which ensures that the tethers do not collide with the body.

8. **Orbital constraint**. When manoeuvring in an asteroid's vicinity, for maximum safety the E-sail platform should remain outside the asteroid's Hill sphere to avoid collision of the tethers with potential asteroid moons.

## 2.3 Mission categories

At top level, we classify the missions as follows:

1. Dawn-type simple remote sensing mission.

2. Flyby missions.

   - For example a fleet of nanospacecraft, each making a flyby of 6-7 asteroids.

3. Single-asteroid inspector spacecraft.

   - Optionally with E-sailed sample return unit.

   2a Inspector spacecraft released from E-sail mothership.

   2b Inspector spacecraft uses E-sail, jettisoned upon arrival.

4. Reusable inspector spacecraft.

   - Inspector spacecraft returns from the asteroid and docks with the E-sailed mothership which gives it a ride to the next asteroid.

The following points are relevant when considering which mission architectures are the most promising:

1. Bringing the E-sail inside the Hill sphere of the asteroid carries some risk of collision between the tethers and possible small unseen moons of the asteroid. Because of this, we do not prefer doing orbital remote sensing of the asteroid from an E-sail platform: remote sensing would benefit from close distance which would however be in conflict with platform safety.

2. The E-sail platform's attitude is fixed by the propulsion system so that if instrument pointing or high-gain antenna (HGA) are needed on the platform, they require gimballing.

3. Unless actively stabilised, an E-sail platform's attitude tends to wobble at 1° amplitude and a few arcminutes per second rate. Instruments on the platform that require accurate pointing call for active stabilisation.

4. Shortening the distance to the target can be quite beneficial. For example, halving the observation distance enables two times smaller aperture diameter, 4 times smaller aperture area and 8 times more lightweight imaging instrument.

5. Telemetry A small platform is less efficient in doing deep space telemetry than a large platform.

These arguments give the motivation to prefer, whenever possible, mission architectures that separate spatially or temporally the science instruments from the opened E-sail.

There is also the choice whether to have one large science spacecraft or several smaller ones. The following points are then relevant:

1. The telemetry bitrate is proportional to available mass raised to power 5/3 (Jan-hunen and Toivanen, 2016, WP1 report, section 5, p. 19). Scaling of power gives a linear relationship and scaling of the high-gain antenna structure gives the rest. Thus a single large platform is more efficient at doing telemetry than a fleet of small platforms with the same total mass. The difference is not dramatic, how-ever: splitting the platform into two, for example, still produces $2 \times 0.5^{5/3} = 63\,\%$ of the original telemetry rate.

2. A single large platform may be less efficient for doing science if risk avoidance prevents undertaking scientifically valuable but slightly risky operations such as low altitude hovering, surface landing, surface hopping and sample collection.

3. The E-sail is novel technology whose qualification starts from small units. Thus the lower the required E-sail thrust is (per spacecraft), the easier it is to get the mission flying regarding resources and time.

The first argument favours large platforms, the other arguments favour small platforms. Thus a compromise must be sought.

### 2.3.1   Science instrument portfolio

The main types of science instruments that have been used to study asteroids are the following:

1. **Optical imaging** is the workhorse instrument. It reveals the asteroid's geometric shape and reveals certain details about the surface materials. Miniaturisation of the instrument is possible if one goes close to the target. Recognising geologic units from the images may tell about the asteroid's interior, for example whether the object is a rubble pile or a monolithic body. Small crater counts tell about surface age. Large craters tell about how big impact the body has withstood with-out shattering, which is relevant information for planetary defence. The optical wavelength range is convenient to use because our eyes can view it directly, but also – and more fundamentally – because the sun produces the peak illuminating photon power at optical wavelengths.

2. A **near infrared (NIR) spectrometer** can be used for recognising surface min-erals. For example the presence of water in the surface minerals can be recognised. The water feature cannot be observed from the ground because the atmospheric water vapour masks the signal so space-based instruments are required.

3. A **thermal infrared instrument** can be used for measuring the surface's thermal inertia (e.g.. how quickly the surface temperature drops when the surface goes into shadow). Thermal inertia is one parameter which helps constraining the nature of the surface. For example a loose regolith has a different thermal inertia than a solid rock.

4. A **UV instrument** can also help in recognising surface minerals.

5. An **X-ray** instrument can recognise surface elements from their X-ray fluores-cence. The illumination is provided by solar X-rays. The sun's X-ray output is highly variable and one may have to wait for suitable flare activity to get proper data.

6. A **gamma ray spectrometer** can recognise elements in the uppermost $\sim 1$ m layer from their characteristic gamma radiation. The illumination source is the cosmic ray flux. Long integration times are typically required and purity requirements may arise for spacecraft materials.

7. A **neutron instrument** can measure how much hydrogen is present in the uppermost $\sim 1$ m layer. Long integration times are typically required and purity requirements may arise for spacecraft materials.

8. A **magnetometer** tells about the presence of ferromagnetic elements in the body. A magnetometer is a simple instrument, but it requires that the spacecraft is magnetically clean or that the magnetometer is placed on the tip of a boom.

9. A soil-penetrating monostatic or multistatic **radar** is among the few instruments that can see the asteroid's deep interior.

10. **Precise orbit determination** using the telemetry radio link (the so-called radio science experiment) can be used to measure the asteroid's gravity field and therefore the internal mass distribution. This is another way to gain information from the interior of the asteroid.

11. A **laser altimeter** can measure the geometric shape of the asteroid directly. Optical images can, however, also yield this information if mathematical inversion is used.

12. If the asteroid is active (produces gas and dust), the released substances can be analysed by special **in situ instruments** in orbit, as was done by Rosetta.

13. By **landing** one can examine small details on the body at a particular location. A lander can change location by **hopping**. Hopping does not require any moving external parts and does not consume propellant. Each hop taken is also a new risk, but in case of fleet missions, such risks are more tolerable than in the traditional large monolithic platforms.

14. **Sample return** is scientifically very valuable, because the sample's complete and accurate elemental, isotopic, minerological and micromorphological composition can be analysed in a large ground-based laboratory. The samples can be taken from the surface regolith (loose grains of the surface) or extracted from the subsurface. **Regolith sampling** is easier than **subsurface sampling**, but has the drawback that the regolith has suffered from space weathering and is thus not quite pristine any more. Sample collection is eligible to miniaturisation and very small reentry capsules are being developed in Europe (MIRKA2 in Stuttgart Institute of Space Systems).

Not all instrument types are needed in order to have a comprehensive study of the asteroid. In particular, sample return has the potential to make many of the other instruments unnecessary, but in order to do so, samples should likely be collected from more than one location. A mission with optical+NIR spectral imaging, precise orbit determination and sample return from multiple locales, some of which are from the subsurface, would reveal the asteroid's shape, geologic units, surface mineral map, internal mass distribution and accurate composition and minerology at selected points.

Such information is comprehensive enough to reveal the role that the asteroid played in solar system history as well as key data for asteroid mining and planetary protection.

If the asteroid is likely to contain subsurface water, a neutron instrument would be a relevant addition. If the internal structure is of high interest, a radar would be beneficial, especially if there are two or more spacecraft so that the radar can be multistatic.

## 2.4 Single spacecraft Dawn-type mission

For getting a rough estimate about the mass budget of E-sail propelled spacecraft, let us consider NASA's Dawn mission as an example and calculate how much would be the launch mass if an equivalent mission is made with E-sail technology. Dawn's mass budget is given in Table 2.4, (Dawn, 2016).

**Table 2.4:** Mass budget of NASA's Dawn mission.

| System | kg | Explanation |
|---|---|---|
| Structure | 108 | Structural and mechanical parts |
| IPS | 129 | 92 mN ion propulsion system dry mass |
| EPS | 204 | Electric power system, 10 kW max at 1au |
| ACS | 37 | Attitude control system |
| RCS | 14 | Reaction control system dry mass |
| TCS | 44 | Thermal control system |
| CDHS | 21 | Command and data handling system |
| Telecom | 28 | Telecommunication subsystem |
| Harness | 82 | Cables and connectors |
| Balance | 13 | |
| Dry spacecraft bus | 680 | Sum of the above |
| FC | 11 | Framing Camera, 2-fold cold redundancy |
| GRaND | 10 | Gamma Radiation and Neutron Detector |
| VIR | 24 | Visible and InfraRed spectrometer |
| Science payload | 45 | FC + GRaND + VIR |
| Dry flight system | 725 | Dry bus + payload |
| Hydrazine | 45 | RCS propellant |
| Neutral mass | 770 | Dry flight system + hydrazine |
| Uncertainty | 20 | |
| Neutral mass + uncert. | 790 | Dry flight system + hydrazine + uncertainty |
| Xenon | 450 | IPS propellant |
| Wet mass at launch | 1240 | Dry flight system + hydrazine + Xe + uncert. |

Firstly we note from Table 2.4 that EPS specific power capability at 1 au is 50 W/kg (10 kW divided by 204 kg). Secondly, we consider that subsystems IPS (129 kg), EPS (204 kg), Xenon propellent (450 kg), CDHS (21 kg), Telecom (28 kg), Payload (45 kg), Harness (82 kg) and Balance (13 kg), total of 972 kg, are the items that must be hosted by the spacecraft bus. The spacecraft bus contains service-oriented subsystems RCS (59kg wet), ACS (37 kg), TCS (44 kg), Structure (108 kg) and Uncertainty(20 kg), total of 268 kg, which is 0.27572 times 972 kg. That is, the wet launch mass of Dawn

(1240 kg) is 1.27572 times the sum of the hosted internal parts (972 kg). The scientific payload mass of 45 kg is only 3.6 % of the wet launch mass. The low payload fraction is due to the necessarily large mass fraction of Dawn's ion propulsion system and its associated power system and xenon tank, given the requirement of large delta-v.

To make an E-version of Dawn, let us asssume $20 \times 20$ km tethers, total tether length 525 km, tether mass 6.6 kg, nominal thrust at 1 au 0.2 N, total E-sail subsystem mass 33 kg. Let us assume a 2 kW EPS, which this includes a considerable reserve since the E-sail needs only about 140 W of high-voltage power at 1 au and going down as $1/r^2$ for other solar distances. Using Dawn EPS' 50 W/kg specific power, the mass of the EPS is 40 kg. For CDHS (21 kg), Telecom (28 kg) and Payload (45 kg) we assume the same masses as in Dawn. For Harness we assume 20 kg which is 25 % of Dawn because the total power is only one fifth of Dawn. This estimate is somewhat conservative because the spacecraft is more compact than Dawn so that the cable lengths are shorter. The total hosted parts are then 187 kg. Using the same factor 1.27572 as for Dawn, we obtain the wet launch mass estimate of 239 kg. With 0.2 N thrust the spacecraft's characteristic E-sail acceleration is 0.84 mm/s$^2$ at 1 au. The payload fraction is 45/239 = 19 %. Compared to Dawn, the wet launch mass went down by factor 5.2 as a result of replacing the ion propulsion system by an electric sail propulsion system.

This calculation exercise shows that roughly, a payload fraction of 19 % (rounded: nearly 20 %) can be expected for straightforward E-sail missions. If additional functionality such as docking or gimballing is required, it reduces the payload fraction to some extent, which must be estimated separately.

The "E-sail Dawn" mission would suffer from the issue, however, that the instruments must be gimballed in order to view the asteroid properly. Also, if the spacecraft is taken inside the Hill sphere to reduce the viewing distance, a risk arises of tether collision with potential asteroid moons. Also the high-gain antenna must be directed either mechanically or electrically. These issues disappear if a separate inspection spacecraft is used to study the asteroid. Such mission architecture will be considered below in Section 2.7.

Table 2.5 shows the key parameters of the "E-sail Dawn".

## 2.5 Flyby missions

The flyby fleet asteroid mission idea was proposed to ESA's "Call for new ideas" in September 2016 and it was selected for further study in March 2017 (Appendix D). We proposed a distributed survey of hundreds of asteroids representing many asteroid families with emphasis on small ($\sim$ 1 km) bodies that are difficult to study from Earth in detail. This can be implemented by a fleet of cubesat-sized spacecraft equipped with small optical and near infrared imaging instrument. Data are stored in flash memory during the mission and downloaded by an Earth flyby at the end. This keeps deep space network telemetry costs down, despite the large number of individual spacecraft ($\sim$ 50) in the fleet. To enable the necessary large delta-v, each spacecraft carries a single Coulomb drag tether (downscaled electric solar wind sail) which taps momentum from the solar wind.

Properties of asteroids are of fundamental importance for constraining solar system evolution models because asteroids are fragments of the planetesimals from which

**Table 2.5:** "E-sail Dawn" mass budget.

| System | kg | Explanation |
| --- | --- | --- |
| Structure | 21 | Structural and mechanical parts |
| E-sail | 33 | $20 \times 20$ km tethers |
| EPS | 40 | Electric power system, 2 kW max at 1au |
| ACS | 7 | Attitude control system |
| RCS | 3 | Reaction control system dry mass |
| TCS | 8 | Thermal control system |
| CDHS | 21 | Command and data handling system |
| Telecom | 28 | Telecommunication subsystem |
| Harness | 20 | Cables and connectors |
| Balance | 3 | |
| Dry spacecraft bus | 184 | Sum of the above |
| FC | 11 | Framing Camera, 2-fold cold redundancy |
| GRaND | 10 | Gamma Radiation and Neutron Detector |
| VIR | 24 | Visible and InfraRed spectrometer |
| Science payload | 45 | FC + GRaND + VIR |
| Dry flight system | 229 | Dry bus + payload |
| Hydrazine | 10 | RCS propellant |
| Wet mass at launch | 239 | Dry flight system + hydrazine |

Earth and other planets once formed. Knowing physical properties of asteroids is also needed for assessment of the asteroid impact threat, for development of techniques for mitigating asteroid impacts and for the emerging field of asteroid mining.

The fleet will obtain image and spectral data from 300+ near-Earth object (NEO) and mainbelt asteroids, which is groundbreaking. It allows us to study those asteroid families and spectroscopic types for which currently no in situ observations are available. The proposed spectrometer will cover wavelengths around the 2.7-$\mu$m absorption band, enabling us to study the presence of OH and hydrated minerals. The image data allow us to measure the size and albedo of the studied asteroids. Mapping the albedo of each spectral type and family allows one to infer the absolute size of any asteroid whose spectral type is or will be known from ground observations. Furthermore, a significant subset of the studied asteroids will have moons. For those asteroids, measurement of the absolute mass is possible by determining the orbit of the moon from the optical flyby images. From the spectral data, surface minerals can be detected. For each asteroid studied we obtain the surface morphology, overall shape, character (monolithic or rubble-pile), presence of dust on the surface, number of type of craters, presence of fault lines and presence of moons. Overall, the proposed mission increases the number of well-known asteroids by more than an order of magnitude and enables a "population geophysics" approach for studying them.

The proposed mission architecture is easily scalable both scientifically and financially. The number of spacecraft can be scaled, as well as the maximum heliocentric reach of the fleet. Launching is very flexible because it can be made either by one shot by a launch vehicle such as the Indian "Polar Satellite Launch Vehicle" (PSLV) or by piggybacking with one or more other Lagrange point, lunar or planetary missions. It is also possible to scale the mission (both scientifically and financially) by scaling the

designed lifetime of each spacecraft. A 3.2-year lifetime mission is sufficient to study the mainbelt, for Hilda family objects one needs 4.3 years, and for Jupiter Trojans 8.3 years. Optionally, some spacecraft in the fleet can perform rendezvous of particularly high-value targets, and some targets may be inspected by more than one spacecraft in the fleet to increase their mapped surface fraction.

The full proposal is included in this document as Appendix D.

## 2.6  Expendable inspector spacecraft

In this section we consider, generically, a mission architecture where the asteroid inspector spacecraft is used to study only one asteroid. We subdivide the consideration into two cases:

1. there is an E-sailed mothership that flies from asteroid to asteroid and leaves an inspector spacecraft at each of them,

2. each inspector spacecraft is equipped with a smaller E-sail by which it flies to its target asteroid independently.

### 2.6.1  E-sail mothership

An E-sailed mothership releases an inspector spacecraft at each asteroid. The benefits of this mission architecture are the following:

– The inspector spacecraft's design is almost decoupled from the desing of the E-sail mothership. It only has to be mated with the mothership in the cruise phase and released upon arrival in a proper direction so that there is no collision risk with the tethers.

– Typically the number of inspector spacecraft is more than one.

– No need for docking, only for releasing.

– By visiting more than one asteroid, we make use of the E-sail's ability to produce large delta-v.

The architecture also has some drawbacks:

– Because several inspector spacecraft are carried onboard the same mothership, the size of the E-sail is larger than if each spacecraft would carry its own E-sail. A larger E-sail is more challenging and costly to develop than a smaller one.

– Those inspector spacecraft that are released later are unnecessarily carried to the earlier asteroids, which unnecessarily increases the total impulse requirement.

### 2.6.2  Inspector spacecraft uses E-sail, jettisoned upon arrival

The inspector spacecraft has its own E-sail by which it flies to the asteroid. Upon arrival, it jettisons the E-sail and enters inspection mode where the E-sail tether rig no longer limits its motion and attitude selection. Jettisoning the E-sail might mean jettisoning the entire E-sail module or it might mean simultaneous cutting of all the tethers. Some of the benefits and drawbacks are complementary to the previous subsection.

Benefits:

– As in the previous subsection, the inspector spacecraft's design is almost decoupled from the E-sail design, because the E-sail is jettisoned before the science phase starts.

– As in the previous subsection, there is no need for docking, only for jettisoning the E-sail (by either separating the E-sail module or by cutting the tethers, or even retracting the tethers).

– The inspector spacecraft goes directly to the target asteroid, thus minimising delta-v requirement.

– The E-sails are of smaller size than in the mothership case, which makes the E-sail easier to develop.

### 2.6.3   Are E-sail tethers a space debris issue?

Abandoning an E-sail tether rig so that it remains orbiting an asteroid or slowly collides with it is not recommended, because then future spacecraft arriving to study the same asteroid might encounter those tethers. However, an E-sail tether rig can be safely abandoned in a generic heliocentric orbit. E-sail tether debris is not dangerous to traditional spacecraft because even in case of collision, the produced scratches on the spacecraft surface are small and similar scratches are made by the natural micrometeoroid flux. However, E-sail tether debris is potentially dangerous to other E-sails, because if two tethers collide at significant speed, both of them are typically cut. A possible simple mitigation strategy is to manufacture the tether so that its wires curl up when tether tension is relieved. Then loose tether pieces naturally curl up to more compact objects.

A sure way of disposing of an E-sail tether rig is to put it in a collision course with a planetary atmosphere. If the E-sail module is jettisoned as one entity and if the module also contains a self-sufficient power, control and navigation systems, the module could actively change its course to do that.

## 2.7   Reusable inspector spacecraft

In this section we consider, again generically, an inspector spacecraft that can be used for several asteroids. The idea is that the inspector spacecraft contains at least a comprehensive remote sensing instrument suite, although including *in situ* items like cubesat landers in the science payload is also possible. The mission sequence is the following:

1. An E-sail mothership travels to the asteroid and is parked at the edge of its Hill sphere.

2. An inspector spacecraft is released and it goes down to study the asteroid.

3. The inspector spacecraft returns and docks with the mothership which takes it to the next asteroid.

The benefit is again that the inspector spacecraft's design is decoupled from the design of the E-sail mothership. It is also a benefit that the same inspector spacecraft remote sensing hardware can be used for more than one asteroid, and that instrument and high-gain antenna pointing are not disturbed by the presence of the E-sail. The drawback is that docking is needed. In the following subsection we study the docking issue in more detail and will find that docking is not too difficult in this case.

## 2.7.1   Docking

Let us consider the problem of docking between the science spacecraft (SS) and the E-sail (ES).

Docking in this case is less challenging than in LEO because the gravity gradient is negligible (see section 2.7.2 below for details). In LEO, the gravity gradient complicates the control algorithm needed in the approach phase. The only complication is that we must stay clear of the tether plane, which implies that the approaching SS must stay inside a certain cone whose apex is at the ES.

The preparatory steps needed to perform docking of SS with the ES:

1. Define the ES approach cone.

2. Define a forbidden sphere around the ES whose radius is some safety factor times tether length.

3. Define point $P$ as the intersection of the ES approach cone axis and the forbidden sphere.

The sequence of operations:

1. SS flies from the asteroid to point $P$, avoiding the forbidden sphere. Depending on which side of the forbidden sphere point $P$ is, this involves either straight path flight or a path composed of two straight segments and one intermediate burn so that one avoids intersecting the forbidden sphere.

2. SS flies from $P$ towards ES along the axis of the approach cone.

3. SS docks with the ES.

As the set of sensors, we propose that both spacecraft have a spherical ($4\pi$) imaging system as well as radio ranging which gives the mutual distance between the spacecraft. If the spacecraft are aligned with the Sun direction, the farther one cannot see the closer one because that part of its view is blinded by the Sun; however, the closer one can see the farther one well. In other cases, both spacecraft can see each other without blinding. Because both spacecraft can also see the background stars, they can thus infer their mutual separation unit vector, and radio ranging gives the magnitude of the separation. As a result, SS knows the position of ES in a coordinate system whose origin is at SS. Likewise, ES knows the position of SS in a coordinate system whose origin is at ES.

The background stars can either be detected by the same $4\pi$ imaging system or by a traditional star sensor having a narrower field of view.

Initially the distance between SS and ES might be so large that they cannot see each other optically. In that phase, both SS and ES can infer its approximate location by observing the direction of the asteroid with respect to the background stars. If

one uses simple algorithms that e.g. only detect the "optical centre of mass" of the asteroid (i.e. ignoring its actual shape and mass distribution), then the navigation accuracy by the asteroid method is comparable to the asteroid's diameter. This is usually enough, however, since a reasonable miniaturised $4\pi$ imaging system can detect the other spacecraft from at least up to few hundred kilometre distance.

If the E-sail has remote units, one option would be to do radio ranging from them to triangulate the SS position relative to the ES. We do not propose this method as the primary one, though, because the optical method already looks attractive.

For the actual docking, we propose to use a cone-shaped mechanical interface because such interfaces allows for some inaccuracy in the position of the spacecraft. We propose that a permanent magnet is used to pull the interfaces together and for keeping them together. During launch, standard release-once launch locks must be used because the magnets are not strong enough to keep the parts together during launch vibrations. To release the interface for separation, an electromagnet is used to temporarily cancel the permanent magnet. If slight overcompensation is used, a small repulsive kick can also be achieved by the magnetic forces. Alternatively one can use spring forces for producing the separation impulse.

If the mission is a sample return mission, the return capsule's reentry shield can probably double as the docking cone.

## 2.7.2 Why docking is not difficult in this case

Docking may have a reputation of being a complex and expensive operation. We think that in our case, however, repeated docking is a straightforward operation which does not much increase the cost or complexity of the mission:

- The gravity gradient is negligible so that unlike in LEO, trajectory control is simple and intuitive. In the equation of motion of the spacecraft, the dynamics in $x$, $y$ and $z$ are not coupled to each other so that the equation of motion breaks down into simple one-dimensional equations of motion for each Cartesian direction separately.

- The sensors needed are only a $4\pi$ camera system (composed of multilple small cameras on different sides of the spacecraft) and signal delay measurement in the radio link. The camera system has no moving parts and its mass overhead is moderate. In the science spacecraft, the $4\pi$ camera system doubles as the navigation camera which is needed in any vehicle performing asteroid proximity operations.

  - We remark that if we could guarantee that the separation between the spacecraft is always sufficiently far from being aligned with the sun, then it would be sufficient to have the $4\pi$ camera system in only one of the spacecraft. Our baseline is that such guarantee cannot be given or would not yield a robust enough mission, so that a camera system is put in both spacecraft.

- The algorithms needed for autonomous docking are not complicated, and analogous although more complicated algorithms are needed in the science spacecraft in any case for the asteroid proximity operations. Similar but more complicated

algorithms are also needed for active debris removal in LEO and for satellite servicing in GEO.

– As actuators for the docking and release, standard thrusters (e.g. monopropellant thrusters) in the science spacecraft are sufficient. In the final approach phase, if corrosion of the spacecraft or the tethers by chemically active thruster plumes turns out to be a risk, one can use cold gas thrusters in the final approach phase.

– The docking mechanical interface has no moving parts. The only active control required is that to perform the release operation, a constant DC current must be turned on briefly in an electromagnet coil.

– Launch locks are needed to fix the spacecraft tightly together during launch, but their complexity is low and reliability high because they are used only once in the beginning of the mission.

– Testing the docking system is inexpensive and possible to do on ground:

  – The trajectory control part can be simulated on computer.

  – A 2-D version of the dock/release mechanism can be tested in an air-bearing table facility. Because the docking cone is cylindrically symmetrical, 2-D testing is representative.

### 2.7.3  An "E-sail Dawn" with dockable E-sail stage

In Section 2.4 we analysed an E-sail version of the Dawn instrument suite and came up with total mass estimate of 239 kg, which includes the 45 kg remote sensing science payload. When one uses the docking architecture and separates the E-sail mothership from the science spacecraft, there is some mass increase due to the docking interface and reduced sharing of subsystems between the two spacecraft. Let us estimate summarily that the total mass is then 300 kg. If so, one can fit 3 or 4 such spacecraft in a Souyz class launcher of an M-class mission, which is capable of lifting 1200-1500 kg to an E-sail qualified orbit (marginal escape orbit or sufficiently high elliptic orbit). If each spacecraft can visit four asteroids during its operational lifetime (Dawn did two), a fleet which is compatible with the M-class constraints can then perform remote sensing analysis of 12-16 asteroids.

## 2.8  E-sailed sample return

In this section we consider E-sailed sample return mission from a single asteroid. The same E-sail is used also when returning. The E-sail mothership is left at the boundary of the Hill sphere of the asteroid to avoid any risk of collision of the tether with a potential moon of the asteroid.

The mission sequence:

1. The spacecraft moves to the asteroid by the E-sail and sets itself at the boundary of the Hill sphere.

2. The science spacecraft (SS) undocks from the E-sail mothership.

- The mothership continues to spin and has its tether voltage turned off. It can fine-tune its orbit, if needed, by cold gas (CG) propulsion. At the boundary of the Hill sphere, the orbital period of the spacecraft around the asteroid is of the order of the heliocentric orbital period of the asteroid. This means that after parking, the spacecraft moves only very slowly by the natural orbital motion, thus fine-tuning of the orbit is likely not necessary.

3. The SS uses propulsion to settle to an asteroid orbit.

4. While orbiting the asteroid, the SS maps the asteroid's surface with its camera and its gravity field by radio science experiment. The spacecraft alternates between three operational phases:

   (a) Load the battery by having the solar panel sunward.

   (b) Gather scientific image data by having the camera pointed towards the asteroid.

   (c) Point the patch antenna towards the Earth to transmit the batch of data just gathered.

       - The patch antenna is on the backside of the solar panel.
       - Run the radio science experiment to map the gravity field.
       - Scientists use the returned data on ground to select the landing site.

5. The SS lands on the asteroid and gathers a dust sample by brushing.

6. The SS lifts off by propulsion and returns to E-sail mothership by the algorithm given in 2.7.1.

7. If we have a single-tether system, then before docking the E-sail mothership must stop its spin by CG propulsion at the remote unit. This has to be done because the centre of mass of the spacecraft plus tether and remote unit system is far from the spacecraft.

8. The SS approaches the mothership from the P-point and docks.

9. The mothership's spin is restarted by CG propulsion and the E-sail is used to fly to Earth.

10. Before reentry, the capsule separates from the SS and is made to spin to ensure its stable orientation during reentry.

11. The capsule makes the reentry.

12. During terminal speed descend, the capsule finds its position by navigation satellites and transmits it to a communication satellite network such as Iridium.

13. The capsule hits ground at the terminal speed.

The capsule contains the samples and some flash memory chips that contain the highest resolution science data. The standard resolution data were transmitted to ground already from the asteroid.

A suitable preliminary design for the capsule is called MIRKA2 weighing 0.45 kg and developed at Stuttgart Institute of Space Systems. As designed, the MIRKA2 is

only capable of reentry from LEO, so the thermal protection shield should be made somewhat thicker to allow reentry from a parabolic orbit.

## 2.9  Two-phase mission architecture

Two mission architectures tend to stand out from the others analysed in this report: the flyby fleet and the sample return fleet.

Mapping the asteroid in flyby mode is at least an order of magnitude cheaper than returning a sample from it. This is because a single small platform can map 6-7 asteroids, while the sample is returned only from one asteroids. Also, the platform needed for sample return is more complex and also somewhat heavier than for flyby inspection. We estimate that the cost of imaging a single main belt asteroid in flyby mode is $\sim 0.2$ M€ while making a sample return costs several million per asteroid. Thus for optimal use of resources, the targets for sample return should be selected carefully and it makes sense to use the flyby fleet data for that purpose. This leads to the natural two-phase mission architecture:

1. Flyby fleet mission (section 2.5) for a large number of asteroids.

   - $\sim 300$ asteroids with 50 spacecraft, if PSLV is used as launch vehicle.

2. Sample return fleet for a smaller number of particularly interesting asteroids.

   - Each spacecraft in the fleet samples one asteroid.
   - The nnumber of spacecraft is $\sim 20$, if PSLV is used as launch vehicle.

# Chapter 3

# WP3: Selection of mission

## 3.1   Mission selection

For more detailed analysis in WP4, we select the sample return mission (Section 2.8). The motivation for this is as follows.

1. Asteroids are a diverse target consisting of a large number of different families. Consequently, a large number of them should be eventually studied. It is sensible to first survey a larger number of asteroids and then study a smaller number of interesting ones in more detail. The flyby fleet described in Section 2.5 accomplishes the survey part. Since the flyby fleet idea was selected and is thus already being studied by ESA, it is not selected for WP4 of this project. Instead, we select a next stage mission concept (sample return fleet) that returns more detailed information from a smaller number of asteroids.

2. As an alternative to the sample return fleet, one can consider a comprehensive remote sensing instrument package that is made to tour several asteroids by the E-sail (Section 2.7). For the following reasons we favour the sample return alternative:

   - Sample return enables analysis in ground-based laboratory and thus provides more detailed analysis of the asteroid soil than even a sophisticated remote sensing instrument package could make.

   - Sample return can be miniaturised by making the sample mass small, whereas some components of a comprehensive remote sensing package such as gamma ray, neutron and X-ray spectrometers are harder to miniaturise because the collecting aperture must be of certain size to collect enough signal.

   - The cost and complexity of making the E-sail grows with the required thrust. Hence we prefer a mission concept where the individual spacecraft is as lightweight as possible. This is well in harmony with the fact that then the fleet size can be increased so that a larger number of asteroids can be studied. Increased fleet size also provides inherent redundancy so that the reliability requirement of the single spacecraft can be lowered. That in turn enables further reduction of the single spacecraft mass by elimination of small component redundancies, and that enables increasing the fleet size and thus science output even more.

   - A fleet consisting of small spacecraft can yield to overall low-cost mission architecture. The R&D cost of developing space hardware is typically pro-

portional to the mass (often a rule of thumb like 1M€/kg is used), so the R&D cost remains moderate as long as the individual spacecraft is small. This economy of scale is being recognised by the space industry's current proposals to build, for example, large LEO constellations for global Internet access.

3. It is to be understood that we really prefer the two-phase mission architecture described in Section 2.9, but since analysis of the first phase is already in progress elsewhere, in WP4 we concentrate in the second phase, i.e. the sample return fleet.

Table 3.1 shows comparison of the remote sensing fleet and two-phase fleet mission architectures, when both are scaled to M-class mission cost level. The M-class level allows implementing both phases of the two-phase strategy because PSLV-class launchers can be used in both phases.

**Table 3.1:** Comparison of the main alternatives for an M-class mission.

| Mission | Remote sensing of 12-16 asteroids by fleet of 3-4 spacecraft. | Flyby fleet of 300 asteroids by fleet of 50 nanosats, followed by sample return fleet of 20 asteroids. |
|---|---|---|
| Launch | One Souyz class launch | Two PSLV class launches or piggybacks |
| Scientific value | Good | Excellent |
| Development risks | Multi-tether E-sail | Miniaturisation of sample return; Autonomous navigation |
| Operational risks | E-sail failure | Autonomous navigation failure |
| Risk mitigation | Moderate, fleet of 3-4 s/c | Good, fleets of 300 and 20 s/c |

## 3.2   Some programmatic remarks

1. The E-sail has strong technical synergy with ongoing space debris efforts (plasma brake).

2. Docking has technical synergy with ongoing space debris efforts (both need similar proximity operations and similar sensors, algorithms and actuators).

   – The type of docking we need is simpler than with space debris because the target is collaborative and because there is no gravity gradient that compliates guidance in the approach phase.

3. Remote sensing instruments for asteroids have technical synergy with Earth observation instruments used for environmental monitoring, commercial and military purposes.

4. Scientific study of asteroids has obvious and large synergy with mineral prospecting of asteroids done for commercial asteroid mining purposes.

5. Scientific study of asteroids has synergy with planetary defence. For example, the largest crater on the asteroid gives an indication of how large impact the body has withstood without shattering into pieces; or if the impact has made it into a rubble pile, one can assess the size of the components. This information is critical if one has to attempt deflection of an Earth-impacting asteroid by colliding a projectile to it or by making an explosion.

6. The launch of E-sailed solar system spacecraft is essentially more flexible than traditional spacecraft, because *any* escape orbit (or high elliptic orbit) launch can be used as the starting trajectory for *any* E-sail spacecraft, no matter where it is targeted to. All E-sail spacecraft need to be first lifted outside Earth's magnetosphere where solar wind exists, but otherwise the parameters of the initial orbit do not matter and do not depend on the target of the mission.

   – This implies that E-sail spacecraft can potentially make efficient use of any piggyback opportunities of beyond-magnetosphere launches such as lunar, Lagrange point or planetary.

# Chapter 4

# WP4: Detailed analysis of selected mission

## 4.1 Objectives and background

The objective of WP4 is to make detailed analysis of the mission selected in WP3, which is sample return from an asteroid.

First we present a common overall mission architecture which is scalable in terms of sample return capsule size. Then we specialise to two cases: a conservative case using traditional capsule concepts and an innovative case that uses a much smaller capsule without parachute.

## 4.2 Introduction

Sample return is scientifically valuable because ground-based laboratories can analyse samples more thoroughly than onboard instruments. On the other hand, we already possess thousands of asteroid samples in the form of meteorites. The meteorites were modified by atmospheric entry and subsequent erosion processes which leads into difficulty of measuring their volatiles. Also, we do not know with certainty which asteroid parent body a given meteorite is a fragment of, and the most fragile types of impactors may be almost missing from the meteorite record. A sample return mission must try and fill these knowledge gaps. Thus it is important e.g. to seal the sample so that atmospheric gases do not contaminate its volatiles. Also those fragile asteroid types that are likely to be underrepresented or missing in the meteorite data are important to consider.

Propulsion is one of the key constraints when designing a sample return mission. Using existing propulsion technology, only one body can be realistically sampled by a single M-class mission. Even if it was possible from the delta-v budget point of view, trying to sample more than one body would probably not be a viable idea because it would create the risk of losing all samples if the spacecraft fails early. Using the E-sail, one avoids carrying propellant for in-space propulsion and consequently the launch mass can be reduced. If the launch mass can be reduced sufficiently, it becomes possible to consider a small fleet of sample returning spacecraft. In addition, each member of the fleet could sample more than one body because the E-sail overcomes delta-v budget issues and because in case of a fleet, a single spacecraft failure is not catastrophic. Thus, if a fleet can be afforded after some miniaturisation effort, the number of bodies sampled may jump from one to perhaps ten or more. As a bonus, lower spacecraft mass decreases the needed E-sail thrust, lowering the E-sail development cost and/or giving larger design margins.

The starting point of design optimisation is critical review of the requirements and an attempt to simplify and reduce them as much as possible. The requirement is to bring a surface regolith sample of the asteroid. The sample size should be preferrably at least 10 grams. The asteroid must be mapped in optical and NIR to document the sample's geophysical context. Other remote sensing like radio science experiment for determining the body's internal mass distribution are nice-to-have features. The science team must select the landing spot based on the orbital mapping. Thus one needs enough telemetry capacity to downlink enough data to enable an informed selection. Higher resolution science data can be returned on memory chips onboard the entry capsule (EC).

## 4.3   Ongoing sample return missions

### 4.3.1   Hayabusa-2

The Japanese Hayabusa-2 mission exemplifies the state of the art of asteroid sampling. Its sampling operation proceeds as follows (Tsuda et al., 2013):

1. The target asteroid has about 1 km diameter, 0.3 mm/s$^2$ surface gravity field and 0.5 m/s escape velocity.

2. Semiautonomous approach towards selected landing spot from 20 km to 100 m altitude guided mainly by LIDAR.

3. Drop target marker sphere to the surface.

4. Enter autonomous mode and lower altitude to 30 m.

5. Align spacecraft attitude to conform to local surface.

6. Descent to surface and perform about one second long touch-and-go sampling operation. A bullet is shot to the surface inside a hood (sampling horn) which prevents most of the ejecta from escaping.

7. The ejecta are gathered into a sample container, which is sealed and moved into EC.

8. The spacecraft lifts off the surface and repeats the sampling operation three times, each using a new bullet and sam ple container.

9. The last sampling operation is performed at the bottom of an artificial crater that has been created by a shaped explosive charge carried by a subspacecraft. This is done to retrieve a sample from few tens of centimetres deep subsurface. Unlike the immediate surface, the subsurface is not space weathered and thus represents better the bulk properties of the asteroid.

Hayabusa-2's dry weight is 500 kg and it attempts to retrieve about 0.01 kg sample, thus the sample mass fraction is $2 \cdot 10^{-5}$. So at least in principle, there is a lot of scope for improvement in the mass ratio.

### 4.3.2 Osiris-Rex

The American Osiris-Rex is another concurrent sample return mission. Osiris-Rex weighs significantly more and also plans to return a larger sample. The sampling hardware blows nitrogen gas to the surface to raise up regolith and catch it in a filter. The sampler head is mounted on a robotic arm so that the spacecraft does not have to touch the surface. The same arm also places the sample head inside the capsule. Both Hayabusa-2 and Osiris-Rex use a touch-and-go strategy i.e. the sampling operation has a short duration.

## 4.4 Mission architecture

There are several aspects specific to the E-sail that must be considered in connection with mission architecture. If the asteroid has an unseen moon, the spinning tethers of the E-sail have a nonzero risk of colliding with it, if the spacecraft stays in the same orbital volume as the moon for an extended time. One also has to avoid collisions between the tethers and the asteroid itself by keeping enough distance or by carefully controlling the geometry. If one goes near the asteroid, one must also take into account the effect of the asteroid's gravity field gradient on the dynamics of the tethers. A multi-tether E-sail spacecraft must have a gimballed platform for pointing the instruments and the high-gain antenna.

We propose to resolve all these constraints by having a two spacecraft mission architecture consisting of an E-sail spacecraft (ESC) mothership and a science spacecraft (SSC). One could also locate EC within SSC, instead of ESC. Having EC in ESC is safer, however, because if the SSC fails, the ESC can return with the already gathered samples. The ESC is parked at the boundary of the asteroid's Hill sphere. The SSC separates from the ESC, performs the asteroid sampling and returns to the ESC for rendezvous and docking. The ESC+SSC combination is then taken by the E-sail to the next asteroid or returns home. The main items carried onboard each component are listed in Table 4.1.

The mission phases are as follows (Fig. 4.1).

1. ESC+SSC uses E-sail to fly to an asteroid and park at the Hill sphere boundary.

2. SSC separates from ESC and uses its AOCS to settle to low asteroid orbit (takes maximum of 5 days for asteroids up to 10 km diametre and somewhat longer for bigger asteroids). ESC goes to parking mode where E-sail is off and photonic pressure cancellation thrusting mode is normally active.

3. SSC maps the asteroid (by default from terminator orbit), downlinking the data required for landing site selection. This takes normally 2 weeks. Other data can be stored and returned on memory chips onboard EC.

4. Based on the downlinked data, the science team selects the landing spot, which takes an additional 4 weeks.

5. SSC lands, takes the sample and lifts off.

6. SSC makes rendezvous and docks with ESC, which again takes 5 days or somewhat longer if asteroid is bigger than 10 km.

**Table 4.1:** Main items carried by each component.

| E-sail mothership (ESC) | – entry capsule (EC)<br><br>– monopropellant thrusters for tether deployment<br><br>– docking interface for SSC |
|---|---|
| Science spacecraft (SSC) | – remote sensing instruments<br><br>– radio science experiment<br><br>– asteroid sampler<br><br>– high-gain antenna and transceiver<br><br>– monopropellant thrusters for AOCS<br><br>– docking interface for ESC |

7. SSC inserts sealed sample canister into ESC's return capsule.

8. SSC+ESC uses E-sail to fly to the next asteroid, and the procedure is repeated.

9. After the last asteroid has been sampled, the SSC is abandoned [1].

10. ESC flies home with the gathered samples in its EC.

Altogether the parking time of the ESC (the time the SSC is away on its sampling trip) takes 52 days, or slightly longer if the asteroid is bigger than 10 km. If 10 asteroids are sampled, the accumulated sampling trip time (the time when SSC and ESC are not docked to each other) is 1.5 years.

## 4.5   Instrument requirements

The optical instruments must serve both science goals and the mission itself. The most important data for selecting the landing spot is morphology. The landing spot should be flat enough and free of boulders so that the spacecraft's solar panels do not touch ground. A terminator orbit facilitates such imaging because shadows cast by rocks are then made visible. The ground pixel size should be $\sim 0.5$ m, i.e. somewhat smaller than spacecraft size. At diffraction limit, an optical telescope with 5 cm aperture has $10^{-5}$ rad angular resolution, which corresponds to 0.5 m ground resolution when the observing distance is 50 km. Height of a safe Keplerian orbit is limited by the asteroid's shape, which is typically rather irregular, but typically, altitude of a safe orbit is roughly equal to the asteroid's effectice diameter. Hence, a 5 cm optical telescope is enough to map the asteroid with enough spatial resolution to select a safe landing spot, if the

---

[1]If wanted and if SSC has propellant left, the SSC could fly back to the asteroid orbit to do remote sensing, or/and land on the asteroid permanently.

asteroid is not larger than 50 km in effective diameter. The number of 0.5 m pixels for a 50 km diameter (spherical) asteroid is $3 \cdot 10^{10}$, i.e. quite large. Thus at least for a 50 km asteroid, heuristics are desirable to reduce the downlinked data volume for landing site selection. One first reduces a lower resolution chart which is used to select a few promising landing areas. Full resolution data for the candidate regions are then downloaded and the actual landing spot is selected.

The data volume that must be downlinked to select the landing spot has a significant effect on the spacecraft mass and mission cost. The data rate of a telemetry system is proportional to $m^{5/3}$ where $m$ is the combined mass of the telemetry system and the associated power system (Eq. 1.2). Linear proportionality comes from the power system and $m^{2/3}$ comes from the high-gain antenna scaling. Hence, for example halving the data volume reduces $m$ by factor $0.5^{3/5} = 0.660$.

The asteroid surface regolith is likely to be rather well mixed so that scientifically it does not matter where the sample is taken from, as long as it is taken from a place which has some regolith. An exception is if one wants to sample a recent natural or
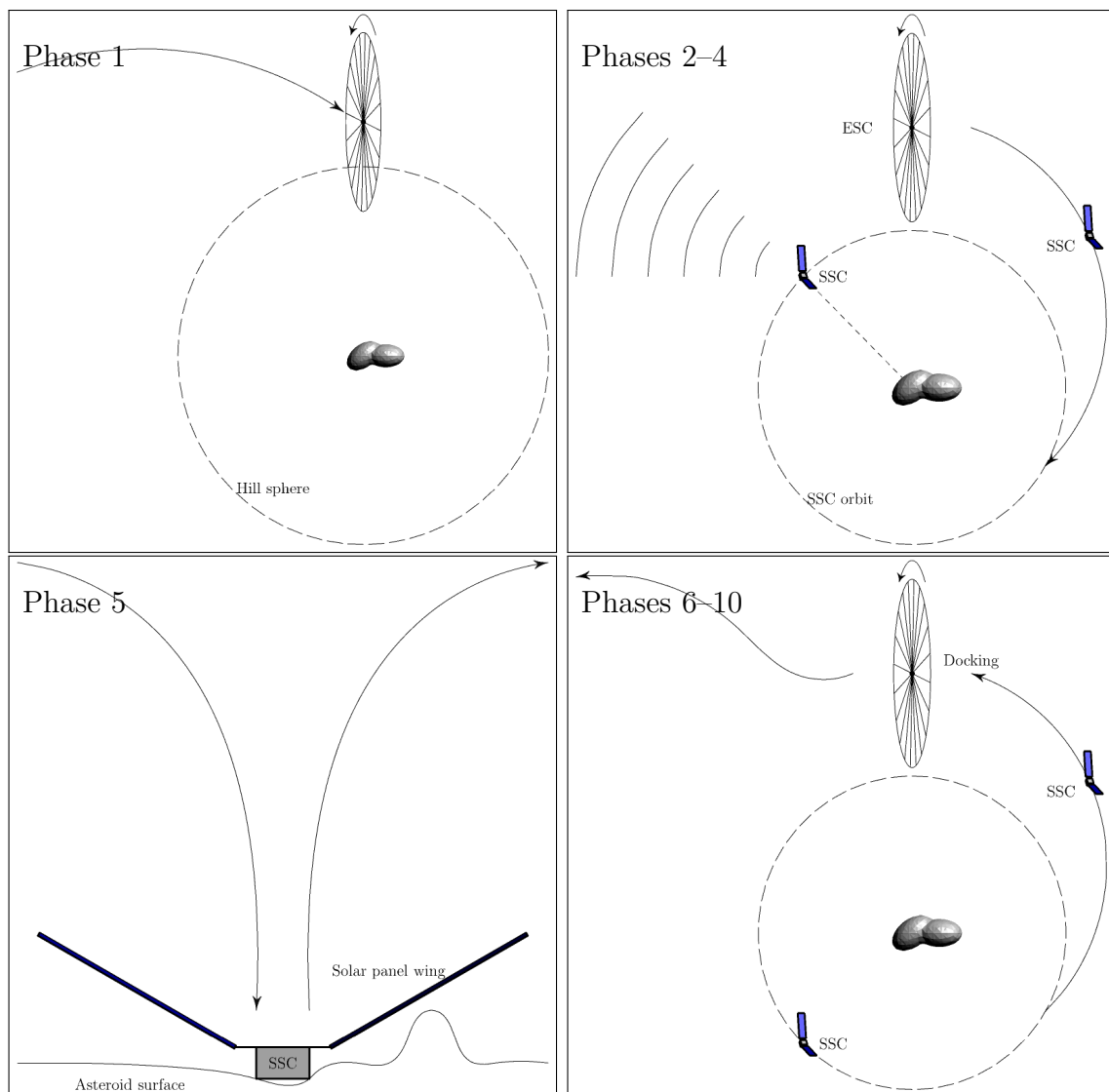


**Figure 4.1:** The mission phases.

artificial crater to effectively retrieve a subsurface sample.

Let us assume a 50 km asteroid and consider the following mapping strategy:

1. Greyscale-image the asteroid from a 50 km altitude terminator orbit at 0.5 m surface resolution at optical wavelengths. When doing the mapping, reduce the data into $100 \times 100$ pixel domains ($50 \times 50$ m physically). For each domain, compute its degree of brightness homogeneity. A homogeneous domain is likely to be smooth (free of boulders and other dangerous landforms) and therefore a candidate for landing.

2. Downlink the surface smoothness data, one byte per domain. The number of domains is 3 million so that the amount of data is 3 MB without compression.

3. The science team selects 10 best domains for landing. For each domain, check also the neighbouring 8 domains. So each of the ten candidate regions becomes an image with size $300 \times 300$ pixels, representing a $150 \times 150$ m region physically. Downloading the ten candidate regions in optical greyscale map corresponds to 0.9 MB of data.

4. Download also NIR data of the candidates domains. The NIR instrument has 5 m surface resolution (10 times less than optical) and each pixel corresponds to 100 spectral values, resulting an additional 0.9 MB of data.

5. The science team picks one of the ten candidates as the actual landing spot.

This scheme requires only 4.8 MB of data to be downlinked. If the data rate is 500 bit/s, for instance, the downlinking needs 20 hours of DSN time. These estimates were made without assuming any data compession.

During the orbital mapping, full resolution optical and NIR data are stored in flash memory chips. This corresponds to 30 GB of uncompressed optical data and the same amount of uncompressed NIR data.

Rosetta used downlink data rate of 23 kbit/s from 2.7 au distance to a 35 m X-band (8 GHz) ground antenna[2]. Rosetta's high-gain antenna was 2.4 m in diameter and transmission power $\sim 25$ W. Now, if the antenna diameter is 0.5 m and transmission power 10 W, for example, then X-band data rate from 2.7 au to 35 m ground antenna becomes 58 times less than for Rosetta, which means 400 bit/s. With this datarate, downlinking the 4.8 MB of data needed for landing site selection takes 27 hours. Hence, it is not unreasonable to adopt 0.5 m diameter and 10 W transmission power as baseline parameters for the downlink telemetry system, keeping in mind that if a somewhat larger antenna can be accommodated on the spacecraft in a natural way, it might be worthwhile to do so.

Figure 4.2 shows the SSC docked with the ESC.

---

[2]http://blogs.esa.int/rosetta/2014/08/05/tracking-the-spacecraft-following-a-comet/
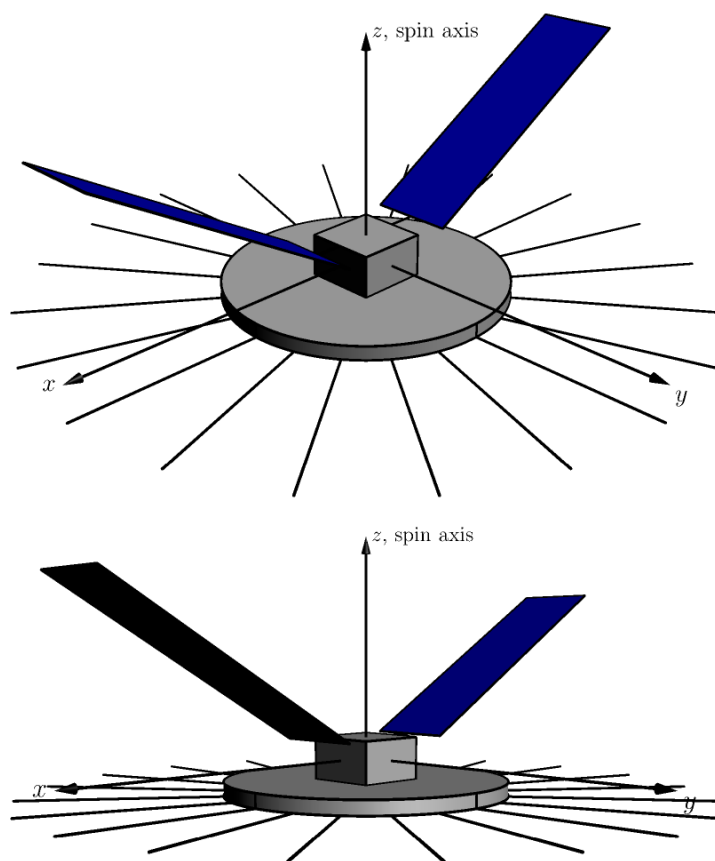
**Figure 4.2:** SSC and ESC docked together, shown from two viewing angles.

## 4.6 Science spacecraft (SSC)

### 4.6.1 Detectors

Table 4.2 summarises the various detectors onboard the SSC.

**Table 4.2:** Detectors.

| Detector | Required by | Nice to have for |
|---|---|---|
| $4\pi$ imaging system | E-sail, docking, AOCS | Science |
| Asteroid imager+NIR | Science | - |
| Laser altimeter | Landing | Science |
| Sampling monitor camera | - | Science |

#### 4.6.1.1 $4\pi$ imaging system

There are different needs for a wide angle imaging system:

1. For proximity operations during docking, the SSC needs an imager that detects the ESC. The SSC approaches ESC from the sunward side so that only SSC needs to see ESC but not vice versa. This imager needs to have wide angle on the side of the SSC that is facing ESC.

2. The attitude determination system needs a star tracker.

3. As a nice to have property, the asteroid can be imaged with the imaging system also, especially during landing, although the main instrument for mapping the asteroid is a separate scientific narrow field camera.

To cover these requirements, we use a spherical ($4\pi$) imaging system on the SSC.

We cover the $4\pi$ space by a number of small cameras. There is a tradeoff between using a larger number of normal field of view cameras and a fewer number of wide angle cameras. We assume wider than 90° field of view so that six cameras is enough. We reserve 90 grams for each camera. This estimate is based on ESTCube-1's 46° × 35° field of view camera (Kuuste et al., 2014) which weighed 30 grams. We multiply the mass by three to account for the deep space radiation tolerance requirement and the wide field optic which requires more lenses than the normal field of view camera. Thus, overall the mass of the $4\pi$ imaging system is 0.72 kg. The average power consumption is 0.75 W, which is six times the average power consumption 118 mW of ESTCube-1 camera.

The "$4\pi$" imaging system need not cover quite full 100.0 % of the full sphere, as long as the parts left out are less than $\sim 10$ %, say. In a spacecraft with solar panel wings, it is not feasible to have a 100 % spherical imaging system because putting cameras at the tips of the solar panels could be technically cumbersome.

#### 4.6.1.2 Asteroid optical+NIR imager

For mapping the asteroid from orbit to select the landing site, we need an asteroid optical+NIR imager which has narrowfield telescope optics. More detailed requirements were given in section 4.5 above. We assume 5 cm aperture and diffraction limited

resolution. A multi-spectral imager covering 0.5-2.5 $\mu$m in three channels has been developed by VTT, Finland (Kohout et al., 2017). In the version adopted for the M-ARGO study its weight was 0.95 kg (Walker et al., 2017). Here we reserve 2 kg for the system, to account for the need for somewhat bigger optics and to have margin for including possible additional features in the package.

#### 4.6.1.3 Laser altimeter

We use a laser altimeter in the landing phase, because with cameras alone it is not so easy to determine distance to the asteroid. A laser altimeter of the M-ARGO study weighed only 33 grams and used 1.8 W of power (Walker et al., 2017). The purpose of the altimeter is to enable safe landing. It can also be used to do science.

#### 4.6.1.4 Sampling monitor camera

We use one camera which is optimised for monitoring and documenting the sampling operation from near distance. For mass estimation purposes we assume a camera similar to ESTCube-1 which weighed 30 grams except that we allocate 60 grams for it to account for the interplanetary space radiation tolerance requirement. The net effect on the power budget is negligible because the sampling camera is used only for a very short time relative to the total science mission duration.

Traditional space-qualified cameras are much heavier than Cubesat cameras such as the ESTCube-1 camera and using them would increase the mass budget significantly. The ESTCube-1 camera worked without problems for two years in LEO until the cubesat lost power for independent reasons. We recommend adopting a cubesat heritage design such as ESTCube-1 and reserving some resources for the additional qualification which is required to guarantee enough longevity in the interplanetary environment.

### 4.6.2 Sampler

The asteroid surface sampler uses the spacecraft's own landing impulse to liberate grains from the surface regolith. The grains are then attracted by a magnet[3] into an open sample canister.[4] The spacecraft lits off using its thrusters and a lid is put on the canister. The interface between the lid and the canister contains fusible alloy which is melted using resistive heating by passing electric current through the container and the lid. Thus the sample canister obtains a gas-tight sealing by soldering.

Upon docking with ESC, the SSC pushes the sealed canister into a hole in the backpanel of EC which is part of ESC. Inside EC there is a storage area into which canisters can be inserted. The SSC has a number of canisters and lids in storage so that multiple asteroids can be sampled.

We allocate 3 kg for the sampling hardware altogether, excluding the camera which monitors the operation (see 4.6.1.4). The average power consumption is negligible because the hardware is used only for short periods of time.

---

[3]Permanent magnet, electromagnet or electropermanent magnet.

[4]Asteroid material is likely to respond to a magnetic field because it contains ferromagnetic elements. Surface material on differentiated bodies like Vesta might not contain ferromagnetic elements, but since we already possess meteorite samples of such bodies, they are not likely to be among the first target candidates for sample return.

Figure 4.3 shows the SSC on the asteroid surface. The solar panels are angled upward to allow clearance for possible surface rocks.
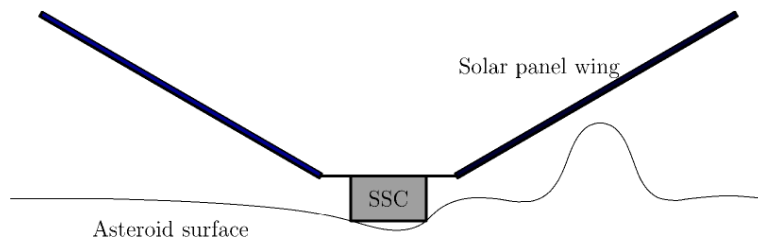


**Figure 4.3:** SSC on asteroid surface.

### 4.6.3 Docking interface

The docking interface between the SSC and ESC has the following features:

- The SSC approaches SSC from the sunward side of the ESC. The SSC sees ESC because it is sunlit. The SSC is the active partner in the approach manoeuvre.

- Permanent magnets are used to pull ESC and SSC together in the final centimetre-scale approach phase. The same magnets also keep the spacecraft mated together during E-sail flight.

- Separation is affected by cancelling one of the permanent magnets temporarily by an electromagnet coil surrounding it. A spring which is weaker than the magnets pushes SSC and ESC gently apart, giving them a small impulse. If one slightly overcompensates the permanent magnet with the electromagnet, magnetic repulsion may also contribute to separation.

- During launch, mechanical open-once launch locks are used to keep ESC and SSC tightly together. The attachment by the permanent magnets would be much too weak to withstand launch vibrations, although it is sufficient to withstand the weak forces during E-sail cruise.

We assume mass for the docking interface on the SSC side which is 5 % of the wet mass of SSC. For the ESC side, we assume the same docking interface mass as on the SSC side, so that as a whole, docking associated mass is assumed to be 10 % of SSC wet mass.

Figure 4.4 shows how the SSC seeks the ESC and docks with it. The SSC leaves from the asteroid and takes direction towards the ESC. To avoid collision with the tethers, the SSC avoids a spherical region around the ESC. SSC goes to point $P$ which is the intersection of the ESC spin axis direction and the forbidden sphere. Then it approaches ESC while remaining inside the entry cone. In the final phase it docks with the ESC (Fig. 4.5).

The SSC approaches ESC nominally along the ESC spin axis. The SSC must stay within the safe entry cone (Fig. 4.4) so that there is no possibility of collision with the tether rig. If the SSC moves out of the entry cone for any reason, it goes into safety mode where it retracts (moves away from the ESC) until it is again in the entry cone or outside the forbidden sphere entirely. Then it tries to approach the ESC again.
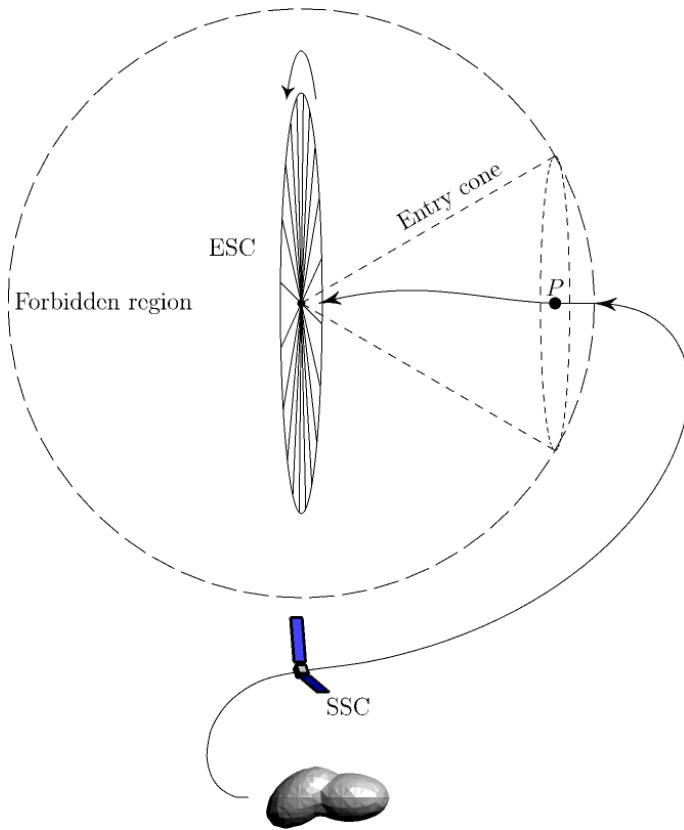
**Figure 4.4:** SSC seeks itself into vicinity of ESC.
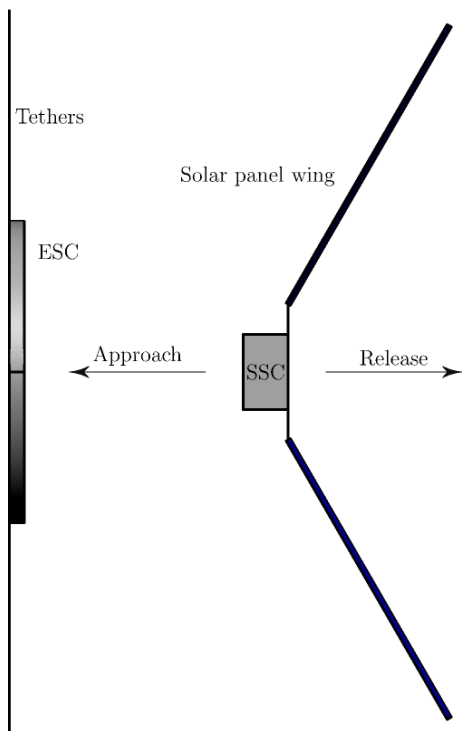


**Figure 4.5:** SSC docking with ESC.

### 4.6.4  Communications

The mass of the communication subsystem is driven by the required high-gain antenna size and transmitter power, which are based on the required data rate. In section 4.5 above, we analysed the instrument and data volume requirements and came to the conclusion that a 50 cm high-gain X-band antenna with 10 W transmitting power is sufficient. To estimate the mass, Dawn mission had 1.5 m diameter antenna, 100 W transmission power and its communication subsystem weighed 28 kg. In principle, mass of a mechanical structure like a high-gain antenna scales with the third power of its diameter. To be conservative, we assume here a quadratic scaling with the diameter, i.e. linear scaling with the antenna area. This gives 3.11 kg as the mass estimate of the communication subsystem. Assuming 50 % efficiency for the transmitter, if the radiating power is 10 W, the consumed power is 20 W.

The communication subsystem contains also the following items:

– Medium-gain antenna that can be steered electronically in at least one axis, to enable communication with ground station during E-sail cruise phases.

– Low-gain antenna for receiving commands from ground.

– Bidirectional data link between SSC and ESC when docked. The link can be wired or wireless.

– Radio science experiment for determining internal mass distribution of the asteroid.

We do not allocate additional mass and power for these items. Roughly similar items existed also in Dawn's communication subsystem, hence we assume that they are included in the 3.11 kg total mass estimate of our communication subsystem.

### 4.6.5  Command and data handling

For command and data handling system (CDHS), we reserve 0.2 kg mass and 0.4 W average power. This corresponds to a single 10 by 10 cm cubesat printed circuit board.

### 4.6.6  Mechanisms

– Solar panel deployment (required).

– Part of the sampler (subsection 4.6.2):

    – Sample canister and lid delivery line (required for science).

    – Lid soldering mechanism (required for science).

    – Mechanism to insert sample canister into EC (required for science).

– Docking with magnetic holding and launch lock (required, subsection 4.6.3).

– Solar panel rotation (nice to have so that energy harvesting continues when spacecraft points its instrument or antenna – the feature enables more science per given orbital time and given solar panel area, also less driving for battery size).

### 4.6.7 Orbit and attitude control system

Attitude control is carried out by reaction wheels. The reaction wheels are desaturated by 1 N hydrazine monopropellant thrusters[5], which are also used for orbit control, landing, liftoff and docking proximity manoeuvres. During docking, a 1 cm/s resolution in velocity control is sufficient, and the less than 0.1 Ns impulse bit size of the 1 N thruster (`spacepropulsion.com`, 2018) is sufficient to accomplish it. Possible problematic plume effects exist in the docking approach phase when the must brake its approach of the ESC and the plumes can partly impinge on the tethers. There are two types of possible effects, thermal and chemical. For the thermal effect, a simple estimation gives the result that if a 1 N thruster fires directly against a tether, a 1 m mutual distance is already sufficient to avoid harmlful heating of the wire. For the chemical effect, hydrazine decomposes into hydrogen, nitrogen and ammonia. Of these, hydrogen might cause embrittlement in metals and ammonia is corrosive to copper (one of the candidate tether materials) in the presence of water, but probably not in the absolutely dry conditions that we have outer space. Let us assume that in the final approach phase one needs to perform a 10 cm/s braking manoeuvre of the SSC. With 43 kg mass of the SSC, it corresponds to 4.3 Ns impulse and 2 grams of hydrazine with specific impulse of 220 s (`spacepropulsion.com`, 2018). If 2 grams of hydrazine decomposition products are spread out over a 1 $m^2$ area for example, the effective layer thickness (assuming water density for simplicity) that falls out over the affected area is 2 $\mu$m. This is so little that even if the material is chemically active and reacts with the metal wire, it can only destroy a surface layer which is one tenth of the wire diameter. In reality the situation is much better because the largest mass fraction is $N_2$ which is inert and because the plume does not fire directly against the tethers, but against the bottom of the ESC.

Using hydrazine thrusters during asteroid landing might contaminate the to-be-sampled asteroid surface. However, the baseline idea is that the spacecraft hits the surface with its original travel speed and uses the thrusters on its roof to prevent a bounce-off. During liftoff the hydrazine plume does affect the underlying surface, but the samples are already sealed in the container at that time.

Four reaction wheels are used of type Blue Canyon Tech RWP 500. This reaction wheel has maximum angular momentum of 0.5 Nms, maximum torque 0.025 Nm, mass 0.75 kg, and at half of the maximum momentum it consumes less than 3 W of power[6].

For the thrusters, we use eight 1 N thrusters where each of them weighs 0.29 kg.[7] Altogether the AOCS weighs $8 \times 0.29 + 4 \times 0.75 = 5.32$ kg without tanks and propellant lines. For the tanks and propellant lines, we assume mass which is 10 % of the propellant mass.

We assume a 500 m/s delta-v budget for orbital changes, which is sufficient for sampling more than ten asteroids. To sample an asteroid, four burns are needed: (i) for departing from the ESC towards the asteroid; (ii) for braking near the asteroid; (iii) for liftoff; (iv) for braking before approaching and re-docking with the ESC. The size of the burns are determined by the travel speed that we wish to use the traverse the Hill

---

[5]Hydrazine can be substituted by green monopropellant such as LMP-103S, if desired.

[6]See `http://bluecanyontech.com/rwp500/`.

[7]1 N hydrazine thrusters sold by Lampoldshausen Orbital Propulsion Centre (`http://space-propulsion.com`) weigh 0.29 kg.

sphere radius distance. To the asteroid landing and liftoff delta-v one has to add the escape velocity of the asteroid. For an asteroid in circular orbit, the Hill sphere radius is given by

$$r_H = r \left( \frac{M}{3M_{\text{Sun}}} \right)^{1/3} \tag{4.1}$$

whereas the escape velocity is

$$v_{\text{esc}} = \sqrt{\frac{2GM}{R}}. \tag{4.2}$$

Here $r$ is the asteroid's heliocentric distance, $R$ is its radius and $M$ is the mass,

$$M = \frac{4}{3}\pi R^3 \rho \tag{4.3}$$

where $\rho = 2 \cdot 10^3$ kg/m$^3$ is the asteroid's density. In order to accomplish the one-way trip in time $t_0$, the travelspeed required is $v = \frac{r_H}{t_0}$ and the total sample fetching delta-v for the asteroid is

$$\Delta v = 4\frac{r_H}{t_0} + 2\sqrt{\frac{2GM}{R}}. \tag{4.4}$$

For example if $r = 3$ au, $R = 5$ km, $\rho = 2 \cdot 10^3$ kg/m$^3$ and $t_0 = 5$ days, $v_{\text{esc}} = 5.3$ m/s, $r_H = 2500$ km, $v = 5.8$ m/s and $\Delta v = 34$ m/s. The required delta-v grows with the asteroid radius $R$. The Hill term is proportional to $R^{3/2}$ and the escape velocity term scales linearly in $R$.

We also need some propellant for desaturing the reaction wheels. The dominant source of angular momentum is likely to be the small centre of mass offset of the thruster force. However, the amount of delta-v is much smaller than the delta-v due to the orbital changes themselves, maximum 1 % and likely smaller. We ignore it in the delta-v budget which anyway contains significant margin and take the 500 m/s to represent the total delta-v budget of the SSC.

## 4.6.8 Power

We use two rotatable solar panel wings, moderately V-inclined to keep them away from the asteroid during landing and away from the tethers during cruise.

We use a battery to enable momentary larger than average power consumption e.g. during landing and to cover asteroid eclipse, if any.

During cruise, SSC power is used to power ESC. We transfer power from SSC to ESC by spring metal contactors of the docking interface. If the contact turns out to be a source of EM noise, energy can be transferred in batches using ESC battery as buffer. In addition, ESC has its own body-mounted solar panels, but they are often partially shadowed by the SSC and its panels, depending on the E-sail inclinaton angle and rotational phase. ESC needs its own panels when SSC is away. Also, if the SSC fails to return, the ESC can fly home with its own solar panels, with the samples and high-resolution data already collected.

For the power system, we assume mass 75 W/kg specific power at 1 au. This figure is halfway between Dawn's value of 50 W/kg and 100 W/kg which was given by Joel Poncy of Thales Alenia Space as private communication. Dawn had high power, long solar panel wings and consequently long cables which increased the power system mass.

The power that must be produced at maximum heliocentric distance (assumed to be 4.0 au) is 52.75 W, which corresponds to 844 W of 1 au power. The power system mass is then 844 W / (75 W/kg) = 11.3 kg. The power budget is shown in Table 4.3.

**Table 4.3:** SSC power budget.

| Subsystem | Mean power |
|-----------|-----------|
| Detectors | 9.55 W |
| Communication | 20 W |
| CDHS | 0.4 W |
| AOCS | 12.8 W |
| Thermal | 10 W |
| Total | 52.75 W |

The thermal subsystem power comes from assumed amount of electric heating that can be required at 4.0 au. Because we are considering average rather than peak power budget, hardware such as the sampler which is used only for short periods does not contribute.

## 4.6.9   Structure

For structure, we assume mass which is 11 % of the internal wet mass carried by it, which comprises detectors, communication, CDHS, sampler, docking, AOCS, power, tank and propellant. This structural fraction is the same as for Dawn.

## 4.6.10   Thermal control

We use a standard approach based on electric heaters and dumping excess power to a resistive radiator. The thermal environment of SSC does not change drastically when docked with ESC. For thermal subsystem we assume 4.5 % of the internal parts (for definition of the internal parts, see subsection 4.6.9 above), which is the same fraction as for Dawn.

The mass budget is shown in Table 4.4.

## 4.6.11   Configuration

We use a box 0.5 m in width and depth and 0.3 m in height. The mass is 43.4 kg, which gives 52.08 kg when adding a 20 % margin. The mean density is then $52.08/(0.5 \times 0.5 \times 0.3) = 694$ kg/m$^3$. This figure is low in comparison to e.g. cubesats, whose density is typically at least 1000 kg/m$^3$ and sometimes 2000 kg/m$^3$. This indicates that the components can be placed inside the box without problems.

To the box we attach to rotatable solar panel wings that are moderately V-inclined to keep them away from the asteroid surface during landing.

**Table 4.4:** Mass budget of science spacecraft (SSC).

|  | $m$ | % |
|---|---|---|
| Detectors | 2.63 kg | 6.07 |
| Communication | 3.11 kg | 7.17 |
| CDHS | 0.2 kg | 0.461 |
| Sampler | 3.0 kg | 6.92 |
| Docking | 2.17 kg | 5.0 |
| AOCS | 5.32 kg | 12.3 |
| Power | 11.3 kg | 25.9 |
| Structure | 4.13 kg | 9.52 |
| Thermal | 1.69 kg | 3.9 |
| Tank | 0.897 kg | 2.07 |
| Propellant (500 m/s delta-v) | 8.97 kg | 20.7 |
| Total wet | 43.4 kg | 100.0 |
| Total wet with 20 % margin | 52.1 kg | |

# 4.7   E-sail spacecraft (ESC)

## 4.7.1   Detectors

The E-sail flight algorithm needs an imaging system which is able to locate the remote units optically. The system needs to cover at least a full circle equatorial band in the tether plane, with enough width of the imaged area to cover any tether bending. We place the cameras at the perimeter so that they have an unobstructed view of the tether plane. We use 8 cameras, each with 60° field of view, so that there is some overlap in covering the 360° circle.

We also add a four more cameras to cover the antisunward side, to be able to see the asteroid's location with respect to background stars. Together, the cameras cover nearly $4\pi$ field of view, excluding the vicinity of the sun direction which would be hard to image in any case.

For each camera we assume 60 grams. This is 2/3 of the mass of the SSC cameras, because the SSC cameras have more scientific tasks than the ESC ones. Total mass of the detectors is then $12 \times 0.06 = 0.72$ kg.

## 4.7.2   Entry capsule (EC)

We assume 19 kg EC mass, which is the same as for Hayabusa. Hayabusa capsule's payload is a $\sim 1$ kg sample container, where most of the mass is taken by the powerful springs that constantly pull the lid to make it airtight. We need multiple sample containers because we want to sample multiple asteroids, and we place the soldering based sealing mechanism for the canisters in the SSC (see subsection 4.6.2 above). The EC only has a passive container volume with a hole in the backpanel through which the SSC actively inserts the canisters which are already sealed in this phase. The hole in the backpanel is closed by a mechanical door after all asteroids have been sampled, but the door need not be airtight and it is only needed to protect the hole against the backside reentry plasma.

During reentry, the ablator material of the heatshield acts as a heat sink. After the capsule has hit the ground, the charred portion of the thermal shield is hot and the heat tends to diffuse through the heatshield into the EC's payload. High temperature has a negative effect on the scientific value of thes sample, and also one must make sure that temperature does not rise so high that the soldering of the sample canister would melt which would destroy the sealing of the sample. Detailed design and modelling is needed to reveal if post-landing heating is a problematic or not. If it is a problem, one can have a mechanism where the mechanical ground impact ejects away the EC's backpanel, either alone or together with the sample canisters. In the first case, the capsule interior is cooled by atmospheric air, in the second case the sample canisters are also physically far from the hot heatshield. In addition to or alternative to the mechanical impact, release of the capsule backpanel may occur also by heating of the capsule interior above certain temperature.

The EC also has high data density flash memory chips inside that are used to return high resolution science data. The flash memory chips are protected against radiation by the relatively thick thermal shielding of the capsule. Image data on them are stored without compression so that single bit errors caused by radiation cause error in only one pixel and can be corrected relatively easily by software in postprocessing on ground. Vital data that must not be corrupted are stored in a separate smaller filesystem whose implementation contains sufficient number of error correcting bits and distant copies of the same data. In place of the image data files, the error correcting filesystem contains addresses (pointers) to the uncompressed image storage arena. The SSC records data in its own memory and transfers them slowly to ESC's EC flash memory chips during the E-sail cruise phases.

### 4.7.3 Communications

We need a radio beacon and low-gain transmitting antenna which sends a signal informing SSC about ESC's current position with respect to the asteroid, that is, the right ascension and declination of the asteroid's optical centroid (defined in some suitable way) as well as the asteroid's apparent size, as seen from the ESC. SSC receives the signal through its high-gain antenna. For this to succeed, SSC needs to maintain knowledge of the approximate location of ESC. This can be done by being in regular contact. If SSC loses ESC's location, it must enter into a mode where it scans the sky systematically to find its radio signal.

We also need a low-gain receiving antenna for receiving connections from SSC's high-gain antenna.

When SSC and ESC are docked together, we need a bidirectional data link between them. For example, E-sail housekeeping data must be transferred from ESC to SSC if one wants to send it to ground station using SSC high-gain antenna. Conversely, the high resolution science data gathered by SSC and stored temporarily in memory must be transferred to EC's flash memory chips.

We reserve 0.5 kg for the mass of these communication subsystems on ESC.

### 4.7.4 Command and data handling

For command and data handling, we reserve 0.2 kg and 0.4 W power, as on the SSC.

## 4.7.5 Mechanisms

- E-sail deployment (required).

- Docking with magnetic holding and launch lock (required).

- EC release (required).

## 4.7.6 Orbit control system

The ESC monoprop thrusters are used during E-sail deployment phase to provide the angular momentum for the SSC+ESC combination to initiate tether deploment. After 300 m of deployment, further angular momentum is obtained by the E-sail effect using the spin control capability of the TI tether rig geometry (Chapter 1). In the baseline case we have 18 maintethers, 0.33 kg remoteunit empty mass and 1.04 kg total auxtether mass, which produces 7.034 kg of total rotating mass, or 0.391 kg per maintether. The deployed maintethers at 300 m length weigh only 60 grams (3.3 gram per maintether) which we ignore here. To give 1 cN maintether centrifugal tension, the required angular speed is $\omega = \sqrt{(10^{-2}\,\mathrm{N})/(0.391\,\mathrm{kg} \times 300\,\mathrm{m})} = 9.23 \cdot 10^{-3}$ rad/s and the angular momentum

$$L = 7.034\,\mathrm{kg} \times (300\,\mathrm{m})^2 \times \omega = 5850\,\mathrm{Nms}. \tag{4.5}$$

For comparison, the fully deployed tether rig with 15 km maintether length has angular momentum $2.3 \cdot 10^6$ Nms. Thus, only 0.26 % of the angular momentum needs to be provided propulsively and the rest comes from the solar wind by the E-sail effect.

The ESC is a disk with radius 1 m. We place the thrusters at 80 cm distance from the centre, to avoid putting the thrusters too close to the tethers to avoid harmful plume effects on the tethers. We also direct the thrusters 30° off the spinplane for plume avoidance reasons, which reduces the effective specifc impulse by factor $\sqrt{3}/2 = 0.87$. Then to yield 5850 Nms angular momentum, one needs an impulse of 7306 Ns. Monopropellant 1 N hydrazine thruster nominal specific impulse is 220 s (`spacepropulsion.com`, 2018) so that the propellant consumption in the tether deployment phase is 7306 Ns/(0.87 × 220 s × 9.81m/s$^2$) = 3.9 kg.

The thruster plume could affect the tether by direct heating and by chemical attack. Concerning direct heating, according to a simple estimation, if the distance between a tether and a 1 N monopropellant thruster which is directed exactly towards it is more than 1 m, then tether heating is not a problem. Concerning possible chemical attack, hydrazine decomposes into hydrogen, nitrogen and ammonia. Of these, hydrogen causes embrittlement in metals and ammonia causes corrosion in copper (which is one of the candidate tether materials) in the presence of water. However, copper may resist ammonia corrosion in dry conditions which is the case here. Qualification tests with the thruster plumes and the tethers would be needed to confirm this, if copper is used as the tether material.

Since the tethers are continuously reeled out, each thruster firing affects a different part of the tether. Thus, possible chemical effects do not accumulate to weaken a single point, which is good. If one wants to minimise the risk of chemical attack, the thrusters should be fired continously or in so small pulses that corrosion effects spread out evenly

over the entire 300 m section of the tether which is outreeled during the propulsive phase of the deployment procedure.

A separate centrally positioned 1 N monoprop thruster on the ESC is used to cancel periodically the accumulated photonic pressure impulse on the tethers when the ESC is parked on the boundary of the asteroid's Hill sphere. The photonic pressure at 1 au is about $1361\,\mathrm{W/m^2}/(3 \cdot 10^8\,\mathrm{m/s}) = 4.5 \cdot 10^{-6}$ Pa. With 18 tethers that are 15 km long and made of 4 round wires, each with $25\,\mu$m diameter, the projected sun-facing area is

$$A = (18 + 2\pi) \times 15 \cdot 10^3\,\mathrm{m} \times 4 \times 25 \cdot 10^{-6}\,\mathrm{m} = 36.4\,\mathrm{m^2} \tag{4.6}$$

where the $2\pi$ term results from the auxtether ring. Multiplying $A$ by the photonic pressure yields 0.16 mN thrust at 1 au. In the calculation we assumed for simplicity that on average photons are reflected by 90° (i.e. sideways) by the wire (in reality, centrally hitting photons are reflected backwards while some of them are reflected by less than 90°). If the total maximum time that the SSC spends in the undocked state on its sample fetching missions is 1.5 years, the maximum photonic impulse that must be cancelled is 7600 Ns which is about the same as during the tether deployment. However, this is only a worst-case overestimate because although the mission is capable of studying also NEOs near 1 au, usually it would rendezvous at least most of its target asteroids in the main belt where the photonic pressure is nearly an order of magnitude less than at 1 au. Propulsive cancellation of the photonic thrust is not strictly necessary, but it is expected to reduce the risk of the SSC and ESC losing each other, and it also reduces the time and propellant needed by the SSC to re-catch the ESC. Depletion of the ESC's propellant reserve does not prevent further asteroids from being sampled, however.

We reserve 7.8 kg of hydrazine of which 3.9 kg (50 %) is consumed during the tether deployment phase and the rest is sufficient for 1.5 years of photonic pressure compensation at 1 au. Notice that unlike it is typically the case, the propellant budget of the ESC does not depend on its mass. The propellant mass need not be recomputed if the mass budget of the ESC changes.

An attitude control system is not needed onboard ESC because during E-sail deployment, SSC's attitude control system can be used, during cruise the E-sail effect takes care of it, and during parking the ESC is spin-stabilised by the large angular momentum of the rotating tether rig. Also the ESC does not need cold-gas thrusters.

### 4.7.7   E-sail

- Main tethers, connected by electrified auxtethers in TI topology.

- Remote units at tips of main tethers, passive after deployment, alternatingly insulating and conducting.

- High-voltage subsystem and electron gun.

- Controller.

- Precise accelerometer (required by E-sail controller).

## 4.7.8 Power

– Power transfer contactors of the docking interface to receive cruise time power from SSC.

– Fixed solar panels for powering the parked state.

ESC also gives power to EC by other spring contactors.
Power budget estimation:

• 400 km total tether length, comprising e.g. 20 15-km long maintethers and the corresponding auxtethers.

• 140 W for 400 km E-sail.

• Include factor 1.5 to account for exceptional solar wind.

• Assume HV source efficiency 0.6.

• $\Rightarrow 1.5 \times 140/0.6 = 350$ W power.

• In addition, assume 20 W of hot cathode heater power and 10 W for controller.

• 1 au power requirement: 380 W.

• 4 au power requirement: $30 + 350/4^2 = 52$ W.

• Assume power must be delivered by 45° inclined solar panels $\Rightarrow$ factor $\sqrt{2} = 1.41$.

• Solar constant 1300 W/m², assume 95 % cell fraction on panel, assume EOL 28 % efficiency $\Rightarrow$ EOL 346 W/m² at 1au in perpendicular illumination.

• 1 au: need $380 \times \sqrt{2} = 537$ W, i.e. 1.55 m² area.

• 4 au: need $52 \times \sqrt{2} = 74$ W, i.e. 3.42 m² area (e.g. disk of 2.09 m diameter, or two wings 1.71 m ×1.0 m each).

## 4.7.9 Structure

– Ring shape.

– Perimeter of ring has E-sail hardware (tether reels, stowed remote units and auxiliary tether).

– Interior area of the ring:

   – EC, nose down, base up

   – docking cone

   – E-sail electronics box (HV source, controller)

   – bottomside of electronics box: electron gun, resistive radiator for dumping excess power, photon pressure cancelling electric thruster

   – solar panels providing parking time power

Drivers for ring diameter:

1. Likely driver: spacing needed between tether roots times number of tethers.

2. Possible driver: needed parking time power.

## 4.7.10 Thermal control

During cruise, overheating is not a problem since SSC shadows the sensitive areas. Electric heating is used when necessary to prevent too cold temperature at the sensitive parts (EC and E-sail electronics box).

During parking, E-sail electronics box and EC must be prevented from becoming too cold at longest heliocentric distance. The EC has electronics, primary battery and landing parachute inside which probably have some thermal limits. Thermal design of sensitive parts is such that with no heating, the parts do not become too warm at shortest heliocentric distance.

During parking, power which is not needed for heating is dumped to the resistive radiator.

The mass budget is shown in Table 4.5.

**Table 4.5:** Mass budget of E-sail spacecraft (ESC).

|  | $m$ | % |
|---|---|---|
| E-sail: | 19.7 kg | 28.7 |
| – tether length 15 km |  |  |
| – 18 tethers | 4.01 kg |  |
| – maintether reels | 7.02 kg | 0.39 kg per reel |
| – remote units | 5.99 kg | 0.333 kg per unit |
| – accelerometer | 0.1 kg |  |
| – HV | 2.55 kg |  |
| Detectors | 0.72 kg | 1.05 |
| Communication | 0.5 kg | 0.729 |
| CDHS | 0.2 kg | 0.292 |
| Entry capsule (EC) | 19 kg | 27.7 |
| Mechanisms | 6.92 kg | 10.1 |
| AOCS | 3 kg | 4.37 |
| Power | 9.37 kg | 13.7 |
| Structure | 6.53 kg | 9.52 |
| Thermal | 2.67 kg | 3.9 |
| Total dry | 68.6 kg | 100.0 |
| Total dry plus 20 % margin | 82.3 kg |  |
| Propellant | 7.8 kg |  |
| Total wet with 20 % margin | 90.1 kg |  |

# 4.8 Motivation for the main design choices

## 4.8.1 Total mass budget

**Table 4.6:** Total mass budget, including the 20 % margin.

|           | $m$      | %     |
|-----------|----------|-------|
| ESC wet   | 90.1 kg  | 63.4  |
| SSC wet   | 52.1 kg  | 36.6  |
| Total wet | 142.2 kg | 100.0 |

The total mass budget is show in Table 4.6.

## 4.8.2 Telemetry system as a driver

— The telemetry system is the key mass budget driver. The telemetry system must return enough data to enable informed and rather quick selection of the landing site.

— There is a tradeoff between telemetry system mass and ground operations costs (antenna tracking time). If the spacecraft's telemetry system is made smaller, one either has to reduce the data rate so that receiving the data takes longer, or one has to use a bigger and more expensive ground station antenna. In the first case, the number of visitable targets per fixed duration mission may also decrease. As a baseline, we allocate the same mass for the telemetry system (28 kg) as was done in Dawn.

— Consequently, miniaturisation down to nanosatellite class is not feasible.

— This implies, in turn, that we need to use a multi-tether E-sail, a single tether is not sufficient.

— Not all data need to be returned through the telemetry system, though, since unurgent data can also be returned in flash memory chips inside EC.

## 4.8.3 Sampling device

— Hayabusa-2 uses large spring forces inside EC to seal the sample canister by pressing its lid tightly. This is the drawback of adding mass inside EC. Mass inside EC is more expensive than mass outside it because it gets multiplied by the mass of entry systems like heat shield and parachute.

— To avoid this issue, we solder the lid onto the sample canister before inserting it into EC.

— We use a magnet to attract sample particles, to increase the sample canister's expected fill fraction. Only asteroids that are collisional fragments of a differentiated body like Vesta might be iron-free and thus nonmagnetic, but such bodies are not among the high priority candidates for sample return because meteorites representing them already exist.

– To make regolith airborne, we perturb the surface by the spacecraft's own landing impulse, possibly repeatedly by using the spacecraft's thrusters. Doing this, we avoid the need to have special hardware like pyrotechnig bullets (Hayabusa-2) or a robotic arm (Osiris-Rex).

### 4.8.4  Geometric configuration

The following factors constrain the geometric configuration (Fig. 4.2):

1. In order to have stable rotation during E-sail cruising phase, the spin axis aligned component of the inertia tensor (excluding the tethers) must be larger than the other components. With our assumptions for subsystem masses, the docked configuration (Fig. 4.2) has spin axis inertial moment tensor component $I_{zz} = 39.7$ kg m$^2$ and the spinplane components $I_{xx} = 20.0$ kg m$^2$ and $I_{yy} = 22.6$ kg m$^2$. In theory, for passive orbital stability it is sufficient if the inertial moment ratio $K = I_{zz}/\max(I_{xx}, I_{yy})$ is larger than unity, but typically one assumes that $K$ should be at least 1.2 for good passive stability. In our case $K = 1.76$ so we are well on the safe side. When the SSC is separated from ESC, the ESC exhibits even larger $K$ ratio.

2. There must be sufficient solar panel area for both ESC and SSC. The area depends on many factors, but especially on the maximum heliocentric distance for sample collection.

3. No part of a solar panel wing should touch the asteroid during sampling. The severity of this constraint depends on how rough or sloped terrain we are prepared to sample.

4. There must be room for high-gain antenna of sufficient diameter.

Ideally, the geometric design should be such that the solar panel area, the maximum terrain slope and the high-gain antenna diameter could be increased or decreased within reasonable limits without changing the topological features of the design.

### 4.8.5  Choice of type of propulsion

We need non-E-sail propulsion for deploying the E-sail, for transferring the SSC to the asteroid surface and back, and for docking. We also use propulsion for cancelling the photonic thrust during Hill sphere parking. We cover all propulsion of both spacecraft by monopropellant hydrazine thrusters. Other options considered were the following:

– The specific impulse of cold gas would not be sufficient for E-sail deployment and for SSC orbital changes.

– The delta-v requirement is not so large that the added complexity and cost of a bipropellant system would be warranted.

– Indium FEEP was considered because its propellant is non-toxic, but was not selected because metal atom deposition on the high-voltage insulator surfaces of the ESC might be risky. Also, the thrust of electric propulsion such as indium FEEP is insufficient for lifting off an asteroid, except the smallest ones.

– The combination of electric propulsion (either indium-FEEP or xenon) and cold gas propulsion would be possible. Cold gas would be used for lift-off from the asteroid and electric propulsion for orbital changes. If needed due to plume effects avoidance reasons, cold gas could also be used during docking instead of electric propulsion. This combination would have the benefit relative to hydrazine of being non-toxic. The drawback would be that a limitation would arise for the size of the asteroids that can be sampled. If the cold gas propellant comprises 5 % of the total mass and its specific impulse is 65 s(`moog.com`, 2018), the cold gas delta-v budget is 31 m/s. If we want to sample ten asteroids, then we need a total of 20 landing and liftoff cold gas thrustings so that 1.5 m/s is available for each, which corresponds to average asteroid diametre of only 3 km. In other words, the summed diameter of the sampled asteroids would have to be less than 30 km. To avoid this restriction, we have selected hydrazine as the baseline.

– Hydrazine and electric propulsion could also be used in combination, with in principle better performance than hydrazine alone (lower mass or larger delta-v budget or both) because the average high specific impulse would be higher. Such combination would become relevant if the objective would be to sample predominantly large asteroids. With the baseline hydrazine and with 500 m/s of SSC delta-v budget, the summed asteroid diameter is limited to $\sim$ 150 km which is reasonably large.

## 4.9   E-sail for asteroid mission: general remarks

The E-sail frees the mission designer from the rocket equation. Concerning scientific missions to asteroids, the main limitations of the E-sail are the following:

1. The attitude and rotational state of the E-sail platform are dictated by the E-sail. This raises the issue how to do pointing.

2. The E-sail platform with its long tethers obviously cannot land on an asteroid. Already if it approaches closer than the tether length, one has to be careful to avoid a collision between a tether and the body. Furthremore, a prolonged stay inside the asteroid's Hill sphere carries a theoretical risk that if the asteroid has unseen minimoons, they could collide with the tethers. The risk is hard to quantify because the commonness of small asteroid moons is not known.

To the pointing problem, we are aware of the following solutions:

1. A single-tether E-sail platform can be pointed. Then the mass of the spacecraft must be of nanosatellite class.

2. For any E-sail, a gimballed instrument platform is an obvious engineering solution to the pointing problem.

3. Using docking and separate science spacecraft is another straightforward engineering solution.

To the approach problem, if one wants to play safe and avoid the Hill sphere, the only solution is to use docking. Since docking also solves the pointing problem, we chose to employ it in this study.

Based on these considerations, in this project we analysed two main mission scenarios:

1. Flyby mission with nanosatellite fleet. The pointing problem is resolved because a spacecraft which is attached to a single tether can be rotated easily in two angles if the tether's attachment point coincides with the spacecraft's centre of mass. The approach problem is avoided by having about 1000 km flyby distance. This mission, under the name 'Multi-asteroid touring' (MAT), was proposed and selected for continuation study in the "Call for new ideas" call in 2016.

2. Landing and sample return mission. We leave the E-sail mothership at the boundary of the Hill sphere and use a separate dockable science spacecraft, which solves the approach and pointing problems. We paid lot of attention to reducing mass, because we hope to enable a sample return fleet. In a fleet, each spacecraft could sample more than one body, because failure of a single spacecraft is tolerable. Thus a fleet can sample a significant number of bodies, which boosts the scientific value. Per sampled body, the fleet mission is likely to be significantly cheaper than a single spacecraft that samples a single asteroid.

As a variant of the landing and sample return mission, one can also consider a remote sensing orbiter which is taken to multiple asteroids by repeated docking with the E-sail mothership. Such mission would be technically simpler than sample return. Scientifically, it would provide information which is complementary to sample return. Technically, it is also possible to consider enhanced versions of sample return where the science spacecraft also has other remote sensing instruments than optical and NIR, but combining too many functions in the same mission is often not advantageous.

If one thinks of E-sail enabled asteroid science as a programme, one would first make MAT to get survey data of a large number of targets, then proceed with a sample return fleet, possibly adding also a remote sensing orbiter fleet. Such programme would address fundamental scientific questions (for example, how did the solar system form and evolve, where did Earth's water come from) as well as provide the necessary basic knowledge and technological tools for planetary defence, asteroid mining and solar system colonisation. MAT needs only nanosat class spacecraft with single-tether E-sails, the later steps need multi-tether with moderate thrust.

# Chapter 5

# WP5: NEO version of Multi-Asteroid Touring

*We present NEOMAT, which is a NEO version of the earlier Multi-Asteroid touring (MAT) mission proposal. We simulate statistically the frequency of NEO flybys in the vicinity of 1 au as function of the E-sail characteristic acceleration. We find that unlike MAT, NEOMAT is not strongly mass-constrained, and consequently it does not require autonomous navigation as normal interactive communications are feasible. We also discover that using purely radial E-sail thrust is possible in this case, which leads to a further simplification since cruise phase spin rate control is not needed and hence the remote unit needs to stay functional only during the E-sail tether deployment. Overall, NEOMAT is a mission architecture which needs no other novel technologies except the E-sail, and for the E-sail, moderate suffices.*

## 5.1   Objectives

The objective of WP5 is to make a NEO version of the Multi-Asteroid Touring (MAT) mission concept. The original MAT(Janhunen et al., 2016; Slavinskis et al., 2018) was our proposal to the "Call for new ideas" of 2016 and an outgrowth of WP2.

## 5.2   Introduction

Near-Earth Objects (NEOs) are a relatively sparse population of originally main-belt asteroids that have experienced orbital modification that has brought their perihelia down to 1 au. Typically NEOs are relatively small. Some of them are collisional fragments, and some are sufficiently small that the orbit has been modified by radiation pressure effects. Geologically, minerals found in NEOs are a sample of minerals occurring in main-belt asteroids.

   The orbit of a NEO is not long-term stable. The orbital lifetime depends on the object's size and other factors, but is typically some millions or tens of millions of years, which is short compared to the 4.5 billion year age of the solar system. The main loss mechanisms are collisions with Earth and other terrestrial planets, drifting too close to the Sun and getting ejected from the solar system. In the geological timescale, formation of new NEOs in the main belt by collisions and radiation pressure drifting and their subsequent collision with Earth is the main mechanism how Earth and its biosphere has been directly affected by solar system bodies.

   The following motivations for NEO missions can be identified:

 – Scientifically, NEOs are samples of main-belt objects. Because NEOs are more accessible than main-belt objects, studying NEOs *in situ* might be a more cost-effective approach than studying the main-belt asteroids directly, although both strategies are needed.

 – From the public safety point of view, NEOs and comets are potentially dangerous. Although both are relevant, the NEO impacts are more frequent than cometary ones.

 – If asteroid mining takes off, space activities can start growing exponentially, fuelled by lowering cost of mass in orbit. NEOs are the primary target for asteroid mining at least in the beginning phase.

## 5.3   Original Multi-Asteroid Touring proposal

Originally, Multi-Asteroid Touring (MAT) was proposed to the "Call for new ideas" in September 2016 (Janhunen et al., 2016) and the theme was selected for CDF studies. Elaboration and details were later added to the concept (Slavinskis et al., 2018). The main characteristics of the original MAT are the following (see Fig. 5.1 for an exploded CAD drawing of the main spacecraft and the remote unit):
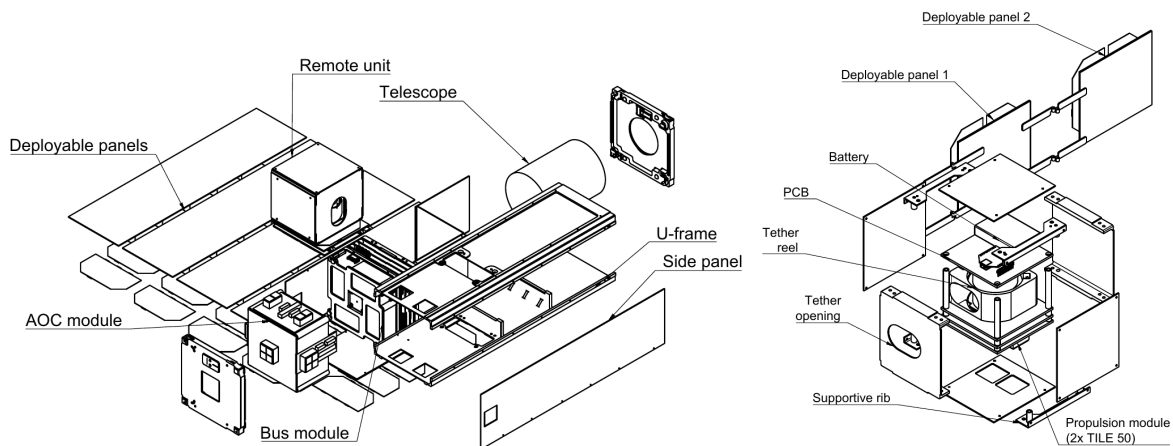


**Figure 5.1:** Exploded view of the main spacecraft (left) and the remote unit (right) of the original MAT (Slavinskis et al., 2018).

 – Single-tether E-sail with 10-20 km length.

 – Total mass $\sim$ 5 kg.

 – The main instrument is 4 cm telescope which is also used for automatica optical navigation based on nearby known (numbered) asteroids.

 – Quasi-elliptic orbit that takes the spacecraft once through the main belt, ending in Earth flyby.

 – During the tour, a preprogrammed set of asteroid flybys are made. The data are stored in flash memory and downloaded during the final Earth flyby.

- Full autonomy during the science mission, except perhaps a "here I am" beacon that can be tracked if wanted.

- Requirement of $\approx 1.0$ mm/s$^2$ E-sail characteristic acceleration, in order to reach the necessary orbit and in order to enable the final Earth flyby.

- 3.2 year mission duration in the baseline case.

- Typically 6-7 asteroid flybys per spacecraft.

- A fleet of identical spacecraft. The fleet size is flexible, but as a baseline, 50 was assumed. Each member of the fleet is programmed individually to make its own tour. Dedicating more than one spacecraft to study a particularly valuable target is an option.

The main technical challenges of the original MAT, as identified in the CDF study, were as follows:

1. The mission is mass-constrained: in order to reach the correct orbit, relatively high characteristic E-sail acceleration of $\approx 1.0$ mm/s$^2$ is needed. For an E-sail tether of 20 km length and biased to 10 kV voltage (or an equivalent combination of length and voltage), the maximum mass is 5 kg. If the voltage can be raised to 20 kV, the maximum mass increases to 10 kg, though.

2. In order to save mass (no high-gain antenna needed) and in order to keep telemetry costs low (high bitrate so that operation time per each retrieved gigabyte is low), each member of the fleet transfers its collected data during the Earth flyby. This requires autonomous navigation capability. Although the required operations were demonstrated already 20 years ago by NASA's DeepSpace-1, developing the necessary autonavigation software is a significant cost item.

3. The cold gas thruster of the remote unit must stay functional throughout the mission, in order to do spinrate management. Spinrate management is needed if the sail is inclined with respect to the Sun direction (i.e., if one generates non-radial thrust with the E-sail). In multi-tether E-sails, spinrate management is possible using the E-sail effect itself, but in single-tether systems such possibility does not exist.

## 5.4 Why NEO is easier

In this Work Package the target is to make a NEO version of MAT. The goal is to address the criticism listed at end of Section 5.3 and thereby to come up with a mission concept (for NEO instead of the main belt) which is implementable without new technology developments apart from the E-sail itself.

The NEO case is easier than the main belt case, for the following reasons:

1. The characteristic acceleration requirement is lower, and the requirement is soft. Thus, a larger total mass is possible, or a simpler E-sail, or both.

2. The thermal design and the power system design are simplified by the fact that we stay in the vicinity of 1 au instead of reaching out to beyond 3 au as in the main belt case.

3. Because of the larger mass possibility and because of a short Earth distance, traditional online telemetry can be used, thus development of a new autonomous navigation software is not required.

4. NEOs can be reached while staying near 1 au. Hence, raising the aphelion distance is not needed, and thus it is not necessary to increase the orbital energy. From this it follows that there is no need to tilt the spinplane of the E-sail, and this implies, in turn, that spinrate management is not needed. The avoidance of spinrate management means that the remote unit and its cold-gas thruster need to stay functional only during tether deployment.

## 5.5   Predicting the frequency of flybys

To simplify the analysis, we make the starting assumption that the NEO flybys occur at their orbital nodes, i.e., the positions where the object crosses the equatorial plane. Thus, the spacecraft stays exactly in the equatorial plane. Relaxing this assumption could somewhat increase the number of flybys that can be made, so the results that we will obtain below can be considered conservative. However, we do not expect that the difference is large.

We downloaded the orbital elements of all known NEOs from the JPL Small Body database (JPL Small Body Database, 2016). We propagated the trajectories of the asteroids for one year and found by numerical root finding the ecliptic plane crossings from the set of trajectories. For each ecliptic plane crossing (orbital node), we recorded its heliocentric distance. Then we calculated how many crossings occurred in the range 0.8–1.2 au in one year, and the answer is 5172. Dividing by the area of the ring that extends from 0.8 to 1.2 au, this gives 2058 nodes per square astronomical unit area of the ecliptic plane per year:

$$\frac{dN_{\mathrm{nodes}}}{dA dt} = 2058 \ \mathrm{au}^{-2}\mathrm{a}^{-1} \tag{5.1}$$

We use this number as input for the next stage of the calculation, which we now describe.

We simulate an ensemble of virtual E-sails that start from circular 1 au orbit (Earth's heliocentric orbit). By the above assumption, we do not perform any inclination changes, so their trajectories stay in the ecliptic plane. We also assume (see above) that the E-sail produces only purely radial thrust, because there is no need to change the orbital energy to chase the NEOs. For each spacecraft in the ensemble, its radial thrust magnitude is modulated as a function of time. We parametrise the modulation by dividing the total time $t_{\mathrm{max}}$ (we select $t_{\mathrm{max}} = 9\mathrm{months}$) into $N = 14$ segments of equal duration. For each segment, we assume that the thrust magnitude is either zero or the maximum allowed by the hardware. Thus, the modulation (programming) of the spacecraft is defined by $N = 14$ bits so that there are $2^N = 16,384$ members in the ensemble. Overall, this is a discrete parametrisation that aims to reproduce the orbits of all possible flight paths that the E-sails can use to reach the NEOs, under the assumptions of purely radial thrust and no inclination changes.

For each member of the ensemble, we calculate the orbit using the specific bit pattern that defines its E-sail thrust modulation as a function of time. We plot the set of points occupied by the ensemble as a function of time. The set is a region that grows rapidly

with time as the spacecraft diverge from each other due to different propulsive forcings. Figure 5.2 shows the spacecraft locations after 9 months. The region is like a bat-wing that starts from the Earth, corresponding to the singular member of the ensemble whose all bits are zero, i.e., no E-sail propulsion whatsoever is applied. The other end of the bat-wing corresponds to the extreme case where all the bits are one and the E-sail is at full throttle setting all the time. The boundaries of the bat-wing have an interesting, nontrivial shape. We also construct a bounadry polygon for the bat-wing numerically in order to calculate its area.
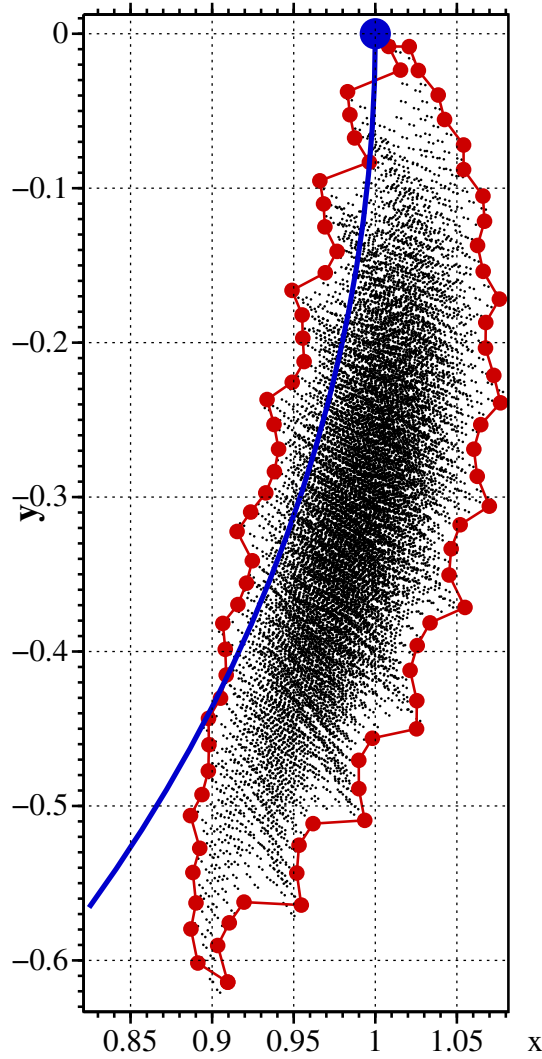


**Figure 5.2:** The reachable set in ecliptic plane after 9 months, in rotating coordinates where Earth (blue dot) is permanently at $(1,0)$ au. The characteristic acceleration was $a_c = 0.3$ mm/s$^2$. Black dots are the reachable set and the red line and dots show its boundary polygon from which its area was calculated. Blue line is Earth orbit.

Let $A(t)$ denote the area of the bat-wing as function of time. The number of node crossings per short time $\delta t$ is

$$\delta N_{\text{nodes}} = \frac{dN_{\text{nodes}}}{dAdt} A(t)\delta t \tag{5.2}$$

and the cumulative number of nodes during $0 \leq t \leq t_{\text{max}}$ is

$$N_{\text{nodes}} = \int_0^{t_{\text{max}}} \frac{dN_{\text{nodes}}}{dAdt} A(t)dt \tag{5.3}$$

where $dN_{\text{nodes}}/(dAdt) = 2058$ au$^{-2}$a$^{-1}$ was given by Eq. (5.1). The area-time integral $\int_0^t A(t)dt$ is shown in Fig. (5.3), together with levels that corresponding to one and three expected NEO crossings, respectively.
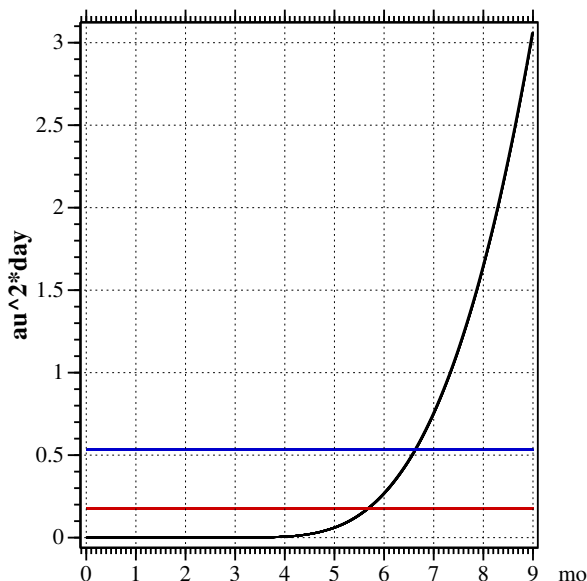


**Figure 5.3:** Area-time integral as function of time in months. Red line (0.177 au$^2\cdot$ day) corresponds to 1 NEO crossing the area on average, blue line to three crossings.

We have tested different $N$ and found that $N = 14$ is large enough. Almost the same results could also be obtained with lesser $N$, but we use $N = 14$ because the calculation is not too slow. The calculation time increases exponentially with $N$.

Most of the generated bit patterns are shuffling between zero and one in a random-looking way. Such thrust modulation would be unlikely to be used in a real mission. This is not a problem, however, since we are only interested in calculating the area (extent) of the resulting set. We are interested in the boundary values of the set, and these will be generated by necessity also, because the search goes through all possible $2^N$ bit patterns.

Finally, we repeat the calculation for different values of the E-sail characteristic acceleration $a_c$, and for each value we solve numerically from data similar to Fig. 5.3 at which point in time the expected number of NEO crossings within the E-sail ensemble area reaches 3. We select 3 instead of 1 in order to be conservative and in order to have freedom of selection in the NEOs targeted for flyby. The result is shown in Fig. 5.4. The result is rather similar to $a_c^{-1/3}$ dependence which we plot for comparison. For an E-sail with characteristic acceleration of 0.3 mm/s$^2$, for example, statistically it takes $\sim 6.5$ months for three NEOs to become accessible in the node flyby mode.

As seen from Fig. 5.4, the number of NEO flybys reached within a mission of some fixed duration depends relatively slowly (roughly as power $-1/3$) of the E-sail's characteristic acceleration. For a fixed E-sail and fixed mission duration, if one increases the mass of the science payload, the number of objects reached is reduced, and vice versa. In this Work Package, we will not study this tradeoff in detail, but will just adopt the value $a_c = 0.3$ mm/s$^2$. This parameters corresponding to this choice are listed in Table 5.1.
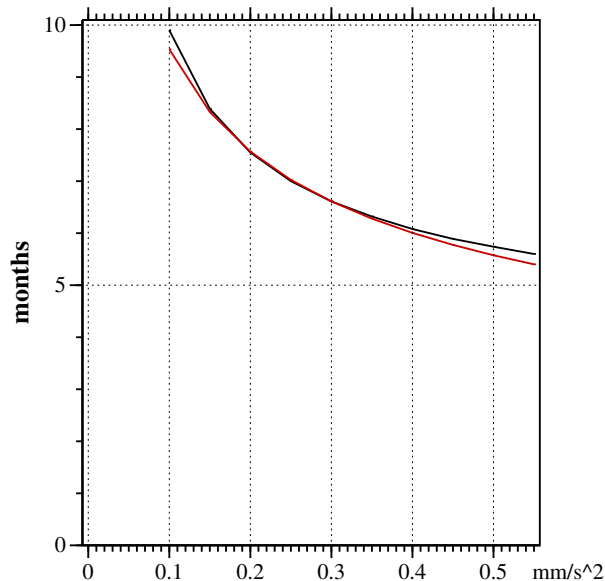
**Figure 5.4:** Time until on average three NEOs have become reachable as function of E-sail characteristic acceleration $a_c$. Red curve is $a_c^{-1/3}$ dependence.

**Table 5.1:** The adopted set of baseline parameters for NEOMAT.

| Parameter | Value |
| --- | --- |
| E-sail tether length | 12 km |
| E-sail voltage in nominal solar wind | 10.5 kV |
| Maximum voltage used in low-density wind | 20 kV |
| E-sail thrust per unit length | 250 nN/m |
| E-sail thrust | 3 mN |
| Total mass | 10 kg |
| Characteristic acceleration $a_c$ | 0.3 mm/s$^2$ |
| Time between NEO flybys | 6.5 months |

## 5.6   Scientific goals and instrument suite

We make flybys of NEOs from at nominally 1000 km closest distance. From our database, we find that the median absolute magnitude is $H = 22$, which corresponds to 170 m object diameter if the albedo is 0.1 (JPL webpage, 2019). At 7 m surface resolution, a 170 m body is resolved with 24 pixels. 80 % of the known NEOs are brighter than $H = 25$, and $H = 25$ corresponds to 43 m diameter which is resolved with 6 pixels. In the orbit analysis we required that three asteroids became accessible: this is to have some freedom of choice regarding the object, for example, one might decide to consider only objects larger than the median diameter of 170 m.

To reach 7 m optical surface resolution from 1000 km distance, one needs $\theta = 7 \cdot 10^{-6}$ rad angular resolution, which at blue $\lambda = 460$ nm wavelength corresponds to $D = 1.22\lambda/\theta = 8.0$ cm diameter telescope at diffraction limit. We follow Slavinskis et al. (2018) in assuming a 8 cm diameter telescope. We also need a near-infrared (NIR) spectral instrument (0.5-5 $\mu$m wavelength) for determining the average surface mineral composition. The NIR instrument does not need spatial resolution, because we are only interested in the average mineral composition. Producing a spatially resolved mineral

map would require a too heavy instrument at least for NEOs of the median diameter. The mineral composition is interesting to science and asteroid mining.

The 8 cm optical telescope is able to discover NEO minimoons down to $\sim 30\,\mathrm{cm}$ in diameter. Whenever a minimoon is discovered, one can determine the mass of the parent NEO by observing the minimoon's orbital speed.

From the optical images one can determine the body's shape (on the sunlit side at least), cratering, presence or non-presence of surface regolith. From these, one can typically characterise the body's nature (primordial collision fragment or rubble pile), surface age and something about the collisional history.

For planetary defense, the size of the largest crater is interesting, because it tells how large impact the body has suffered without shattering. This information can be used to assess the risk that the object is shattered in case one needs to try and deflect it quickly using impactors or nuclear explosives. Fragmentation of the body is unwanted, because the fragments might produce more widespread damage on ground than a single impact.

## 5.7 Mass budget

Table 5.2 shows the mass budget of NEOMAT, with values of the original MAT(Slavinskis et al., 2018) also displayed. Relative to MAT, we make the following changes:

1. We add a high-gain antenna (HGA) of 1 kg mass to enable deep-space communication with Earth.

2. We add 1.4 kg to the science payload.

3. We increment the structural mass by 50 % conform with the increased mass of the carried items. This adds 486 grams to the total.

The baseline HGA is a parabolic dish of 50 cm diameter, installed on the opposite end of the spacecraft than the telescope. Using such placement, it is possible to direct the HGA almost freely, despite the rotation of the tether, in the similar way as the telescpe can be turned freely (Janhunen et al., 2016; Slavinskis et al., 2018). To estimate the link budget, we using scaling from an exemplary Rosetta communication session (Rosetta blog, 2014). In this case, Rosetta used the X-band communication with a 35 m dish Deep Space Network station, was at 2.7 au distance, transmitted $\sim$25 W of radio power through its 2.4 m diameter HGA, and reached 23 kbit/s downlink telemetry rate. In our case a typical distance is 1 au, the transmitter radio power $\sim$2 W, hence the telemetry rate is predicted to be

$$\mathrm{bitrate} = \left(\frac{0.5\,\mathrm{m}}{2.4\,\mathrm{m}}\right)^2 \times 2.3 \cdot 10^4 \mathrm{bit/s} \times \left(\frac{2\,\mathrm{W}}{25\,\mathrm{W}}\right) \times \left(\frac{2.7\,\mathrm{au}}{2\,\mathrm{au}}\right)^2 = 580\ \mathrm{bit/s}. \qquad (5.4)$$

This bitrate allows retrieval of 200 megabytes of data per month, so for example one might decide to retrieve data for 8 hours per working day during a 4-month period following each NEO flyby, which repeats after each 6.5 months. It is also possible, mimicking the original MAT, to arrange for an Earth flyby at the end to retrieve some higher-resolution data gathered during the mission.

**Table 5.2:** Mass budgets of of MAT and NEOMAT. Differences to MAT are shown in bold.

| Component | Count | MAT Mass/g | MAT Total/g | NEOMAT Mass/g | NEOMAT Total/g |
|---|---|---|---|---|---|
| Bus PCB | 4 | 75 | 300 | 75 | 300 |
| Battery | 4 | 80 | 320 | 80 | 320 |
| Battery PCB | 2 | 40 | 80 | 40 | 80 |
| ACS RW200–15 | 1 | 21 | 21 | 21 | 21 |
| ACS RW–0.01 | 2 | 120 | 240 | 120 | 240 |
| Sun sensor | 6 | 5 | 30 | 5 | 30 |
| Patch antenna | 1 | 64 | 64 | 64 | 64 |
| Dipole antenna | 1 | 100 | 100 | 100 | 100 |
| **HGA** | 1 | – | – | **1000** | **1000** |
| HV source PCB | 1 | 75 | 75 | 75 | 75 |
| HV insulation | 1 | 23 | 23 | 23 | 23 |
| TILE 50 | 5 | 55 | 275 | 55 | 275 |
| Depl. panels | 4 | 102 | 408 | 102 | 408 |
| Hinges | 16 | 5 | 80 | 5 | 80 |
| **Structure** | 1 | 972 | 972 | **1458** | **1458** |
| Screws, nuts, inserts | 1 | 100 | 100 | 100 | 100 |
| **Science payload** | 1 | 1000 | 1000 | **2400** | **2400** |
| Remote unit | 1 | 662 | 662 | 662 | 662 |
| Tether (20 km) | 1 | 200 | 200 | 200 | 200 |
| Total w/o margin | | | 4950 | | **7836** |
| Total with 20 % margin | | | 5940 | | **9403** |

We ignore the following minor things which would reduce the mass of NEOMAT: We retain a 64 g patch antenna even though the HGA antenna replaces it, and we budget the mass of 20 km tether even though the tether length is only 12 km.

In case one wants to use CubeSat standard sizes, NEOMAT seems compatible with the 6-U format. The payload and therefore the mission size are also scalable. Considerations of science/cost tradeoffs are left beyond the scope of this study. For example, by increasing the size of the HGA, one can increse the amount of science data downloaded (or alternatively decrease the tracking cost per retrieved byte), with some increase in the cost and mass of the spacecraft. An example is provided by the M-ARGO design which can do 2.5 kbit/s (820 megabytes per month) from 1 au using 5 W transmission power to 35 m dish in X-band, using a 3.0 kg (with margin) telecommunication subsystem (M-ARGO CDF Study Report, 2018, Fig. 16–4 on page 239).

## 5.8 Summary and conclusions

A NEO version of MAT (NEOMAT) was presented. Even under the assumption of purely nodal flybys, a reasonable NEO flyby frequency of once per 6.5 months is possible, even if the E-sail tether is a stripped-down version relative to the original MAT. NEOMAT addresses all the criticisms raised in the CDF of MAT: autonomous navigation is not required and the design is not mass-constrained. As a further bonus,

enabled by novel the purely radial thrusting strategy, the cold-gas thruster of the remote unit is needed only during tether deployment so the remote unit does not need to stay functional after that.

# Chapter 6

# WP6: Retrieving NEO material to LEO

*We describe a 6-U, 8 kg cubesat spacecraft for collecting and retrieving 300 kg of near Earth object (NEO) asteroid regolith to low Earth orbit (LEO) using electric sail propulsion. The spacecraft uses field effect electric propulsion (FEEP) for controlling the E-sail tether spin, and it employs cold gas propulsion for orbiting, landing and lifting off the asteroid. The spacecraft flies to the NEO using the electric sail, abandons the tether and uses cold gas propulsion to settle to orbit the asteroid. From the orbit, a small onboard camera is used to map the asteroid at ∼2 cm surface resolution, and the image data are transmitted to the ground station using a patch antenna that covers the bottomside of the 6-U box. The ground team analyses the images for suitable regolith mining areas and marks dangerous rocks. The spacecraft deploys a snail-shaped regolith collector bag and lands. The regolith is collected into the snail using a simple wedge-shaped tool with one degree of freedom. The spacecraft crawls on the asteroid surface by internal impulsive kickers. When enough material is collected, the spacecraft lifts off by cold gas propulsion and deploys a second E-sail tether to to fly to Earth C3 orbit. It then deploys a drogue parachute aerobrake for gradually lowering the apogee to LEO. The customer must make a rendezvous at LEO altitude to get access to the 300 kilograms of NEO regolith that the spacecraft contains.*

## 6.1 Objectives

The objective of WP6 is to study the possibility of retrieving material from NEO to LEO using E-sail technology in combination with conventional propulsion and aerobraking.

## 6.2 Introduction and motivation

In the context of asteroid mining, why bring unqualified rocky material to LEO? The following arguments are relevant:

1. LEO has some potential near-term customers for asteroid-derived materials. For example, SpaceX is planning reusable upper stages that leave the payload in LEO and use propellant to brake, re-enter and land the stage. In such case, each kilogram of return propellant that the stage needs for landing reduces the payload by the same amount. If some of the return propellant can be tanked in LEO, the maximum payload mass is increased by the same amount. Most of the propellant mass is oxidiser, i.e. liquid oxygen (LOX), so it does not matter much if only LOX but not fuel is available in LEO.

2. LEO has the lowest access and operating cost of any orbit. If one brings material first to LEO, follow-up missions to process the material are affordable. In addition to the low launch cost of LEO, the LEO radiation environment is benign so that COTS components can often be used, as many university CubeSats have proven.

3. Real-time, low latency teleoperation is possible in LEO, because the physical distance to Earth is short. Compared to processing performed on an asteroid where the communication time delay is tens of minutes, this greatly reduces the amount of 'intelligence' that the software needs.

4. Rocky material consists of oxygen, silicon and metals. As pointed out above, oxygen is potentially near-term sellable in LEO. In the medium term, also metals and silicon are probably sellable, because one could make structures and solar panels from them, for example. Thus, if one decomposes rocky material to the elements, no material might have to be abandoned. The silicon and metals are solid so they can be put aside for later use, if the infrastructure to use them is not yet available in the initial stage.

5. By deciding to retrieve just rocky material and not, for example, water-bearing minerals, we increase the fraction of asteroids that are suitable. Then there is less need for expensive remote sensing campaigns, and the risk that the mining mission comes back empty is reduced.

While there have been many approaches to extracting oxygen from lunar or other regolith over the years, recently Lomax et al. (2019) showed that the FFC Cambridge process (Fig. 6.1) is able to extract up to 96 % of the oxygen during 50 hours or a smaller fraction in a shorter time. The process leaves a metal-rich residue. It needs calcium chloride molten electrolyte brought from Earth which can, however, be circulated.
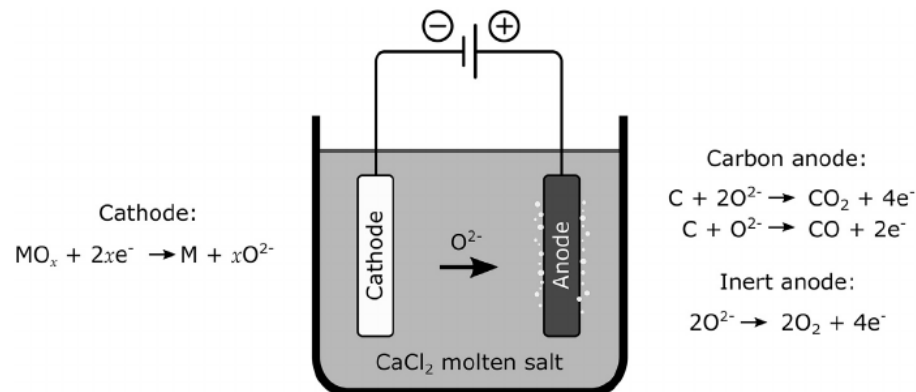


**Figure 6.1:** FFC Cambridge process for extracting $O_2$ from regolith (Lomax et al., 2019).

## 6.3 Getting NEO material

### 6.3.1 Collecting regolith

#### 6.3.1.1 Regolith ponds

Regolith means powder, sand, gravel or equivalent which exists on the surface of many asteroids (Fig. 6.2). It is thought that regolith is made by meteoroid impacts. Thermal expansion and contraction of rock might also break rock and thus contribute to the formation of regolith. In microgravity, the weight of the regolith is not sufficient to compress it appreciably, hence regolith particles may be quite loose. We think that regolith tends to accumulate in "ponds", i.e. it tends to fill low areas of the asteroid's gravity potential. Small asteroids are typically rather strongly non-spherical so that the local gravity field direction may deviate significantly from the geometric vertical in some places. This affects also the presence and shape of regolith ponds.
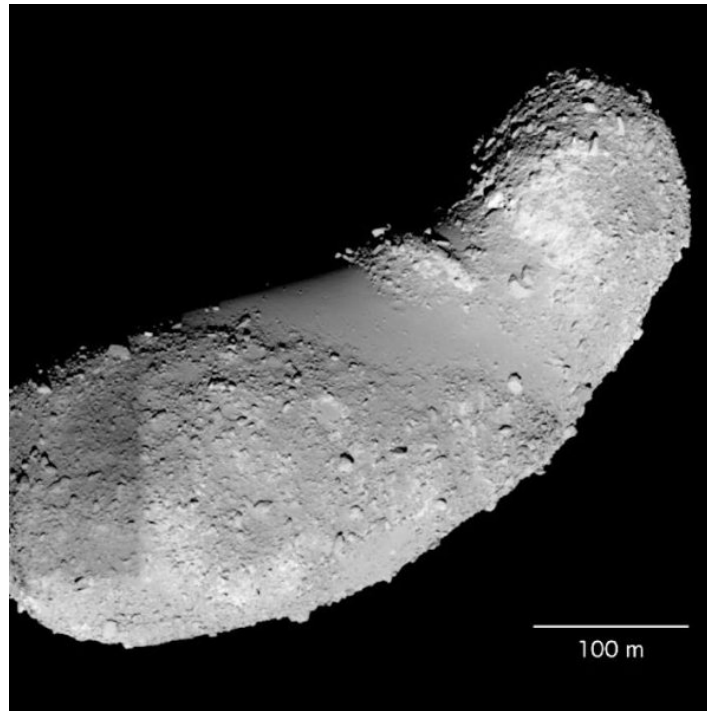


**Figure 6.2:** Asteroid Itokawa has some regolith-covered areas in the middle. Photo: JAXA.

The regolith grain size seems to display at least some anticorrelation with the asteroid size (Gundlach and Blum, 2012), and small asteroids might have rather large regolith grains. Specifically, the mean grain size on Itokawa (320 m diameter) was estimated to be as large as 2.1 cm, on 1998 WT24 (diameter 420 m) it was estimated to be 0.64 mm and on 1999 JU3 (diameter 920 m) again larger, 1.8 cm. Thus there seems to be significant variation from asteroid to asteroid in the subkilometre class. Because only three subkilometre bodies were included in the studied of Gundlach and Blum (2012), it is hard to draw more specific conclusions.

### 6.3.1.2    Wedge tool

We need way of digging regolith and throwing it upwards into a feed tube which leads to the regolith container (see 6.3.1.3 and Fig. 6.4). A tool such as spoon, shovel or spade could be used, for example. However, to simplify the design and to keep the number of moving parts to minimum, we prefer a tool with only one degree of freedom. For this purpose we propose to use a wedge-shaped tool (Fig. 6.3) which is pressed into the regolith and then lifted up at a calculated speed so that it gives the attached regolith particles an upward velocity $v_0$ that is enough to raise them to some altitude $h$.
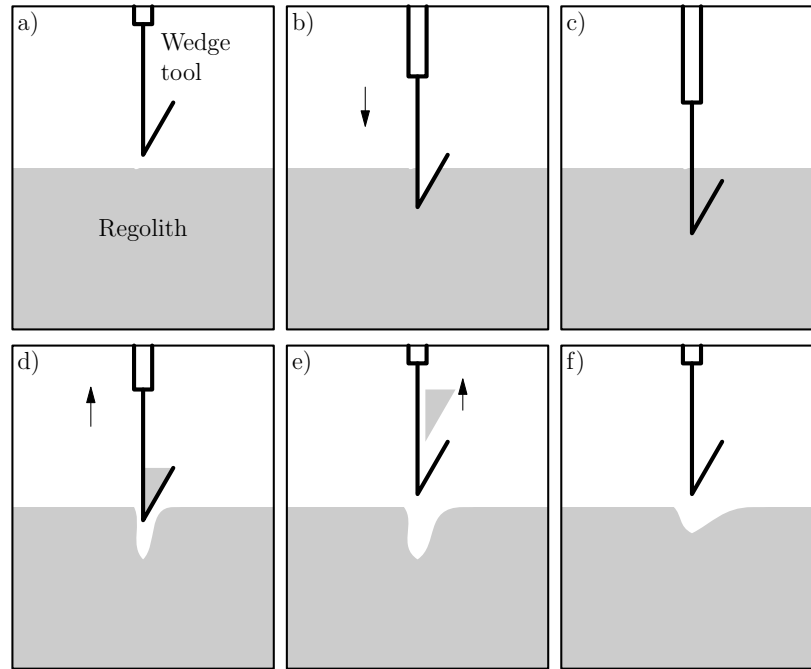


**Figure 6.3:** The wedge tool (a). The tool is pushed down, possibly by series of impulses to assist penetration (b). Regolith fills the tool (c). Tool is lifted up at speed $v_0$ (d). Movement of tool stops, the regolith chunk continues upward into the feed tube (e). Ready for next operation (f).

The altitude $h$ must be at least higher than the highest point of the feed tube; for example, we can put $h = 1\,\text{m}$. If the asteroid's gravity field is $a_g$, the kinetic energy must be equal to the gravitational potential energy at altitude $h$ so that

$$\frac{1}{2}v_0^2 = a_g h \tag{6.1}$$

from which

$$v_0 = \sqrt{2a_g h}\ . \tag{6.2}$$

If, for example, $a_g = 5 \cdot 10^{-5}\ \text{m/s}^2$ (corresponding to asteroid with 150 m diameter) and $h = 1\,\text{m}$, $v_0 = 1\,\text{cm/s}$. The maximum altitude grows as the square of the tool's upward speed $v_0$. One could potentially increase the speed of the regolith gathering process by increasing the speed $v_0$. On the other hand, if the speed is too high, regolith particles might bounce so many times in the container that some of them return back through the feed tube.

When lifting the wedge tool up, the upward speed is stopped abruptly so that the regolith particles detach from the tool optimally. When it is pushed down, one might apply a series of small impulses to assist penetration of the tool into the regolith.

The wedge tool may be a rigid body, or, to make the downward penetration easier, the inclined part could be made flexible so that it is adjacent to the main part in the down-pushing phase and is separated from it in the uplifting phase by the inertia of the regolith particles that get trapped in the way. However, while the flexible wedge may require less force to push down, it may also require a longer distance for pushing down, because in the uplifting phase it gathers the maximum number of regolith particles only after it has expanded inside the regolith. Dynamical simulations using a code such as Box2D (Box2D, 2019) or some three-dimensional equivalents of it might be used to evaluate the effectiveness of different tool designs.

We reserve 100 grams mass budget for the wedge tool subsystem. The wedge should be a few centimetres in size so that it can lift up regolith particles of up to 2 cm diameter (Table 6.4). The mass of the tool is a few grams, but the actuator to move it up and down weighs more so that we reserve 100 grams for the whole subsystem. This estimate is probably conservative.

### 6.3.1.3   Snail-shaped regolith container

We collect the regolith in a deployed container that we call a snail (Fig. 6.4) because of its shape. The snail trails the spacecraft as it kicks its away ahead along the surface. The snail is rigid in the microgravity environment, although it would be flexible in Earth's gravity field. The snail is made of plastic material such as 12.6 $\mu$m thin kapton or Nomex, metallised from the outside so that it will tolerate atomic oxygen (ATOX) later during the aerobraking phase. The metallisation also prevents formation of static electricity so that there is no risk that electrostatic forces could increase the friction between the membrane and the asteroid surface. The membrane structure has embedded thin metallic springs in strategic places to give the snail some rigidity which keeps it in shape in the microgravity environment. The volume of the snail is 400 litres so that it is sufficient to holding 300 kg of loosely packed regolith.

The regolith is injected into the snail by the wedge tool through a feed tube (Fig. 6.4). The wedge tool is pushed into the regolith and then lifted up at a calculated speed which is sufficient to throw the regolith particles into the feed tube so that many of them end up in the snail container.

The snail shown in Fig. 6.4 is double-ellipsoidal in shape, 64 cm wide, 29 cm high, 4 m long and with 400 litres internal volume. The amount of fabric required is about 5.2 m$^2$ and if made of 12.6 $\mu$m kapton (the thinnest ITAR-free polyimide sheet), the fabric weighs 0.1 kg. [1]

The feed tube has a one-time mechanism for closing it. When enough regolith has been collected, the tube is closed so that the regolith does not come out when the spacecraft is spun to deploy the E-sail or other subsequent mission phases. The closing mechanism need not be gas-tight since its purpose is only to prevent the collected regolith particles from escaping.

---

[1]Topologiclaly, the snail and the feed tube form a *Klein bottle*, a famous example of a non-orientable surface.
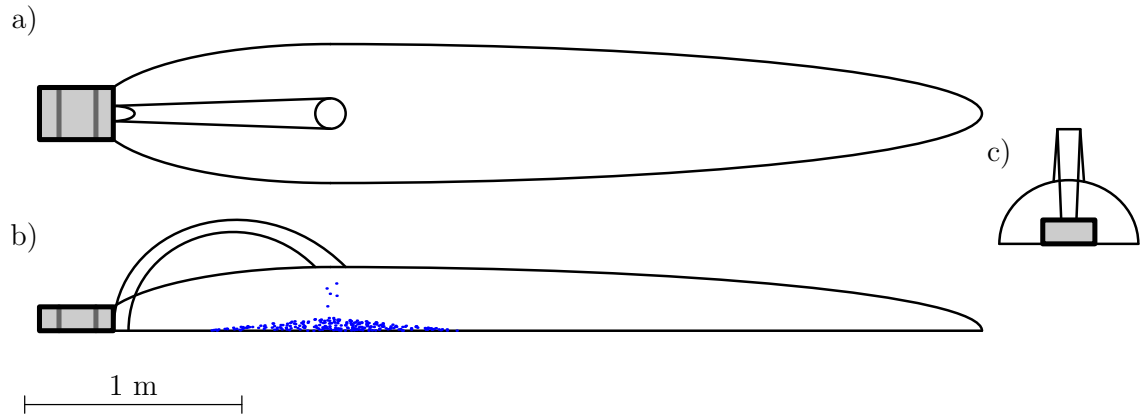
**Figure 6.4:** Top (a), side (b) and front (c) view of the deployed snail and its feed tube. The spacecraft box (grey) is divided into front, middle and back sections (see 6.5.10). The regolith piling up in the container as shown as blue.

### 6.3.1.4 NEOs with regolith

Table 6.1 lists the 15 most accessible asteroids. The data were downloaded from JPL's Small Body Database in 2014 so observations of the last five years are not included in it. The delta-v that was used to rank accessibility was calculated using bi-impulsive Hohmann transfer and fused inclination change starting from a circular 1 au orbit, without taking Earth's mass into account. This delta-v is a lower limit of the low-thrust delta-v which is relevant to the E-sail, and for orbits not too far from a circular 1 au orbit, the approximation is expected to be relatively good. Notice that we ignore Earth's mass on purpose when calculating the bi-impulsive delta-v. If Earth mass would be included, the bi-impulsive transfer would benefit from the Oberth effect with Earth, which would worsen the approximation because low thrust propulsion cannot make use of the Oberth effect. The asteroid diameter was estimated from the absolute magnitude *H* by assuming an albedo of 0.15, which is typical to S-type asteroids.

The delta-v's are low, for five asteroids it is less than 1 km/s. However, all asteroids in Table 6.1 are quite small, the largest being $\sim 39\,\text{m}$ in diameter. We do not know their character (S-type, C-type, M-type, etc.) and we do not know if they carry regolith on their surface or not. The smaller the body, the smaller is the escape velocity so that meteoroid impacts may more easily eject away the regolith particles that form. In any case, some asteroids like 25143 Itokawa ($\sim 330\,\text{m}$ diameter) is known positively to have regolith even though its escape velocity is only 17 cm/s.

In Table 6.2 we again show 15 most accessible asteroids, but now adding the criterion that the diameter must be at least 100 m. Now the delta-v's are larger, the smallest one is 2.7 km/s. Still we are not positively sure if any of these asteroids contain regolith because none of them have been visited. It is quite likely that at least some of them do, however, since three of them (Apophis, 2001 SW169 and 1989 UQ) are larger than Itokawa, which is known to have regolith.

Finally, Table 6.3 shows ten most accessible asteroids that are at least 300 m in estimated diameter.

It should be noted that physical parameters (and sometimes even orbital parameters) describing small bodies can be imprecisely known. For example, for Itokawa's diameter we give the value 500 m in Table 6.3, but a more accurate estimate of the mean diameter

**Table 6.1:** 15 most accessible asteroids in terms of impulsive Hohmann transfer delta-v from Earth C3.

| Asteroid | Delta-v | Perih./au | Aphelion/au | Inclin./° | Diameter/m |
|----------|---------|-----------|-------------|-----------|------------|
| 2009 BD | 670 | 0.967 | 1.050 | 0.385 | 8 |
| 2011 UD21 | 734 | 0.949 | 1.008 | 1.062 | 7 |
| 2006 RH120 | 932 | 0.979 | 1.018 | 1.526 | 4 |
| 2007 UN12 | 949 | 0.990 | 1.118 | 0.235 | 6 |
| 2000 SG344 | 998 | 0.912 | 1.043 | 0.111 | 39 |
| 2008 UA202 | 1036 | 0.962 | 1.104 | 0.264 | 5 |
| 2010 VQ98 | 1107 | 0.995 | 1.051 | 1.476 | 8 |
| 2010 UE51 | 1123 | 0.992 | 1.118 | 0.624 | 8 |
| 2012 TF79 | 1129 | 1.010 | 1.090 | 1.005 | 11 |
| 2008 EA9 | 1253 | 0.975 | 1.144 | 0.425 | 10 |
| 1991 VG | 1279 | 0.976 | 1.077 | 1.445 | 7 |
| 2013 BS45 | 1335 | 0.910 | 1.077 | 0.773 | 23 |
| 2013 RZ53 | 1387 | 0.981 | 1.045 | 2.095 | 2 |
| 2014 QN266 | 1419 | 0.955 | 1.150 | 0.488 | 19 |
| 2010 UJ | 1441 | 0.855 | 1.034 | 0.370 | 20 |

(the asteroid is not spherical) is 330 m, based on Hayabusa *in situ* observation. This is because Itokawa's albedo is higher than the value 0.15 that we used when preparing the tables.

In the rest of this WP, we assume that the E-sail delta-v value is ∼ 3700 m/s. We adopt this value because it is sufficient for reaching several asteroids more than 100 m in diameter, including Apophis which is in the 300 m class, and because it is the same as the maximum low-thrust delta-v value that was adopted in the recent M-ARGO CDF study (M-ARGO CDF Study Report, 2018).

A lunar flyby capture manoeuvre could be used to take ∼ 1000 − 1500 m/s off the delta-v. In this case, the set of accessible asteroids increases dramatically and includes also e.g. Itokawa which is explicitly known, by Hayabusa's *in situ* inspection, to have regolith. If the sub-100 m asteroids would turn out to contain regolith, one could reduce the E-sail delta-v requirement significantly.

If the sub-100 m asteroids also have regolith, one could mine them with a delta-v of less than 1 km/s. However, at the present time this is not known, and in the longer run, the amount of regolith on very small bodies is limited, which limits the commercial value. As in all mining, asteroid resources are discovered by exploration and they can be classified (in increasing level of geological knowledge and confidence) in inferred, indicated and measured resources(wikipedia/Mineral resource classification, 2019). For example, the presence of regolith on many or most NEOs can be considered an inferred resource, while the regolith on Itokawa is a measured resource.

A delta-v of 3700 m/s corresponds to 3.7 year duration of the return trip if we use an E-sail with 1 km/s per year characteristic acceleration. If the tether length is 20 km and the nominal voltage 20 kV, the thrust per length is 500 nN/m and the thrust is 10 mN. The characteristic acceleration of 1 km/s/year then corresponds to 315 kg total mass. In the rest of this WP, we adopt the requirement that the maximum gathered regolith mass is 300 kg. The spacecraft itself weighs only ∼ 8 kg, so it can be ignored

**Table 6.2:** 15 most accessible asteroids whose estimated diameter is at least 100 m.

| Asteroid | Delta-v | Perih./au | Aphelion/au | Inclin./° | Diameter/m |
|---|---|---|---|---|---|
| 2001 CQ36 | 2744 | 0.772 | 1.105 | 1.261 | 110 |
| 225312 1996 XB27 | 2997 | 1.120 | 1.258 | 2.464 | 160 |
| 2013 PA7 | 3208 | 1.053 | 1.255 | 3.474 | 100 |
| 2011 CG2 | 3340 | 0.991 | 1.364 | 2.757 | 170 |
| 99942 Apophis | 3368 | 0.746 | 1.099 | 3.331 | 390 |
| 350751 2002 AW | 3703 | 0.796 | 1.345 | 0.571 | 240 |
| 2006 CT | 3745 | 0.844 | 1.350 | 2.741 | 120 |
| 350523 2000 EA14 | 3757 | 0.891 | 1.343 | 3.555 | 210 |
| 2011 UC292 | 3856 | 0.799 | 1.357 | 1.685 | 100 |
| 163000 2001 SW169 | 3864 | 1.184 | 1.313 | 3.554 | 540 |
| 251732 1998 HG49 | 3882 | 1.065 | 1.336 | 4.195 | 150 |
| 2005 YA37 | 3965 | 0.988 | 1.572 | 2.240 | 110 |
| 2014 NZ64 | 3988 | 0.845 | 1.307 | 4.136 | 110 |
| 2004 EO20 | 4019 | 1.152 | 1.287 | 4.542 | 130 |
| 65679 1989 UQ | 4039 | 0.673 | 1.157 | 1.299 | 450 |

**Table 6.3:** Ten most accessible asteroids whose estimated diameter is at least 300 m.

| Asteroid | Delta-v | Perih.au | Aphelion/au | Inclin./° | Diameter/m |
|---|---|---|---|---|---|
| 99942 Apophis | 3368 | 0.746 | 1.099 | 3.331 | 390 |
| 163000 2001 SW169 | 3864 | 1.184 | 1.313 | 3.554 | 540 |
| 65679 1989 UQ | 4039 | 0.673 | 1.157 | 1.300 | 450 |
| 341843 2008 EV5 | 4097 | 0.878 | 1.038 | 7.437 | 340 |
| 98943 2001 CC21 | 4200 | 0.806 | 1.259 | 4.809 | 680 |
| 138911 2001 AE2 | 4210 | 1.239 | 1.460 | 1.661 | 520 |
| 25143 Itokawa | 4248 | 0.953 | 1.695 | 1.621 | 500 |
| 89136 2001 US16 | 4293 | 1.013 | 1.698 | 1.905 | 310 |
| 10302 1989 ML | 4442 | 1.099 | 1.446 | 4.378 | 470 |
| 401954 2002 RW25 | 4544 | 0.589 | 1.062 | 1.327 | 600 |

in this context. For the asteroid, we assume a 150 m diameter, which corresponds to 10 cm/s escape velocity and a surface gravity field of $5 \cdot 10^{-5}$ m/s$^2$. These assumptions come into play when estimating telemetry requirements and cold gas delta-vs. For convenience, the requirements are summarised in Table 6.4.

## 6.3.2   Rejected strategies for getting NEO material

### 6.3.2.1   Asteroid minimoon

The tracking problem is solved if the rock orbits a larger, trackable asteroid as a minimoon. Currently such small moons are not known, however, so a remote sensing fleet mission such as MAT should be made in order to discover at least one of them. With luck, one might discover a minimoon by observing a NEO which passes near Earth and that happens to have a minimoon. The NEO should be large enough to be trackable so that a long observation arc can be obtained which allows a precise enough orbit to

**Table 6.4:** Adopted mission requirements and main E-sail parameters.

| | | |
|---|---|---|
| Unidirectional E-sail delta-v | $\sim 3700$ m/s | |
| Typical asteroid diameter | 150 m | or less |
| Typical surface gravity field | 0.05 mm/s$^2$ | |
| Typical escape velocity | 10 cm/s | |
| Regolith grain size | 2 cm | or less |
| Maximum collected regolith mass | 300 kg | |
| Tether length | 20 km | (return trip) |
| Tether voltage | 20 kV | |
| E-sail thrust at 1 au | 10 mN | (return trip) |
| Characteristic acceleration | 1 km/s/year | (return trip) |
| Return trip duration | $\sim 3.7$ years | |

be determined so that the asteroid can be found again from the sky when it becomes visible the next time.

An asteroid minimoon probably cannot be grabbed directly by an E-sail, because it typically orbits closer to the parent body than the tether length so that safe approach of an E-sail spacecraft at such distance is not feasible. Another challenge in the minimoon approach is that the mass of the minimoon probably remains rather poorly known until it is grabbed.

### 6.3.2.2 Standalone asteroid

A straightforward way is to find a small standalone asteroid and move it to LEO in its entirety. The benefit is that there is no need to break or manipulate the asteroid, just attach to it. The drawback is that asteroids that are large enough to be observable from ground so that the orbit can be known are probably too heavy to be carried by a reasonably-sized E-sail. Even though occasionally a small rock flies by Earth so that it can be briefly observed by ground-based telescopes, the observation arc is too short to determine its trajectory with sufficient accuracy to predict the orbit for spacecraft rendezvous.

### 6.3.2.3 Detaching a surface rock

One could also create a freestanding rock by actively detaching it from the surface of an asteroid. The Hayabusa-2 mission showed that at least asteroid Ryugu's surface has lots of boulders (Fig. 6.5), some of which might be separable from the body by moving a small lander between a protruding rock and the asteroid and applying mechanical force e.g. by pyrotechnics or a spring force. The programmatic challenge with such approach is that it is hard to guarantee success beforehand. Also, moving on a very rocky terrain such as this is usually risky for a lander. While the risk might be dealt with by having a redundant number of small landers, meeting the mass ratio goal of 20 would seem challenging.

A benefit of the surface rock approach is that if the entire mass of the asteroid becomes usable and not only the surface regolith, then large-scale commercial activity could be based on the sub-100 m scale NEOs which are much more accessible in terms of

delta-v than bigger NEOs (see 6.3.1.4 above). Thus the method might become relevant in the future.



**Figure 6.5:** Asteroid Ryugu's rocky surface as imaged by MASCOT lander of Hayabusa-2. There may be detachable rocks, but such rough terrain is risky for landing. Photo: DLR.

# 6.4   Mission requirements

## 6.4.1   Mass ratio of at least 20

The task is to fetch material from NEO to LEO with high mass ratio $M_r$, i.e. the ratio of the retrieved regolith mass versus the initial mass of the spacecraft. This ratio must be much larger than one in order to make asteroid mining potentially economically feasible. In fact, it should be larger than $\sim 20$, namely:

1. When the miner is lifted from LEO to C3 orbit by chemical propulsion, we lose factor $\sim 3$ in mass.

2. Because asteroid rocky material contains only $\sim 40\,\%$ of oxygen, one has to bring back $\sim 2.5$ times more material than the mass of the final product, i.e. LOX.

3. To pay for the miner, the LEO LOX factory and to produce economical profit, we estimate that we need an extra factor of $\sim 2-3$.

When one multiplies the three factors together, one gets a factor of $\sim 20$. To be conservative and to stay in the realm of near-term scenarios, we do not include the potential economic value of the solid residue rich in reduced metals and elemental silicon which is a natural byproduct of the oxygen separation process.

## 6.4.2   Delta-v budget

The mission phases and their rough delta-v's are listed in Table 6.5.

   The unloaded mass is $\sim 8$ kg and the (maximum expected) loaded mass is 300 kg. The loaded cold gas delta-v budget of 1.2 m/s corresponds to 0.52 kg of cold gas,

**Table 6.5:** Mission phases and their typical delta-v's.

| Mission phase | Loaded | Typical delta-v | Propulsion |
|---|---|---|---|
| **1** Launch to Earth C3 | No | $\sim 12500$ m/s | Chemical launcher |
| **2** Sail to asteroid parking orbit | No | $\sim 3700$ m/s | E-sail 1 |
| **3** To asteroid orbit | No | 1 m/s | Cold gas |
| **4** Corrections during orbiting | No | 1 m/s | Cold gas |
| **5** Landing | No | 0.1 m/s | Cold gas |
| **6** Liftoff and exit from asteroid | Yes | 0.2 m/s | Cold gas |
| **7** Sail to Earth C3 | Yes | $\sim 3700$ m/s | E-sail 2 |
| **8** From C3 to LEO | Yes | 3200 m/s | Aerobraking |
| **9** Orbit corrections during aerobraking | Yes | $\sim 1$ m/s | Cold gas |

assuming specific impulse of 70 s. The unloaded delta-v of 2.1 m/s adds only 25 grams to the amount.

One point of consideration is that the aerobraking phase takes in all cases a rather long time and the orbit goes through the radiation belts. Hence the accumulated total radiation dose is rather high during this phase, so the cold gas AOCS used for orbit corrections during the aerobraking as well as the jettisoning mechanism of the aerobrake must be made radiation tolerant.

### 6.4.3 Link budget

From $\sim 1$ au distance, we need to return a surface map of the asteroid, in order to learn where the regolith-covered areas are and where are large rocks that must be avoided. Based on these data, the ground team decides the landing spot and the approximate path taken on the surface to collect the regolith. Rocks that are of the same size or larger than the spacecraft ($\sim 10$ cm) pose the risk that the spacecraft might get stuck if it encounters them during crawling[2]. To identify such rocks, we need to have $\sim 2$ cm surface resolution in the images. At diffraction limit, this resolution can be achieved from 400 m viewing distance by a 1 cm diameter aperture at 500 nm wavelength. The median NEO diameter is 150 m. For an asteroid of such size, an orbital altitude of 400 m should be feasible.

If the asteroid diameter is 150 m and if it is spherical, the surface area is $7 \cdot 10^4$ m$^2$. Because most asteroids are elongated, let us multiply the area estimate by two, so that the area is $1.4 \cdot 10^5$ m$^2$. Mapping this area at 2 cm resolution corresponds to 350 million pixels to be transmitted to ground. Using 8-bit greyscale imaging and using JPG compression to compress the images by factor of 8, the number of bits is the same as the number of pixels, i.e. 0.35 Gbit. This can be considered an underestimate, because images overlap and taking images in different light conditions is also preferable. However, also the 2 cm resolution requirement that we used above can be overkill for recognising dangerous rocks. All in all, we think that by using 2 cm resolution and assuming that each point is imaged only once gives a rough idea of the realistic link budget.

---

[2]The probability of getting stuck is probably low since we can apply left/right kicking to get around the obstacle, but also low risks at worth avoiding when doing so is not expensive in terms of costs and mass.

This link budget is by factor 4.3 smaller than the 1.5 Gbit link budget of M-ARGO (M-ARGO CDF Study Report, 2018), so if all else is equal, we can have 4 times smaller high-gain antenna area than M-ARGO. M-ARGO's high-gain antenna has $3 \times 6$-U (54 cm $\times$ 34 cm) area, so we can make the area three times smaller so that it fits in a body-mounted way on one side of the 6-U box without need for antenna deployment mechanism. Also, since the link budget is 4.3 times smaller while the antenna area is only 3 times smaller, we gain an extra margin factor of 1.43. Unlike M-ARGO which uses a reflectarray antenna, we prefer a patch antenna because then we avoid the protruding antenna feeder. We want to avoid protrusions because they would increase the risk of getting stuck during surface operations.

Consequently, for the communication subsystem mass, we allocate 1.0 kg which is one third of the communication subsystem allocation in M-ARGO. Our high-gain antenna area is one third of M-ARGO and our link budget requirement is 4.3 times less.

### 6.4.4   Power budget

The power budget is mainly driven by the E-sail. Although also data transmission from asteroid orbit and crawling on the surface consume power, these subsystems are turned off when the E-sail operates. The E-sail consumes 7 W of high-voltage (HV) power. With assumed 70 % efficiency of the HV source, this means 10 W bus power consumption during E-sail flight, plus the power consumed by E-sail controller and navigation system.

The dimensions of the 6-U box are $36 \times 24 \times 11$ cm. By covering the roof by body-mounted panels we obtain 25 W power if the fill factor of solar cells is 85 % and the end of life (EOL) efficiency of the panels is 25 %. During E-sail flight the tether spinplane might be inclined by up to 45° with respect to the sunlight, which reduces the power by factor $1/\sqrt{2}$, thus leaving 17.6 W. The E-sail takes 10 W of it so there is 7.6 W left for other tasks like housekeeping, navigation and controller. Hence we can manage without deployable panels, which is a benefit (and virtually a requirement) because deployables would create a potential risk of getting stuck when operating on the surface of the asteroid.

### 6.4.5   Aerobraking

When returning from the asteroid, we put the spacecraft in a high elliptic orbit with suitably low perigee using E-sail propulsion, then cut the E-sail tether at such moment of rotation that the tether and the remote unit receive such delta-v vector that they enter an orbit leading into Earth's atmosphere. Then we deploy an aerobrake so that at each perigee pass, the apogee of the orbit is lowered. Small orbit corrections may be needed at apogees to keep the perigee altitude in a desired range. At some point when the orbit is not yet completely circular but has some eccentricity left, we jettison the aerobrake to greatly slow down the descent rate of the apogee, so that a customer spacecraft can more easily rendezvous with it. The customer spacecraft must perform an apogee burn to raise the perigee so that the orbit becomes stable.

We considered options to raise the perigee by using our own propulsion, but decided not to do so because the necessary propulsion system would be rather heavy compared

with the rest of the spacecraft. It is more efficient in terms of mass budgeting that the propulsion system needed to raise the perigee does not make a full round trip to the asteroid surface and back, but is simply launched to LEO with the rest of the customer's material utilisation mission.

### 6.4.6   Semi-rigid drogue parachute

Our baseline choice for the drag device is a semi-rigid drogue parachute. By this we mean a deployed element that is shaped like a typical drogue parachute, but which also contains weak stiffening springs inside, ensuring that the shape does not collapse even in microgravity vacuum conditions, i.e. when the spacecraft is flying outside the atmosphere and is executing slow attitude control and orbit correction thrusting manoeuvres. During perigee passes, the aerodynamic force ensures correct shape and enforces a stable attitude, as for any drogue parachute.

### 6.4.7   Rejected concepts

#### 6.4.7.1   Spinning drag tether

A drag tether that spins in cartwheel mode (i.e., the spinplane of the tether is the same as the orbital plane of the spacecraft) experiences drag during the perigee passage, which slows down the spin. The drag is generated because when the tether moves against the ram flow in its rotation, it experiences slightly higher dynamic pressure than when it's moving tailwind. However, when the tether spins in the vertical plane, the tip of the tether encounters slightly different atmospheric densities, because the atmospheric density depends on altitude. This effect can either decelerate or accelerate the spin depending on the sense of the rotation. We derived an analytic model for the situation (4 pages of algebra, not included in this report) which showed that when the rotation rate $\omega$ is approximately equal to

$$\omega \approx \frac{-U_x}{3H}, \tag{6.3}$$

then the two effects cancel each other and the spinrate remains unchanged by the perigee passages that are lowering the apogee. Here $U_x \sim 8.5 - 11\,\mathrm{km/s}$ is the ramflow speed (i.e., the orbital speed at perigee) and $H \sim 7\,\mathrm{km}$ is the atmospheric scale height at the altitude ($\sim 110\,\mathrm{km}$) where the perigee pass occurs. The minus sign reminds us that one must select the sense of the rotation in the right way. Thus, numerically the spin period of the tether should be $\sim 13\,\mathrm{s}$ for spinrate balancing to occur.

When the apogee is lowered, the perigee speed $U_x$ decreases. Also, towards the end we want to start raising the perigee so that we do not need to raise it at one go. At higher altitude the drag is lower and $H$ is larger. Both the lowering of $U_x$ and the increase of $H$ contribute to lowering of $\omega$. This is unproblematic, because when the perigee altitude increases, the drag force decreases so that a lower spinrate $\omega$ suffices to keep the tether straight.

We recommend using a drag tether with cylindrically symmetric cross section, because then the tether produces pure drag and no lift. It is conceivable that aerodynamic lift might lead into dynamical fluttering instabilities. The material must also tolerate

heat, and as usual, the mass per drag area should be minimised. Our baseline solution is a $\sim 10$ cm diameter tubular tether made of $\sim 10\,\mu$m titanium foil, which is forced into tubular shape during deployment by a pressurant gas, which also assist in the deployment. The dynamical pressure that the tether encounters is only of order $\sim 7$ Pa. The force is low enough that the metal foil tube should be able to withstand it without internal pressure, so the pressurisation is needed only in the initial stage to force the folded foil into a smooth cylindrical shape. Other solutions for the drag tether are probably also feasible. For example, one could have a hairy tether which looks like a bottlebrush.

### 6.4.7.2    Other rejected ideas

1. The rock itself as aerobrake, without any attached apparatus. Rendesvouz it by another spacecraft near LEO to raise the perigee to stable altitude. Rejected for the following reasons:

    (a) Because the rock's shape is irregular, its trajectory cannot be predicted accurately, which makes rendezvous a challenge.

    (b) In the early phases when the apogee is still high, lunar perturbations may affect the orbit near the apogee, which can change the perigee altitude unpredictably. The aerobraking can then become too quick and too violent, or it can become too slow. Lunar perturbations can affect the perigee already at geostationary transfer orbit (Lamy et al., 2011), so at higher apogee such effects are even more severe.

2. The rock itself as aerobrake, with an attached AOCS module which controls its orbit. During perigee passages the AOCS module keeps the rock oriented so that the module is in its wake, so that the module is not exposed to the heat flux. Rejected because keeping the rock properly oriented might need a relatively high delta-v, because the rock's shape is irregular so that the aerodynamic forces may tend to rotate it.

3. The rock itself as aerobrake, with a "shepherd" spacecraft flying in its vicinity, which uses an ion beam to correct the rock's trajectory near apogee and which flies in the rock's wake during perigee passes to protect itself against the heat flux. Rejected because flying in the wake is dynamically unstable. The rock is decelerated by the drag, so the shepherd spacecraft tends to fall against it back. A physical contact between them would be risky, because the rock probably rotates so the contact would throw the shepherd spacecraft into the airflow. If the shepherd spacecraft prevents this by using propulsion, it needs the same amount of delta-v (3.2 km/s) than what the rock experienced from the atmospheric drag. This delta-v comes in addition to the delta-v required for managing the rock's orbit near apogee and raising the rock's perigee at the end.

4. The same, but the shepherd spacecraft altering its trajectory at every orbit so that it flies through the atmosphere with a higher altitude than the rock, which is selected so that both receive the same braking delta-v from the atmosphere (the difference in altitude compensating for their different ballistic coefficients). Rejected because while possible, changing the orbit requires significant delta-v,

and more importantly, the distance between the shepherd and the rock is not small which creates the challenge of navigation and finding the rock.

5. Equip the shepherd spacecraft with thermal protection so that it can fly through the atmosphere at the same altitude than the rock, and design it so that its ballistic coefficient equals the ballistic coefficient of the rock. Rejected because the ballistic coefficient of the rock is not known beforehand, so the shepherd's ballistic coefficient should be made dynamically adjustable, which would add further complexity.

6. The rock itself, but equipped by an aerodynamic tail which enforces the right yaw and pitch, and which has movable control surfaces that can be used to control and to prevent roll. This would be possible in principle, but we rejected the idea because the tail have to tolerate high temperature and making the control surfaces movable would add complexity and weight.

Additionally, in all concepts where the rock itself is used as the aerobrake, the brake area is small so that the perigee altitude and heat flux become high. The high heat flux might break up the rock.

## 6.5 Mission design

### 6.5.1 Mission phases

We divided the mission in 12 phases:

1. Deploy E-sail 1 (tether 1, remote unit 1).

2. Make rendezvous to the asteroid's vicinity, jettison E-sail 1 tether.

3. Go to orbit the asteroid, map it from orbit, sending data to ground. Imaging and telemetry sessions are interleaved. The ground team selects the landing site and makes the mining plan.

4. Deploy the snail regolith collector and land.

5. Collect regolith into the snail by crawling forward on the surface using the internal kickers and lift the regolith using the wedge tool.

6. Close the regolith bag, lift off and go to escape trajectory from the asteroid using cold gas propulsion.

7. Deploy E-sail 2 (tether 2, remote unit 2).

8. Sail to Earth C3.

9. Jettison E-sail 2 so that it burns in Earth's atmosphere, and deploy the aerobrake.

10. Perform aerobraking at perigee passes, controlling the orbit at apogees using cold gas propulsion.

11. Jettison the aerobrake, it deorbits quickly because the perigee altitude and the aerobrake's ballistic coefficient are low.

12. The drag-induced apogee reduction continues at a slower rate. Customer makes rendezvous with the unit to gain access to the asteroid regolith material.

Jettisoning E-sail1 near the asteroid leaves it in a heliocentric orbit. A multi-wire tether is such that the breaking probability grows with a high power of time. For example, if the tether is made of four wires, its braking probability increases as $\sim t^4$. This means that the tether does not create long-term space debris in the solar system. Also, the tether would only be potentially dangerous to other E-sails, not to traditional spacecraft. Furthermore, to minimise the cross section of the abandoned tether, one might curl up the wires in the manufacturing phase. Then the tether and its broken pieces start to curl up from the free ends and form a "nest" of wires, which has much lower cross section for collision with active E-sail tethers than the original straight tether piece.

In phase 5 (collecting the regolith into the snail), the spacecraft snail preferably lands in a valley from which it climbs upwards. This is to avoid crawling steep downhill, which might cause some of the already swallowed regolith to be "vomited". Of course, the concept of a valley must be understood relative to the local gravity potential. Possibly, depending on the particulars of the asteroid, the snail might lift off and re-land even multiple times before the wanted amount of regolith mass has been collected.

### 6.5.2 Remote unit delta-v

During the return trip, the remote unit needs four TILE 50 units. The dimensions of a single TILE 50 are $3 \times 7 \times 1.2$ cm, the dry mass is 50 grams, the specific impulse 1250 s, the total impulse 20–60 Ns (1.6–4.9 grams of propellant), the thrust 50 $\mu$N and the power consumption 1.5 W. Thus, four TILE 50 units stacked together make a $3 \times 7 \times 4.8$ cm box. We assume that the remote unit's total mass is $m_{\mathrm{RU}}$=0.35 kg, of which 0.2 kg is the mass of four TILE 50 units.

A $R$=20 km E-sail tether weighs $m_t$=0.22 kg if made of four 35 $\mu$m aluminium wires. If $F_{\mathrm{cf}}$ is the wanted centrifugal tension at the tether root, the angular speed of the rotating tether is

$$\omega = \sqrt{\frac{F_{\mathrm{cf}}}{\left(\frac{1}{2}m_t + m_{\mathrm{RU}}\right) R}} \tag{6.4}$$

The moment of inertia of the tether and the remote unit is

$$I = \left(\frac{1}{3}m_t + m_{\mathrm{RU}}\right) R^2 \tag{6.5}$$

The angular momentum is

$$L = I\omega = \left(\frac{1}{3}m_t + m_{\mathrm{RU}}\right) R^{3/2} \sqrt{\frac{F_{\mathrm{cf}}}{\frac{1}{2}m_t + m_{\mathrm{RU}}}} \ . \tag{6.6}$$

When orbiting the Sun at distance $r$ with the E-sail inclined at angle $\alpha$ with respect to the radial direction, the spinrate $\omega(t)$ changes secularly according to (Toivanen and Janhunen, 2013, equation 32)

$$\omega(t) = \omega_0 e^{\Omega t \tan \alpha} \tag{6.7}$$

where $\Omega = \sqrt{GM_{\mathrm{Sun}}/r^3}$ is the angular speed of the spacecraft's orbit. This effect is due to the orbital Coriolis force. Equivalently, it can be understood as arising from the need to track the Sun with the tether's spin axis. Equation (6.7) implies that the rotating tether experiences an angular acceleration $d\omega/dt$ given by

$$\frac{d\omega}{dt} = \Omega \tan\alpha \; \omega. \tag{6.8}$$

Notice that the angular acceleration is proportional to $\tan\alpha$. If $\alpha = 0$, i.e. if the tether's spin plane is perpendicular to the solar direction so that the produced E-sail force is radial, the angular acceleration is zero. Although some missions can be accomplished with $\alpha = 0$ (see WP5), in the present case we assume that $\alpha$ is nonzero and typically of order $\sim 30° - 45°$.

Denote again the mass of the tether by $m_t$, the mass of the remote unit by $m_{\mathrm{RU}}$, the tether length by $R$ and the tension at the tether root by $F_{\mathrm{cf}}$. Then the spinrate $\omega$ is given by (6.4). To cancel the angular acceleration (6.8), one needs to apply torque $\tau = I\, d\omega/dt$. Hence we obtain

$$\begin{aligned} \tau &= \left(\frac{1}{3}m_t + m_{\mathrm{RU}}\right) R^2 \Omega \tan\alpha \; \omega \\ &= \left(\frac{1}{3}m_t + m_{\mathrm{RU}}\right) R^2 \Omega \tan\alpha \sqrt{\frac{F_{\mathrm{cf}}}{\left(\frac{1}{2}m_t + m_{\mathrm{RU}}\right) R}}. \end{aligned} \tag{6.9}$$

The delta-v requirement of the remote unit for $N_{\mathrm{orb}}$ revolutions around the Sun is

$$\begin{aligned} \Delta v_{\mathrm{RU}} &= N_{\mathrm{orb}} \frac{p_{\mathrm{RU}}}{m_{\mathrm{RU}}} = N_{\mathrm{orb}} \frac{\tau}{m_{\mathrm{RU}} R} \cdot \frac{2\pi}{\Omega} \\ &= 2\pi N_{\mathrm{orb}} \left(1 + \frac{m_t}{3m_{\mathrm{RU}}}\right) \tan\alpha \sqrt{\frac{F_{\mathrm{cf}} R}{\frac{1}{2}m_t + m_{\mathrm{RU}}}}. \end{aligned} \tag{6.10}$$

The tether's centrifugal tension $F_{\mathrm{cf}}$ is proportional to the E-sail thrust:

$$F_{\mathrm{cf}} = k \frac{dF}{ds} R \tag{6.11}$$

where $dF/ds \approx 500$ nN/m is the E-sail thrust per tether length and $k$ is a numerical constant. For a single tether E-sail, our dynamical simulations have shown that $k \approx 3$ is sufficient for stability, while for multi-tether E-sails, $k \approx 5$ must be used. Substituting (6.11) in (6.10) we obtain

$$\Delta v_{\mathrm{RU}} = 2\pi N_{\mathrm{orb}} \sqrt{k} \tan\alpha \left(1 + \frac{m_t}{3m_{\mathrm{RU}}}\right) \frac{R}{\sqrt{m_{\mathrm{RU}}}} \sqrt{\frac{dF/ds}{1 + \frac{m_t}{2m_{\mathrm{RU}}}}} . \tag{6.12}$$

For $N_{\mathrm{orb}}$=4 (i.e., 4 year duration of the return trip), $k$=3, $\alpha$=35°, $m_{\mathrm{RU}}$=0.25 kg, $m_t$=0.22 kg, $R$=20 km and $dF/ds$=500 nN/m we obtain $\Delta v_{\mathrm{RU}} = 770$ m/s, impulse $p_{\mathrm{RU}}$=$m_{\mathrm{RU}}\Delta v_{\mathrm{RU}} = 270$ Ns and average thrust 2.1 $\mu$N. The thrust is unproblematic, but the impulse exceeds slightly the maximum (240 s) of four TILE 50 units. We make an assumption that TILE 50 could be modified by loading slightly more propellant to it to increase its impulse by 13 %.

These numbers hold for the return trip. For the forward trip the delta-v requirement of the remote unit is much smaller because the carried load is lower by a factor of $\sim 37$ (the ratio of 300 kg load during the return trip to the $\sim 8$ kg mass of the 6-U spacecraft during the forward trip). For the forward trip, two TILE 50 units suffice. Even one unit would suffice from the impulse point of view, but we need at least two to be able to control the remote unit's one-dimensional attitude during thrusting.

Numerically, the required average thrust of 2.1 $\mu$N is only fraction $2.1 \cdot 10^{-4}$ (0.018 %) of the 10 mN nominal E-sail thrust produced simultaneously by the 20 km long tether at 1 au solar distance. We can express the impulse ratio in analytic form:

$$\frac{p_{\mathrm{RU}}}{p_{\mathrm{Esail}}} = \frac{m_{\mathrm{RU}} \Delta v_{\mathrm{RU}}}{N_{\mathrm{orb}} \frac{2\pi}{\Omega} R \left( dF/ds \right)} = \sqrt{k} \tan \alpha \frac{1 + \dfrac{m_t}{3 m_{\mathrm{RU}}}}{\sqrt{1 + \dfrac{m_t}{2 m_{\mathrm{RU}}}}} \frac{\Omega \sqrt{m_{\mathrm{RU}}}}{\sqrt{dF/ds}} \ . \tag{6.13}$$

Here $\Omega = \sqrt{GM_{\mathrm{Sun}}/r^3}$ and the E-sail thrust per unit length is inversely proportional to the solar distance $r$:

$$\frac{dF}{ds} = \frac{1\,\mathrm{au}}{r} \cdot \left( \frac{dF}{ds} \right)_{1\,\mathrm{au}} , \tag{6.14}$$

hence

$$\frac{p_{\mathrm{RU}}}{p_{\mathrm{Esail}}} = \sqrt{k} \tan \alpha \frac{1 + \dfrac{m_t}{3 m_{\mathrm{RU}}}}{\sqrt{1 + \dfrac{m_t}{2 m_{\mathrm{RU}}}}} \frac{\sqrt{GM_{\mathrm{Sun}}}}{r^{3/2}} \sqrt{\frac{r}{1\,\mathrm{au}}} \sqrt{\frac{m_{\mathrm{RU}}}{(dF/ds)_{1\,\mathrm{au}}}}$$

$$= \sqrt{k} \tan \alpha \frac{1 + \dfrac{m_t}{3 m_{\mathrm{RU}}}}{\sqrt{1 + \dfrac{m_t}{2 m_{\mathrm{RU}}}}} \left( \frac{r}{1\,\mathrm{au}} \right)^{-1} \sqrt{\frac{GM_{\mathrm{Sun}}}{(1\,\mathrm{au})^3}} \sqrt{\frac{m_{\mathrm{RU}}}{(dF/ds)_{1\,\mathrm{au}}}}$$

$$= \pi \sqrt{2k} \tan \alpha \frac{1 + \dfrac{m_t}{3 m_{\mathrm{RU}}}}{\sqrt{1 + \dfrac{m_t}{2 m_{\mathrm{RU}}}}} \left( \frac{r}{1\,\mathrm{au}} \right)^{-1} \frac{1}{1\,\mathrm{year}} \sqrt{\frac{2 m_{\mathrm{RU}}}{(dF/ds)_{1\,\mathrm{au}}}} \ . \tag{6.15}$$

For $r = 1\,\mathrm{au}$ (which is approximately valid for our NEO mission) the first factor is

$$\pi \sqrt{2k} \tan \alpha \frac{1 + \dfrac{m_t}{3 m_{\mathrm{RU}}}}{\sqrt{1 + \dfrac{m_t}{2 m_{\mathrm{RU}}}}} \left( \frac{r}{1\,\mathrm{au}} \right)^{-1} = 5.68 \tag{6.16}$$

(we assumed $m_t = 0.22$ kg and $m_{\mathrm{RU}} = 0.35$ kg as above), and the last factor is

$$\frac{\sqrt{\dfrac{2 m_{\mathrm{RU}}}{(dF/ds)_{1\,\mathrm{au}}}}}{1\,\mathrm{year}} = 3.75 \cdot 10^{-5} \ . \tag{6.17}$$

The quantity $\sqrt{2 m_{\mathrm{RU}}/(dF/ds)_{1\,\mathrm{au}}}$ has the dimensionality of time and a value of 1200 s. It is equal to the time that it takes for a short piece of tether attached to mass $m_{\mathrm{RU}}$ to

accelerate over a distance that is equal to its length, assuming that it is kept perpendicular to the solar wind. It is the shortness of this time relative to the orbital period (one year at 1 au) which is why the impulse ratio $p_{\mathrm{RU}}/p_{\mathrm{Esail}}$ is so small.

### 6.5.3 Main spacecraft cold gas delta-v

From Table 6.5, cold gas propulsion is used for settling to orbit the asteroid (1 m/s), for making trajectory corrections while orbiting it (1 m/s) and for landing (0.1 m/s). These operations (2.1 m/s in total) occur with an unloaded spacecraft weighing nominally 8 kg. Assuming specific impulse of 70 s for cold gas, this phase consumes 25 grams of propellant. After the regolith has been collected, cold gas propulsion is used to lift off and to separate from the asteroid (0.2 m/s) and for making orbital corrections during aerobraking, for which we reserve 1 m/s. This 1.2 m/s of loaded delta-v requires an impulse of 360 Ns (assuming total mass 300 kg), which corresponds to 0.52 kg of cold gas propellant.

### 6.5.4 Snail regolith container

The snail collector was described in 6.3.1.3 above. The snail is made from heat-tolerant plastic or textile material such as kapton or Nomex which is metallised from the outside to withstand ATOX later in aerobraking phase. The snail is deployed from a canister. Weak ridigisation springs are embedded in the structure in order to gain enough stiffness so that the asteroid's microgravity is insufficient for significantly altering its shape. The area of membrane needed is 6 m² (or actually 5.2 m² but we calculate with 6 m² to be conservative), and we multiply this value by four to get the total mass of the device. The factor four contains the embedded stiffening springs and the stowage canister and its lock release mechanism.

The area on the asteroid where the spacecraft crawls forward collecting regolith must meet some criteria:

1. It must have regolith at least in places.

2. 'Large' rocks must be known beforehand from the maps and navigated around using the left/right kicker. Here 'large' means a rock of the same size as the spacecraft or large, i.e. $\sim$ 10 cm diameter or larger. A head-on encounter with a large rock might present some risk of getting stuck, although use of the left/right kicker would likely be able to rectify the situation. Thus we have double certainty: as a baseline strategy we shall avoid large rocks using the maps made from orbit, but even if we encounter an unmapped rock for some reason or another, we can probably get around it.

3. The gravity field should be reasonably vertical, i.e. the component of the local gravity field which is along the geometric surface should not be too large. A large horizontal field is equivalent to steeply sloped terrain. In particular, if the forward component of the gravity field is positive and large so that the snail crawls downhill, there is a risk that some of the already collected regolith might leak out from the snail through the feed tube[3] The first landing can occur in a valley (a

---

[3]Figuratively speaking, the snail feels sick and vomits.

low point in the gravity potential) from which the snail mainly crawls uphill, avoiding moving downhill along steep slopes. Depending on the specific case of the asteroid, it is also possible for the spacecraft to lift off using propulsion and re-land elsewhere. Such manoeuvre typically consumes only $\sim 10$ cm/s of delta-v, depending of course on the asteroid size and the geometric characteristics.

### 6.5.5 Aerobrake

In Appendix E we derive the following approximate formula for atmospheric braking in elliptic orbit by perigee passes. The braking impulse received at the perigee pass is (E10)

$$I = C_D \sqrt{\frac{\pi}{2e}} \left(1 + e\right) A \rho_0 \sqrt{GM_E H} \tag{6.18}$$

and the delta-v is $\Delta v = I/m_{\text{tot}}$. Here $C_D$ is the drag coefficient, $e$ is the orbit's eccentricity, $A$ is the cross-sectional area of the spacecraft, $\rho_0$ is atmospheric mass density at perigee point (which is equal to the maximum density encountered during the perigee pass), $G$ is the gravitational constant, $M_E$ is Earth mass and $H$ is the atmospheric scale height.

The maximum drag force occurs at the perigee point and is given by (E11)

$$F_{\text{max}} = \frac{1}{2} C_D \rho_0 A \frac{GM_E}{r_0} \left(1 + e\right). \tag{6.19}$$

The maximum heat flux $u_{\text{max}}$ in the nearly collisionless regime (high Knudsen number) is

$$u_{\text{max}} = \frac{1}{2}\rho_0 v^3 = \frac{1}{2}\rho_0 \left[(1 + e) \frac{GM_E}{r_0}\right]^{3/2}. \tag{6.20}$$

If approximating the parachute as a flat plate perpendicular to the flow, its maximum radiative equilibrium temperature $T_{\text{max}}$ is determined by the Stefan-Boltzmann law

$$2\epsilon\sigma_{\text{SB}} T_{\text{max}}^4 = u_{\text{max}}. \tag{6.21}$$

Here $\epsilon$ is the infrared emissivity which we take to be $\epsilon \approx 0.9$, $\sigma_{\text{SB}} = 5.67 \cdot 10^{-8}$ W/(m$^2$ K$^4$) and the factor 2 comes from the fact that the parachute has a frontside and a backside. By substituting (6.20) in (6.21) and solving for $\rho_0$ we obtain

$$\rho_0 = \frac{4\epsilon\sigma_{\text{SB}} T_{\text{max}}^4}{v^3} = \frac{4\epsilon\sigma_{\text{SB}} T_{\text{max}}^4}{\left[(1 + e) \frac{GM_E}{r_0}\right]^{3/2}}. \tag{6.22}$$

For example if the maximum temperature $T_{\text{max}}$ is set to 300° C (573.15 K), Eq. 6.22 gives $\rho_0 = 1.65 \cdot 10^{-8}$ kg/m$^3$, which is a density that occurs at 121 km altitude. At this altitude, the scale height $H$ is 11 km, and Eq. (6.18) predicts the impulse per area of 184 Ns/m$^2$. We assumed that for a parachute-shaped object the drag coefficient is $C_D \approx 2$ and we assumed a parabolic orbit for simplicity so that the eccentricity $e=1$. For example, if the aerobrake area is 6 m$^2$ (the same as the membrane area of the regolith

collecting snail) then the impulse per perigee pass is 1100 Ns and the corresponding delta-v is 3.7 m/s if the total mass is 300 kg. The total delta-v from C3 orbit to LEO is 3200 m/s so with these parameters we need 860 orbits. From Eq. (6.19) the maximum thrust is $F_{\max} = 12$ N and the maximum deceleration with 300 kg mass is 4 milligee. The thrust is low enough that mechanical requirements of the parachute are reasonably small.

How long does the aerobraking process take? In Appendix F we show that the average rate of reduction of the semimajor axis $a$ is given by (F6):

$$
\begin{aligned}
\frac{da}{dt} &= -\frac{1}{\pi}\Delta v \sqrt{\frac{2a}{r_0} - 1} \\
&= -\frac{1}{\pi}\Delta v \sqrt{\frac{r_A}{r_0}}
\end{aligned}
\tag{6.23}
$$

where $r_A$ is the apogee radius. The relationship between the semimajor axis $a$, the perigee radius $r_0$ and $r_A$ is $a = (r_0 + r_A)/2$. Also, since $dr_0/dt = 0$, we have $dr_A/dt = 2da/dt$, thus

$$
\frac{dr_A}{dt} = -\frac{2}{\pi}\Delta v \sqrt{\frac{r_A}{r_0}}.
\tag{6.24}
$$

The time $t$ required to reduce $r_A$ from $r_A^{\text{init}}$ to $r_A^{\text{final}}$ is

$$
\begin{aligned}
t = \int dt &= -\int_{r_A^{\text{init}}}^{r_A^{\text{final}}} dr_A \frac{\pi}{2}\sqrt{\frac{r_0}{r_A}}\frac{1}{\Delta v} \\
&= \pi \frac{\sqrt{r_0}}{\Delta v}\left(\sqrt{r_A^{\text{init}}} - \sqrt{r_A^{\text{final}}}\right).
\end{aligned}
\tag{6.25}
$$

It is of interest to notice that Eq. (6.25) depends only on the orbit geometry and the perigee delta-v, but not e.g. on Earth's mass. If $r_0 = R_E + 121\,\text{km}$[4], $r_A^{\text{init}} = 40R_E$, $r_A^{\text{final}} = 1.5R_E$ and if $\Delta v = 3.7\,\text{m/s}$ as above, then the aerobraking time to come from 40 $R_E$ apogee down to 3186 km altitude is $t = 11$ months.

It is not self-evident what value one should pick for the initial apogee. One consideration is that if one uses a lunar flyby manoeuvre to kill up to $\sim 1 - 1.5$ km/s of the hyperbolic delta-v and to capture the spacecraft in a bound orbit, then the initial apogee is, in the best case, around $\approx 2/3$ of the lunar distance, i.e. around $\approx 40R_E$. If one does not use a lunar manoeuvre, the situation is different. If $r_A = 100R_E$, for example, then the aerobraking time prediction increases to $\sim$1.5 years.

The aerobraking time is inversely proportional to the aerobrake area. In the above calculation we rather arbitrarily assumed an area of 6 m$^2$, because it needs the same area of membrane material as the regolith snail. The choice happened to yield a rather reasonable duration of little less than one year for aerobraking (if the lunar capture manoeuvre is used).

With the above parameters, the mass per aerobrake area is 300 kg/6 m$^2$ = 50 kg/m$^2$ = 0.5 kg/dm$^2$, i.e. about half of the mass per area of a typical 1-U cubesat.

For the aerobrake device, we assume a mass budget of four times the mass of a 12.6 $\mu$m kapton membrane. The material is not necessarily kapton, but could be

---

[4]$R_E = 6371.2\,\text{km}$ is the Earth radius.

e.g. Nomex which is more heat resistant. The factor four includes the mass of the stowage canister and its release lock mechanism. The mass of 6 m$^2$ kapton membrane is 0.11 kg and when multiplied by four it becomes 0.45 kg. The factor four is an educated guess and is meant to be conservative.
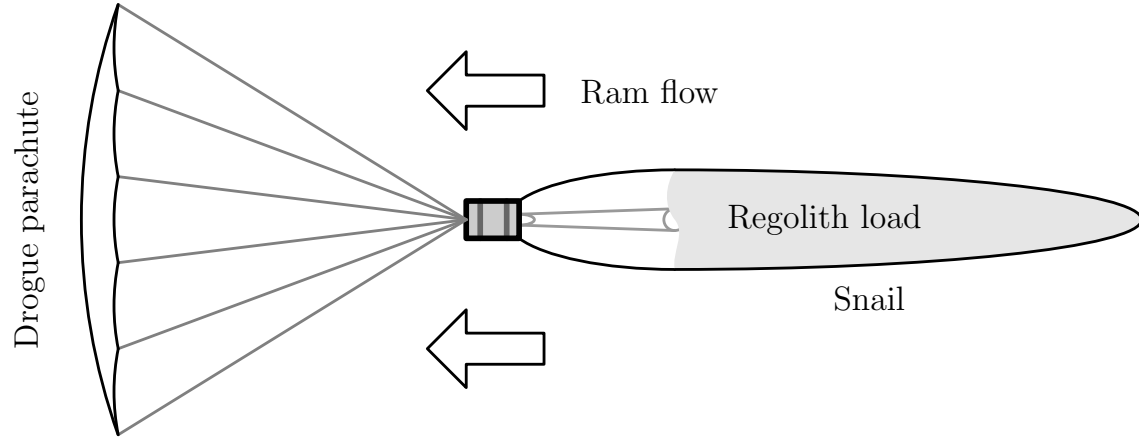


**Figure 6.6:** The drogue parachute aerobrake in operation during perigee pass.

In the aerobraking phase, the regolith-filled snail protects at least partly the space-craft box from the atmospheric flow. The aerobraking phase is also aerodynamically stable (the centre of pressure is well behind the centre of mass) because the heavy regolith-filled snail is flying first and the aerobrake trails the configuration.

Coincidentally, the aerobrake has the same mass budget as the snail. The reason is that both have the same area of 6 m$^2$, and during aerobraking they have to face similar mechanical $\sim$ 12 N force from the aerodynamics. The temperature tolerance requirements are also similar because the back end of the snail faces the ram flow as does the aerobrake[5]

### 6.5.6 Forward kicker

The spacecraft crawls forward on the surface of the asteroid by an asymmetrically back and forth moving mass somewhere within the spacecraft. The kicker mass is accelerated forward, it kicks a wall, bounces back, and the cycle is repeated. The acceleration phase must be mild enough so that the static friction force between the spacecraft and the asteroid is able to overcome it.

Let $a_g$ be the acceleration of gravity on the asteroid's surface, let $m_{\text{tot}}$ be the total mass of the spacecraft including the mass of the regolith existing in the snail, let $m_k$ be the mass of the moving kicker and let $s_k$ be the kicker stroke length. Let $a_k$ be the kicker acceleration during the acceleration phase. The weight is $G = m_{\text{tot}}a_g$ and the maximum static friction force induced by it is

$$F_s = \mu_s G = \mu_s m_{\text{tot}} a_g \tag{6.26}$$

where $\mu_s$ is the static friction coefficient between the spacecraft and the asteroid. The

---

[5]The regolith inside the snail might help cool the membrane to some extent, but to remain conservative we do not take this effect into account.

forward force needed to accelerate the kicker must be less than $F_s$. Hence the acceleration $a_k$ of the kicker must obey

$$a_k < \frac{F_s}{m_k} = \frac{\mu_s m_{\text{tot}} a_g}{m_k} \ . \tag{6.27}$$

The speed $v_k$ of the kicker when it hits the wall is

$$v_k = \sqrt{2a_k s_k} < \sqrt{\frac{2\mu_s m_{\text{tot}} a_g s_k}{m_k}} \ . \tag{6.28}$$

The kicker is much lighter than $m_{\text{tot}}$. Let us also assume that the relative loss modulus of the kicker and the wall are low. Then the kicker bounces back almost fully and delivers an impulse to the spacecraft which is nearly twice its original forward impulse:

$$I = 2m_k v_k < \sqrt{8\mu_s m_k m_{\text{tot}} a_g s_k} \ . \tag{6.29}$$

The impulse causes a momentary large force which overcomes the static friction and causes the spacecraft to move forward at an initial speed

$$v_0 = \frac{I}{m_{\text{tot}}} < \sqrt{\frac{8\mu_s m_k a_g s_k}{m_{\text{tot}}}} \ . \tag{6.30}$$

The initial speed is slowed down by kinetic friction

$$F_k = \mu_k G = \mu_k m_{\text{tot}} a_g \ . \tag{6.31}$$

where $\mu_k$ is the kinetic friction coefficient. The deceleration is $a_d = F_k/m_{\text{tot}} = \mu_k a_g$. The distance $\Delta x$ that the spacecraft jumps forward is solved from the relationship $v_0 = \sqrt{2a_d \Delta x}$:

$$\Delta x = \frac{v_0^2}{2a_d} < \frac{8\mu_s m_k a_g s_k}{2m_{\text{tot}} \mu_k a_g} = 4\frac{\mu_s}{\mu_k}\frac{m_k}{m_{\text{tot}}}s_k. \tag{6.32}$$

In reality the static friction coefficient $\mu_s$ is larger than the kinetic friction coefficient $\mu_k$. The most conservative upper bound for $\Delta x$ is obtained by setting them equal so that

$$\Delta x < 4\frac{m_k}{m_{\text{tot}}}s_k. \tag{6.33}$$

The time needed to accelerate the kicker from rest to $v_k$ is $v_k/a_k$. Because the kicker bounces back, the time interval $\Delta t$ between kicks is two times this:

$$\Delta t = 2\frac{v_k}{a_k} = 2\frac{\sqrt{2a_k s_k}}{a_k} = \sqrt{\frac{8s_k}{a_k}} > \sqrt{\frac{8s_k m_k}{\mu_s m_{\text{tot}} a_g}} \ . \tag{6.34}$$

We can then compute the average crawling speed of the spacecraft $\langle v \rangle$:

$$\langle v \rangle = \frac{\Delta x}{\Delta t} < 4\frac{m_k}{m_{\text{tot}}}s_k\sqrt{\frac{\mu_s m_{\text{tot}} a_g}{8s_k m_k}} = \sqrt{\mu_s\frac{m_k}{m_{\text{tot}}}}\sqrt{2a_g s_k} \ . \tag{6.35}$$

110

The expression $\sqrt{2a_g s_k}$ is the speed at which an object hits the asteroid if it is dropped from height $s_k$. The dimensionless expression at the front $\sqrt{\mu_s(m_k/m_{\text{tot}})}$ is much less than unity because $m_k \ll m_{\text{tot}}$.

Let us introduce typical numbers. Take asteroid gravity to be $g_a=5 \cdot 10^{-5}$ m/s$^2$, which corresponds to an asteroid with 150 m diameter. Assume total mass $m_{\text{tot}}=300$ kg, kicker mass $m_k=0.1$ kg, static friction coefficient $\mu_s=0.3$ and stroke length $s_k = 5$ cm. Then $\sqrt{2a_g s_k} = 2.2$ mm/s, the dimensionless expression $\sqrt{\mu_s(m_k/m_{\text{tot}})}=0.01$ and $\langle v \rangle = 22\mu$m/s, which is 8 cm/hour and 190 cm per day. One step is 67 $\mu$m in length and each step takes three seconds. The kicker acceleration $a_k=0.045$ m/s$^2$ (4.6 milligee) and the speed at which the kicker hits the wall is 6.7 cm/s. The corresponding kinetic energy is 0.2 mJ so if none of the energy would be recovered, the power consumption would be 75 $\mu$W, which is negligible. The force by which the kicker must be accelerated is 0.45 cN. The weight of a fully loaded 300 kg spacecraft is 1.5 cN, which corresponds to the weight of 1.5 gram mass on Earth's surface.

The snail is some $\sim 6$ m long. Typically in order to fill itself with regolith, it should move a distance on the asteroid that is at least few times its length. If we take 1 m/day to be a conservative speed (above we obtained 1.9 m/day), then after moving for one month the spacecraft has covered a 30 m distance. In suitable conditions that distance might already be sufficient to collect a full load of regolith.

The crawling speed $\langle v \rangle$ (Eq. 6.35) depends on the square root of the asteroid's surface gravity $a_g$ (and hence, on the square root of the asteroid's diameter), on the square root of the stroke length $s_k$, on the square root of the mass ratio of the kicker versus total $m_k/m_{\text{tot}}$ and on the square root of the friction coefficient $\mu_s$.

The three design parameter in (6.35) are the kicker mass $m_k$, the stroke length $s_k$ and the friction coefficient $\mu_s$. To maximise $\langle v \rangle$, all three parameters should be maximised. The dependence on them is by the square root, however, so large improvements in $\langle v \rangle$ are challenging to make. One idea might be to use an already existing part of the spacecraft such as battery, propellant tank or a larger subsystem as the moving mass, in order to eliminate dead weight.

One way to improve the speed (if it needs to be improved – the above estimate of 1.9 m/day might already be considered sufficient) might be to make the bottom of the spacecraft and the bottom of the snail "furry" so that sliding forward presents lower friction than sliding backward. Such method might be effective when moving over rocks that are anchored within the soil so that they do not move when pushed against. When moving over plain regolith the difference is likely to be smaller, but in that case the speed need not be increased because the collection of regoglith proceeds at optimal rate.

In the above analysis, we treated the spacecraft system, which includes the snail and its regolith content, as a rigid body. We assume that the snail is rigidised using e.g. deployed springs. The amount of rigidisation needed is rather minimal since all forces involved are weak in comparison to earthly standards.

## 6.5.7 Left/right kicker

Usually the spacecraft crawls forward, but if it hits head-on with an obstacle rock and cannot push through, it is good to have also a left/right kicker so that we can get around the rock. The left/right kicker can be smaller than the forward one. It should

be able to switch its polarity from left so that the mover can bang either at the left or the right wall.

An alternative to the left/right kicker would be if the spacecraft's front is sharpened to conical shape so that it tends to push aside obstacles. However, such shape would interfere with the CubeSat format or would require a deployable structure. Since the front already hosts the return trip E-sail and the aerobrake, adding a third deployable might make things complicated, hence we prefer the left/right kicker.

### 6.5.8 Camera

The camera can be quite small. In subsection 6.4.3 above we found that 1 cm aperture diameter is sufficient to map the asteroid at 2 cm resolution at 500 nm wavelength from 400 m orbiting distance at diffraction limit. The only use of the data is to see where the regolith-covered regions are and to see where exist rocks that are of the same size as the spacecraft or larger, because such rocks are potentially harmful for surface mobility. Since the spacecraft is a 6-U box, 2 cm resolution is quite sufficient to recognise rocks that are of $\sim 10$ cm diameter or larger. The camera can be black and white and no spectral capabilities are needed. The camera can be placed at the front so it can be used also during surface mobility to detect obstacles. We reserve 50 grams for the camera. This mass estimate is probably rather generous, because the optics weighs only a few grams or less.

### 6.5.9 Mass budget

The overall mass budget is given in Table 6.6.

### 6.5.10 Layout

We place the subsystems in the following way:

1. The roof is entirely covered by body-mounted solar panels.

2. The bottom is dedicated to the high-gain patch antenna. We do not use a reflectarray antenna, because that would require a protruding feeder unit. When landed on the surface, our high-gain antenna cannot be used and any communication must be slow and use a low-gain antenna.

3. The wedge tool and the snail are deployed from the back, because the spacecraft pulls the snail on the surface when hammered forward by the internal kickers.

4. The E-sail for the return trip and the aerobrake are deployed from the front (Fig. 6.7), because the snail reserves the back of the spacecraft.

5. The E-sail for the forward trip is deployed from the back, because in the front there is no room for it as the front is taken by the aerobrake and the return trip E-sail. The empty slot left by the forward-trip remote unit can be utilised by the wedge tool as part of the room where the regolith particles fly towards the feed tube.

The subsystems fall naturally into front, middle and back sections (Table 6.7).

**Table 6.6:** Mass budget.

| Component | Mass | Remark |
|---|---|---|
| **Payload:** | | |
| Tether 1 | 0.07 kg | 6.7 km, $1.1 \cdot 10^{-5}$ kg/m |
| Tether reel 1 | 0.22 kg | Three times mass of tether 1 |
| Remote unit 1 | 0.25 kg | wet; Two TILE 50 thrusters plus 150 gram bus |
| Tether 2 | 0.22 kg | 20 km, $1.1 \cdot 10^{-5}$ kg/m |
| Tether reel 2 | 0.66 kg | Three times mass of tether 2 |
| Remote unit 2 | 0.35 kg | wet; Four TILE 50 thrusters plus 150 gram bus |
| HV subsystem | 0.28 kg | 7 W, 40 kg/kW, 2× more than Janhunen et al. (2013) |
| Aerobrake | 0.45 kg | 6 m$^2$ 12.6 $\mu$m kapton equivalent, multiplied by four |
| Snail | 0.45 kg | 6 m$^2$ 12.6 $\mu$m kapton equivalent, multiplied by four |
| Wedge tool | 0.1 kg | Few centimetre tool, one degree of freedom actuator |
| Camera | 0.05 kg | 1 cm diameter aperture |
| Forward kicker | 0.2 kg | Mover mass 0.1 kg, stroke length 5 cm |
| Left/right kicker | 0.1 kg | Smaller than forward kicker |
| *Payload total* | 3.40 kg | |
| **Bus:** | | |
| Frame | 1.1 kg | ISIS, 6-U primary+secondary mass(ISISpace, 2016) |
| Power system | 0.25 kg | 100 W/kg specific power without battery |
| | | 25 W, 25 % efficiency EOL, 85 % fill factor |
| Reaction wheels | 0.72 kg | Three Blue Canyon Tech RWP050 units |
| Battery | 0.18 kg | Four CGR18650C (2004), total 4.4 Ah×7.2 V=32 Wh |
| Cold gas system | 1 kg | wet; Includes 0.55 kg of propellant |
| Communication | 1.0 kg | 1/3 of M-ARGO, 1/3 of HGA area |
| Computer | 0.15 kg | One 1-U PCB |
| *Bus total* | 4.40 kg | |
| Total | 7.8 kg | |
| 'Limit' | 8.0 kg | 1.33 kg per unit, but not a hard limit |
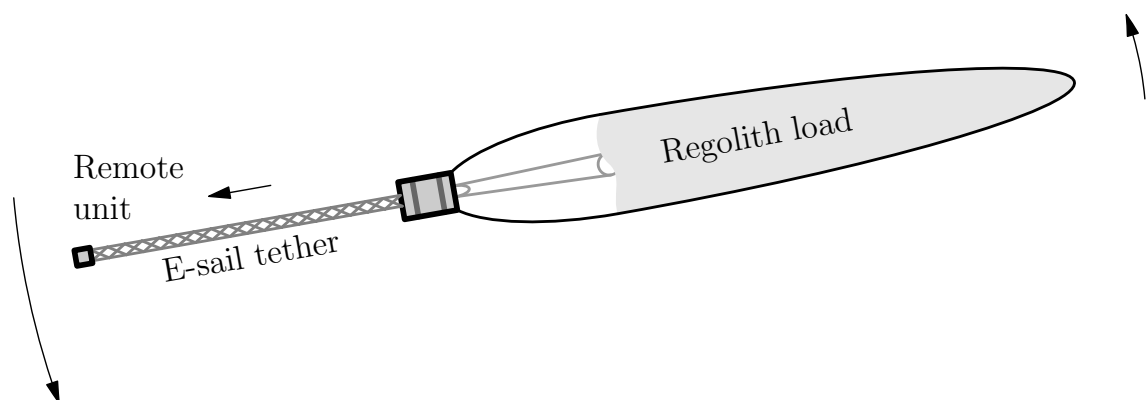


**Figure 6.7:** Deployment of E-sail 2 after leaving the asteroid.

Table 6.7: Placement of subsystems in front, middle and back sections.

| Section hardware | Mass | Length |
|---|---|---|
| **Front section** | **1.83 kg** | 9 cm |
| E-sail 2 remote unit and reel unit with tether | 0.35+0.66+0.22=1.23 kg | |
| Aerobrake | 0.45 kg | |
| Camera | 0.05 kg | |
| Left/right kicker | 0.1 kg | |
| **Middle section** | **3.78 kg** | 17 cm |
| HV subsystem | 0.28 kg | |
| Forward kicker | 0.2 kg | |
| Onboard computer | 0.15 kg | |
| Electric power system with battery | 0.43 kg | |
| Radio | 1.0 kg | |
| Reaction wheels | 0.72 kg | |
| Cold gas propulsion system | 1 kg | |
| **Back section** | **1.09 kg** | 7 cm |
| E-sail 1 remote unit and reel unit with tether | 0.25+0.22+0.07=0.54 kg | |
| Snail | 0.45 kg | |
| Wedge tool | 0.1 kg | |
| **Sections together** | **6.7 kg** | 33 cm |
| 6-U frame | 1.1 kg | |
| **Total** | **7.8 kg** | 33 cm |

## 6.6    Summary and conclusions

### 6.6.1    Mass ratio goal is reached

Our baseline economic scenario is to bring asteroid regolith to LEO, separate oxygen from it, liquefy, and sell the LOX to a launch company such as SpaceX that operates reusable launchers. Only the retrieval problem was considered in this work package, but the other steps have been considered earlier in the context of lunar regolith mining. In this application, each kilogram of LOX tanked into the launch vehicle as return propellant increases the vehicle's payload capacity by the same amount. To make this economically viable, the mass ratio (the mass of retrieved regolith versus the mass of the miner that was sent) must be at least $\sim 20$.

Our E-sail mission design has a mass factor of $\sim 37$ so we are well positioned in the economically profitable regime. The design is meant to be realistic regarding mass. The only point where some technical extrapolation was exercised was that we assumed 13 % higher TILE 50 thruster total impulse than the official specifications. Thus the ideas proposed in this work package provide an exemplary scenario of how to implement economically profitable asteroid mining using only low level of initial investment.

### 6.6.2    Risks

A mission that must bring NEO material to LEO must contain many phases, and many things could go wrong. The most risky phase is probably the operation on the asteroid's surface, because the details of the surface are not known. To an extent, this seems unavoidable in any asteroid mining mission: risks can be reduced, but trying to eliminate them completely would be very challenging and probably also not economically optimal. The landing spot and the regolith collection area must be sufficiently smooth, with reasonably vertical gravity field, and devoid of rocks of the same size or larger than the spacecraft. To select a good area and to map the locations of large rocks, we image the asteroid from orbit before landing.

We have fitted everything in a 6-U box. If the design becomes too constrained in terms of mass and volume, going to 12-U format is an option. The mass ratio of $\sim 20$ would still be achievable. One benefit of a 6-U box is that it is less likely to fall over on the asteroid surface than the 12-U box which is two times higher.

### 6.6.3    Inventive steps

Our mission plan contains, we think, several nontrivial ideas for achieving various tasks, in addition to the E-sail itself:

1. The simple wedge tool for digging up regolith, with only one mechanical degree of freedom (6.3.1.2).

2. The use of the snail geometry and the feed tube for containing the regolith (6.3.1.3).

3. The use of impulsive kickers to cause mobility on the surface (6.5.6–6.5.7).

4. It was not clear *a priori* that there is a way to place all subsystems for which there are geometric constraints (the two E-sails, the snail, the aerobrake, the solar panel and the high-gain patch antenna) so that all missions phases (E-sail flight with tethers 1 and 2, asteroid imaging, data transmission, landed operation, liftoff and aerobraking) work. However, a solution to this problem exists as we have shown (6.5.10).

### 6.6.4   Future

In the future, the first priority should be the increase of the TRL of the E-sail, because it is the key enabling technology of this and other types of missions. Also, the asteroid surface operations using the wedge tool and the regolith snail should be subjected to numerical testing to get more insight of the regolith collection process and its risks. If a two-dimensional simulation is deemed sufficient for qualitative analysis, then suitable codes such as Box2D (2019) exist in the public domain.

# Bibliography

ESAIL FP7 project website `http://www.electric-sailing.fi/fp7`.

Envall, J., P. Janhunen, P. Toivanen, M. Pajusalu, E. Ilbis, J. Kalde, M. Averin, H. Kuuste, K. Laizans, V. Allik, T. Rauhala, H. Seppänen, S. Kiprich, J. Ukkonen, E. Hæggström, T. Kalvas, O. Tarvainen, J. Kauppinen, A. Nuottajärvi and H. Koivisto, E-sail test payload of ESTCube-1 nanosatellite, *Proc. Estonian Acad. Sci.,* **63**, 210–221, 2014.

Grün, E., H.A. Zook, H. Fechtig and R.H. Giese, Collisional balance of the meteoritic complex, *Icarus,* **2**, 244–272, 1985.

Janhunen, P., Electric sail for spacecraft propulsion, *J. Prop. Power,* **20**, 763–764, 2004.

Janhunen, P.: Electric sail for producing spacecraft propulsion, U.S. Pat. 7641151, priority date March 2, 2006.

Janhunen, P., P.K. Toivanen, J. Polkko, S. Merikallio, P. Salminen, E. Haeggström, H. Seppänen, R. Kurppa, J. Ukkonen, S. Kiprich, G. Thornell, H. Kratz, L. Richter, O. Krömer, R. Rosta, M. Noorma, J. Envall, S. Lätt, G. Mengali, A.A. Quarta, H. Koivisto, O. Tarvainen, T. Kalvas, J. Kauppinen, A. Nuottajärvi and A. Obraztsov, Electric solar wind sail: Toward test missions, *Rev. Sci. Instrum.,* **81**, 111301, 2010.

Janhunen, P., Photonic spin control for solar wind electric sail, *Acta Astronaut.,* **83**, 85–90, 2013.

Janhunen, P., Description of E-sail dynamic simulator codes, ESAIL FP7 project deliverable D51.1., `http://www.electric-sailing.fi/fp7/docs/D511.pdf`.

Janhunen, P., A.A, Quarta and G. Mengali, Electric solar wind sail mass budget model, *Geosci. Instrum. Method. Data Syst.,* **2**, 85–95, 2013.

Janhunen, P., Electric sail, photonic sail and deorbiting applications of the freely guided photonic blade, *Acta Astronaut.,* **93**, 410–417, 2014.

Janhunen, P., Electric solar wind sail for asteroid touring missions and planetary protection, *Asteroids, Comets and Meteors ACM-2014 meeting,* Helsinki, July 1, 2014. Available at `http://www.electric-sailing.fi/slides/ACM2014-PJ.pdf`.

Janhunen, P. and P. Toivanen, An intrinsic way to control E-sail spin, Unpublished manuscript, `http://arxiv.org/abs/1406.6847`, 2014.

Janhunen, P., P. Toivanen, J. Envall, S. Merikallio, G. Montesanti, J. Gonzalez del Amo, U. Kvell, M. Noorma and S. Lätt, Overview of electric solar wind sail applications, *Proc. Estonian Acad. Sci.,* **63**, 267–278, 2014.

Janhunen, P. and P. Toivanen, TI tether rig for solving secular spinrate change problem of electric sail, Acta Astronaut., submitted, 2016.

Kestilä, A., T. Tikka, P. Peitso, J. Rantanen, A. Näsilä, K. Nordling, H. Saari, R. Vainio, P. Janhunen, J. Praks and M. Hallikainen, Aalto-1 nanosatellite – technical description and mission objectives, *Geosci. Instrum. Method. Data Syst.,* **2**, 121–130, 2013.

Kleshch, V.I., E.A. Smolnikova, A.S. Orekhov, T. Kalvas, O. Tarvainen, J. Kauppinen, A. Nuottajärvi, H. Koivisto, P. Janhunen and A.N. Obraztsov, Nano-graphite cold cathodes for electric solar wind sail, *Carbon,* **81**, 132–136, 2015.

Lätt, S., A. Slavinskis, E. Ilbis, U. Kvell, K. Voormansik, E. Kulu, M. Pajusalu, H. Kuuste, I. Sünter, T. Eenmäe, K. Laizans, K. Zalite, R. Vendt, J. Piepenbrock, I. Ansko, A. Leitu, A. Vahter, A. Agu, E. Eilonen, E. Soolo, H. Ehrpais, H. Lillmaa, I. Mahhonin, J. Mõttus, J. Viru, J. Kalde, J. Subitidze, J. Mucenieks, J. Sate, J. Kütt, J. Polevskis, J. Laks, K. Kivistik, K.-L. Kusmin, K.-G. Kruus, K. Tarbe, K. Tuude, K. Kalnina, L. Joost, M. Lõoke, M. Järve, M. Vellak, M. Neerot, M. Valgur, M. Pelakauskas, M. Averin, M. Mikkor, M. Veske, O. Schlere, P. Liias, P. Laes, R. Rantsus, R. Soosaar, R. Reinumägi, R. Valner, S. Kurvits, S.-E. Mändmaa, T. Ilves, T. Peet, T. Ani, T. Tilk, T.H.C. Tamm, T. Scheffler, T. Vahter, T. Uiboupin, V. Evard, A. Sisask, L. Kimmel, O. Krömer, R. Rosta, P. Janhunen, J. Envall, P. Toivanen, T. Rauhala, H. Seppänen, J. Ukkonen, E. Hæggström, R. Kurppa, T. Kalvas, O. Tarvainen, J. Kauppinen, A. Nuottajärvi, H. Koivisto, S. Kiprich, A. Obraztsov, V. Allik, A. Reinart and M. Noorma, ESTCube-1 nanosatellite for electric solar wind sail in-orbit technology demonstration, *Proc. Estonian Acad. Sci.,* **63**(2S), 200–209, 2014.

Mengali, G., A.A. Quarta and G. Aliasi, Summary of orbit calculations supporting WP61, ESAIL FP7 project deliverable D62.1 `http://www.electric-sailing.fi/fp7/docs/D62.1.pdf`.

Polkko, J., Auxiliary tether report, ESAIL FP7 project deliverable D24.1 `http://www.electric-sailing.fi/fp7/docs/D241_auxtether.pdf`.

Seppänen, H., S. Kiprich, R. Kurppa, P. Janhunen and E. Hæggström, Wire-to-wire bonding of um-diameter aluminum wires for the Electric Solar Wind Sail, *Microelectronic Engineering,* **88**, 3267–3269, 2011.

Seppänen, H., T. Rauhala, S. Kiprich, J. Ukkonen, M. Simonsson, R. Kurppa, P. Janhunen and E. Hæggström, One kilometer (1 km) electric solar wind sail tether produced automatically, *Rev. Sci. Instrum.,* **84**, 095102, 2013.

Thornell, G., Remote Unit test results, ESAIL FP7 project deliverable D41.4, `http://www.electric-sailing.fi/fp7/docs/D414.pdf`.

Toivanen, P.K. and P. Janhunen, Electric sailing under observed solar wind conditions, *Astrophys. Space Sci. Trans.,* **5**, 61–69, 2009.

Toivanen, P. and P. Janhunen, Spin plane control and thrust vectoring of electric solar wind sail by tether potential modulation, *J. Prop. Power,* **29**, 178–185, 2013.

Wagner, S., J. Sundqvist, and G. Thornell, Design description of the Remote Unit, ESAIL FP7 project deliverable D41.2, `http://www.electric-sailing.fi/fp7/docs/D412.pdf`.

Janhunen, P. and P. Toivanen, Asteroid touring by electric sail technology, Work package 1: E-sail designs (WP1 report of this project), ESA, 2016.

`http://dawn.jpl.nasa.gov/mission/Dawn_overview.pdf`

Kohout, T., A. Näsilä, T. Tikka, M. Granvik, A. Kestilä, A. Penttilä, J. Kuhno, K. Muinonen and K. Viherkanto, Feasibility of asteroid exploration using CubeSats – ASPECT case study, *Adv. Space Res.*, in press, 2017.

Kuuste, H., T. Eenmäe, V. Allik, A. Agu, R. Vendt, I. Ansko, K. Laizans, I. Sünter, S. Lätt and M. Noorma, Imaging system for nanosatellite proximity operations, *Proc. Estonian Acad. Sci.*, **63**(2S), 250–257, 2014.

Tsuda, Y., M. Yoshikawa, M. Abe, H. Minamino and S. Nakazawa, System design of the Hayabusa 2 -asteroid sample return mission to 1999 JU3, Acta Astronaut., 91, 356–362, 2013.

Walker, R., D. Koschny, C. Bramanti and ESA CDF study team, Miniaturised asteroid remote geophysical observer (M-ARGO): a stand-alone deep space CubeSat system for low-cost science and exploration missions, 6th Interplanetary CubeSat Workshop, Cambridge, UK, 30 May, 2017.

`http://www.space-propulsion.com/spacecraft-propulsion/hydrazine-thrusters/1n-hydrazine-thruster.html`

Moog cold gas thrusters, `http://www.moog.com/content/dam/moog/literature/Space_Defense/Spacecraft/Propulsion/ColdGasThrusters_0717.pdf`.

Janhunen, P., P. Toivanen J. Envall and 10 coauthors, Multi-Asteroid Touring, Proposal to "Call for new ideas", September 2016.

Slavinskis, A., P. Janhunen, P. Toivanen and 21 coauthors, Nanospacecraft fleet for multi-asteroid touring with electric solar wind sails, 2018 IEEE Aerospace Conference at Big Sky, Montana, USA, 3–10 March, 2018.

`https://ssd.jpl.nasa.gov/sbdb_query.cgi`

`https://cneos.jpl.nasa.gov/tools/ast_size_est.html`

`http://blogs.esa.int/rosetta/2014/08/05/tracking-the-spacecraft-following-a-comet/`

M-ARGO CDF Study Report CDF-171(A), ESA, 2017.

Box2D, a 2-D physics engine for games, `http://www.box2d.org`

Gundlach, B. and J. Blum, A new method to determine the grain size of planetary regolith, Icarus, 223, 479–492, 2013.

Heppenheimer, T.A., Approximate analytic modeling of a ballistic aerobraking planetary capture, J. Spacecr. Rockets, 8(5), 554–555, 1971.

ISIS CubeSat structure broschure, `https://www.isispace.nl/wp-content/uploads/2016/02/ISIS-CubeSat-Structures-Brochure-v1.pdf`

Janhunen, P., A.A. Quarta and G. Mengali, Electric solar wind sail mass budget model, Geosci. Instrum. Method. Data Syst., 2, 85–95, 2013, `http://www.geosci-instrum-method-data-syst.net/2/85/2013/`

Lamy, A., C. Le Fevre and B. Sarli, Analysis of geostationary transfer orbit long term evolution and lifetime, 22nd Int. Symp. Space Flight Dynamics, São José dos Campos, Brazil, Feb 28–March 4, 2011, `http://issfd.org/ISSFD_2011/S1-Orbit.Dynamics.1-ODY1/S1_P2_ISSFD22_PF_056.pdf`

Lomax, B.A., M. Conti, N. Khan, N.S. Bennett, A.Y. Ganin and M.D. Symes, Proving the viability of an electrochemical process for the simultaneous extraction of oxygen and production of metal alloys from lunar regolith, Planet. Space Sci., in press, 2019.

M-ARGO CDF Study Report CDF-171(A), ESA, 2017.

Panasonic CGR-18650 C battery specification, `http://www.rosebatteries.com/pdfs/Panasonic%20CGR18650C.pdf`

Toivanen, P. and P. Janhunen, Spin plane control and thrust vectoring of electric solar wind sail by tether potential modulation, *J. Prop. Power,* **29**, 178–185, 2013.

Wikipedia article on ellipse, `http://en.wikipedia.org/wiki/Ellipse`

Wikipedia article on mineral resource classification, `http://en.wikipedia.org/wiki/Mineral_resource_classification`

# Appendix A

# TI tether rig article

Janhunen, P. and P. Toivanen,
"TI tether rig for solving secular spinrate change problem
of electric sail," manuscript, March 2016.

Material published later in:
Janhunen, P. and P. Toivanen, "A scheme for controlling
the E-sail's spin rate by the E-sail effect itself",
*Space Propulsion 2018 conference*, Seville, Spain,
13–18 May, 2018.

# TI tether rig for solving secular spinrate change problem of electric sail

Pekka Janhunen[a,*], Petri Toivanen[a]

*[a]Finnish Meteorological Institute, Helsinki, Finland*

## Abstract

The electric solar wind sail (E-sail) is a way to propel a spacecraft by using the natural solar wind as a thrust source. The problem of secular spinrate change was identified earlier which is due to the orbital Coriolis effect and tends to slowly increase or decrease the sail's spinrate, depending on which way the sail is inclined with respect to the solar wind. Here we present an E-sail design and its associated control algorithm which enable spinrate control during propulsive flight by the E-sail effect itself. In the design, every other maintether ("T-tether") is galvanically connected through the remote unit with the two adjacent auxtethers, while the other maintethers ("I-tethers") are insulated from the tethers. This enables one to effectively control the maintether and auxtether voltages separately, which in turn enables spinrate control. We use a detailed numerical simulation to show that the algorithm can fully control the E-sail's spin state in real solar wind. The simulation includes a simple and realistic set of controller sensors: an imager to detect remote unit angular positions and a vector accelerometer. The imager resolution requirement is modest and the accelerometer noise requirement is feasible to achieve. The TI tether rig enables building E-sails that are able to control their spin state fully and yet are actuated by pure tether voltage modulation from the main spacecraft and requiring no functionalities from the remote units during flight.

*Keywords:* electric sail, control algorithm, solar wind

## Nomenclature

| | |
|---|---|
| au | Astronomical unit, 149 597 871 km |
| $A$ | Auxiliary factor |
| $\mathrm{clamp}\,(x, a, b)$ | Clamp function, limitation of $x$ in $[a, b]$ |
| $d_{\max}$ | Maximum thrust reduction for $f_4$, 0.05 |
| $\hat{\mathbf{e}}_r$ | Radial unit vector |
| $f(t)$ | Generic function of time $t$ |
| $f_1(t), f_2(t), \tilde{f}(t)$ | Gap filler functions |
| $f$ | Total throttling factor |
| $f_1, f_2, f_3$ | Individual throttling factors |
| $f_4, f_5$ | Throttling factors for oscillation damping |
| $f_6$ | Throttling factor for setting thrust |
| $f_6^{\max}$ | Maximum allowed $f_6$, 1.01 |
| $f_6^{\mathrm{old}}$ | Previous value of $f_6$ |
| $\mathbf{F}$ | Generic thrust vector |
| $F_{\mathrm{goal}}$ | Goal E-sail thrust, 100 mN |
| $\mathbf{F}_n$ | Spinplane normal component of thrust |
| $\mathbf{F}_{\mathrm{rig}}$ | Thrust on tether rig |
| $\mathbf{F}_s$ | Spinplane component of thrust |
| $\mathbf{F}_{\mathrm{sc}}$ | Thrust on spacecraft |
| $\mathbf{F}_{\mathrm{tot}}$ | Total thrust, $\mathbf{F}_{\mathrm{sc}} + \mathbf{F}_{\mathrm{rig}}$ |
| $\mathbf{F}_{\mathrm{tot}}^{\mathrm{ave}}$ | Time-averaged version of $\mathbf{F}_{\mathrm{tot}}$ |
| $F_0$ | Typical tether tension |
| $g$ | Acceleration due to gravity, 9.81 m/s$^2$ |
| $g_{\mathrm{d}}$ | Greediness factor for damping in $f_4$, 3.0 |
| $g_{\mathrm{s}}$ | Greediness factor for spinrate change, 2.0 |
| $g_{\mathrm{t}}$ | Greediness factor for spinplane turning, 1.0 |
| $K$ | Spin axis orientation keeper factor |
| $\mathbf{L}$ | Angular momentum vector |
| $\mathbf{L}(0)$ | Initial angular momentum vector |
| $m_{\mathrm{rig}}$ | Mass of tether rig, 11 kg |
| $m_{\mathrm{sc}}$ | Mass of spacecraft body, 300 kg |
| $m_{\mathrm{tot}}$ | Total mass, 311 kg |
| $\max(a, b)$ | Maximum of $a$ and $b$ |
| $\min(a, b)$ | Minimum of $a$ and $b$ |

*Corresponding author
*Email address:* pekka.janhunen@fmi.fi (Pekka Janhunen)
*URL:* http://www.electric-sailing.fi (Pekka Janhunen)

| | |
|---|---|
| $\hat{\mathbf{n}}_{goal}$ | Goal orientation unit vector of spin axis |
| $\hat{\mathbf{n}}_{SW}$ | Unit vector along (nominal) SW, (0,0,1) |
| $N_w$ | Number of tethers |
| $\mathbf{p}$ | Momentum of tether rig |
| $\mathbf{r}$ | Position of remote unit |
| $\hat{\mathbf{s}}$ | Unit vector along spin axis |
| $S$ | Spinrate increase factor |
| $t$ | Time |
| $t_1, t_2$ | Starttime and endtime of data gap |
| $\mathbf{v}$ | Velocity of remote unit |
| $v_s$ | Spin axis aligned speed of remote units |
| $v_{tot}$ | Average rotation speed of remote units |
| $x, y, z$ | Cartesian coordinates in inertial frame |
| $x', y', z'$ | Spin axs aligned Cartesian coordinates |
| $\hat{\mathbf{x}}', \hat{\mathbf{y}}', \hat{\mathbf{z}}'$ | Unit vectors along $x', y', z'$ |
| $\alpha$ | Sail angle, angle between SW and spin axis |
| $\Delta t$ | Timestep how often controller is called, 2 s |
| $\Delta t_d$ | How often damper is called, 20 s |
| $\tau_{d5}, \tau_{d6}$ | Timescale parameters, 1200 s |
| $\omega$ | Angular frequency of the sail spin |
| $\Omega$ | Angular frequency of heliocentric orbit |

## 1. Introduction

The solar wind electric sail (E-sail) is a concept how to propel a spacecraft in the solar system using the natural solar wind (SW) [1, 2]. The E-sail uses a number of thin metallic and centrifugally stretched tethers which are biased at high positive potential (Fig. 1). The biasing is effected by an onboard electron gun which continuously pumps out negative charge from the tethers.
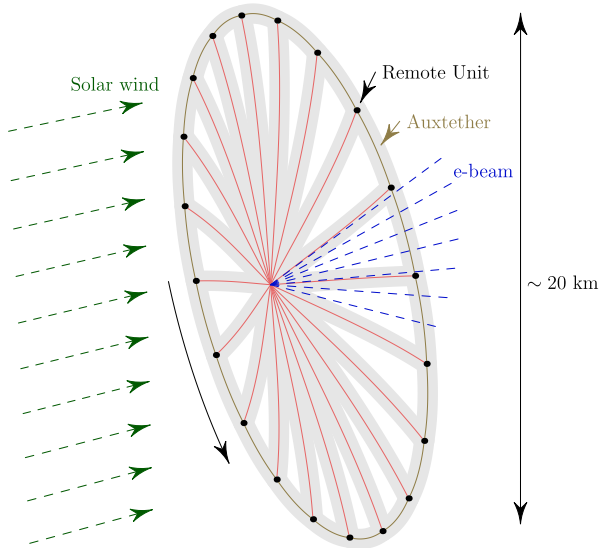


Figure 1: Schematic presentation of the E-sail.

The following secular spinrate change problem was, however, identified [11]. When an E-sail orbits around the sun with the sail inclined with respect to the SW, the orbital Coriolis effect causes a secular increase or decrease of the spinrate. Inclining the sail is necessary if one wants to produce transverse thrust perpendicular to the SW direction, which is usually the case. Specifically, if the sail is inclined so that it brakes the orbital motion and keeps the spacecraft spiralling towards the sun, the spinrate decreases, and if the sail is inclined in the opposite way so that the orbit is an outward moving spiral, the spinrate increases. The rate of spinrate increase or decrease obeys approximately the equation

$$\omega(t) \approx \omega(0)e^{\pm(\Omega \tan \alpha)t}. \qquad (1)$$

Here $\Omega$ is the angular frequency of the heliocentric orbit and $\alpha$ is the sail angle, i.e. the (positive) angle between the sail spin axis and the SW direction. For example if $\alpha$ is 35° and the spacecraft is in a circular orbit at 1 au distance, the spinrate changes by 9 % in each week. To overcome the problem, various technical solutions were proposed and analysed, for example the use of ionic liquid field-effect electric propulsion (FEEP) thrusters [8, 9, 7] or photonic blades [5] on the remote units.

In this paper we present a novel design concept (the TI tether rig) for the E-sail which overcomes the secular spinrate problem and yields a technically simple hardware. We also present a control algorithm and demonstrate by detailed numerical simulation that the algorithm is able to fly the E-sail in real SW with full capability to control the orientation of the spin plane and the spinrate. We also demonstrate that the algorithm is able to accomplish its task using a simple set of sensors (remote unit position imager and vector accelerometer) with realistic amount of measurement noise.

The structure of the paper is as follows. We show that electric auxtethers enable spinrate control, present the TI tether rig design, the control algorithm, the dynamical simulation model and the simulation results. The paper closes with summary and conclusions.

## 2. Electric auxtethers enable spinrate control

We consider an E-sail as in Fig. 2 where the auxiliary tethers (auxtethers) are metallic and can be biased at high voltage, similarly to the maintethers. A segment of an auxtether then generates E-sail thrust which is perpendicular to it. Our aim is then to show that if the auxtether voltages can be controlled independently from the maintether voltages, spinrate control becomes possible.

2
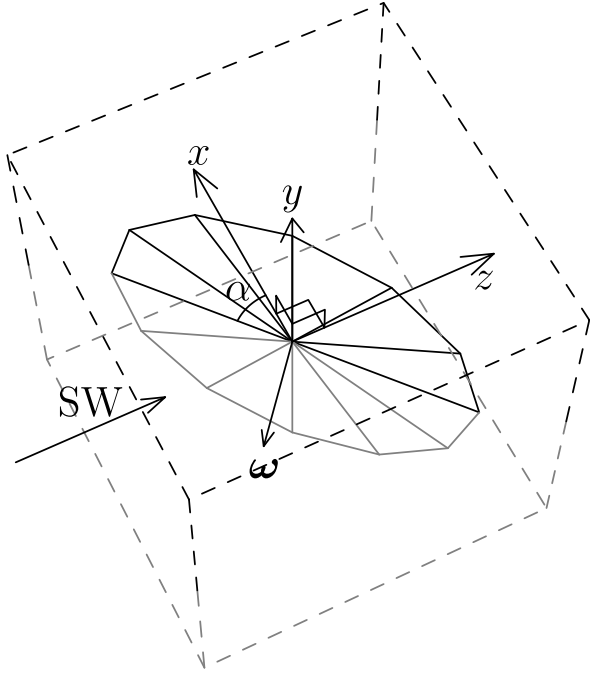
Figure 2: Three-dimensional schematic presentation of spinning planar E-sail inclined at angle $\alpha$ with respect to SW flow ($\alpha$ lies in the $xz$ plane). Lines below $y == 0$ plane are drawn in greyscale to ease visualisation. The $z$ coordinate is along the SW.

Figure 3a again shows an E-sail inclined at angle $\alpha$ to the SW flow, but now viewed from the top, antiparallel to the $y$ axis. Consider a maintether in the $xz$ plane i.e. in the plane of Fig. 3a. The maintether generates a thrust vector **F** which is perpendicular to itself.

Figure 3b shows the same maintether 90° rotation later when it is parallel to $y$ axis. Now, because the tether is perpendicular to the SW, its thrust vector **F** is aligned with the SW. We decompose **F** in spinplane component **F**$_s$ and spinplane normal component **F**$_n$. The spinplane component **F**$_s$ brakes the tether's spinrate when it moves upstream and accelerates it 180° rotation later, and the net effect vanishes.

Panel 3c is the same as panel 3b, but we have added a charged auxtether segment at the tip of the maintether. The thrust vector **F** is now a vector sum of the maintether thrust and the auxtether thrust. The maintether thrust is still along the SW flow as it was in 3b, but the auxtether's thrust contribution is perpendicular to the auxtether, i.e. perpendicular to the spin plane. As a result, **F** is not aligned with the SW and the ratio $F_s/F_n$ depends on the ratio of the auxtether thrust versus the maintether thrust. In particular, by modulating the auxtether and maintether voltages separately, the ratio $F_s/F_n$ can be different when the maintether is paral-

lel or antiparallel with the $y$ axis. By having the same $F_n$ but different $F_s$ in the upstream and downstream portions of the maintether's rotation cycle, we can modify the sail's spin rate while keeping its orientation fixed. Separate control of sail spinrate and spinplane orientation becomes possible because one has two control parameters in each angular segment, namely maintether voltage and auxtether voltage.

### 3. TI tether rig

To enable separate control of auxtether and maintether voltages, one could use various technical means, for example, each remote unit could carry a potentiometer or other means of regulating the auxtether voltage between zero and the maintether voltage. However, we propose a simpler arrangement where the remote units need no active parts. We propose that even-numbered maintethers are such that their remote unit is galvanically connected with both the left-side and right-side auxtethers (Fig. 4, blue), while odd-numbered maintethers are electrically insulated from the remote unit (Fig. 4, red). We call the even-numbered tethers the T-tethers because of the T-shaped shape of the blue equipotential region, and odd-numbered tethers are correspondingly called I-tethers.
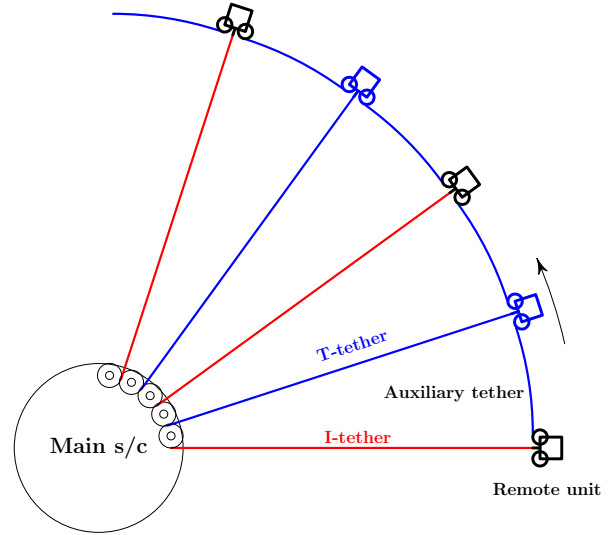


Figure 4: Schematic presentation of the TI tether rig.

In a given angular sector of the sail, we can effectively increase (decrease) the auxtether voltages by setting T-tethers to higher (lower) voltage than I-tethers. The auxtethers are always at the same potential as their associated T-tether so that no potentiometers or other functional parts are needed on the remote units. Two types of
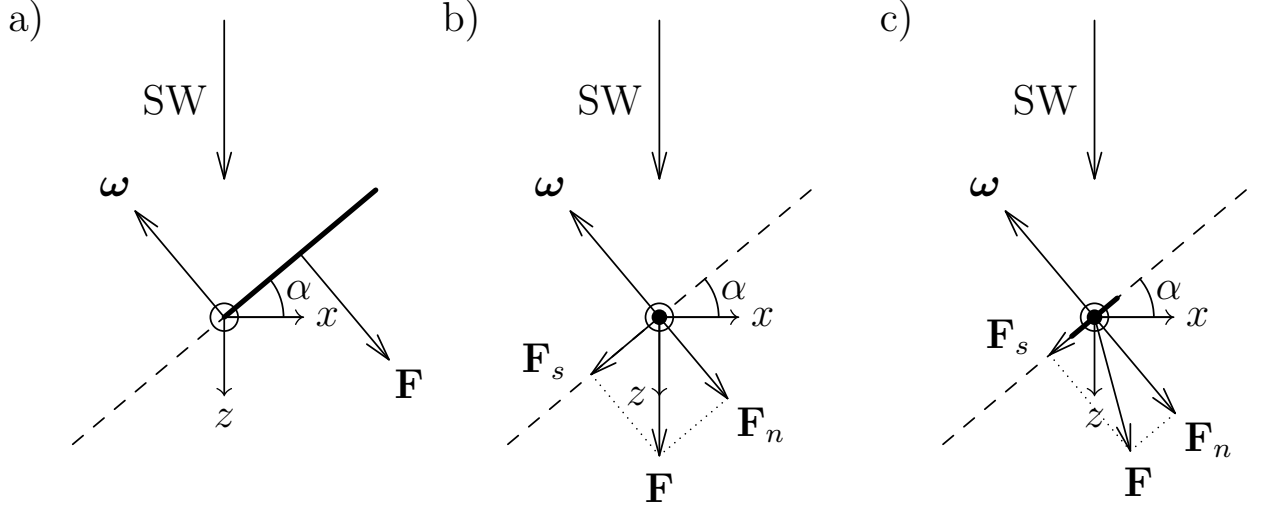
Figure 3: E-sail force components. (a) Maintether in *xz* plane, (b) maintether parallel to *y*, (c) maintether parallel to *y* plus auxtether segment.

remote units are needed: ones that provide galvanic connection between the maintether and the two auxtethers, and ones that provide an insulating connection between all three connecting tethers. As usual, the remote units contain reels of the auxtethers which are used during deployment phase. During propulsive flight, no functionality is required from the remote units. The units only have to continue to provide the mechanical and electrical connection which is of galvanic and insulating type of even and odd-numbered units, respectively. Because of the presence of T-tethers and I-tethers, we call the design as a whole the TI tether rig.

## 4. Control algorithm

The control algorithm consists of six throttling factors which are multiplied together at the end to yield the voltage throttling of each maintether. The six factors and their roles in the control algorithm are listed in Table 1.

Table 1: The six throttling factors.

| | |
|---|---|
| $f_1$ | Turning the spinplane |
| $f_2$ | Maintaining the spinplane |
| $f_3$ | Changing the spinrate |
| $f_4$ | Damping collective oscillations |
| $f_5$ | Damping oscillations of tethers |
| $f_6$ | Setting thrust to wanted value |

Let $\mathbf{r} = (x, y, z)$ be the remote unit's position vector relative to the spacecraft and $\hat{\mathbf{e}}_r = \mathbf{r}/r$ is the corresponding unit vector. We denote the angular momentum of the tether rig by $\mathbf{L}$ and the corresponding unit vector (spin axis vector) by $\hat{\mathbf{s}} = \mathbf{L}/L$. The controller computes instantaneous angular momentum $\mathbf{L}_{\text{inst}}$ approximately from imaged positions r of the remote units and their velocities v found by finite differencing with $\Delta t = 2$ s timestep. The angular momentum $\mathbf{L}$ used by the control algorithm below is a time-averaged version of $\mathbf{L}_{\text{inst}}$ which is obtained by continuously solving the differential equation

$$\frac{d\mathbf{L}}{dt} = \frac{\mathbf{L}_{\text{inst}} - \mathbf{L}}{\tau_{\text{L}}} \tag{2}$$

where $\tau_{\text{L}} = 1200$ s is timescale used in the time-averaging.

### 4.1. Factor $f_1$

The first throttling factor is

$$f_1 = \max\left(0, 1 - g_{\text{t}}\hat{\mathbf{e}}_r \cdot \hat{\mathbf{s}} \times \hat{\mathbf{n}}_{\text{goal}}\right) \tag{3}$$

where $g_{\text{t}} = 1.0$ is a greediness parameter for spinplane turning and $\hat{\mathbf{n}}_{\text{goal}}$ is the goal spin axis orientation. The factor $f_1$ is responsible for turning the spinplane when $\hat{\mathbf{s}} \neq \hat{\mathbf{n}}_{\text{goal}}$. It modulates the tether voltages so that the SW thrust applies a torque to the tether rig.

### 4.2. Factor $f_2$

The second throttling factor $f_2$ takes care of keeping the spinplane orientation constant. The second factor is

$$f_2 = (1 - A)K + A \tag{4}$$

4

125

where the 'spinplane keeper factor' $K$ is

$$K = \frac{1}{|\hat{\mathbf{n}}_{\text{SW}} - \hat{\mathbf{e}}_r(\hat{\mathbf{e}}_r \cdot \hat{\mathbf{n}}_{\text{SW}})|^2} \quad (5)$$

and the auxiliary factor

$$A = \frac{1}{1 + N_w/(2\pi)}. \quad (6)$$

The algorithm works moderately well even if $A = 0$, but it works better if $A$ has the value (6). The denominator of $K$ is the tether-perpendicular component of $\hat{\mathbf{n}}_{\text{SW}}$. If the tethers spin rapidly so that they move nearly in a plane without coning, $K$ does not depend on tether phase angle. However, in a real sail some coning occurs. Then the $K$ factor decreases and increases thrust on the upwind and downwind orientations of the spinning tether, respectively, to keep the total torque zero.

### 4.3. Factor $f_3$

The third throttling factor $f_3$ takes care of increasing or decreasing the spin rate. First we define the spinrate increase factor $S$ by

$$S = g_s \left[ s_{\text{goal}} - \frac{|\mathbf{L}|}{|\mathbf{L}(0)|} \right]. \quad (7)$$

Here $g_s = 2.0$ is the spinrate increase greediness factor and $s_{\text{goal}}$ is the goal for the relative spinrate, i.e. the angular momemtum magnitude relative to the initial angular momentum magnitude $|\mathbf{L}(0)|$. The throttling factor is given by

$$f_3 = 1 - \text{clamp}\,(\pm S\,\hat{\mathbf{v}} \cdot \hat{\mathbf{n}}_{\text{SW}}, -c_{\text{st}}, c_{\text{st}}). \quad (8)$$

Here $\mathbf{v}$ is the instantaneous velocity of the remote unit (relative to the spacecraft, similarly to r) and $c_{\text{st}} = 0.2$ is the maximum allowed amplitude of our sawtooth tether modulation. Plus sign is selected for T-tethers and minus sign for I-tethers. The function clamp forces the first argument within given limits $a$ and $b$, $a \leq b$. For any $x$, clamp $(x)$ is defined by

$$\text{clamp}\,(x, a, b) = \max(a, \min(x, b)) \quad (9)$$

The controller algorithm as described up to now works, but it does not damp tether oscillations that are produced by SW variations and the spinplane manoeuvres. Neither does it set the E-sail thrust to a wanted value. The purpose of the remaining factors $f_4$, $f_5$ and $f_6$ is to take care of these.

### 4.4. Factor $f_4$

For the first damping related factor, $f_4$, we measure the spin-axis aligned speed $v_s$ (sign convention: positive sunward) of the remote units relative to the spacecraft, averaged over the remote units. The measurement is done by finite differencing the imaged remote unit angular positions and the throttling factor is

$$f_4 = 1 + \min\left(0, g_d \frac{v_s}{v_{\text{tot}}}\right) \quad (10)$$

where $g_d = 3.0$ is greediness factor for damping and $v_{\text{tot}}$ is the average rotation speed of the remote units with respect to the spacecraft. The idea is that if the tether rig oscillates collectively along the spin axis so that the tether cone angle changes periodically, the oscillation is damped if voltages are slightly throttled down when the rig is moving in the direction of the SW.

### 4.5. Factor $f_5$

The factor $f_4$ reduces collective oscillation of the whole tether rig, but each tether can also oscillate individually like a guitar string between the spacecraft and the remote unit. For reducing these a bit faster oscillations we introduce throttling factor $f_5$. We measure the instantaneous thrust force $\mathbf{F}_{\text{sc}}$ acting on the spacecraft body (at 20 s resolution) by an onboard vector accelerometer. Notice that $\mathbf{F}_{\text{sc}}$ is the force exerted on the spacecraft by the tethers which is usually not equal to the total E-sail force exerted on the whole tether rig, except as an average over a long enough time period. When $|\mathbf{F}_{\text{sc}}|$ increases significantly, we apply overall throttling $f_5$ to tether voltages where

$$f_5 = 1 - \text{clamp}\,\left(\tau_{d5} \frac{1}{F_0} \frac{d|\mathbf{F}_{\text{sc}}|}{dt}, 0, d_{\text{max}}.\right) \quad (11)$$

Here $\tau_{d5} = 1200$ s is a damping timescale parameter, $d_{\text{max}} = 0.05$ is the maximum applied thrust reduction due to damping and $F_0$ is the typical tether tension multiplied by the number of tethers $N_w$. We set the typical tension equal to the tether tension in the initial state.

### 4.6. Factor $f_6$

The final throttling factor $f_6$ is used to settle the E-sail thrust to a wanted value $F_{\text{goal}}$. We estimate the E-sail thrust on the tether rig as

$$\mathbf{F}_{\text{rig}} = \frac{d\mathbf{p}}{dt} + \frac{m_{\text{rig}}}{m_{\text{tot}}} \mathbf{F}_{\text{sc}} \quad (12)$$

where $\mathbf{p}$ is the momentum of the tether rig relative to the spacecraft (determined by imaging and finite differencing the remote unit angular positions) and $m_{\text{rig}}$, $m_{\text{tot}}$

is the mass of the tether rig and the total mass, respectively. The first term is due to acceleration of the tether rig with respect to the spacecraft body and the second term is due to acceleration of the spacecraft with respect to an inertial frame of reference. The time average of the first term is obviously zero, but its instantaneous value is usually nonzero and it carries information about tether rig oscillations that we want to damp. The instantaneous thrust exerted on the whole system (spacecraft plus tether rig) is

$$\mathbf{F}_{\mathrm{tot}} = \mathbf{F}_{\mathrm{sc}} + \mathbf{F}_{\mathrm{rig}}. \tag{13}$$

From the instantaneous $\mathbf{F}_{\mathrm{tot}}$ we calculate a time-averaged version $\mathbf{F}_{\mathrm{tot}}^{\mathrm{ave}}$ by keeping on solving the time-dependent differential equation

$$\frac{d\mathbf{F}_{\mathrm{tot}}^{\mathrm{ave}}}{dt} = \frac{\mathbf{F}_{\mathrm{tot}} - \mathbf{F}_{\mathrm{tot}}^{\mathrm{ave}}}{\tau_{\mathrm{d6}}} \tag{14}$$

where $\tau_{\mathrm{d6}} = 1200$ s is another damping timescale parameter. Finally the overall throttling factor $f_6$ is calculated as

$$f_6 = \mathrm{clamp}\left(f_6^{\mathrm{old}} + \frac{\Delta t_{\mathrm{d}}}{\tau_{\mathrm{d6}}} \frac{F_{\mathrm{goal}} - |\mathbf{F}_{\mathrm{tot}}^{\mathrm{ave}}|}{F_{\mathrm{goal}}}, 0, f_6^{\mathrm{max}}\right) \tag{15}$$

where $\Delta t_{\mathrm{d}} = 20$ s is the timestep how often the damping algorithm is called, $f_6^{\mathrm{old}}$ is the previous value of $f_6$ and $f_6^{\mathrm{max}} = 1.01$ is $f_6$'s maximum allowed value. Equation (15) resembles solving a differential equation similar to (2) and (14), except that (15) also clamps the solution if it goes outside bounds $(0, f_6^{\mathrm{max}})$.

### 4.7. Combining the throttling factors

The total throttling factor is

$$f = \frac{f_1 f_2 f_3}{\max(f_1 f_2 f_3)} f_4 f_5 \min(1, f_6). \tag{16}$$

where the maximum is taken over the maintethers.

Factors $f_4$, $f_5$ and $f_6$ are updated at $\Delta t_{\mathrm{d}} = 20$ s intervals while $f_1$, $f_2$ and $f_3$ are updated with $\Delta t = 2$ s time resolution. The motivation for using slower updating of $f_4$, $f_5$ and $f_6$ is only to save onboard computing power. The computing power requirement is low in any case, but as a matter of principle we want to avoid unnecessary onboard computing cycles.

Factors $f_4$ and $f_5$ make only small modifications to the total throttling factor $f$. Despite this, their ability to damp tether rig oscillations is profound.

The tether voltages are modulated by $f$. We assume in this paper that the E-sail force depends linearly on $V$ so that we can achieve the wanted force throttling by simply modulation the voltages by $f$. This should be a rather good approximation (see equation 3 of Janhunen et al. [2]). Were this assumption not made, the nonlinear relationship should be modelled or determined experimentally and then used during flight to map thrust modulation values $f$ into voltage modulation values.

### 5. Simulation model

We use a dynamical simulator which was build for simulating dynamical behaviour of the E-sail tether rig [3, 4]. The simulator models the E-sail as a collection of point masses, rigid bodies and interaction forces between them. Also external forces and torques can be included. The core of the simulator solves the ordinary differential equations corresponding to Newton's laws for the collection the bodies. The solver is an eight order accurate adaptive Runge-Kutta solver adapted from Press et al. [10]. The solver provides in practice fully accurate discretisation in time. The only essential approximation is replacing continuous tethers by chains of point masses connected by interaction forces that model their elasticity. The E-sail force is included in the model. Synthetic or satellite-measured SW data can be used as the source. Table 2 summarises the main parameters of the simulation used in this paper.

Table 2: Simulation parameters.

| | |
|---|---|
| Number of tethers $N_{\mathrm{w}}$ | 20 |
| Tether length | 10 km |
| Thrust goal $F_{\mathrm{goal}}$ | 100 mN |
| Solar distance | 1 au |
| Baseline tether voltage | 20 kV |
| Maximum tether voltage | 40 kV |
| Spacecraft body mass $m_{\mathrm{sc}}$ | 300 kg |
| Initial tether tension | 5 cN |
| Initial spin period | 2000 s |
| Tether linear mass density | $1.1 \cdot 10^{-5}$ kg/m |
| Tether parallel wires | $3 \times \phi{=}20\,\mu$m |
| Tether wire Young modulus | 100 GPa |
| Tether wire relative loss modulus | 0.03 |
| Remote unit imager resolution | 0.17° |
| Onboard accelerometer noise | $1.5\,\mu g/\sqrt{\mathrm{Hz}}$ |
| Synthetic SW density | 7.3 cm$^{-3}$ |
| Synthetic SW speed | 400 km/s |
| Number of tether discr. points | 10 |
| Placement of discretisation points | Parabolic |
| Number of auxtether discr. points | 1 |
| Simulation length | 3 days |

6

The control algorithm needs only two types of sensors. Firstly, we need imaging sensors to detect the angular positions of the remote units with moderate angular 0.17° resolution and 2 s temporal resolution. The angular resolution requirement corresponds to about 2200×530 pixels, either in a single panoramic imager or several small imagers along the spacecraft's perimeter. Secondly, we need a vector accelerometer onboard the main spacecraft, for which we assume noise level of 1.5 $\mu g/\sqrt{\text{Hz}}$. A low-noise low-noise accelerometer such as Colibrys SF-1500 has noise level five times smaller than this. The imager resolution and accelerometer noise level were found by numerical experimentation. The chosen values are optimal in the sense that smaller measurement error in sensors would not noticeably improve the fidelity of the control and its oscillation damping properties.

In Table 3 we summarise the parameters of the control algorithm, including its virtual sensors.

Table 3: Default parameters of the control algorithm and its virtual sensors.

| | | |
|---|---|---|
| $d_{\max}$ | Maximum thrust reduction for $f_4$ | 0.05 |
| $f_6^{\max}$ | Maximum allowed $f_6$ | 1.01 |
| $F_{\text{goal}}$ | Goal E-sail thrust | 100 mN |
| $g_d$ | Greediness for damping in $f_4$ | 3.0 |
| $g_s$ | Greediness for spinrate change | 2.0 |
| $g_t$ | Greediness for spinplane turning | 1.0 |
| $\Delta t$ | Controller call interval | 2 s |
| $\Delta t_d$ | Damper call interval | 20 s |
| $\tau_{d5}$ | Timescale for damping oscillations | 1200 s |
| $\tau_{d6}$ | Timescale for regulating thrust | 1200 s |
| $\tau_L$ | Ang. momentum averaging time | 1200 s |

## 6. Simulation results

All simulations start from an initial state where the sail rotates perpendicular to the SW. Synthetic constant SW is used in first three runs. In the last run, real SW is used. In all runs the thrust is modulated by $1 - \exp(-t/(4h))$ so that it starts off gradually from zero. This is done to avoid inducing tether oscillations as an initial transient: although the algorithm can damp such oscillations, damping would not occur immediately.

In Run 1 (Fig. 5), the tilt angle goal (panel a) is zero until 12 h, then it is set to 45° where it remains for 18 hours. The sail starts turning when the angle is set and reaches almost 45° angle after 18 hours. Then the $\phi$ angle goal is changed from 90° to -90° so that the sail starts turning again, via zero to the opposite direction. At 48

h the $\alpha$ angle goal is returned back to zero. Thus, Run 1 exercises a back and forth swing of the tether rig. Spinrate regulation greediness parameter $g_s$ is set to zero in Run 1 so that we can observe the natural tendency of the spinrate to vary during the turning manoeuvre. The spinrate (Fig. 5, panel d) increases up to 25 % from the initial value when the sail reaches $\approx 45°$ angle. The increase is due to conservation of the sun-directed angular momentum component $L_z$: $|\mathbf{L}| = \sqrt{L_x^2 + L_y^2 + L_z^2}$ must increase if $L_x^2 + L_y^2$ increases while $L_z$ remains constant.
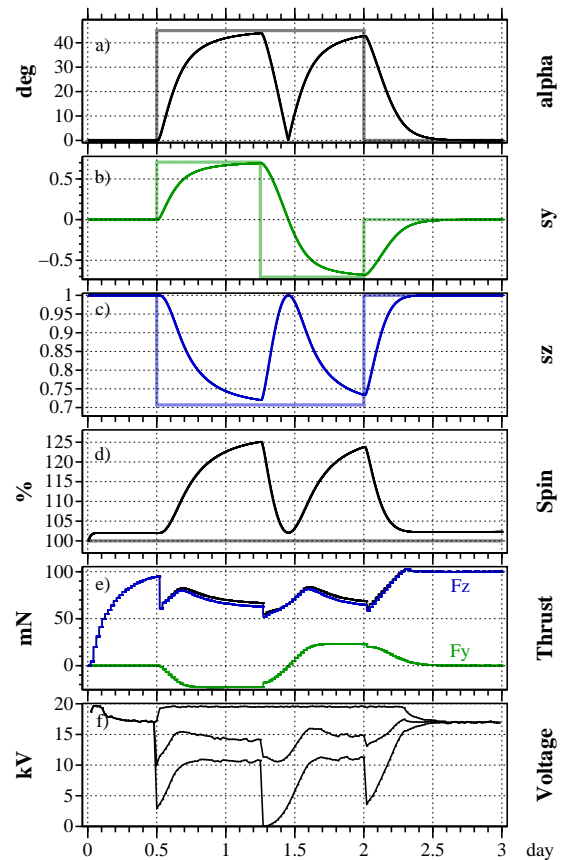


Figure 5: Result of Run 1. (a) angle $\alpha$ between SW and spin axis; (b) $\hat{s}_y$ ($y$ component of spin axis unit vector $\hat{s}$); (c) $\hat{s}_z$ ($z$ component of $\hat{s}$); (d) spin angular momentum relative to initial angular momentum in percent; (e) thrust along SW (blue, $F_z$), perpendicular to it (green, $F_y$) and total (black); (f) tether instantaneous minimum, mean and maximum voltages. In a-d, thicker grey and pastel lines show the commanded goal of each parameter.

The thrust direction (Fig. 5, panel e) varies according to the spinplane orientation. The total thrust is somewhat smaller when the spinplane is actively turned, which is due to the fact some tethers are then throttled

in voltage (Fig. 5, panel f).

In Run 2 (Fig. 6), the goal $\alpha$ angle is put to 35° throughout. The spinrate control greediness parameter $g_d$ is put to its normal value of 2.0. The spinrate goal is 110 % spin for the first 18 hours and is put to very large value after that. The controller turns the spin-plane smoothly to 35° which also increases the spinrate moderately because of $L_z$ conservation. When the spinrate goal is put high, the spinrate starts to increase almost linearly, reaching 60 % increase at the end of the run which is 2.25 days since setting the spinrate goal high. As a byproduct of the spinrate increase part of the algorithm, the sail angle (Fig. 6, panel a) decreases slightly from 35° to about 30°. The reason is that the spinrate modification and tilt angle modification parts of the controller algorithm slightly compete with each other because both use the same tether voltages for actuation. We do not expect this competition to be a practical issue because usually (to compensate the secular trend) the wanted spinrate change is much slower than in Run 2. In any case, Run 2 shows that if needed for any reason, the spinrate can be increased in a matter of few days with the model sail.

Run 3 (Fig. 7) is similar to Run 2, but now we demonstrate decreasing rather than increaseing of the spinrate. The spinrate goal is put to 40 % at 18 h. The spin slows down obediently. In this case the sail angle increases somewhat above the goal value 35°.

Finally, in Run 4 we simulate a typical use case of the E-sail. We set the sail angle $\alpha$ goal to 35° and the spinrate goal at 100 %. In Run 4 we also use real SW data to drive the E-sail where $t = 0$ corresponds to epoch January 1, 2000, 00:00 UT. The used SW data comes from NASA/GSFCV's OMNI 1-minute resolution dataset through OMNIWeb (Fig. 9,[6]).

Gaps in OMNI data were filled by the following simple algorithm (Fig. 10). Let $f(t)$ be the data which has a gap at $t_1 < t < t_2$. Mirror the data before $t_1$ to make a function $f_1(t) = f(2t_1 - t)$. Now, function $f_1(t)$ fills the gap $[t_1, t_2]$ with data that has the same spectral content as the real data $f(t)|t<t_1$. The filler $f_1(t)$ has, however, a discontinuity where the gap ends at $t_2$ and we return to real data $f(t)|t>t_2$. To remedy this, we carry out a similar procedure at the other end, mirroring data around $t_2$ to get $f_2(t) = f(2t_2 - t)$. Finally we construct the filler $\tilde{f}(t)$, $t_1 < t < t_2$, by linear interpolation between $f_1(t)$ and $f_2(t)$: $\tilde{f}(t) = (1 - u)f_1(t) + uf_2(t)$ where $u = (t - t_1)/(t_2 - t_1)$.

## 7. Summary and conclusions

We have presented a new E-sail design and its accompanying control algorithm and sensor set which satisfies
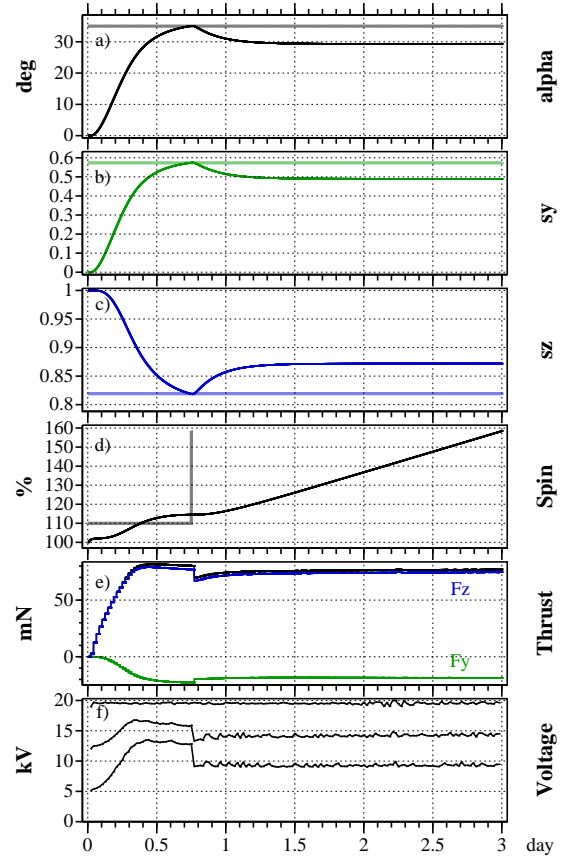


Figure 6: Same as Fig. 5 but for Run 2: demonstration of rapid spin increase.

the following requirements:

1. Control of tether voltages from the main spacecraft is the only actuation mechanism.

2. Capability to control the orientation of the spin plane and thereby the orientation of the E-sail thrust vector.

3. Delivery of the wanted amount of E-sail thrust.

4. Spinrate acceleration and deceleration capability. With typical parameters, the spinrate modification control authority is many times larger than what is needed to overcome the heliocentric orbit Coriolis effect.

5. Remote units have no functionality requirements after deployment.

6. Algorithmic automatic capability to damp tether oscillations.

7. Both maintethers and auxtethers are biased and thereby propulsive.

8
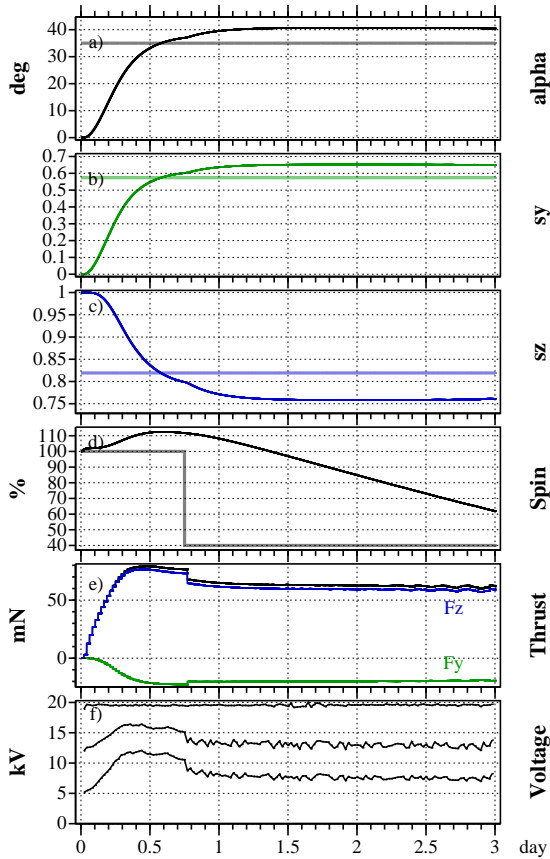
Figure 7: Same as Fig. 5 but for Run 3: demonstration of spin decrease.
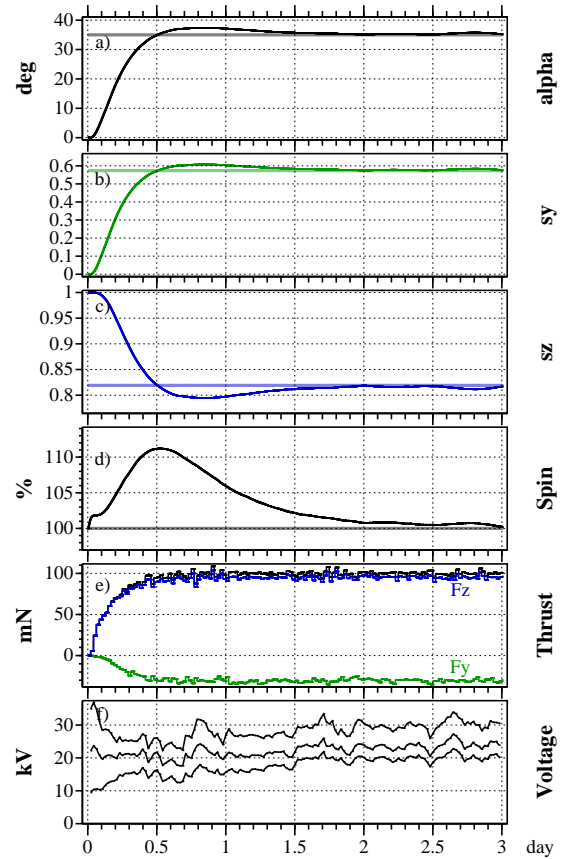


Figure 8: Same as Fig. 5 but for Run 4: typical use case of E-sail with real SW.

8. Only two sensors are needed: remote unit angular position detection by imaging and accelerometer.

9. Moderate resolution suffices for the imaging sensors.

10. The accelerometer should have low noise ($<$ $1.5\mu g/\sqrt{Hz}$), but devices exist (e.g. Colibrys SF-1500) whose noise level is even five times less.

In the simulations of this paper we did not study deployment, but an obvious question is if the spinrate increase capability of the algorithm would be enough to deploy the sail in reasonable time. Based on our preliminary analysis, the answer seems to be yes, provided that deployment to a few hundred metre tether length is first achieved by some other means.

Another future work that could be performed with our simulation is systematic analysis of average and maximum tether tension. Although not reported here, we have already monitored tether tension in our simulations, and the version of the control algorithm presented in this paper (Table 3) was arrived at partly by trial and error minimisation of the maximum tether tension when thrust was kept fixed.

We think that the TI tether rig is a significant step forward in E-sail design particularly because it enables full control of the angular momentum vector while not requiring any functionality from the remote units during flight. As a result, the secular spinrate problem originally identified by Toivanen and Janhunen [11] gets solved in a simple way.

## 8. Acknowledgement

9
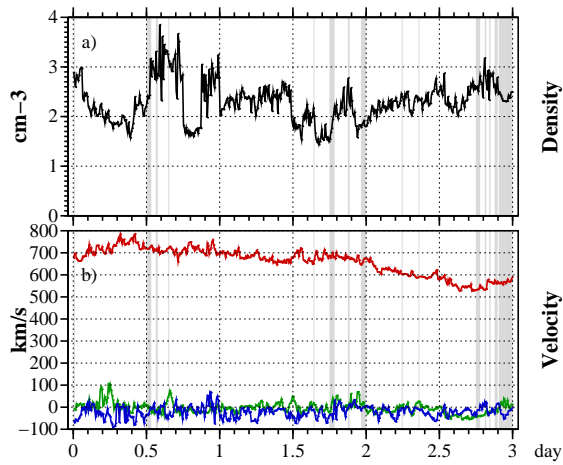
Figure 9: SW data used in Run 4 (Fig. 8). (a) plasma density, (b) SW velocity components (blue *x*, green *y*, red *z*). Filled data gaps are shown as grey.

## References

[1] P. Janhunen, Electric sail for spacecraft propulsion, J.Propuls.Power 20 (4) (2004) 763–764.

[2] P. Janhunen, et al., Electric solar wind sail: towards test missions, Rev.Sci.Instrum. 81 (2010) 111301.

[3] P. Janhunen, Description of E-sail dynamic simulator codes, Deliverable D51.1 of ESAIL FP-7 project, `http://www.electric-sailing.fi/fp7/docs/D511.pdf`, 2013 (accessed March 16, 2016).

[4] P. Janhunen, Report of performed runs, Deliverable D51.2 of ESAIL FP-7 project, `http://www.electric-sailing.fi/fp7/docs/D51.2.pdf`, 2013 (accessed March 16, 2016).

[5] P. Janhunen, Photonic spin control for solar wind electric sail, Acta Astronaut. 83 (2013) 85–90.

[6] J.H. King, N.E. Papitashvili, Solar wind spatial scales in and comparisons of hourly Wind and ACE plasma and magnetic field data, J.Geophys.Res. 110 (2005) A02104.

[7] S. Marcuccio, N. Giusti, A. Tolstoguzov, Characterization of linear slit FEEP using an ionic liquid propellant, IEPC-09-180, Proc. 31th International Electric Propulsion Conference, Ann Arbor, MI (2009).

[8] P. Pergola, N. Giusti, S. Marcuccio, Simplified FEEP test report, Deliverable D46.2 of ESAIL FP-7 project, `http://www.electric-sailing.fi/fp7/docs/D462.pdf`, 2013 (accessed March 17, 2016).

[9] P. Pergola, N. Giusti, S. Marcuccio, Cost assessment for industrial product, Deliverable D46.3 of ESAIL FP-7 project, `http://www.electric-sailing.fi/fp7/docs/D463.pdf`, 2013 (accessed March 17, 2016).

[10] W.H. Press, S.A. Teukolsky, W.T. Vetterling, B.P. Flannery, Numerical Recipes, third ed., Cambridge, 2007.

[11] P.K. Toivanen, P. Janhunen, Spin plane control and thrust vectoring of electric solar wind sail by tether potential modulation, J.Propuls.Power 29 (2013) 178–185.
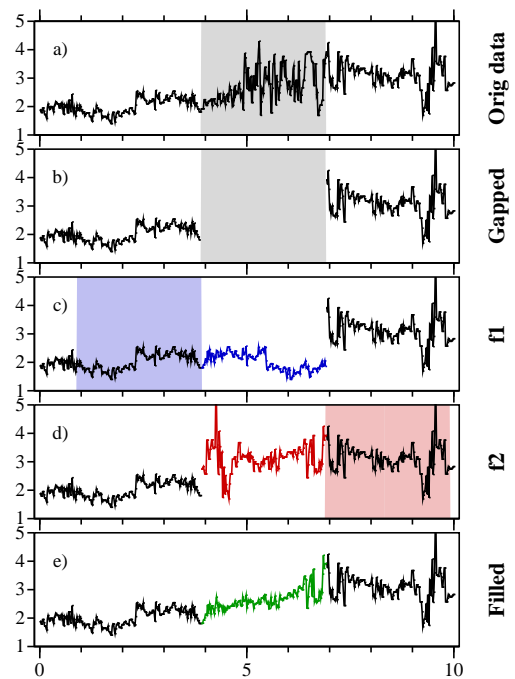


Figure 10: SW data gap filling algorithm. (a) original data, (b) original data with gap removed, (c) gap filled by mirroring left side function, (d) gap filled by mirroring right side function, (e) linear interpolation of c and d removes jumps at gap boundaries.

10

# Appendix B

# Lua source code of `"TImodel.lua"`

Lua source code of dynamic simulation of TI tether rig used in Appendix A and in section 1.4.

The code includes:
– loading of solar wind data from file
– control algorithm to set thrust, spin, orientation
– simulated remote unit imaging sensor for the controller
– interactive or batch mode operation
– simulated accelerometer for the controller
– actuation by tether potential modulation
– diagnostics and saving results to files
– some summary results are included in comments at the end

```lua
--------------------------------------------------------------------------------
-- TImodel.lua   PJ Feb 8-Mar 7, 2016
-- E-sail flight simulator for 'TI' tether rig
-- * electrically controllable auxtethers
-- * voltage control of main- and auxtethers from main spacecraft
-- * every other tether ('T'-tether) is galvanically connected to its two auxtethers
-- * every second tether ('I'-tether) is not
-- * spinrate controlled by 'sawtooth' modulation of adjacent 'T' and 'I' tethers
-- * controller also implements a damper algorithm to damp tether oscillations
-- * remote units only contain auxtether reels and are passive during flight
-- * needed sensory information:
--    * remote unit instantaneous angular positions (2 s time resolution, 3 millirad/pixel)
--    * onboard accelerometer (0.3 micro-gee at 20 s time resolution)
-- * sensor noise is also modelled
-- * needed actuation: tether voltages
--------------------------------------------------------------------------------
spacecraft = {}
ru = {}; rumid = {}; tether = {}; controller  = {}; repulsion = {}; statistics = {}
controller.sensors = {}; spacecraft.damper = {}
------------------------------ USER-MODIFIABLE PARAMETERS: -----------------------------------------
Nw = 30                       -- number of tethers
Np = 2*10                        -- number of discretisation points along tether, can be zero
Npaux = 1                     -- number of discretisation points along auxtether, must be >=1
spinup_mode = false           -- if true, do spinup/deployment sim, otherwise do propulsive flight sim
interactive_mode = false      -- if true, enable certain keys to modify orientation and spinrate during run
use_real_solar_wind = true    -- if true, use real solar wind data, otherwise use constant solar wind
write_throttle_file = true    -- if true, write tether throttle values in text file throttle.dat
write_tensions_file = true    -- if true, write tensions etc. in text file tensions.dat
write_attitude_file = true    -- if true, write s/c attitude vectors in attitude.dat
write_RUdiff_data = true      -- if also write_attitude_file is true, write also |rRU(1)-rRU(2)| in attitude file
write_state_files = false     -- if true, save object data in statennnn.cdf files periodically
write_info_file = true        -- if true, write theta,phi etc (same info as on screen) to info.dat
have_tether_repulsion = false--true  -- if true and Np>0, add mutual damped Coulomb repulsion between tethers
r_au = 2.5                    -- solar distance (au), used to scale thrust by 1/r_au
thrustcoeff = 0.18            -- overall multiplicative coefficient for dF/dz (dimensionless,paper9 eqn3)
Vbase = 20e3                  -- voltage (V) which consumes 100% of available power when n=SWn0
Vmax = 40e3                   -- maximum voltage that hardware allows (V)
SWn0 = 7.3e6                  -- base value of solar wind density at 1 au
SWv0 = 400e3                  -- base value of solar wind speed at 1 au
tmax = 14*24*3600.0           -- maximum simulation time (s)
spacecraft.mass = 300.0       -- main spacecraft is cylindrical, with given mass (kg)
spacecraft.radius = 0*1.5       -- main spacecraft radius (m) (if zero, is modelled as a point mass)
spacecraft.height = 0.5       -- main spacecraft cylinder height (m)
spacecraft.have_damper = true -- if true, spacecraft.damper code is in use to damp ~2min spacecraft oscillations
spacecraft.damper.deltar = 0.2-- distance of pullpoint from attachment point
spacecraft.damper.mass = 10e-3-- mass of pullpoint
spacecraft.damper.springconst1 = 30.0 -- (large) springconst (N/m) of connection between spacecraft and pullpoint
spacecraft.damper.springconst2 = 1e-3 -- (small) springconst (N/m) of pullpoint transverse attachment
spacecraft.damper.dampconst = 2.0     -- dampconst (N/(m/s)) of pullpoint transverse movement
tether.wanted_tension = spinup_mode and 2e-2 or 3e-2 -- wanted maintether tension (N)
tether.lambda = 1.1e-5        -- tether mass per unit length (kg/m)
tether.auxlambdarel = 1       -- auxtether kg/m relative to maintether kg/m
tether.len = spinup_mode and 500.0 or 15e3 -- tether length (m)
tether.rel_lossmodulus = 0.03       -- tether material relative lossmodulus (dimensionless)
-- rel_lossmodulus is important to be nonzero, but 0.015 works almost as well as 0.03 (~10% increase in maxtens)
tether.Young = 100e9                 -- tether Young modulus (Pa), 300e9 produces almost the same result as 100e9
tether.area = 3*math.pi*10e-6^2      -- tether cross-sectional area (used to calculate spring constant) (m^2)
tether.auxangle = math.rad(2.0)--math.rad(5)      -- how much auxtether bulges outward (deg)
tether.deployment_speed = spinup_mode and 10e-3 or 0 -- (m/s)
tether.aux_rellengthen = 0-- -0.002      -- relative lengthening of auxtethers after init (dimensionless)
tether.aux_rellengthen_time = 4*3600.0 -- time during which auxtether lengthening is carried out (s)
tether.use_nonuniform_points = true
controller.wanted_thrust = 90e-3   -- the wanted E-sail thrust (N)
controller.greediness_tilt = 1.0   -- how quickly to turn spinplane (dimensionless)
controller.greediness_spinrate = 2.0-- how quickly to regulate spinrate (goal is to keep |L(t)|==|L(0)|)
controller.greediness_damper = 3.0 -- how quickly to damp axial oscillation (dimensionless, typically ~2..4)
controller.fastdamp_tau = 1200.0   -- timescale greediness for damping fast tether oscillations (typically 1200s)
controller.fastdamp_max = 0.05     -- max throttle due to fast damper (tether oscillation damper, typically 0.05)
controller.scaler_dt = 20.0        -- how often to apply scaler (s)
controller.scaler_tau = 1200.0     -- time constant (s) used in thrust estimation (tested: 1200s best)
controller.maxoverallfactor = 1.01 -- max overall scaler factor used in its diff.eqn
controller.theta_goal_deg = 0      -- spin axis theta angle goal (deg)
controller.phi_goal_deg = 90       -- spin axis phi angle goal (deg)
controller.spin_goal = 100         -- spinrate goal (100=initial spinrate)
controller.maxallow_sawtooth = 0.2 -- odd/even sawtooth signal for spinrate modulation
controller.sharp_ampl = 0*2.0      -- parameter to increase thrust angle with same sail inclination (0..~1.5)
controller.use_approximate_angular_momentum = true   -- estimate angmom from RU position data (usually true)
controller.use_angular_momentum_time_averaging = true -- usually true: improves algorithm a lot
controller.have_accelerometer = true     -- usually true
controller.angular_momentum_time_averaging_tau = 1200.0 -- testing showed best value to be 1200 (s)
controller.sensors.RUangle_error = 3e-3 -- assumed gaussian error in sensed remote unit location angles (rad)
controller.sensors.RUvelocity_timescale = 100.0  -- timescale used in numerical differentiation of RU velocity (s)
controller.sensors.accelerometer_error_1Hz = 5*3e-6  -- assumed accelerometer gaussian error (m/s^2) at 1Hz
-- Colibrys SF1500 noise level 0.3 micro-gee/sqrt(Hz)
-- Cheap accelerometer: 150 micro-gee/sqrt(Hz), turned out to be too bad
-- Another cheap one (STM LIS344ALH): 50 micro-gee/sqrt(Hz)
ru.mass_odd = 0.4                       -- remote unit mass of odd-numbered units (kg)
ru.mass_even = 0.4                      -- remote unit mass of even-numbered units (kg)
have_one_lightru = false                -- have one remote unit lighter than other ones (usually false)
ru.lighter_mass = 0.2                   -- mass of the lighter unit (kg) (ignored if have_one_lightru is false)
have_electric_auxtethers = true     -- usually true
-- repulsion parameters, used if have_tether_repulsion is true:
repulsion.V0 = 20e3                 -- tether voltage (V)
repulsion.rwstar = 1e-3             -- tether effective electric radius (m)
repulsion.rel_lossmodulus = 0.3     -- ohmic dissipation is relatively large (dimensionless)
repulsion.r0rel = 0.85              -- repulsion starts when nearest gridpoints approached this relative distance
dt = spinup_mode and 0.5 or 2.0     -- simulation timestep (s)
--------------------------- END OF USER-MODIFIABLE PARAMETERS ------------------------------
epsilon0 = 8.854187817e-12          -- vacuum permittivity (As/(Vm))
mproton = 1.6726231e-27             -- proton mass (kg)
echarge = 1.60217662e-19            -- electron charge (As)
tether.auxlambda = tether.lambda*tether.auxlambdarel
rumid.mass = tether.auxlambda*(2*math.pi*tether.len/Nw)/Npaux    -- auxtether point mass (kg)
```

```lua
tether.aux_rellengthen_ongoing = true
controller.scaler_modcnt = math.max(1,math.floor(controller.scaler_dt/dt+0.5)) -- how often to apply scaler
controller.sensors.accelerometer_error=controller.sensors.accelerometer_error_1Hz/math.sqrt(controller.scaler_dt)
controller.sensors.eRUpos_prev = {} -- vector of previous unit vectors pointing to remote units
controller.sensors.RUomega_ave = {} -- vector of time-averaged angular velocities of remote units
controller.oldFscmagn = 0.0
controller.oldp = Vector.new({0,0,0})
controller.Ftot = Vector.new({0,0,0})
controller.sc_ext_force = Vector.new({0,0,0}) -- solar wind force vector exerted on spacecraft itself
controller.masterthrottle = 0.0
--controller.asc = Vector.new({0,0,0})
statistics.sumFmain = 0.0
statistics.maxFmain = 0.0
statistics.sumFaux = 0.0
statistics.maxFaux = 0.0
statistics.cumsumFmain = 0.0
statistics.cummaxFmain = 0.0
statistics.cumsumFaux = 0.0
statistics.cummaxFaux = 0.0
statistics.cnt = 0
statistics.cntaux = 0
statistics.cumcnt = 0
statistics.cumcntaux = 0
statistics.thrust_vector = Vector.new({0,0,0})
if spacecraft.radius==0 and write_attitude_file then
   print("- Setting write_attitude_file=false because spacecraft is pointmass")
   write_attitude_file = false
end
if spacecraft.radius==0 and spacecraft.have_damper then
   print("- Setting spacecraft.have_damper=false because spacecraft is pointmass")
   spacecraft.have_damper = false
end
if not spacecraft.have_damper and spacecraft.damper.deltar~=0 then
   print("- Setting spacecraft.damper.deltar=0 because spacecraft.have_damper=false")
   spacecraft.damper.deltar = 0.0
end
---
function CheckNum(x) -- check that x is a number and return it
   if (type(x) ~= "number") then
      print(debug.traceback("*** CheckNum: table value is not numeric",2))
      error("")
   end
   return x
end
---
gaussrand_is_saved = false
function gaussrand()
-- Generate a Gaussian deviate with zero mean and unit
-- standard deviation.
-- Algorithm: Generate random pairs (x,y) from unit square
-- -1 <= x <= 1, -1 <= y <= 1 until (x,y) is within
-- the unit circle. Compute fac = sqrt(-2.0*log(r2)/r2),
-- where r2 = x^2 + y^2. Then, x*fac and y*fac are two Gaussian
-- random numbers.
   local result,fac,x,y,r2
   if (gaussrand_is_saved) then
      result = gaussrand_saved
      gaussrand_is_saved = false
   else
      repeat
         x = 2*math.random() - 1
         y = 2*math.random() - 1
         r2 = x^2 + y^2
      until r2 < 1.0
      -- On average, this do loop is executed 4/pi = 1.27324 times
      fac = math.sqrt(-2.0*math.log(r2)/r2)
      result = x*fac
      gaussrand_saved = y*fac
      gaussrand_is_saved = true
   end
   return result
end
---
function gaussrand3()
   return Vector.new({gaussrand(),gaussrand(),gaussrand()})
end
---
function KthTetherPointMass(k)
   local s = k/(Np+1)
   local m1
   if tether.use_nonuniform_points then
      m1 = 2*s*tether.m1
      s = s^2
   else
      m1 = tether.m1
   end
   return s,m1
end
---
if Npaux == 1 then
   rumid.r =
      (spacecraft.radius+spacecraft.damper.deltar+tether.len)*
      (math.cos(math.pi/Nw)+math.sin(math.pi/Nw)*math.tan(tether.auxangle))
else
   rumid.r = spacecraft.radius+spacecraft.damper.deltar+tether.len
end
controller.scal = 1.0
controller.scal_overall = 0.0
controller.watermillmode = false -- false initially, is set to true by controller after 6h, if spinup_mode is true
local omegamagn = math.sqrt(
   tether.wanted_tension/
      ((math.max(ru.mass_even,
                 ru.mass_odd)
```

```lua
                +0.5*tether.lambda*tether.len)*(spacecraft.radius+spacecraft.damper.deltar+tether.len)
        + Npaux*rumid.mass*rumid.r))
local spinperiod = 2*math.pi/omegamagn
print(string.format("spinperiod               = %g s",spinperiod))
print(string.format("rumid.mass               = %g g",1e3*rumid.mass))
print(string.format("ru.mass_even             = %g g",1e3*ru.mass_even))
print(string.format("rumid.r                  = %g m",rumid.r))
print(string.format("controller.scaler_modcnt = %d",controller.scaler_modcnt))
local omega = Vector.new({0,0,omegamagn})
tether.springconst = tether.Young*tether.area/tether.len
vesSetParams(
    {eps_rel=1e-5,eps_abs=1e-6,rcamera=(spinup_mode and 180 or 18)*tether.len,
     dt=CheckNum(dt),skip_zeroforcedrawings=true})
vesSetWindowTitle(" 'TI' electric auxtether model ")
if spacecraft.radius > 0 then
    Spacecraft = vesCreateBody(
        "cylinder",
        {mass=CheckNum(spacecraft.mass),radius=CheckNum(spacecraft.radius),
         height=CheckNum(spacecraft.height),omega=omega})
else
    Spacecraft = vesCreateBody(
        "pointmass",
        {mass=CheckNum(spacecraft.mass)})
end
pullpoint = {}; RU = {}; Tether = {}; TetherSparams = {}
tether.m1 = Np > 0 and tether.lambda*tether.len/Np or 0
statistics.totalmass = spacecraft.mass+Nw*(0.5*(ru.mass_even+ru.mass_odd)+Npaux*rumid.mass+Np*tether.m1)
for j=1,Nw do
    local phi = (j-1)*2*math.pi/Nw
    local e_r = Vector.new({math.cos(phi),math.sin(phi),0})
    if spacecraft.have_damper then
        local rp = (spacecraft.radius+spacecraft.damper.deltar)*e_r --pullpoint radius vector
        pullpoint[j] = vesCreateBody(
            "pointmass",
            {mass=CheckNum(spacecraft.damper.mass),
             rCM=rp,v=CrossProduct(omega,rp)})
        vesDefineInteractionForce(
            Spacecraft,pullpoint[j],
            spacecraft.radius*e_r,{0,0,0},
            {springconst=CheckNum(spacecraft.damper.springconst1),r0=CheckNum(spacecraft.damper.deltar)})
        vesDefineInteractionForce(
            Spacecraft,pullpoint[j],
            rp,{0,0,0},
            {springconst=CheckNum(spacecraft.damper.springconst2),dampconst=CheckNum(spacecraft.damper.dampconst)})
    end
    local r = (spacecraft.radius+spacecraft.damper.deltar+tether.len)*e_r -- RU radius vector
    RU[j] = vesCreateBody(
        "pointmass",
        {mass=CheckNum((j==1 and have_one_lightru) and ru.lighter_mass or (j%2==0 and ru.mass_even or ru.mass_odd)),
         rCM=r,v=CrossProduct(omega,r)})
    controller.sensors.eRUpos_prev[j] = e_r
    controller.sensors.RUomega_ave[j] = omega
    if Np>0 then
        Tether[j] = {}
        TetherSparams[j] = {}
        Tether[j].forces = {}
        local svec = {}
        for k=1,Np do
            local s,m1 = KthTetherPointMass(k)
            local r1 = (1-s)*(spacecraft.radius+spacecraft.damper.deltar)*e_r+s*r
            Tether[j][k] = vesCreateBody("pointmass",{mass=CheckNum(m1),rCM=r1,v=CrossProduct(omega,r1)})
            TetherSparams[j][k] = s
        end
--      local L1 = tether.len/(Np+1)
        local L1 = tether.len*TetherSparams[j][1]
        local opts = {
            r0=L1,
            r0dot=tether.deployment_speed*(L1/tether.len),
            springconst=tether.Young*tether.area/L1,
            rel_lossmodulus=CheckNum(tether.rel_lossmodulus)}
        if spacecraft.have_damper then
            Tether[j].forces[1] =
                vesDefineInteractionForce(pullpoint[j],Tether[j][1],{0,0,0},{0,0,0},opts)
        else
            Tether[j].forces[1] =
                vesDefineInteractionForce(Spacecraft,Tether[j][1],spacecraft.radius*e_r,{0,0,0},opts)
        end
        for k=1,Np-1 do
            local L1 = tether.len*(TetherSparams[j][k+1]-TetherSparams[j][k])
            local opts = {
                r0=L1,
                r0dot=tether.deployment_speed*(L1/tether.len),
                springconst=tether.Young*tether.area/L1,
                rel_lossmodulus=CheckNum(tether.rel_lossmodulus)}
            Tether[j].forces[k+1] = vesDefineInteractionForce(Tether[j][k],Tether[j][k+1],{0,0,0},{0,0,0},opts)
        end
        L1 = tether.len*(1-TetherSparams[j][Np])
        opts = {
            r0=L1,
            r0dot=tether.deployment_speed*(L1/tether.len),
            springconst=tether.Young*tether.area/L1,
            rel_lossmodulus=CheckNum(tether.rel_lossmodulus)}
        Tether[j].forces[Np+1] = vesDefineInteractionForce(Tether[j][Np],RU[j],{0,0,0},{0,0,0},opts)
    else
        if spacecraft.have_damper then
            Tether[j] = vesDefineInteractionForce(
                pullpoint[j],RU[j],{0,0,0},{0,0,0},
                {r0=CheckNum(tether.len),
                 r0dot=tether.deployment_speed,
                 springconst=CheckNum(tether.springconst),rel_lossmodulus=CheckNum(tether.rel_lossmodulus)})
        else
            Tether[j] = vesDefineInteractionForce(
                Spacecraft,RU[j],spacecraft.radius*e_r,{0,0,0},
```

```lua
                {r0=CheckNum(tether.len),
                 r0dot=tether.deployment_speed,
                 springconst=CheckNum(tether.springconst),rel_lossmodulus=CheckNum(tether.rel_lossmodulus)})
        end
    end
end
if have_tether_repulsion and Np>0 then
    -- add mutual Coulomb repulsion for first gridpoints of tethers
    local tether_firstlen = tether.len*TetherSparams[1][1]
    repulsion.r0 = repulsion.r0rel*tether_firstlen*(2*math.pi/Nw) -- electron sheath radius (m)
    print(string.format("repulsion.r0 = %g m",repulsion.r0))
    local dFdz = 2*math.pi*epsilon0*repulsion.V0^2/(math.log(repulsion.r0/repulsion.rwstar)^2*(repulsion.r0/2))
    for j=1,Nw do
        local jnext = j<Nw and j+1 or 1
        for k=1,1 do
            vesDefineInteractionForce(
                Tether[j][k],Tether[jnext][k],{0,0,0},{0,0,0},
                {springconst=-dFdz*tether_firstlen,r0=-repulsion.r0,rel_lossmodulus=-repulsion.rel_lossmodulus})
            -- Negative springconst and negative r0 give repulsive potential which is zero outside |r0|
            -- and grows linearly inward, reaching maximum value |r0|*springconst when r=0.
            -- rel_lossmodulus also must be given as a negative number in this case.
        end
    end
end
-- add auxtethers, modelled by RUmid objects:
RUmid = {}; Auxtether = {}
for j=1,Nw do
    local jnext = j<Nw and j+1 or 1
    local dphi = 2*math.pi/Nw
    RUmid[j] = {}
    Auxtether[j] = {}
    local L = (2/(Npaux+1))*(
        spacecraft.radius+spacecraft.damper.deltar+tether.len)*math.sin(dphi/2)/math.cos(tether.auxangle)
    tether.auxlen_init = L
    local r0dot_aux = tether.aux_rellengthen*L/tether.aux_rellengthen_time
    local opts = {
        r0=L,
        r0dot=tether.deployment_speed*(L/tether.len)+r0dot_aux,
        springconst=tether.Young*tether.area/L,
        rel_lossmodulus=CheckNum(tether.rel_lossmodulus)}
    for k=1,Npaux do
        local phi = (j-1+k/(Npaux+1))*dphi
        local e_r = Vector.new({math.cos(phi),math.sin(phi),0})
        local r = rumid.r*e_r
        RUmid[j][k] = vesCreateBody("pointmass",{mass=CheckNum(rumid.mass),rCM=r,v=CrossProduct(omega,r)})
        local prev = k==1 and RU[j] or RUmid[j][k-1]
        Auxtether[j][k] = vesDefineInteractionForce(prev,RUmid[j][k],{0,0,0},{0,0,0},opts)
    end
    Auxtether[j][Npaux+1] = vesDefineInteractionForce(RUmid[j][Npaux],RU[jnext],{0,0,0},{0,0,0},opts)
end
cnt = 0
statecnt = 0
dvold = {0,0,0}
told = -1
if interactive_mode then
    print("Keys:")
    print("   J and K to decrease/increase theta,")
    print("   U and I to decrease/increase phi,")
    print("   N and M to decrease/increase spinrate")
end
if write_throttle_file then
    fp = io.open("throttle.dat","w")
end
if write_tensions_file then
    fptens = io.open("tensions.dat","w")
    fptens:write("# t(s)  truethrustvector(N)   |thrust| thrust_SCspinaxis   maxtensMain maxtensAux avetensMain avete
nsAux (all cN)  voltage(V) origvoltage(V)\n")
end
if write_attitude_file then
    fpatt = io.open("attitude.dat","w")
    fpatt:write("# t(s) qs qx qy qz")
    if write_RUdiff_data then
        fpatt:write("  |RU2-RU1|")
    end
    fpatt:write("\n")
end
if write_info_file then
    fpinfo = io.open("info.dat","w")
    fpinfo:write("# t(s)  theta thetagoal  phi phigoal  spin spingoal [angles in deg, spin in percent]\n")
end
---
function FormatTime(t)
    local d = math.floor(t/(24*3600))
    local t1 = t - d*(24*3600)
    local h = math.floor(t1/3600)
    local t2 = t1 - h*3600
    local m = math.floor(t2/60)
    local t3 = t2 - m*60
    local s = string.format("%dd %.2d:%.2d:%.2d",d,h,m,math.floor(t3))
    return s
end
---
function Norm(x)
    return math.sqrt(DotProduct(x,x))
end
---
function Round(x)
    return math.floor(x+0.5)
end
---
function Clamp(x,a,b)
    return math.max(math.min(x,b),a)
end
```

```lua
---
function controller.sensors.GetRUPositionsAndVelocities(dt)
   -- Simulates continuous imaging detection of remote units.
   -- Returns remote unit positions and velocities relative to main spacecraft.
   -- Input dt is the timestep at which the function is called.
   -- It must be the same in all calls.
   local dataSC = vesGetBodyData(Spacecraft)
   local rSC = Vector.new({dataSC.x,dataSC.y,dataSC.z})
   local vSC = Vector.new({dataSC.vx,dataSC.vy,dataSC.vz})
   local rRU={}; local vRU={}
   local mixer = math.min(1.0,dt/controller.sensors.RUvelocity_timescale)
   for j=1,Nw do
      local data = vesGetBodyData(RU[j])
      local r = Vector.new({data.x,data.y,data.z})
      local e_r =
         Normalise(Normalise(r-rSC) + controller.sensors.RUangle_error*gaussrand3())
      local omega_inst = CrossProduct(controller.sensors.eRUpos_prev[j],e_r)/dt
      controller.sensors.eRUpos_prev[j] = e_r
      controller.sensors.RUomega_ave[j] = (1-mixer)*controller.sensors.RUomega_ave[j] + mixer*omega_inst
      rRU[j] = tether.len*e_r
      vRU[j] = CrossProduct(controller.sensors.RUomega_ave[j],rRU[j])
   end
   return rRU,vRU
end
---
function controller.sensors.GetAcceleration()
   -- Returns vector acceleration experienced by the main spacecraft.
   -- In real world, this function would read an onboard accelerometer.
   -- Here we simulate it by calculating the sum of forces
   -- exerted by the tethers on the main spacecraft.
   local F = Vector.new({0,0,0})
   local dataSC = vesGetBodyData(Spacecraft)
   local rSC = Vector.new({dataSC.x,dataSC.y,dataSC.z})
   for j=1,Nw do
      local F1magn = vesGetForceValue(Np==0 and Tether[j] or Tether[j].forces[1])
      local obj = Np==0 and RU[j] or Tether[j][1]
      local data = vesGetBodyData(obj)
      local u = Normalise(Vector.new({data.x,data.y,data.z})-rSC)
      local F1 = F1magn*u
      F = F + F1
   end
   F = F + controller.sc_ext_force
   -- controller.sc_ext_force is the part of E-sail force exerted directly on main spacecraft
   return (1/spacecraft.mass)*F + controller.sensors.accelerometer_error*gaussrand3()
end
---
function controller.ApproximateAngularMomentum(rRU,vRU)
   -- Returns approximate angular momentum of the spacecraft plus tether rig as 3-vector.
   -- The angular momentum is calculated with respect to the centre of mass.
   -- rRU,vRU must be positions and velocities of remote units, relative to spacecraft.
   -- The result is approximate because rumid and tether contributions are estimated
   -- from remote unit locations and velocities.
   -- (1) calculate centre of mass rCM and centre of mass velocity vCM
   local mr=Vector.new({0,0,0}); local mv=Vector.new({0,0,0})
   local meff_odd =  ru.mass_odd  + Npaux*rumid.mass + 0.5*tether.lambda*tether.len
   local meff_even = ru.mass_even + Npaux*rumid.mass + 0.5*tether.lambda*tether.len
   for j=1,Nw do
      local rumass = j%2==0 and meff_even or meff_odd
      mr = mr + rumass*rRU[j]
      mv = mv + rumass*vRU[j]
   end
   local m = spacecraft.mass + Nw*(0.5*(ru.mass_even+ru.mass_odd) + Npaux*rumid.mass + tether.lambda*tether.len)
   local rCM = mr/m -- position of centre of mass
   local vCM = mv/m -- velocity of centre of mass
   -- (2) calculate angular momentum relative to rCM and vCM
   L = spacecraft.mass*CrossProduct(-rCM,-vCM) -- main spacecraft's contribution
   local meff_odd_for_L  = ru.mass_odd  + Npaux*rumid.mass + tether.lambda*tether.len/3.0
   local meff_even_for_L = ru.mass_even + Npaux*rumid.mass + tether.lambda*tether.len/3.0
   for j=1,Nw do
      local rumass = j%2==0 and meff_even_for_L or meff_odd_for_L
      L = L + rumass*CrossProduct(rRU[j]-rCM,vRU[j]-vCM)
   end
   return L
end
---
function controller.ExactAngularMomentum(dum1,dum2)
   -- Returns exact angular momentum of the spacecraft plus tether rig as a 3-vector.
   -- Dummy input arguments so that call form is identical with ApproximateAngularMomentum().
   --
   -- (1) take data to local arrays
   local dataSC = vesGetBodyData(Spacecraft)
   local rSC = Vector.new({dataSC.x,dataSC.y,dataSC.z})
   local vSC = Vector.new({dataSC.vx,dataSC.vy,dataSC.vz})
   local rRU = {}; local vRU = {}; local rRUmid = {}; local vRUmid = {}
   for j=1,Nw do
      local data = vesGetBodyData(RU[j])
      rRU[j] = Vector.new({data.x,data.y,data.z})
      vRU[j] = Vector.new({data.vx,data.vy,data.vz})
      rRUmid[j] = {}; vRUmid[j] = {}
      for k=1,Npaux do
         local data = vesGetBodyData(RUmid[j])
         rRUmid[j][k] = Vector.new({data.x,data.y,data.z})
         vRUmid[j][k] = Vector.new({data.vx,data.vy,data.vz})
      end
   end
   local rTether = {}; local vTether = {}
   if Np>0 then
      for j=1,Nw do
         rTether[j] = {}; vTether[j] = {}
         for k=1,Np do
            local data = vesGetBodyData(Tether[j][k])
            rTether[j][k] = Vector.new({data.x,data.y,data.z})
            vTether[j][k] = Vector.new({data.vx,data.vy,data.vz})
```

```lua
            end
         end
      end
      -- (2) calculate centre of mass rCM and centre of mass velocity vCM
      -- NOTE:
      -- The quantities rCM and vCM are in fact zero, because it is enforced by vesvision.
      -- However, in case we ever include any detached or ejected objects in the system,
      -- this assumption would silently fail (and fail miserably).
      -- Therefore we calculate rCM and vCM explicitly even though it takes a bit of CPU time.
      local mr = spacecraft.mass*rSC
      local mv = spacecraft.mass*vSC
      local m = spacecraft.mass
      for j=1,Nw do
         local rumass = j%2==0 and ru.mass_even or ru.mass_odd
         mr = mr + rumass*rRU[j]
         mv = mv + rumass*vRU[j]
         for k=1,Npaux do
            mr = mr + rumid.mass*rRUmid[j][k]
            mv = mv + rumid.mass*vRUmid[j][k]
         end
      end
      m = m + Nw*(0.5*(ru.mass_even+ru.mass_odd)+Npaux*rumid.mass)
      if Np>0 then
         for j=1,Nw do
            for k=1,Np do
               mr = mr + tether.ml*rTether[j][k]
               mv = mv + tether.ml*vTether[j][k]
            end
         end
         m = m + Nw*Np*tether.ml
      end
      local rCM = mr/m -- position of centre of mass
      local vCM = mv/m -- velocity of centre of mass
      -- (3) calculate angular momentum relative to rCM and vCM
      L = spacecraft.mass*CrossProduct(rSC-rCM,vSC-vCM)
      for j=1,Nw do
         local rumass = j%2==0 and ru.mass_even or ru.mass_odd
         L = L + rumass*CrossProduct(rRU[j]-rCM,vRU[j]-vCM)
         for k=1,Npaux do
            L = L + rumid.mass*CrossProduct(rRUmid[j][k]-rCM,vRUmid[j][k]-vCM)
         end
      end
      if Np > 0 then
         for j=1,Nw do
            for k=1,Np do
               L = L + tether.ml*CrossProduct(rTether[j][k]-rCM,vTether[j][k]-vCM)
            end
         end
      end
      -- (4) return result
      return L
end
---
local rRU,vRU = controller.sensors.GetRUPositionsAndVelocities(dt)
controller.AngularMomentum =
   controller.use_approximate_angular_momentum
   and controller.ApproximateAngularMomentum
   or controller.ExactAngularMomentum
local L0 = controller.AngularMomentum(rRU,vRU) -- L0 is initial angular momentum vector
controller.L0magn = math.sqrt(DotProduct(L0,L0)) -- L0magn=|L0|
controller.Lrel = Normalise(L0)
---
function controller.AveRUSpeeds(n,rRU,vRU)
   -- Returns two quantities:
   -- (1) average velocity of all remote units along unit vector n
   -- (2) average total speed of remote units relative to spacecraft
   -- Inputs:
   -- n is spin axis unit vector, sign convenction such that n.nSW<0 (i.e. n points sunward, not antisunward)
   -- rRU,vRU are remote unit positions and velocities (Nw-vectors of 3-vectors), relative to main spacecraft
   local vs, vtot = 0.0, 0.0
   for j=1,Nw do
      local v = vRU[j]
      vs = vs + DotProduct(v,n)
      vtot = vtot + Norm(v)
   end
   vs = vs/Nw
   vtot = vtot/Nw
   return vs,vtot
end
---
function controller.MeanRUAngle(n,rRU)
   -- n is angular momentum aligned unit vector, positive sunward
   -- rRU is array of remote unit positions, relative to main spacecraft
   local alpha = 0.0
   for j=1,Nw do
      local r = math.sqrt(DotProduct(rRU[j],rRU[j]))
      local z = -DotProduct(rRU[j],n)  -- minus, so that z is positive in normal case of hanging rig
      local alpha1 = math.asin(z/r)
      alpha = alpha + alpha1
   end
   alpha = alpha/Nw
   return alpha
end
---
function controller.func(nSW,t,dt)
   -- Returns three quantities:
   -- (1) throttle vector (0..1)
   -- (2) Lrel 3-vector (angular momentum normalised to initial angular momentum)
   -- (3) ngoal (goal orientation of spin axis, unit 3-vector)
   -- Inputs: nSW is unit vector along nominal solar wind, t is time, dt is timestep how often called
   if not interactive_mode then
      controller.theta_goal_deg = spinup_mode and 60 or 35.0 -- wanted theta angle
--    controller.phi_goal_deg = spinup_mode and 90 or (t<=12*3600 and 90 or 270)   -- wanted phi angle
```

```lua
        controller.phi_goal_deg = 90.0
        controller.spin_goal = spinup_mode and 1e30 or 100 -- wanted spin rate, 100 is initial spinrate
        controller.watermillmode = spinup_mode and t>6*3600
    end
    local theta_goal = math.rad(controller.theta_goal_deg)
    local phi_goal = math.rad(controller.phi_goal_deg)
    local ngoal = Vector.new( -- goal orientation of spin axis
        {math.sin(theta_goal)*math.cos(phi_goal),
         math.sin(theta_goal)*math.sin(phi_goal),
         math.cos(theta_goal)})
    local rRU,vRU = controller.sensors.GetRUPositionsAndVelocities(dt)
    local Lrel = controller.AngularMomentum(rRU,vRU)/controller.L0magn
    if controller.use_angular_momentum_time_averaging then
        local mixer = math.min(1.0,dt/controller.angular_momentum_time_averaging_tau)
        controller.Lrel = (1-mixer)*controller.Lrel + mixer*Lrel
    else
        controller.Lrel = Lrel
    end
    local n = Normalise(controller.Lrel) -- unit vector along angular momentum
    local throttle = {}
    if controller.watermillmode then
        -- watermillmode: put voltage to max in all tethers moving downstream and to zero in those moving upstream
        for j=1,Nw do
            throttle[j] = DotProduct(vRU[j],nSW)>0 and 1.0 or 0.0
        end
    else
        -- normal case, no watermillmode
        local maxval = 0.0
        local spinrate_increase = controller.greediness_spinrate*(controller.spin_goal*0.01-Norm(controller.Lrel))
        local auxfract = 1/(1+Nw/(2*math.pi))
        local znew = Normalise(controller.Lrel)
        local znew_cross_nSW = CrossProduct(znew,nSW)
        local xnew = Normalise(znew_cross_nSW)
        local ynew = CrossProduct(znew,xnew)
        local tiltfact = Norm(znew_cross_nSW)
        local sharpfact = math.min(0.8,controller.sharp_ampl*tiltfact)
        for j=1,Nw do
            local r = rRU[j]  -- position of remote unit relative to spacecraft
            local v = vRU[j]  -- velocity of remote unit relative to spacecraft
            local e_r = Normalise(r) -- unit vector along position of remote unit
            local keeperfactor = 1/Norm(nSW-e_r*DotProduct(e_r,nSW))^2
            local X = DotProduct(e_r,xnew)
            local Y = DotProduct(e_r,ynew)
            local cos2phi = X^2-Y^2
            local throt = math.max(
                0.0,
                1.0 - sharpfact*cos2phi
                    - controller.greediness_tilt*DotProduct(e_r,CrossProduct(n,ngoal)))
            throt = throt*((1-auxfract)*keeperfactor + auxfract)
            throt = throt*(1 - Clamp(spinrate_increase*(j%2==0 and 1 or -1)*DotProduct(Normalise(v),nSW),
                                    -controller.maxallow_sawtooth,controller.maxallow_sawtooth))
            maxval = math.max(maxval,throt)
            throttle[j] = throt
        end
        for j=1,Nw do -- enforce maximum throttle[j] to be 1.0
            throttle[j] = throttle[j]/maxval
        end
        --
        if cnt % controller.scaler_modcnt == 0 then
            local mixer = math.min(1,(controller.scaler_modcnt*dt)/controller.scaler_tau)
            local nsunward = DotProduct(n,nSW)<=0 and n or -n
            local vRUsunward,vRUtotal = controller.AveRUSpeeds(nsunward,rRU,vRU)
            controller.scal = 1+math.min(0.0,controller.greediness_damper*vRUsunward/vRUtotal)
            local asc -- spacecraft acceleration vector
            if controller.have_accelerometer then
                asc = controller.sensors.GetAcceleration()
--              local alpha = controller.MeanRUAngle(nsunward,rRU)
--              local F1magn = 1.7*(Nw*tether.wanted_tension)*math.tan(alpha)
--              local F1dir = Normalise(-nsunward+nSW)
--              local F1 = F1magn*F1dir
--              local ascl = F1/(spacecraft.mass+0.5*Nw*tether.len*tether.lambda)
--              if cnt % 100 == 0 then
--                  print(string.format("ACC %g %g",Norm(ascl)/Norm(asc),math.deg(math.acos(DotProduct(F1dir,Normalise(
asc))))))
--              end
            else
                local alpha = controller.MeanRUAngle(nsunward,rRU)
                local F1magn = 1.7*(Nw*tether.wanted_tension)*math.tan(alpha)
                local F1dir = Normalise(-nsunward+nSW)
                local F1 = F1magn*F1dir
                asc = F1/(spacecraft.mass+0.5*Nw*tether.len*tether.lambda)
            end
            local Fsc = (spacecraft.mass+0.5*Nw*tether.len*tether.lambda)*asc -- F=m*a, thrust from acceleration
            local Fscmagn = math.sqrt(DotProduct(Fsc,Fsc)) -- thrust magnitude
            local F0 = Nw*tether.wanted_tension -- summed tension of all tethers, used for normalisation
            local s = -- throttling factor (0<s<=1) because of increasing thrust
                1-Clamp(((Fscmagn-controller.oldFscmagn)/F0)*(controller.fastdamp_tau/(controller.scaler_modcnt*dt)),
                        0,controller.fastdamp_max)
            controller.scal = controller.scal*s -- apply throttling due to increasing thrust, if any
            controller.oldFscmagn = Fscmagn
            --
            local p = Vector.new({0,0,0}) -- p becomes the momentum vector of tether rig
            for j=1,Nw do
                p = p + vRU[j]
            end
            local ml = 0.5*(ru.mass_even+ru.mass_odd)+Npaux*rumid.mass+0.5*tether.len*tether.lambda
            p = ml*p -- now p is ready
            local Frig = (p-controller.oldp)/(controller.scaler_modcnt*dt) + Nw*ml*asc -- thrust on rig
            controller.oldp = p
            controller.Ftot = (1-mixer)*controller.Ftot + mixer*(Fsc+Frig)
            local Ftotmagn = math.sqrt(DotProduct(controller.Ftot,controller.Ftot))
            -- d(overall)/dt = (1/tau)*(wanted_thrust-F)/wanted_thrust
            -- overall = overall_old + (dt/tau)*(wanted_thrust-F)/wanted_thrust
```

```lua
        local wantedthrust = controller.masterthrottle*controller.wanted_thrust
        controller.scal_overall =
            Clamp(
                controller.scal_overall + mixer*(wantedthrust-Ftotmagn)/(wantedthrust+1e-16),
                0,controller.maxoverallfactor)
        controller.scal = controller.scal*math.min(1,controller.scal_overall)
      end
      for j=1,Nw do -- notice: must do this every timestep even if scaler_modcnt>1
        throttle[j] = controller.scal*throttle[j]
      end
    end
  end
  return throttle,controller.Lrel,ngoal
end
---
function RotateXZ(u,alpha)
  -- rotate vector u by angle alpha (rad) in XZ-plane, that is, around Y-axis
  return Vector.new(
      {math.cos(alpha)*u[1] - math.sin(alpha)*u[3],
       u[2],
       math.sin(alpha)*u[1] + math.cos(alpha)*u[3]})
end
---
function GetAttitudeFromData(data)
  -- return triple of unit vectors e1,e2,e3 defining attitude of body
  -- data must have been obtained by vesGetBodyData(body)
  -- e1 is unit vector along x, etc.
  local s = data.qs
  local vx = data.qx
  local vy = data.qy
  local vz = data.qz
  local norm = 1/(math.sqrt(s^2 + vx^2 + vy^2 + vz^2) + 1e-16)
  s = s*norm
  vx = vx*norm
  vy = vy*norm
  vz = vz*norm
  local col1 = Vector.new({1-2*(vy^2+vz^2), 2*(vx*vy+s*vz),  2*(vx*vz-s*vy)})
  local col2 = Vector.new({2*(vx*vy-s*vz),  1-2*(vx^2+vz^2), 2*(vy*vz+s*vx)})
  local col3 = Vector.new({2*(vx*vz+s*vy),  2*(vy*vz-s*vx),  1-2*(vx^2+vy^2)})
  return col1,col2,col3
end
---
function RUMisalignmentDiagnostics(dataSC,t)
  -- how much remote unit actual directions differ from directions
  -- deduced from main spacecraft orientation
  local e1,e2,e3 = GetAttitudeFromData(dataSC)
  local rSC = Vector.new({dataSC.x,dataSC.y,dataSC.z})
  local zave,phiave=0,0
  local zmax,phimax=0,0
  for j=1,Nw do
      local phi = (j-1)*2*math.pi/Nw
      local e_r = math.cos(phi)*e1 + math.sin(phi)*e2
      local dataRU = vesGetBodyData(RU[j])
      local rRU = Vector.new({dataRU.x,dataRU.y,dataRU.z})
      local e_r_RU = Normalise(rRU-rSC)
      local anglediff_z = math.asin(math.abs(DotProduct(e_r_RU,e3)))
      local e_proj = Normalise(e_r_RU-e3*DotProduct(e3,e_r_RU))
      local anglediff_phi = math.acos(DotProduct(e_proj,e_r))
      zave = zave + anglediff_z
      phiave = phiave + anglediff_phi
      zmax = math.max(zmax,anglediff_z)
      phimax = math.max(phimax,anglediff_phi)
  end
  zave = zave/Nw
  phiave = phiave/Nw
  print(string.format(
          "%s RU orient diff %1.3g/%1.3g deg Phi, %1.3g/%1.3g deg Z",
          FormatTime(t),math.deg(phiave),math.deg(phimax),math.deg(zave),math.deg(zmax)))
end
---
function vesPeriodicTask(t)
  if t > tmax and not interactive_mode then
      os.exit()
  end
  local u   -- unit vector along real solar wind
  local dFdz0 -- base value of E-sail force per unit length (dF/dz) in current solar wind
  local V   -- voltage
  local sw_tilt = 0 --wanted solar wind tilt angle
  local unominal = RotateXZ(Vector.new({0,0,-1}),sw_tilt)
  local throttle,Lrel,ngoal = controller.func(unominal,t,dt)
  local n,v -- solar wind density (m-3) and velocity vector (m/s)
  if use_real_solar_wind then
     n,v = vesGetSolarWind(t) -- gives n in 1/m^3, v vector in m/s
     vesSolarWindGraph(t)
  else
     n = SWn0
     v = SWv0*Vector.new({-1,0,0})
  end
  local rho = mproton*n
  local v2 = DotProduct(v,v)
  local Pdyn = rho*v2
  -- P=n0*Vbase^(3/2)=n*V^(3/2) ==> V=Vbase*(n/n0)^(-2/3)
  V = math.min(Vmax,Vbase*(n/SWn0)^(-2/3))
  Vorig = V
  local V1 = 0.5*mproton*v2/echarge
  dFdz0 = thrustcoeff*(1/r_au)*math.max(0,V-V1)*math.sqrt(epsilon0*Pdyn)
  v = Normalise(v)
  u = RotateXZ(Vector.new({v[2],v[3],v[1]}),sw_tilt)
  --
  local maxthrottle = 0.0
  for j=1,Nw do
     maxthrottle = math.max(maxthrottle,throttle[j])
  end
  dFdz0 = dFdz0*maxthrottle
```

```lua
if maxthrottle > 0 then
    for j=1,Nw do
        throttle[j] = throttle[j]/maxthrottle
    end
end
V = V1 + dFdz0/(thrustcoeff*(1/r_au)*math.sqrt(epsilon0*Pdyn))
--
local dataSC = vesGetBodyData(Spacecraft)
local rSC = Vector.new({dataSC.x,dataSC.y,dataSC.z})
controller.masterthrottle = 1-math.exp(-t/(4*3600.0))
-- zero forces:
vesSetExternalForce(Spacecraft,{0,0,0})
controller.sc_ext_force = Vector.new({0,0,0})
for j=1,Nw do
    vesSetExternalForce(RU[j],{0,0,0})
    for k=1,Npaux do
        vesSetExternalForce(RUmid[j][k],{0,0,0})
    end
    if Np>0 then
        for k=1,Np do
            vesSetExternalForce(Tether[j][k],{0,0,0})
        end
    end
end
-- increment forces after zeroing:
for j=1,Nw do
    local dataRU = vesGetBodyData(RU[j])
    local rRU = Vector.new({dataRU.x,dataRU.y,dataRU.z})
    if Np>0 then
        local F = {}
        for k=1,Np+1 do
            local prev = k==1 and Spacecraft or Tether[j][k-1]
            local curr = k<=Np and Tether[j][k] or RU[j]
            local dataprev = vesGetBodyData(prev)
            local datacurr = vesGetBodyData(curr)
            local r = Vector.new({datacurr.x,datacurr.y,datacurr.z})
            local rprev = Vector.new({dataprev.x,dataprev.y,dataprev.z})
            local dr = r-rprev;
            local drmagn2 = DotProduct(dr,dr)
            local uPerp = u-(DotProduct(u,dr)/drmagn2)*dr
            F[k] = dFdz0*controller.masterthrottle*throttle[j]*math.sqrt(drmagn2)*uPerp
        end
        vesAddExternalForce(Spacecraft,F[1]/2)
        controller.sc_ext_force = controller.sc_ext_force + F[1]/2
        for k=1,Np do
            vesAddExternalForce(Tether[j][k],(F[k]+F[k+1])/2)
        end
        vesAddExternalForce(RU[j],F[Np+1]/2)
    else
        local dr = rRU-rSC
        local drmagn2 = DotProduct(dr,dr)
        local uPerp = u-(DotProduct(u,dr)/drmagn2)*dr
        local F = dFdz0*controller.masterthrottle*throttle[j]*math.sqrt(drmagn2)*uPerp
        vesAddExternalForce(Spacecraft,F/2)
        controller.sc_ext_force = controller.sc_ext_force + F/2
        vesAddExternalForce(RU[j],F/2)
    end
end
if have_electric_auxtethers then
    -- increment forces after zeroing, for electric auxtethers:
    for j=1,Nw do
        local jnext = j<Nw and j+1 or 1
        local data1 = vesGetBodyData(RU[j])
        local data2 = vesGetBodyData(RU[jnext])
        local r1 = Vector.new({data1.x,data1.y,data1.z})
        local r2 = Vector.new({data2.x,data2.y,data2.z})
        local throttle1 = j%2==0 and throttle[j] or throttle[jnext]
        local rmid = {}
        for k=1,Npaux do
            local datamid = vesGetBodyData(RUmid[j][k])
            rmid[k] = Vector.new({datamid.x,datamid.y,datamid.z})
        end
        for k=1,Npaux+1 do
            local rA = k==1 and r1 or rmid[k-1]
            local rB = k==Npaux+1 and r2 or rmid[k]
            local dr = rB-rA
            local drmagn2 = DotProduct(dr,dr)
            local uPerp = u-(DotProduct(u,dr)/drmagn2)*dr
            local Faux1 = dFdz0*controller.masterthrottle*throttle1*math.sqrt(drmagn2)*uPerp
            local objA = k==1 and RU[j] or RUmid[j][k-1]
            local objB = k==Npaux+1 and RU[jnext] or RUmid[j][k]
            vesAddExternalForce(objA,Faux1/2)
            vesAddExternalForce(objB,Faux1/2)
        end
    end
end
-- stop auxtether initial lengthening process
if tether.aux_rellengthen_ongoing and t > tether.aux_rellengthen_time then
    local L = tether.auxlen_init*(1+tether.aux_rellengthen)
    for j=1,Nw do
        for k=1,Npaux+1 do
            vesRedefineInteractionForce(Auxtether[j][k],{r0dot=0,r0=L})
        end
    end
    if tether.aux_rellengthen > 0 then
        print(string.format("%s Auxtether lengthening stopped",FormatTime(t)))
    elseif tether.aux_rellengthen < 0 then
        print(string.format("%s Auxtether shortening stopped",FormatTime(t)))
    end
    tether.aux_rellengthen_ongoing = false
end
-- update tether tension statistics:
if t > 3600 then
```

```lua
      -- find max tether tension for main and auxtethers, exclude first hour which may have unphysical transients
      local sumFmain,sumFaux,maxFmain,maxFaux = 0.0, 0.0, 0.0, 0.0
      for j=1,Nw do
         local Fmain = vesGetForceValue(Np==0 and Tether[j] or Tether[j].forces[1])
         local Faux = 0.0
         for k=1,Npaux+1 do
            local Faux = vesGetForceValue(Auxtether[j][k])
            sumFaux  = sumFaux  + Faux
            maxFaux  = math.max(maxFaux,Faux)
         end
         sumFmain = sumFmain + Fmain
         maxFmain = math.max(maxFmain,Fmain)
      end
      statistics.sumFmain = statistics.sumFmain + sumFmain
      statistics.maxFmain = math.max(statistics.maxFmain,maxFmain)
      statistics.sumFaux = statistics.sumFaux + sumFaux
      statistics.maxFaux = math.max(statistics.maxFaux,maxFaux)
      statistics.cnt = statistics.cnt + Nw
      statistics.cntaux = statistics.cntaux + Nw*(Npaux+1)
      statistics.cumsumFmain = statistics.cumsumFmain + sumFmain
      statistics.cumsumFaux = statistics.cumsumFaux + sumFaux
      statistics.cummaxFmain = math.max(statistics.cummaxFmain,maxFmain)
      statistics.cummaxFaux = math.max(statistics.cummaxFaux,maxFaux)
      statistics.cumcnt = statistics.cumcnt + Nw
      statistics.cumcntaux = statistics.cumcntaux + Nw*(Npaux+1)
   end
   -- print some diagnostic output to stdout:
   if cnt % 900 == 0 then
      local n = Normalise(Lrel)
      print(string.format(
            "%s L=(%g,%g,%g),err=%g, |L|=%g",
            FormatTime(t),Lrel[1],Lrel[2],Lrel[3],Norm(n-ngoal),Norm(Lrel)))
      if write_throttle_file then
         fp:write(string.format("%d",math.floor(t+0.5)))
         for j=1,Nw do
            fp:write(string.format(" %g",throttle[j]))
         end
         fp:write("\n")
         fp:flush()
      end
      local dv = Vector.new(vesGetDeltav())
      local F = statistics.totalmass*(dv-dvold)/(t-told)
      statistics.thrust_vector = F
      local Fmagn = Norm(F)
      local Fpar = DotProduct(F,u)
      local Fperp = F-Fpar*u
      dvold = dv;
      told = t;
      print(string.format(
            "%s %1.4g, %1.4g/%1.4g cN (max %1.4g,%1.4g, ave %1.4g,%1.4g cN)\n|F|=%g mN, |Fperp|=%g mN, %g deg,
V=%1.3g kV",
            FormatTime(t),
            100*vesGetForceValue(Np==0 and Tether[1] or Tether[1].forces[1]),
            100*vesGetForceValue(Auxtether[1][1]),
            100*vesGetForceValue(Auxtether[1][Npaux+1]),
            100*statistics.cummaxFmain,
            100*statistics.cummaxFaux,
            100*(statistics.cumsumFmain/math.max(statistics.cumcnt,1)),
            100*(statistics.cumsumFaux/math.max(statistics.cumcntaux,1)),
            1e3*Fmagn,1e3*Norm(Fperp),math.deg(math.acos(math.abs(Fpar)/Fmagn)),
            V*1e-3))
      if spacecraft.radius > 0 then
         RUMisalignmentDiagnostics(dataSC,t)
      end
   end
   -- update info string:
   if cnt % 10 == 0 then
      local theta = math.deg(math.acos(Lrel[3]/Norm(Lrel)))
      if controller.watermillmode then
         vesSetInfoString(string.format("th=%d,watermill",Round(theta)))
      else
         local thetastr,spinstr
         if Round(theta)==Round(controller.theta_goal_deg) then
            thetastr = string.format("th=%d",Round(theta))
         else
            thetastr = string.format("th%d/%d",Round(theta),Round(controller.theta_goal_deg))
         end
         local spin = 100*Norm(Lrel)
         if Round(spin)==Round(controller.spin_goal) then
            spinstr = string.format("s%d",Round(spin))
         else
            spinstr =
               string.format("s%d/%s",
                             Round(spin),
                             controller.spin_goal>300 and "*" or string.format("%d",Round(controller.spin_goal)))
         end
         vesSetInfoString(
            string.format(
               "%s,ph%d,%s",
               thetastr,Round(controller.phi_goal_deg),spinstr))
         if write_info_file and cnt % 30 == 0 then
            local phi = math.deg(math.atan2(Lrel[2],Lrel[1]))
            fpinfo:write(string.format("%d  %g %g  %g %g  %g %g\n",
                                       math.floor(t+0.5),
                                       theta,controller.theta_goal_deg,
                                       phi,controller.phi_goal_deg,
                                       spin,controller.spin_goal))
         end
      end
   end
   -- write tension file (fptens) if requested:
   if write_tensions_file and cnt % 30 == 0 then
      local F = Vector.new({0,0,0})
```

```
        for j=1,Nw do
            local Flmagn = vesGetForceValue(Np==0 and Tether[j] or Tether[j].forces[1])
            local obj = Np==0 and RU[j] or Tether[j][1]
            local data = vesGetBodyData(obj)
            local u = Normalise(Vector.new({data.x,data.y,data.z})-rSC)
            local Fl = Flmagn*u
            F = F + Fl
        end
        local nSC
        if spacecraft.radius > 0 then
            nSC = Normalise(Vector.new({dataSC.Lx,dataSC.Ly,dataSC.Lz}))
        else
            nSC = Normalise(Lrel)
        end
        fptens:write(
            string.format("%d  %g %g %g  %g %g  %g %g %g %g  %g %g\n",
                          math.floor(t+0.5),
                          statistics.thrust_vector[1],statistics.thrust_vector[2],statistics.thrust_vector[3],
                          100*math.sqrt(DotProduct(F,F)),
                          100*DotProduct(F,nSC),
                          100*statistics.maxFmain,
                          100*statistics.maxFaux,
                          100*(statistics.sumFmain/math.max(statistics.cnt,1)),
                          100*(statistics.sumFaux/math.max(statistics.cntaux,1)),
                          V,Vorig))
        statistics.maxFmain = 0
        statistics.maxFaux = 0
        statistics.sumFmain = 0
        statistics.sumFaux = 0
        statistics.cnt = 0
        statistics.cntaux = 0
    end
    -- write attitude file (fpatt) if requested
    if write_attitude_file then
        fpatt:write(string.format(
                    "%d %g %g %g %g",
                    math.floor(t+0.5),dataSC.qs,dataSC.qx,dataSC.qy,dataSC.qz))
        -- add also |rRU(2)-rRU(1)| in this file, if requested
        if write_RUdiff_data then
            local dataRU1 = vesGetBodyData(RU[1])
            local dataRU2 = vesGetBodyData(RU[2])
            local r1 = Vector.new({dataRU1.x,dataRU1.y,dataRU1.z})
            local r2 = Vector.new({dataRU2.x,dataRU2.y,dataRU2.z})
            fpatt:write(string.format(" %g",Norm(r2-r1)))
        end
        fpatt:write("\n")
    end
    -- write state CDF files if requested:
    if write_state_files and cnt % (24*1800) == 0 then
        local fn = string.format("state%.4d.cdf",statecnt)
        vesDumpState(fn)
        print(string.format("%s dumped state in %s",FormatTime(t),fn))
        statecnt = statecnt + 1
    end
    -- increment global counter:
    cnt = cnt + 1
end
---
if interactive_mode then
    function vesKeypressHandler(key,t)
        if key == "j" then
            controller.theta_goal_deg = math.max(0,controller.theta_goal_deg-5)
            return true
        elseif key == "k" then
            controller.theta_goal_deg = math.min(85,controller.theta_goal_deg+5)
            return true
        elseif key == "u" then
            controller.phi_goal_deg = math.max(0,controller.phi_goal_deg-15)
            return true
        elseif key == "i" then
            controller.phi_goal_deg = math.min(360,controller.phi_goal_deg+15)
            return true
        elseif key == "n" then
            controller.spin_goal = math.max(25,controller.spin_goal-2)
            return true
        elseif key == "m" then
            controller.spin_goal = math.min(400,controller.spin_goal+2)
            return true
        end
        return false
    end
end


-------------------------------------------------
-- Thrust for Nw=20,Np=4,wanted_tension=4cN(*)
--              |F|    F_perp
-------------------------------
-- theta=0      1.30   0
-- theta=5      1.28   0.057
-- theta=10     1.25   0.107
-- theta=15     1.20   0.155
-- theta=20     1.13   0.196
-- theta=25     1.05   0.225
-- theta=30     0.977  0.244
-- theta=35     0.889  0.254    <-- max F_perp
-- theta=40     0.800  0.253
-- theta=45     0.70   0.240
-- theta=50     0.60   0.223
-- theta=55     0.50   0.194
-- theta=60     0.41   0.161
-- theta=65     0.31   0.13
-- (*) Normalised to theta=0 thrust at high spin
--     without auxtether thrust contribution.
```

143

```
    -------------------------------------------------
    -- 10-day runs, with nSW=unominal (not u):
    -- exactL                        5.255 cN
    -- exactL,RU-err                 5.444 cN
    -- exactL,acc.err                5.185 cN
    -- exactL,RU-err,acc.err         5.204 cN
    -- exactL-3RU-err                5.116 cN
    -- exactL-3acc-err               5.348 cN
    -- exactL-3RU-err,3accerr        5.059 cN
    -- approxL                       7.433 cN
    -- approxL/rumid                 6.515 cN  (but "blue forest is denser" than in approxL)
    -- approxL/RUonly                7.201 cN
    -- approxL/ave60                 6.460 cN
    -- approxL/ave180                5.265 cN
    -- approxL/ave600                4.958 cN
    -- approxL/ave900                5.029 cN
    -- approxL/ave1200               4.912 cN  <--- best value 1200s
    -- approxL/ave3600               5.623 cN
    -- approxL,RU-err                7.844 cN
    -- approxL,acc.err               7.854 cN
    -- approxL,RU-err,acc.err        6.044 cN
    -- approxL,3*RU-err,acc.err      6.541 cN
    -- approxL,RU-err,3*acc.err      6.463 cN
    -- approxL,3*RUerr,3*acc.err     6.438 cN
    --
    -- approxL/ave1200,RU-err,acc.err
    --
    --     ** NEW **
    ------------------
    -- baseline: RUangerr=3e-3,accerr=3e-6,RUvelocity_timescale=100
    -- baseline                            5.133 cN
    -- RUvelocity_timescale=300            5.292 cN
    -- accerr=1e-5                         5.498 cN
    -- angerr=1e-2                         4.857 cN
    -- angerr=0,accerr=0                   5.257 cN
    -- RUvelocity_timescale=30             5.587 cN
    -- angerr=0                            5.024 cN
    -- accerr=0                            5.275 cN
    -- Conclusions:
    --------------
    -- * accerr=3e-6 is good: making it 3 times larger increases tension by 10%,
    --   while making it smaller does not decrease it.
    -- * angerr /improves/ the situation (??)
    -- * RUvelocity_timscale=100 is good: making it larger or smaller increases tension.
    -- baseline with wanted=3.6cN:         4.637 cN
    -- baseline with wanted=3.2cN:       >=4.926 cN
    -- baseline with Npaux=2:             4.983 cN
    -- baseline with Npaux=1:             5.011 cN (4.942 cN)  <--- new baseline (different roundoff errors?)
    -- baseline with Np=20,Npaux=5:       5.477 cN
    -- baseline with Np=80,Npaux=20:      esimissä ..., toistaiseksi 5.598
    -- baseline, no accelerometer         7.230 cN
    -- baseline, tether-individual damping:.  large (bad idea)
    -----------------
    --
    --      *** New thrust model, thrust limiting, SF-1500 ***
    --
    -------------------
    -- 90mN                             6.192 cN
    -- 100mN                            6.777 cN
    -- 60mN-SF1500                      5.416 cN
    -- 70mN-SF1500                      5.775 cN
    -- 80mN-SF1500                      6.428 cN
    -- 90mN-SF1500                      6.479 cN ; SF1500 is worse here(!)
    -- 100mN-SF1500                     6.695 cN
    -- 60mN-SF1500-repuls               5.416 cN ; same as without repulsion
    -- 80mN-SF1500-repuls               5.245 cN
    -- 100mN-SF1500-repuls              5.332 cN
    ----- Same but with masterthrottle fixed (accerr 5*3e-6 mm/s^2: 5 time worse than SF1500):
    -- 60mN                             4.620 cN
    -- 70mN                             5.259 cN
    -- 80mN                             5.619 cN
    -- 90mN                             5.638 cN
    -- 100mN                            6.470 cN
    -- 60mN-repuls                      5.856 cN ; single large spike, otherwise below 4.6cN
    -- 70mN-repuls                      5.118 cN
    -- 80mN-repuls                      5.298 cN
    -- 90mN-repuls                      5.184 cN
    -- 100mN-repuls                     5.810 cN
    -- 90mN-big                         6.317 cN
    -- 90mN-repuls-big                  5.471main, 6.118aux ; Np=50,Npaux=15
    -- 90mN-Nw50-repuls                 5.413 cN ; max auxtens 3.95cN
    -- 90mN-repuls-auxang1              6.226 cN ; worse than baseline case (auxang5)
    -- 90mN-repuls-auxang2.5            6.143 cN
    -------------------------------------------------
    --
    -- Runs with Nw=40,tether.len=10km,wanted_tension=2cN:
    -- (by default, auxangle=5deg)
    --
    -------------------------------------------------
    -- 90mN,Np=10,Npaux=1,repuls               3.526main, 7.565aux (8d)
    -- 90mN,Np=10,Npaux=1,repuls               3.410main, 7.370aux
    -- 90mN,Np=20,Npaux=2,repuls               3.919main, 8.705aux
    -- 90mN,Np=10,Npaux=1,repuls,auxang=2.5    3.080main, 6.631aux
    -- 90mN,Np=10,Npaux=1,repuls,auxang=1.0    3.322main, 5.370aux
    -- 90mN,Np=10,Npaux=1,repuls,auxang=0      3.480main, 5.453aux
    -- 90mN,Np=40,Npaux=5,repuls,auxang=1.0    3.180main, 5.831aux
    -- 90mN,Np=80,Npaux=10,repuls,auxang=1.0   3.239main, 5.754aux
    -------------------------------------------------
    --
    -- Runs with Nw=30,tether.len=15km,wanted_tension=3cN:
    -- (by default, auxangle=2deg)
    --
    -------------------------------------------------
```

144

```
-- 90mN,Np=10,Npaux=1,repuls                3.944main, 5.403aux  ; max phi error 1.96deg
-- 90mN,Np=50,Npaux=10,repuls               4.236main, 5.716aux  ; max phi error 4.84deg
-- 90mN,Np=10,Npaux=1                        4.323main, 6.506aux  ; max phi error 3.66deg
-- 100mN,Np=10,Npaux=1,repuls               4.033main, 6.369aux  ; max phi error 1.72deg
-- 100mN,Np=50,Npaux=10,repuls              4.536main, 6.112aux  ; max phi error 6.19deg
-- 90mN,Np=10,Npaux=1,repuls,have_damp      3.943main, 5.140aux  ; max phi error 1.11deg
-- 90mN,Np=50,Npaux=10,repuls,have_damp     4.309main, 6.038aux  ; max phi error 2.58deg
--
-- Runs with use_nonuniform_points,Np=20,Npaux=1, by default wanted_thrust=3cN:
--
-- 90mN,repuls,have_damp                    4.695main, 6.789aux  ; max phi error 2.58deg
-- 90mN,repuls,have_damp,wanted_thrust=4e-2 5.131main, 6.427aux  ; max phi error 1.42deg
-- 90mN,norepuls,have_damp                  4.992main, 6.669aux  ; max phi error 1.61deg
-- 90mN,norepuls,SCpointmass                4.663main, 6.439aux
```

# Appendix C

# Realistic sail shape article

# Thrust vectoring of an electric solar wind sail with a realistic sail shape

P. Toivanen and P. Janhunen

*Finnish Meteorological Institute, FIN-00101, Helsinki, Finland*

**Abstract**

The shape of a rotating electric solar wind sail under the centrifugal and solar wind forcing is modelled to address the sail attitude maintenance and thrust vectoring. The sail rig assumes centrifugally spanned main tethers that extent radially outward from the spacecraft in the sail spin plane. Furthermore, the tips of the main tethers host remote units that are connected by auxiliary tethers at the sail rim. Here, we derive the equation of main tether shape and present both a numerical solution and an analytical approximation for the shape as parametrized both by the centrifugal to electric sail force ratio and the sail orientation with respect to the solar wind direction. The resulting shape is such that near the spacecraft the roots of the main tethers form a cone whereas towards the rim, this coning is flattened by the centrifugal force, and the sail is coplanar with the sail spin plane. Our approximate for the sail shape is parametrized only by the tether root coning angle and the main tether length. Using the approximative shape, the torque and thrust of the electric sail force to the sail are obtained. As results, the amplitude of the tether voltage modulation required for the sail attitude maintenance is given as a torque-free solution. The amplitude is smaller than that previously obtained for a rigid single tether resembling a spherical pendulum. This implies that less thrusting marginal is requred for the sail attitude maintenance. For the given voltage modulation, the thrust vectoring is then considered in terms of the radial and transverse thrust components.

*Keywords:*
Electric solar wind sail, Attitude control, Transverse thrust

## Nomenclature

| | | |
|---|---|---|
| a | = | voltage modulation torque-free |
| c | = | cosine funtion |
| $\mathbf{e}$ | = | unit vector |
| $\mathbf{F}$ | = | electic sail force |
| $\mathfrak{F}$ | = | total sail thrust |
| $\mathbf{G}$ | = | centrifugal force |
| g | = | voltage modulation general |
| $\mathcal{I}$ | = | integral |
| k | = | force ratio |
| L | = | main tether length |
| l | = | coordinate along the main tether |
| M | = | total mass |
| N | = | number of main tethers |
| m | = | single main tether mass |
| s | = | sine funtion |
| $\mathbf{T}$ | = | main tether tension |
| $\mathfrak{T}$ | = | electric sail torque |
| $\mathcal{T}$ | = | total sail torque |
| u | = | local tether tangent |
| $\mathbf{v}$ | = | solar wind velocity |
| $(x, y, z)$ | = | Cartesian coordinates |
| $\alpha$ | = | sail angle |
| $\gamma$ | = | local tether coning angle |
| $\Delta t$ | = | rotation period |
| $\mu$ | = | linear mass density |
| $\psi$ | = | Thrusting angle |
| $(\rho, \phi, z)$ | = | circular cylindrical coordinates |
| $\tau$ | = | angular torque density |
| $\xi$ | = | electric sail force factor |
| $\omega$ | = | sail spinrate |

*Subscripts*

| | | |
|---|---|---|
| 0 | = | tether root |
| i | = | index |
| mt | = | main tether |
| q | = | vector component index |
| ru | = | remote unit |
| s | = | sail |
| $(x, y, z)$ | = | Cartesian coordinates |
| $\alpha$ | = | sail angle |
| $\gamma$ | = | local tether coning angle |
| $(\rho, \phi, z)$ | = | circular cylindrical coordinates |

*Superscripts*

| | | |
|---|---|---|
| j | = | summation index |

## 1. Introduction

The electric solar wind sail is a spacecraft propulsion system that uses the solar wind proton flow as a source of momentum for spacecraft thrust [1]. The momentum is transfered to the spacecraft by electrically charged light-weight tethers that deflect the proton flow. The sail electrostatic effective area is then much larger than the mechanical area of the tethers, and the system promises high specific acceleration [2]. As the tethers are in high positive potential they attract electrons that in turn tend to neutralize the tether charge state. However, only a modest amount of electric power is required to run electron guns to maintain the tether charge state, and the sail can easily be powered by solar panels [3]. The main tethers are centrifugally spanned radially outward from the spacecraft in the sail spin plane (Fig. 1). To tolerate the micro-meteoroid flux each tether has a reduntant structure that comprises a number (typically 4) of 20-50 $\mu$m metal wires bonded to each other, for example by ultrasonic welding [4]. As a baseline design, the tips of the main tethers host remote units that are connected by auxiliary tethers at the sail perimeter to give the sail mechanical stability [5].
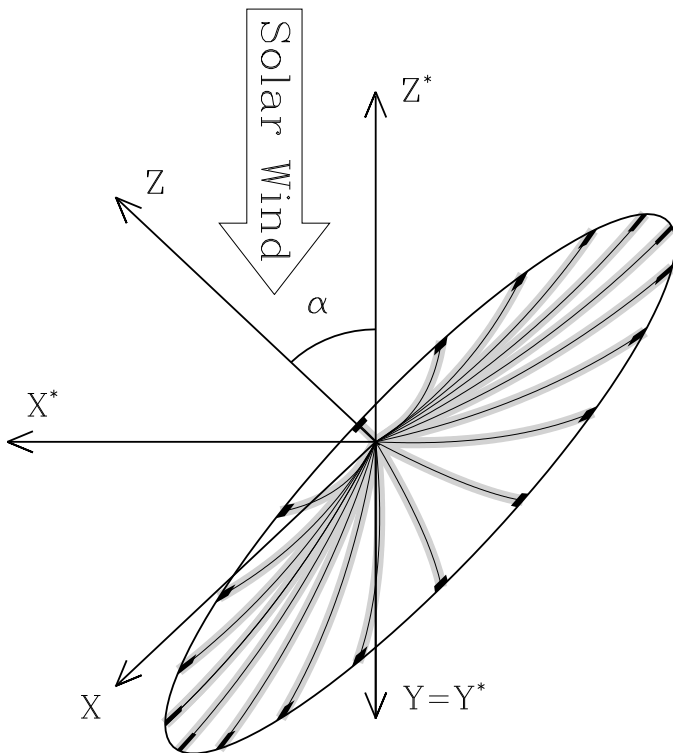


Figure 1: Electric sail flight configuration and coordinate systems.

As the electric sail offers a large effective sail area with modest power consumpsion and low mass, it promises a propellantless continuous low thrust system for spacecraft propulsion for various kinds of missions [6]. These includes fast transit to the heliopause [7], missions in non-keplerian orbit such as helioseismology in a solar helo orbit [8], space weather monitoring with an extended warning time (closer to the sun than L1), multi-asteroid touring mission. In addition to scientific mis-

sions, the electric sail can be harnessed for planetary defence as a gravity tractor [9] and to rendezvous such Potentially Hazardous Objects that cannot be reached by chemical propulsion [10]. The electric sail has also been suggested as a key component in logistic chain in asteroid mining and specifically aquiring water from asteroids for in-orbit LH2/LOX production by electrolysis to provide cost efficient way of transporting infrastructure associated with manned Mars missions [11].

The electric sail has an intrinsic means for spin plane attitude control, maintanance, and maneuvers. These can be realized by differential tether voltage modulation [12] that algorithmically is analogous to flying a helicopter. Furthermore, the sail can fully be turned off for orbital coasting phases or proximity maneuvers near light weight targets such as small asteroids. The coasting phases are also central to optimal transfer orbits between circlular, for example, planetary orbits [13] (reaching a target in an elliptical orbit such as the comet 67P/Churyumov-Gerasimenko coasting phases are not needed [14]). Navigation to the target is also feasible, in spite of the variable nature of the solar wind [15].

In this paper, we derive an integral equation for the sail main tether shape under the electric sail and the centrifugal forces in Sec. 2.1. The resulting equation of tether shape is then solved numerically (Sec. 2.2) and an analytical approximate for the shape is then obtained (Sec. 2.3). Using this approximate, we acquire general expressions as results for the thrust (Sec. 3.1) and torque (Sec. 3.2) arising from the solar wind forcing to the sail. Here, in Sec. 4.1, we seek for a tether voltage modulation that leads to torque-free sail motion. Finally, in Sec. 4.2, we consider the sail thrust vectoring in terms of the radial and transverse thrusts.

The coordinate systems used in this paper are described in Fig. 1. One of the systems $(X^*, Y^*, Z^*)$ is such that $Z^*$ points to the sun. In the other system $(X, Y, Z)$, $Z$ is aligned with the sail spin axis, and $X$ is chosen so that the solar wind is in $XZ$ plane. These two systems are related by rotation around $Y^*$ axis by the sail angle $\alpha$. For example, on a circular heliocentric orbit on the ecliptic plane $Y^*$ points then to south, $X^*$ is along the sail orbital speed, and $Z^*$ points to the sun. In the $XYZ$ system, the circular cylindrical coordinates $(\rho, \phi, z)$ are used. These coordinates are not inertial. In this work, we have neglected the fictitious forces, especially the Coriolis force that arises from the sail orbital motion around the sun as they have no effect on the results shown in this paper. As the Coriolis force, however, leads to a secular variation in the sail spin rate [12], it will be considered in a future study that addresses the electric sail spin rate variations and control using the model developed in this paper.

## 2. Tether shape

### 2.1. Equation of tether shape

The electric sail tether shape under the solar wind forcing can be obtained by writing an integral equation similar to that of a catenary. Fig. 2 shows the electric sail force and the centrifugal

force dictating the tether shape. Local unit vectors parallel and perpendicular to the tether can be written as

$$
\begin{aligned}
\mathbf{e}_\parallel &= c_\gamma \mathbf{e}_\rho + s_\gamma \mathbf{e}_z & (1) \\
\mathbf{e}_\perp &= s_\gamma \mathbf{e}_\rho - c_\gamma \mathbf{e}_z & (2)
\end{aligned}
$$

in terms sine and cosine of the local coning angle $\gamma$. The total force $\mathbf{T}$ that equals the tether tension is split to $\rho$ and $z$ components as

$$
\frac{T_z}{T_\rho} = \tan\gamma = \frac{dz}{d\rho} \equiv u(\rho). \tag{3}
$$

An equation for the tether shape can then simply be written as

$$
u = \frac{F_z}{G + F_\rho}. \tag{4}
$$

Note that the forces present here are the total forces integrated over the tether from the reference point $\rho$ to the tether tip at $\rho_L$.
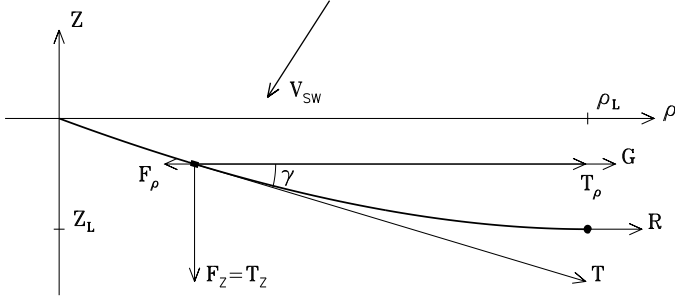


Figure 2: Electric sail tether (thick solid curve), remote unit (black dot).

For a tether segment $dl$ with a mass of $dm_{\mathrm{mt}}$, the centrifugal force ($dG = \omega^2 \rho \, dm_{\mathrm{mt}}$) can be given in terms of the tether linear mass density $\mu$ ($dG = \mu\omega^2\rho \, dl$). As the length of the tether segment reads as

$$
dl = \sqrt{1 + \left(\frac{dz}{d\rho}\right)^2} \, d\rho = \sqrt{1 + u^2} \, d\rho, \tag{5}
$$

the total centrifugal force can be integrated to read as

$$
G = \mu\omega^2 \int_\rho^{\rho_L} \rho \sqrt{1 + u^2} \, d\rho + m_{\mathrm{ru}}\omega^2\rho_L, \tag{6}
$$

where the second term is the centrifugal force of the remote unit including the auxiliary tether mass.

The electric sail force per unit tether length is directed along the solar wind component perpendicular to the tether

$$
\frac{d\mathbf{F}}{dl} = \xi\mathbf{v}_\perp \tag{7}
$$

where $\mathbf{v}_\perp$ is the solar wind component perpendicular to the main tether and $\xi$ is a force factor arising from the electric sail thrust law [3]. Similarly to the centrifugal force above, the electric sail force can be integrated to read as

$$
\mathbf{F} = \int_\rho^{\rho_L} \xi\mathbf{v}_\perp \sqrt{1 + u^2} \, d\rho. \tag{8}
$$

The solar wind velocity can be given as

$$
\mathbf{v} = v(s_\alpha \mathbf{e}_\rho + c_\alpha \mathbf{e}_z) \tag{9}
$$

in terms of the sail angle. The component perpendicular to the tether can be expressed in terms of the unit vector of Eq. (2) as

$$
\begin{aligned}
\mathbf{v}_\perp &= (\mathbf{v} \cdot \mathbf{e}_\perp)\mathbf{e}_\perp \\
&= v(s_\alpha s_\gamma^2 - c_\alpha s_\gamma c_\gamma)\mathbf{e}_\rho + v(c_\alpha c_\gamma^2 - s_\alpha s_\gamma c_\gamma)\mathbf{e}_z. \tag{10}
\end{aligned}
$$

Using trigonometric identities to express $s_\gamma$ and $c_\gamma$ in terms of $\tan\gamma$ ($\tan\gamma = u$), $\rho$ and $z$ components of the electric sail force (8) can be written as

$$
F_\rho = -\xi v \int_\rho^{\rho_L} \frac{(c_\alpha - s_\alpha u)u}{\sqrt{1 + u^2}} \, d\rho \tag{11}
$$

and

$$
F_z = \xi v \int_\rho^{\rho_L} \frac{c_\alpha - s_\alpha u}{\sqrt{1 + u^2}} \, d\rho \tag{12}
$$

Finally, inserting the integral force terms in Eq. (4), the equation of shape of the tether can be written as

$$
u = \frac{\xi v \int_\rho^{\rho_L} \frac{c_\alpha - s_\alpha u}{\sqrt{1+u^2}} \, d\rho}{\mu\omega^2 \int_\rho^{\rho_L} \rho\sqrt{1+u^2}\, d\rho + m_{\mathrm{ru}}\omega^2\rho_L - \xi v \int_\rho^{\rho_L} \frac{(c_\alpha - s_\alpha u)u}{\sqrt{1+u^2}}\, d\rho} \tag{13}
$$

In addition, the tether extent in $\rho$, $\rho_L$ is determined by the tether length and shape as

$$
L = \int_{\rho_0}^{\rho_L} \sqrt{1 + u^2} \, d\rho. \tag{14}
$$

The shape of the tether can then be solved using Eqs. (13) and (14).

## 2.2. Numerical solution

Numerical solution to Eq. (13) can be found by considering $z(\rho)$ being locally linear as $z_i = u_i\rho + c_i$ at $\rho = \rho_i$. All integrals in Eq. (13) depends only on $u$ and $\rho$, and we are left to find a recurrence relation only for $u_i$. To do so, an integral $\mathcal{I}$ of any general function $h(\rho, u)$ can be written as

$$
\mathcal{I}_i = \int_{\rho_i}^{\rho_L} h(\rho, u) d\rho = h(\rho_i, u_i)\Delta\rho_i + \mathcal{I}_{i-1}. \tag{15}
$$

An equation for $u_i$ can be obtained by substituting all integrals in Eq. (13) with Eq. (15), accordingly. After some algebra, $u_i$ can be written as

$$
u_i = \frac{\xi v c_\alpha \Delta L + F_{i-1}^z}{(\xi v s_\alpha + \mu_t\omega^2\rho_{i-1})\Delta L + G_{i-1} + m_R\omega^2\rho_L - F_{i-1}^\rho}. \tag{16}
$$

Given an intial starting point $\rho_L$, a numerical solution can be found recursively using Eq. (16) over the tether length. As $\rho_L$ is unknown, depending on the intial guess of $\rho_L$, the process is iterated until the solved tether root distance equals to the actual tether attachment point at the spacecraft. Fig. 3 shows the tether shape $z(\rho)$ and the local tether tangent $u$. Parameter values used are $L = 20$ km, $\alpha = 45°$, $\Delta t = 125$ min, $m_{\mathrm{ru}} = 1$ kg, $\mu = 10$

3

g/km, $\xi v = 0.5$ mN/km. Note that the rotation period of 125 min is practically too long as the resulting tether tension is too low. It is used here to better visualize the tether shape as the tether coning is prominent. Note that the solution can be easily verified by calculating the force intergrals in Eq. (13) as shown in bottom panel of Fig. 3 and equating these against $u$ as in Eq. (13).
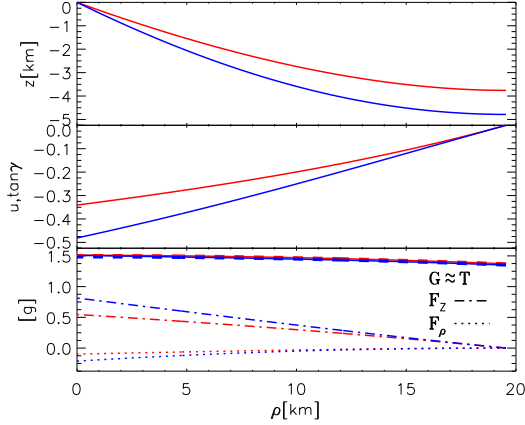


Figure 3: Tether shape (top), tether tangent (middle), and the force terms of the equation of tether shape (bottom) for a slowly rotating sail with low tether tension of 1.5 grams. Red (blue) curve corresponds to the tether azimuth angle, $\phi = 0$ ($\phi = \pi$).

*2.3. Analytical approximate*

An analytical approximate for the tether shape can be obtained for weakly coning sail ($u \approx 0$). As our present version of the tether is such that its tensile strength is about 13 grams [4]. Thus our baseline tether tension is 5 grams that leaves a clear safety margin to 13 grams. Fig. 4 shows the numerically obtained tether shape with a realistic maximum tether tension of 5 grams. The parameter values are the same as in Fig. 3 except the sail spin is faster, and the rotation period, $\Delta t = 70$ min. In general, an approximate for the equation of shape (13) can be found as an expansion of $\rho = b_0 + b_1 u + b_2 u^2$. After solving the coefficients ($b_0, b_1, b_2$) using Eqs. (13) and (14), $u$ can be solved from the expansion above. However, for the purposes of this paper we simplify the analysis and consider only the linear terms so that $u$ can be written as

$$u = u_0 \left(1 - \frac{\rho}{\rho_L}\right) \tag{17}$$

As it can be seen in Fig. 4, this is well justified, and $u = u_0$ at $\rho = 0$ and $u = 0$ at $\rho = \rho_L$ as it is the case. The tether shape can then be integrated ($dz/d\rho = u$) to read as

$$z = u_0 \rho \left(1 - \frac{\rho}{2\rho_L}\right). \tag{18}$$

To finalize our model for the tether shape we are left to solve $\rho_L$ and $u_0$ as functions of the sail and solar wind parameters. Using Eq. (14), expanding $\sqrt{1 + u^2}$ as a power series in $u$, and integrating, $\rho_L$ can be expressed in terms of the total tether length
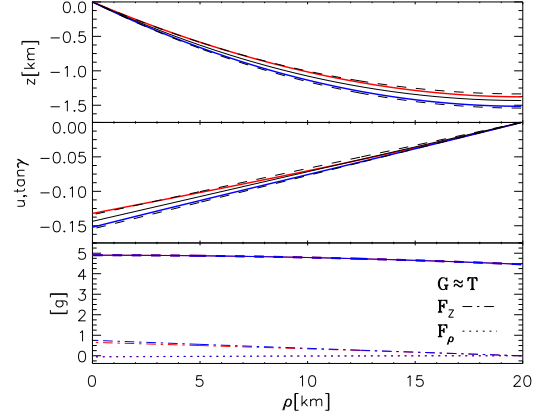


Figure 4: Tether shape (top), tether tangent (middle), and the force terms of the equation of tether shape (bottom) for a sail with maximum tether tension of 5 grams. Red (blue) curve corresponds to the tether azimuth angle, $\phi = 0$ ($\phi = \pi$). Dashed lines shows the corresponding analytical approximates and black line is the sail shape.

as

$$\rho_L = L \left(1 - \frac{1}{6} u_0^2\right) \tag{19}$$

The equation of shape (13) at $\rho = 0$ can be written as

$$u_0 = \frac{\xi v \int_0^{\rho_L} (c_\alpha - s_\alpha u) \, d\rho}{\mu \omega^2 \int_0^{\rho_L} \rho \, d\rho + m_r \omega^2 \rho_L - \xi v \int_0^{\rho_L} c_\alpha u \, d\rho} \tag{20}$$

by excluding terms higher than first order in $u_0$ ($\sqrt{1 + u^2} \approx 1$). Noting that $\int_0^{\rho_L} u \, d\rho = \rho_L u_0 / 2$, one can solve $u_0$ to read as

$$u_0 = \frac{2k \cos \alpha}{2 + k \sin \alpha}, \tag{21}$$

where

$$k = \frac{2\xi v}{(m_{\text{mt}} + 2m_{\text{ru}})\omega^2}, \tag{22}$$

the ratio of the electric sail force to the centrifugal force. Fig. 4 shows the approximates for the shape for the sail angles of $-\alpha$ and $\alpha$ corresponding to the tether azimuth locations of $\phi = 0$ and $\phi = \pi$, respectively.

*2.4. Sail shape*

The shape of the model sail can be fixed when the radial extent of the sail ($\rho_s$) and the tangent of the sail coning angle ($u_s$) at the spacecraft are given. The sail radial extent is trivial and it equals to the single tether length up to second order in $u_s$ as in Eq. 19, and we are left to only determine $u_s$.

Here, we present two estimates for $u_s$ based on the results shown above. One solution is to use Eq. (21) to give the sail coning tangent as an avererage of the tether tangents at $\pm \alpha$,

$$u_s = \frac{4k \cos \alpha}{4 - k^2 \sin^2 \alpha}. \tag{23}$$

The other solution is to consider the solar wind vector to be rotated around the $z$ axis in sail coordinates to the locations of the individual tethers. Then, as the solar wind components in

4

the sail plane cancel when averaging over the tethers, we are left with an effective solar wind $z$ component $v_{\text{eff}} = v \cos \alpha$. Then, using Eq. (21) with the zero effective sail angle, the sail coning tangent is given as

$$u_s = k_{\text{eff}} = k \cos \alpha. \tag{24}$$

As the centrifugal force is typically much larger than the electric sail force ($k \ll 1$), Eqs. (23) and (24) are essentially equal.

## 3. Sail thrust and torque

### 3.1. Thrust

The total thrust to the sail is calculated by summing over the number of tethers ($N$) and integrating over the single tethers as

$$\mathcal{F}_q = \sum_{j=1}^{N} \int_0^L \frac{dF_q^j}{dl} dl \tag{25}$$

By changing variables ($l \rightarrow \rho \rightarrow u$), the integral in Eq. (25) can be written as

$$\mathcal{F}_q = \sum_{j=1}^{N} \int_0^{u_s} \frac{\rho_L}{u_s} \frac{dF_q^j}{dl} \sqrt{1 + u^2} du \tag{26}$$

Next, we assume that the sail comprises such a large number of tethers ($N \gtrsim 12$) that the summation over the tethers in Eq. (25) can be replaced by integration over the tether azimuthal locations in $\phi$ as

$$\sum_{j=1}^{N} F(\phi_j) \rightarrow N \int_0^{2\pi} f(\phi) d\phi, \tag{27}$$

where $f(\phi) = F(\phi)/2\pi$ can be considered as the angular thrust density. The total thrust is then an integral of the trust density and it can be written as

$$\mathcal{F}_q = N \int_0^{2\pi} \int_0^{u_s} \frac{\rho_L}{u_s} \frac{df_q}{dl} \sqrt{1 + u^2} du d\phi. \tag{28}$$

According to the electric sail force law, Eq. (7), the thrust on a line segment $dl$ is given as

$$\frac{d\mathbf{F}}{dl} = g_\phi \xi \mathbf{v}_\perp, \tag{29}$$

where we have added the tether voltage modulation $g_\phi$. The modulation is scaled to the maximum voltage, and $g_\phi \in [0, 1]$. We also assume for simplicity that the solar wind velocity is given as

$$\mathbf{v} = v_x \mathbf{e}_x + v_z \mathbf{e}_z. \tag{30}$$

Its component perpendicular to the tether reads then as

$$\begin{aligned} \mathbf{v}_\perp &= \mathbf{v} - (\mathbf{v} \cdot \mathbf{e}_\|)\mathbf{e}_\| \\ &= \mathbf{v} - (v_x c_\gamma c_\phi + v_z s_\gamma)\mathbf{e}_\|, \end{aligned} \tag{31}$$

where the unit vector parallel to the tether is given as $\mathbf{e}_\| = c_\gamma \mathbf{e}_\rho + s_\gamma \mathbf{e}_z$ as in Eq. (1). Since $\mathbf{e}_\rho = c_\phi \mathbf{e}_x + s_\phi \mathbf{e}_y$ in the circular cylindrical coordinate system, the thrust components per line segment can be expressed as

$$\begin{aligned} \frac{dF_x}{dl} &= g_\phi \xi [v_x - (v_x c_\gamma c_\phi + v_z s_\gamma) c_\gamma c_\phi] \\ \frac{dF_y}{dl} &= -g_\phi \xi (v_x c_\gamma c_\phi + v_z s_\gamma) c_\gamma s_\phi \\ \frac{dF_z}{dl} &= g_\phi \xi [v_z - (v_x c_\gamma c_\phi + v_z s_\gamma) s_\gamma]. \end{aligned} \tag{32}$$

The next step is to integrate over the tether, i.e., from zero to $u_s$ in terms of $u$. We assume that the shape of the tether is given by Eq. (17) and determine the thrust to the second order in $u_s$. This can be accomplished by using any computer algebra system such as Maxima [16], and the angular thrust density can be given as

$$\begin{aligned} f_x &= \frac{g_\phi \xi L}{2\pi} \left[ v_x - \frac{1}{2} v_z u_s c_\phi - v_x \left(1 - \frac{1}{3} u_s^2 \right) c_\phi^2 \right] \\ f_y &= -\frac{g_\phi \xi L}{2\pi} \left[ \frac{1}{2} v_z u_s s_\phi + v_x \left(1 - \frac{1}{3} u_s^2 \right) s_\phi c_\phi \right] \\ f_z &= \frac{g_\phi \xi L}{2\pi} \left[ v_z \left(1 - \frac{1}{3} u_s^2 \right) - \frac{1}{2} v_x u_s c_\phi \right]. \end{aligned} \tag{33}$$

Note that to obtain the total force to the entire sail Eq. (33) has to be integrated over the sail in $\phi$ for a given voltage modulation. In Sec. 4.2, this will be done for the modulation that results in torque-free sail dynamics.

### 3.2. Torque

By definition, the torque on a tether segment $dl$ generated by the electric sail force Eq. (32) is given as

$$\frac{d\mathfrak{T}_q}{dl} = g_\phi \xi \left[ \mathbf{r} \times \mathbf{v}_\perp \right]_q. \tag{34}$$

Writing $\mathbf{v}_\perp$ as in Eq. (31) and $\mathbf{r} = \rho c_\phi \mathbf{e}_x + \rho s_\phi \mathbf{e}_y + z \mathbf{e}_z$, the cross product $\mathbf{r} \times \mathbf{v}_\perp$ can be obtained and the torque per line segment can be written as

$$\begin{aligned} \frac{d\mathfrak{T}_x}{dl} &= g_\phi \xi [\rho v_z s_\phi - (v_x c_\gamma c_\phi + v_z s_\gamma)(\rho s_\gamma - z c_\gamma) s_\phi] \\ \frac{d\mathfrak{T}_y}{dl} &= g_\phi \xi [z v_x - \rho v_z c_\phi + (v_x c_\gamma c_\phi + v_z s_\gamma)(\rho s_\gamma - z c_\gamma) c_\phi] \\ \frac{d\mathfrak{T}_z}{dl} &= -g_\phi \xi \rho v_x s_\phi. \end{aligned} \tag{35}$$

The angular torque density can then be obtained by integration over the tether length as in Eq. (33), and the torque density reads as

$$\begin{aligned} \tau_x &= \frac{g_\phi \xi L^2}{4\pi} \left[ v_z \left(1 - \frac{1}{6} u_s^2 \right) s_\phi + \frac{1}{3} v_x u_s c_\phi s_\phi \right] \\ \tau_y &= \frac{g_\phi \xi L^2}{4\pi} \left[ \frac{2}{3} v_x u_s - v_z \left(1 - \frac{1}{6} u_s^2 \right) c_\phi - \frac{1}{3} v_x u_s c_\phi^2 \right] \\ \tau_z &= -\frac{g_\phi \xi L^2}{4\pi} v_x \left(1 - \frac{1}{4} u_s^2 \right) s_\phi. \end{aligned} \tag{36}$$

Note that Eq. (36) has to be integrated over the sail in $\phi$ for a given voltage modulation to obtain the total sail torque.

Table 1: Terms of second order in $u_s$.

| Var. | Eq. | $O(u_s^2)$ | Value |
|------|-----|------------|-------|
| a | 39 | $(\tan^2\alpha + \frac{1}{6})u_s^2$ | 0.026 |
| $\mathcal{F}_x$ | 40 | $-(\tan^2\alpha - \frac{1}{6})u_s^2$ | -0.019 |
| $\mathcal{F}_z$ | 41 | $(\frac{3}{4}\tan^2\alpha - \frac{1}{3})u_s^2$ | 0.009 |
| $\mathcal{F}_\parallel$ | 42 | $\frac{1}{2}(\tan^2\alpha - 1)u_s^2$ | 0.000 |
| $\mathcal{F}_\perp$ | 43 | $\tan^2\alpha u_s^2$ | 0.023 |
| $\tan\psi$ | 44 | $-\frac{(3\tan^2\alpha + 2)u_s^2}{6(2 - \sin^2\alpha)}$ | -0.013 |

Values of the second order terms are evaluated at $\alpha = 45°$ and $u_s = 0.15$.

## 4. Results

### 4.1. Torque-free sail dynamics

In order to find torque-free dynamics for the sail, we apply a modulation given as

$$g_\phi = 1 - a(1 \pm c_\phi). \tag{37}$$

where $\pm$ corresponds to $\pm\alpha$. After integrating Eq. (36), the total torque has only $y$ component, and it can be expressed as

$$\mathcal{T}_y = \frac{1}{4}N\xi L^2\left[v_x u_s - a\left(v_x u_s \mp (v_z - \frac{1}{6}v_z u_s^2)\right)\right]. \tag{38}$$

Setting $\mathcal{T}_y$ equal to zero, the amplitude $a$ can be solved and it is seen that with the modulation given in Eq. (37), the sail dynamics is free of torque when

$$a = -u_s\tan\alpha\left(1 + u_s\tan\alpha + O(u_s^2)\right), \tag{39}$$

where $v_x/v_z$ is replaced with $\pm\tan\alpha$. For a non-inclined ($\alpha = 0°$) or fully planar ($u_s = 0$) sail, the efficiency equals to one as no voltage modulation is needed for the sail attitude control. Otherwise, a portion of the available voltage is required for the sail control on the cost of the sail efficiency as shown in Fig. 5. Note that the second order terms here and expressions below are given in Tab. 1 merely as an estimate for the validity of the power series expansions, and any geometric interpretations based on these terms are conceivably irrelevant.

As a comparison, for a rigid tether model without auxiliary tethers, the modulation amplitude equals to $3\tan\Lambda\tan\alpha$ [12], where $\Lambda$ is the rigid tether coning angle. The percentual difference between these two models is shown in Fig. 6. For this model, the angular velocity of the tether varies as the tethers are not mechanically coupled, and the tether angluar velocity varies over the rotation phase enhancing the amplitude of the voltage modulation. Also a model with rigid tethers and auxiliary tethers can be considered (the sail resembles a chinese hat). The analysis of such a model is similar to the one carried out in this paper, and the modulation amplitude for such a model equals to $2\tan\Lambda\tan\alpha$. It can be seen that both the mechanical coupling and the realistic tether shape increase the sail efficiency as shown by Eq. (39).
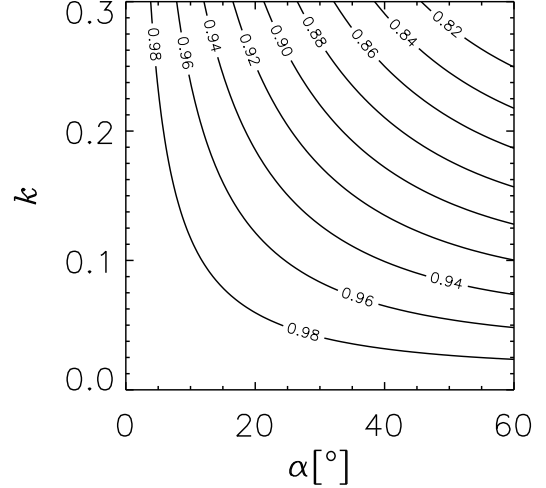


Figure 5: Efficiency of the tether votage modulation.
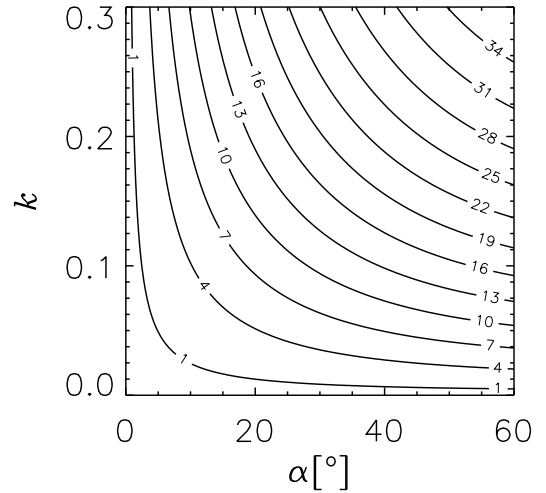


Figure 6: Percentual difference in sail efficiency between the realistic sail model and single mechanically uncoupled tether model [12].

### 4.2. Thrust vectoring

Using the voltage modulation (37) in Eq. (33), the total thrust can be integrated over the tethers in the case of the torque-free sail flight orientation determined by the sail angle $\alpha$,

$$\mathcal{F}_x = \mp\frac{1}{2}N\xi Lv\sin\alpha\left(1 + u_s\tan\alpha + O(u_s^2)\right) \tag{40}$$

$$\mathcal{F}_z = -N\xi Lv\cos\alpha\left(1 + u_s\tan\alpha + O(u_s^2)\right). \tag{41}$$

There thrust components can then be rotated by the sail angle $\alpha$ to give the transverse and radial thrust components as

$$\mathcal{F}_\parallel = \pm\frac{1}{4}N\xi Lv\sin 2\alpha\left(1 + u_s\tan\alpha + O(u_s^2)\right) \tag{42}$$

$$\mathcal{F}_\perp = -N\xi Lv\left(1 - \frac{1}{2}\sin^2\alpha\right)\left(1 + u_s\tan\alpha + O(u_s^2)\right) \tag{43}$$

Fig. 7 shows the transverse thrust component of the sail thrust. Naturally, the transverse thrust is enhanced as the sail angle increases reaching the maximum of about one fourth of the total electric sail force at $\alpha = 45°$. As a comparison, the decay of

6

the transverse thrust in $k$ is somewhat slower than that of the single tether model. This is clarified in Fig. 8 that shows the percentual difference in transverse thrust magnitudes between these two models.
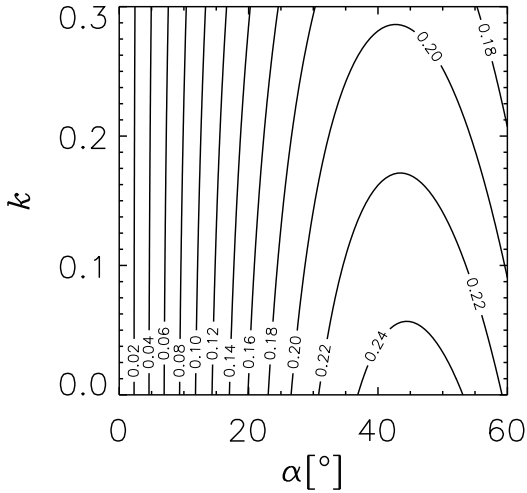


Figure 7: Transverse thrust component normalized to the maximum available Esail force.
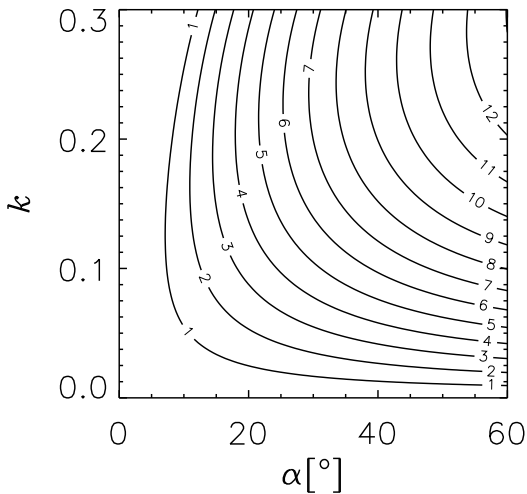


Figure 8: Percentual difference in transverse thrust between the realistic sail model and single mechanically uncoupled tether model.

Finally, the tangent of the thrusting angle can then be written as

$$\tan \psi = \mp \frac{\sin 2\alpha}{2(2 - \sin^2 \alpha)} \left( 1 + O(u_s^2) \right). \qquad (44)$$

It can be seen that the thrusting angle (Fig. 9) has only a weak dependence on the sail root coning tangent $u_s$. Thus the thrusting angle can be computed by assuming that the sail is fully planar ($\tan \psi = \mp \sin 2\alpha/(4 - 2 \sin^2 \alpha)$).

## 5. Discussion and conclusions

In this paper, we assumed that the solar wind is nominal flowing radially from the sun. This served the purposes of this paper
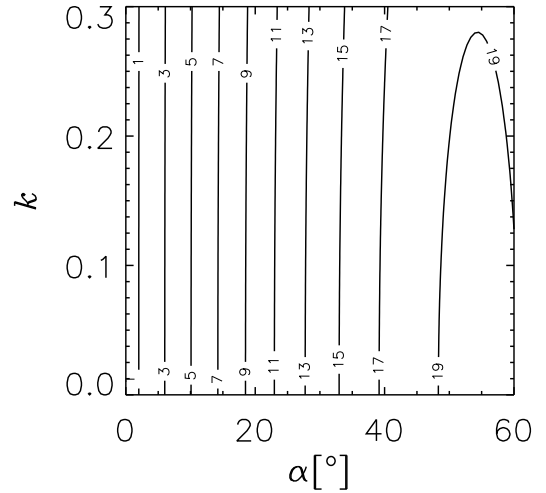


Figure 9: Thrusting angle.

which was to estimate the effects of the actual sail shape to the efficiency of the sail control and thrust vectoring. When solar wind temporal variations are considered, the solar wind *y* component must be added in the sail torque components in order to write a complete rigid body simulation for the electric solar wind sail. Furthermore, the Euler equations require also the moments of inertia in addition to the torques given in this paper. However, both the general thrust components in the sail body frame and moments of intertia can be attained with a resonable effort by following the analysis of this paper, especially, when using a computer algebra. Such a complete Euler description of the electric solar wind sail can then be used, for example to address the effects of the solar wind variation to the sail navitation, and spin rate control and evolution in sail orientation maneuvers.

As results of this paper, we derived the equation of tether shape, solved it by a simple numerical iteration, and presented an analytical approximate for the single tether shape. Our approximate is parametrized by the tether root coning angle and the tether length. The latter is a free parameter whereas the former depends both on the ratio of the electric sail force to the centrifucal force and the sail angle with respect to the sun direction. This ratio then depends on the tether voltage, solar wind density and speed, sail spin rate, and total mass of the tether and remote unit combined. The sail coning angle at the spacecraft is essentially the tether root coning angles averaged over the tether locations in the sail rig. The resulting sail shape is such that the coning decreaces and the sail surface tangential to the tethers approaches to the sail spin plane towards the perimeter of the sail.

Having obtained the model for the sail, we derived expressions for the angular thrust and torque densities. Introducing a tether voltage modulation that results in torque-free sail dynamics, we solved the amplitude of the modulation. This amplitude has to be reserved for the sail control and correspondingly the voltage available for thrusting is less than the maximum designed voltage increasing the sail efficiency. We showed that this amplitude is 3 times smaller for the sail model introduced

153

here than for that derived using a single tether model [12]. Finally, the total thrust to the sail was obtained for the torque-free sail motion. The transverse thrust is somewhat larger (up to about 10%) than that of the single rigid tether model. The reason is that a portion of the sail near the perimeter of the sail is coplanar with the sail spin plane. The thrusting angle was shown to be essentially equal to the fully planar sail being about 20° at sail angles higher than 45°.

## Acknowledgements

## References

[1] P. Janhunen, Electric sail for spacecraft propulsion, *J. Propul. Power*, 20(4), 763–764, 2004.

[2] P. Janhunen, P. K. Toivanen, J. Polkko, S. Merikallio, P. Salminen, E. Haegström, H. Seppänen, R. Kurppa, J. Ukkonen, S. Kiprich, G. Thornell, H. Kratz, L. Richter, O. Krömer, R. Rosta, M. Noorma, J. Envall, S. Lätt, G. Mengali, A. A. Quarta, H. Koivisto, O. Tarvainen, T. Kalvas, J. Kauppinen, A. Nuottajärvi, A. Obraztsov, Electric solar wind sail: Towards test missions, *Rev. Sci. Instrum.*, Vol. 81, 111301, 2010.

[3] P. Janhunen, A. Sandroos, Simulation study of solar wind push on a charged wire: basis of solar wind electric sail propulsion, *Ann. Geophys.*, Vol. 25, 755–767, 2007.

[4] H. Seppänen, T. Rauhala, S. Kiprich, J. Ukkonen, M. Simonsson, R. Kurppa, P. Janhunen and E. Hæggström, One kilometer (1 km) electric solar wind sail tether produced automatically, *Rev. Sci. Instrum.*, Vol. 84, 095102, 2013.

[5] ESAIL FP7 project deliverables [Retrieved on April 26, 2016] <http://www.electric-sailing.fi/fp7/fp7docs.html>.

[6] P. Janhunen, P. Toivanen, J. Envall, S. Merikallio, G. Montesanti, J. Gonzalez del Amo, U. Kvell, M. Noorma, S. Ltt, Overview of Electric Solar Wind Sail Applications, *Proc. Estonian Acad. Sci.*, 63, 267-278, 2014.

[7] A. A. Quarta and G. Mengali, Electric sail mission analysis for outer solar system exploration, *J. Guid. Contr. Dyn.*, 33, 740-755, 2010.

[8] G. Mengali and A. A. Quarta, Non-Keplerian orbits for electric sails, *Cel. Mech. Dyn. Astron.*, 105, 179-195.

[9] S. Merikallio and P. Janhunen, Moving an asteroid with electric solar wind sail, *Astrophys. Space Sci. Trans.*, 6, 41-48, 2010.

[10] A. A. Quarta and G. Mengali, Electric sail missions to potentially hazardous asteroids, *Acta Astronaut.*, 66, 1506-1519, 2010.

[11] P. Janhunen, S. Merikallio, and M. Paton, EMMI - Electric solar wind sail faciliated Manned Mars Initiative, *Acta Astronaut.*, 113, 111-119, 2015.

[12] P. Toivanen, P. Janhunen, Spin plane control and thrust vectoring of electric solar wind sail by tether potential modulation, *J. Prop. Power*, 29, 178-185, 2013.

[13] G. Mengali, A. A. Quarta, P. Janhunen, Electric sail perfromance analysis, *J. Spacecr. Rockets*, 45, 122-129, 2008.

[14] A. A. Quarta, G. Mengali and P. Janhunen, Electric sail option for cometary rendezvous, 9th IAA Symposium on the future of space exploration: towards new global programmes, Torino, Italy, July 7-9, 2015.

[15] P. Toivanen and P. Janhunen, Electric sailing under observed solar wind conditions, *Astrophys. Space Sci. Trans.*, 5, 61-69, 2009.

[16] Maxima, a Computer Algebra System [Retrieved on April 26, 2016], <http://maxima.sourceforge.net>.

# Appendix D

# The 'Call for new ideas' proposal

# Multi-Asteroid Touring

## Lead Proposer: Dr. Pekka Janhunen

Contributing authors: Pekka Janhunen, Petri Toivanen, Jouni Envall, Liisa Juusola (Finnish Meteorological Institute, Finland), Karri Muinonen, Antti Penttilä, Mikael Granvik, Tomas Kohout, Maria Gritsevich (University of Helsinki, Finland), Kai Viherkanto, Antti Näsilä (VTT Technical Research Centre of Finland), Rami Vainio (University of Turku, Finland), Andris Slavinskis (Tartu Observatory, Estonia).

Lead proposer: **Dr. Pekka Janhunen**

Research Manager, PhD

Finnish Meteorological Institute

Erik Palménin aukio 1

FI-00560, Helsinki

Finland

Email: pekka.janhunen@fmi.fi

Phone: +358-295394635

The Lead Proposer is available to support the study activities.

# Executive summary

We propose a distributed survey of hundreds of asteroids representing many asteroid families with emphasis on small (~1 km) bodies that are difficult to study from Earth in detail. This can be implemented by a fleet of cubesat-sized spacecraft equipped with small optical and near infrared imaging instrument. Data are stored in flash memory during the mission and downloaded by an Earth flyby at the end. This keeps deep space network telemetry costs down, despite the large number of individual spacecraft (~50) in the fleet. To enable the necessary large delta-v, each spacecraft carries a single Coulomb drag tether (downscaled electric solar wind sail) which taps momentum from the solar wind.

Properties of asteroids are of fundamental importance for constraining solar system evolution models because asteroids are fragments of the planetesimals from which Earth and other planets once formed. Knowing physical properties of asteroids is also needed for assessment of the asteroid impact threat, for development of techniques for mitigating asteroid impacts and for the emerging field of asteroid mining.

The fleet will obtain image and spectral data from 300+ near-Earth object (NEO) and mainbelt asteroids, which is groundbreaking. It allows us to study those asteroid families and spectroscopic types for which currently no *in situ* observations are available. The proposed spectrometer will cover wavelengths around the 2.7-µm absorption band, enabling us to study the presence of OH and hydrated minerals. The image data allow us to measure the size and albedo of the studied asteroids. Mapping the albedo of each spectral type and family allows one to infer the absolute size of any asteroid whose spectral type is or will be known from ground observations. Furthermore, a significant subset of the studied asteroids will have moons. For those asteroids, measurement of the absolute mass is possible by determining the orbit of the moon from the optical flyby images. From the spectral data, surface minerals can be detected. For each asteroid studied we obtain the surface morphology, overall shape, character (monolithic or rubble-pile), presence of dust on the surface, number of type of craters, presence of fault lines and presence of moons. Overall, the proposed mission increases the number of well-known asteroids by more than an order of magnitude and enables a "population geophysics" approach for studying them.

The proposed mission architecture is easily scalable both scientifically and financially. The number of spacecraft can be scaled, as well as the maximum heliocentric reach of the fleet. Launching is very flexible because it can be made either by one shot by a launch vehicle such as the Indian "Polar Satellite Launch Vehicle" (PSLV) or by piggybacking with one or more other Lagrange point, lunar or planetary missions. It is also possible to scale the mission (both scientifically and financially) by scaling the designed lifetime of each spacecraft. A 3.2-year lifetime mission is sufficient to study the mainbelt, for Hilda family objects one needs 4.3 years, and for Jupiter Trojans 8.3 years. Optionally, some spacecraft in the fleet can perform rendezvous of particularly high-value targets, and some targets may be inspected by more than one spacecraft in the fleet to increase their mapped surface fraction.

# 1. Science case

## 1.1 Overarching science motivation

The geological and geophysical properties of asteroids, including near-Earth objects (NEO), main-belt objects (MBO) and more distant populations such as Jupiter Trojans, are of fundamental importance for constraining solar system evolution models (including Earth's early history, e.g., the origin of Earth's oceans). Asteroid families (i.e., the present collisional fragments of the original parent bodies) are the key subpopulations for understanding the composition and structure of the planetesimals from which, e.g., the Earth once formed. Knowing physical properties of asteroids is also needed for assessment of the asteroid impact threat, for development of techniques for mitigating asteroid impacts and for the emerging field of asteroid mining.

## 1.2 Present knowledge

Our current knowledge of the geophysical properties of asteroids (such as size, shape, mass, density, and composition) has been obtained by ground-based astronomical telescopes that are typically used for asteroid photometry and spectrometry in the visual and infrared wavelengths. Ongoing asteroid surveys, such as the Catalina Sky Survey (CSS) and the Panoramic Survey Telescope And Rapid Response System (Pan-STARRS), continue to increase the number of known asteroids which is currently at about 720,000, according to JPL's Small-Body Database.

There are about 470,000 asteroids for which the orbit is known accurately enough to allow ephemerides to be predicted with an accuracy of better than a few arcseconds for the next decade (Jedicke et al., 2015). Diameter and albedo estimates are available for about 120,000 asteroids (the diameter mainly from WISE infrared observations; Masiero et al., 2011), but the spectral type (either SMASSII or Tholen classification) is available for only about 1,900 asteroids. We have estimates for the diameter and Tholen spectral type for about 900 MBOs, but only about 150 of them are smaller than 20 km in diameter, and *none of them* is smaller than 2.5 km in diameter.

The typical limiting V (visual) magnitude for ongoing surveys that produce both astrometric and photometric data can be up to 22 (Pan-STARRS), but this is not the case for spectrometric data that are typically obtained only for objects with V<20. Convex asteroid shapes can be inferred from photometric lightcurves obtained by ground-based telescopes and there are currently about 900 asteroids with such shape information[1].

Ground-based asteroid observation techniques also include radars and stellar occultation observations. The Arecibo radar observatory is the most powerful radar instrument for resolving asteroid sizes and shapes, but its capabilities are limited when it comes to mainbelt asteroids due to the relatively large distances and small asteroids involved. Occultation observations — where an asteroid passes the line of sight between a background star and

---

[1] http://astro.troja.mff.cuni.cz/projects/asteroids3D/web.php

the observer — give good estimates for the object size, but do not provide information on details such as mineralogy. Recently, also a novel radio occultation based size determination method was introduced (Lehtinen et al., 2016). The method uses a distant galaxy as a radio source and the asteroid's size is obtained from the observed diffraction pattern.

The ground-based observations are supplemented by space missions. Missions to asteroids have provided detailed geological and geophysical knowledge of about a dozen mainly S-type (i.e., stony) asteroids, including the Hayabusa mission with sample return from near-Earth asteroid Itokawa. Upcoming missions will target (162173) Ryugu (Hayabusa II, JAXA) and (101955) Bennu (OSIRIS-REx, NASA). These targets are carbonaceous C-type asteroids.

Asteroid masses can be inferred from the gravitational perturbations on the trajectory of another asteroid passing close by or orbiting the perturber. The accurate astrometry obtained by ESA's Gaia mission is expected to increase the number of mass determinations based on asteroid-asteroid encounters to about 100, if counting cases with less than 50% relative uncertainty. Mass determinations by binary asteroids may become equally (if not more) important because about 15% of asteroids are estimated to be binary systems (Margot et al., 2015). Some tight binary asteroid system candidates can be identified by their lightcurves. MBO targets cannot usually be resolved by radar and stellar occultations are rare, but close flyby observations would provide a ground-truth enabling to accept or reject candidate binary asteroid systems. Another approach is to identify binary asteroids by searching for the astrometric wobble of the primary component (or both components, if bright enough). ESA's Gaia satellite is the only instrument that can currently detect astrometric binary asteroids in larger quantities. Taken together, an asteroid's size, shape and mass result in a rough estimate of its bulk density.

To summarise the present and planned future knowledge, geological and geophysical properties, including spectral information, are only known for a handful of large main-belt asteroids such as (1) Ceres, (4) Vesta, (21) Lutetia, and (253) Mathilde, and a similar number of relatively small NEOs such as (433) Eros and (25143) Itokawa. In addition to targeting asteroids belonging to different size regimes in the main belt and the near-Earth population, *in situ* studies by space missions have shown that all asteroids visited so far are virtually unique. This has made it challenging to draw generic conclusions about, e.g., asteroid surface geology and geophysics. If the current format for space missions to asteroids (one expensive spacecraft visits a single target during a multiyear mission) does not change, then the kind of detailed imaging that resolves asteroid surfaces will be available only for a very modest number of objects in the coming decades. Building a coherent picture about the geological and geophysical features in different asteroid families and asteroids showing different spectra is not possible if we have available, with decent image resolution, only solitary objects within each group.

## 1.3 Novel approach enabling "population geophysics"

We propose that surface geology and geophysics of asteroids should be studied in a statistical sense, across the entire population or a meaningful fraction thereof. Lacking a more standard term, we will here call this approach *population geophysics* and it should focus on understanding the generic features of asteroid surface geology, geophysics, and thermal properties. For example, impact cratering rates and geological features (by constraining the interior structure) provide constraints for collisional evolution models, thermal properties constrain thermal recoil forces such as Yarkovsky and YORP (Yarkovsky - O'Keefe - Radzievskii - Paddack effect), which are of utmost importance for understanding the long-term evolution of the asteroid belt, while the mineralogical composition of asteroids (when combined with models of the orbital evolution of the asteroid belt) provide constraints on the compositional gradient in the protoplanetary disk. Asteroid families are key subpopulations for understanding the composition and structure of the planetesimals from which, e.g., the Earth once formed. Therefore we should have a reliable statistical view to size and compositional distributions at least for the largest families. An asteroid family is thought to correspond to collisional fragments of a single original parent body.

We propose an *in situ* characterisation of asteroids belonging to different asteroid families. A fleet of small spacecraft will tour multiple asteroids and gather near-range measurements of a much larger number of asteroids than have thus far been studied at close range. Each spacecraft is equipped with a small electric solar wind sail to give it unlimited $\Delta v$ so that it can tour the asteroids indefinitely (i.e., limited only by the mission lifetime) and return data to ground during a final Earth flyby. The science payload onboard each spacecraft is lightweight — the main instrument is an imaging system (multispectral camera or optical camera with a Vis-NIR integrating spectrometer up to 3–4 µm wavelengths) similar to the ASPECT instrument proposed for the AIM mission and a close relative of which will also be flight-demonstrated with the Aalto-1 CubeSat (launch: Q4/2016). Specifically, we propose to distribute our mission into smaller, centimeter-scale telescopes that are brought close (~1,000 km) to targets. The 4-cm telescope that we suggest for each spacecraft is able to collect as many photons from a main-belt object as a 10-km telescope on Earth. This fact will make this proposal unparalleled as an imaging survey.

We will be able to study tens of targets of each interesting group, i.e., asteroid family and/or spectral type. Therefore, the proposed mission will not only increase our knowledge on individual asteroids, but provide geological and geophysical data that can be analysed in a statistical sense.

## 1.4 New science in detail

The current knowledge  is summarised in the Asteroids IV compilation (Michel et al., 2015). Following that, we point out several important knowledge gaps:

### 1.4.1 Geological and geophysical properties of small main-belt asteroids

Our proposed mission would provide geological information and geophysical properties, including sizes, spectral classification, and albedos, for small MBOs with diameters 1 km < *D* < 20 km. As tens of asteroids from interesting subgroups in the mainbelt are studied, we can provide size statistics for the small end of the size distribution for individual subgroups.

Small MBOs are difficult to study in detail from the Earth. The apparent magnitude for a 1-km C-type asteroid at 3 au, observed from the Earth at opposition, is V≈22.5, that is, too faint to be detected by current surveys let alone detailed follow-up observations such as disk-resolved spectrometry. In principle, similar information on NEOs can be used to derive estimates for MBOs. NEOs are constantly replenished by MBOs that have drifted into orbital resonances and subsequently evolved to planet-crossing orbits. The dynamical migration mechanisms of MBOs into NEOs are well understood. However, it is not clear if the NEOs represent the asteroid belt at large (DeMeo et al., 2015), because we do not have direct, disk-resolved images of more than about a dozen MBOs and NEOs.

### 1.4.2 Targeted survey of special asteroid families

Provided that the maximum heliocentric reach of our fleet is sufficient, we can dedicate subfleets to Hildas, Trojans and active asteroids, for example. The Hildas are quite far in the main belt with semi-major axis around 4 au. They appear to be quite homogeneous in their composition with D-, P- and C-type bodies. These types are currently considered to have formed in the outer region of the protoplanetary disk and thus are a likely source for Earth's oceans. The Hilda population would be a particularly suitable population for the study of space-weathering effects among low-albedo carbonaceous asteroids (see Sect. 1.4.4).

The sub-mission to Hildas with a subfleet of vessels would imply an approximately 4.3 year mission. If even longer sub-missions are considered feasible, a 8.3 year mission can be extended to Trojan asteroids. There are currently no *in situ* or high-resolution imaging observations for either Hildas or Trojans.

The third asteroid subgroup that we would especially want to gather information of are the so-called active asteroids (main-belt comets), i.e., asteroids that occasionally show comet-type dust tails. While the activity of comets is driven by the outgassing of water and other volatiles, the mechanism driving the non-impact-generated activity on asteroids (and main-belt comets) has never been directly identified. In situ high-resolution imaging and spectral information could reveal the mechanism behind asteroid activity, the surface structure, and the composition of the ejecta (Jewitt et al., 2015).

### 1.4.3 Spectral characteristics of non-ordinary-chondrite like bodies

The link between ordinary chondrite -type (OC) meteorites and S-type asteroids is nowadays quite well established. The so-called space weathering process, the surface regolith alteration due to interaction with cosmic rays, solar radiation and micrometeorites, can explain the slightly different spectral characteristics that we see between OC meteorites and their suggested parent bodies, the S-type asteroids. However, the same link is not that well constrained with other meteorite types. For example, the relation between carbonaceous

chondrites (CC) with carbonaceous low-albedo asteroids such as C-, P- and D-types through the space-weathering mechanism is not well known (Reddy et al., 2015). The evolution of the mafic mineral absorption bands with these objects in space environment is not studied well enough, partly due to their low albedo and the minute changes in the absorption bands that are difficult to observe sensitively enough from Earth.

### 1.4.4 Hydrated minerals in asteroids

The atmospheric absorption band around 2.7 µm makes it difficult, if not impossible, to observe absorption bands on asteroids due to water ice, OH, and hydrated minerals from the ground (Rivkin et al., 2015, 2002). As seen in Fig. 1.1, in VIS-NIR the major 1 and 2 µm silicate bands and several hydration bands can be observed. In MIR range additional major broad hydration band between 2.7 and 3 µm and several organics C-H bands between 3.1 and 3.6 µm can be observed.
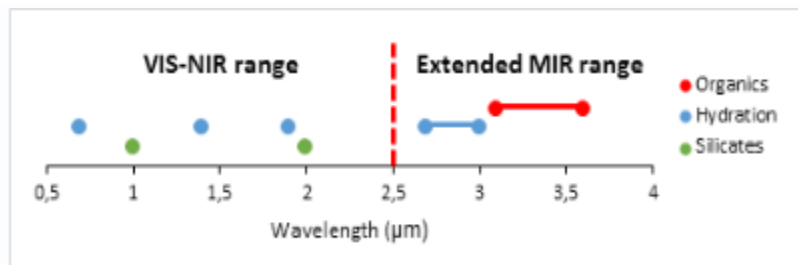


Figure 1.1. Comparison of detectable spectral features using common visual and near infrared (VIS-NIR) range 0.5–2.5 µm and extended range including mid-infrared (MIR) up to 4 µm.

### 1.4.5 Asteroid densities

Accurate estimates for asteroid density require accurate knowledge about the size and shape of the body, together with the mass. Our proposed mission will provide direct image-based constraints on the sizes and shapes (and hence volume) of several hundreds of objects. As we make close flyby observations, we will be able to observe the orbital dynamics of binary systems (about 15% of all asteroids are binaries), and thus infer the masses of the objects. Combining masses and volumes allows us to estimate bulk densities for binary asteroids. Targeting several asteroid families will give us density estimates for some tens of family members for each population. The information can be used to constrain the evolutionary history of the family (Masiero et al., 2015).

### 1.4.6 Asteroid resources and mitigation of asteroid impacts

The abovementioned science topics are also relevant for the two major practical aspects related to asteroids — resource utilization and mitigation of asteroid impacts. Understanding geophysical properties of asteroids such as mass, interior structure (e.g., rubble pile or monolith), and composition are important when selecting suitable targets and technologies for resource utilisation. The same geophysical properties are also of critical importance when developing impact mitigation strategies and technologies (Harris, 2015).

# 2. Scientific requirements

Our scientific requirements result from the cornerstone of our science case, i.e. the idea of enabling a *population geophysics* viewpoint. The direct requirement of this is that we need to visit an adequate number of each subpopulation targets that we want to study. We divide the asteroids into subpopulations shown in Table 2.1.

Table 2.1. Asteroid subpopulations to be studied.

| | | | |
|---|---|---|---|
| Families | Baseline: ~5 mainbelt families, active asteroids | Extended I: Hilda family at >3.7 au semi-major axis | Extended II: Trojan family at 5.2 au semi-major axis |
| Sizes | Less than 20 km diameter | Less than 2 km diameter | |
| Spectral types | Baseline: S-, C-, M-types | Extended: P-, D-, V-types | |
| No. of targets in group | Baseline: 10 objects (3 active asteroids) | Extended: 20 objects (5 active asteroids) | |

From Table 2.1 we can compute the minimum number of individual target to be visited for a baseline mission, 5 families × 2 size groups × 3 spectral types × 10 objects + 3 active asteroids makes 303 targets in total. We can scale the returned science value up by selecting extended configurations, e.g., 7 families × 2 size groups × 6 spectral types × 20 objects + 5 active asteroid, in total 1685 targets.

One justification for the baseline selection of ten objects per subpopulation is that we want to have decent probabilities for encountering a binary body or bodies for every subpopulation, enabling the density estimation. With ten targets having 15% chance of being a binary, we have 80% probability that at least one of them is a binary, and 46% probability that at least two are. With extended choice of 20 targets the probabilities are 96% (at least one) and 82% (at least two). One can also select targets that are known binary candidates, but this may reduce the range of characteristics in terms of, e.g., size and spectral type.

In addition to the target population requirements, we have requirements for the observations for a single target. The requirements concern the image pixel resolution at the target, and the spectral coverage and resolution. Table 2.2 shows an overview of the possible geological features that can be observed with given pixel resolution, with Figs. 2.1–2 visualising the cases.

Table 2.2. Example of imaging capabilities on a 1 km asteroid with different pixel coverage.

| Pixels / diameter | Resolution (m/px) | Observable geological features |
|---|---|---|
| 10 | 100 | <ul><li>Global albedo features</li><li>Large craters (hundreds meters in diameter or larger, Fig. 2.1)</li><li>Global faults and linear features covering at least half of the body (Fig. 2.1)</li></ul> |
| 100 | 10 | <ul><li>Same as above plus:</li><li>Mid-sized craters (tens of meters in diameter)</li><li>Main geological features resolved within large craters (ejecta, landslides, faults)</li><li>Local albedo contrast</li></ul> |
| 1000 | 1 | <ul><li>Same as above plus:</li><li>Small craters and detailed crater geological mapping (Fig. 2.2)</li><li>Crater secondaries</li><li>Individual boulders on surface</li><li>Resolution of fine fractures</li><li>Changes in surface roughness</li><li>Detailed local albedo contrast mapping</li></ul> |
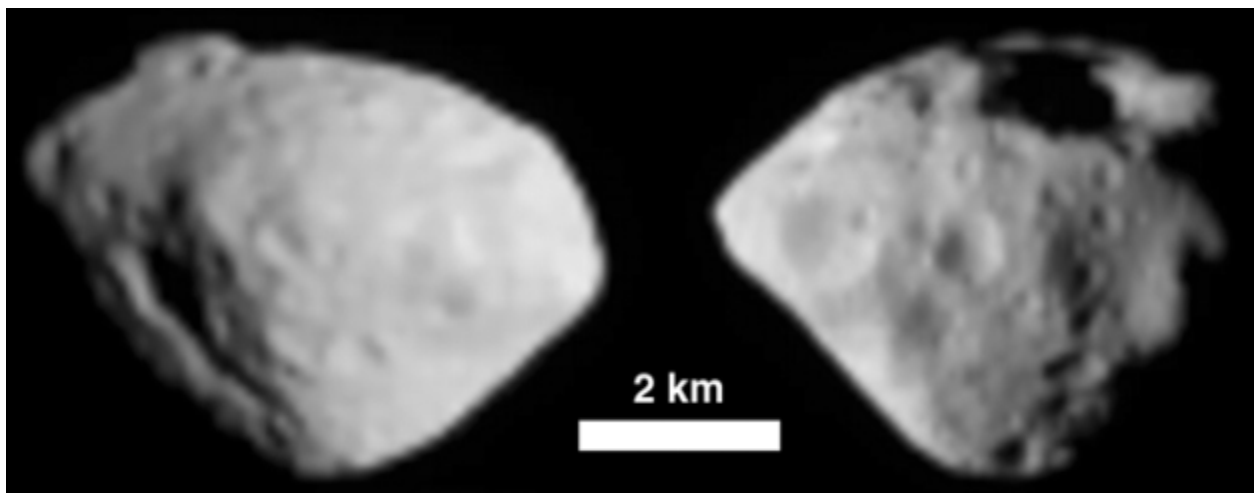


Figure 2.1. Images of Asteroid 2867 Steins (~5 km) from 800 km distance with 100 m/px resolution captured during Rosetta flyby. The imaging geometry is similar to that of proposed mission. Global features as large craters,large fracture (left), or or large crater on top and vertical string of smaller craters or pits (right) are distinguished. Image from www.esa.int.
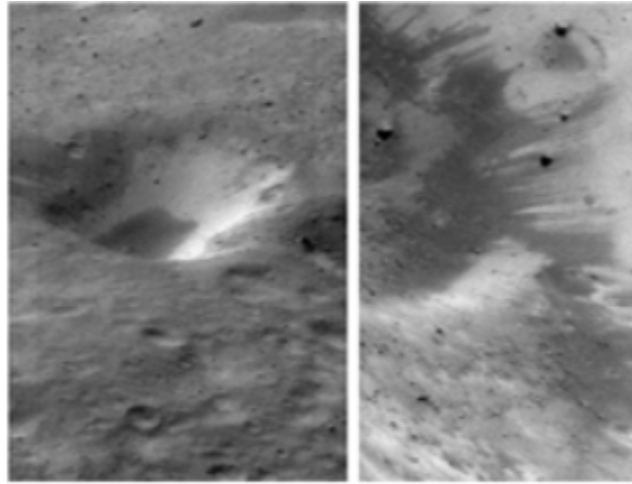
Figure 2.2. Example of local geology observed ~m/px resolution on asteroid Eros by NEAR spacecraft. Left: Approx. 1 km crater with visible albedo contrast on the crater walls (most likely due to exposed fresh material) and accumulated darker landslide material in the center (originating most likely from crater rim). Right: Downslope movement of a dark material. Image from Gaffey et al. (2010).

For the science from the spectral observations we conclude that, for hydration features, we need to start from ~0.5 µm wavelength and cover wavelengths up to ~3.2 µm in order to detect the hydration bands at 2.7–3 µm (see Fig. 1.1). If the spectral range is extended to 4 µm, also absorption bands related to organics can be detected. The absorption bands in minerals are generally quite wide, tens of µm, so the required spectral resolution can be in the order of 5–10 µm.

# 3. Measurements concept

## 3.1 Mission requirements

We need to make optical and NIR flyby measurements of a large number of asteroids representing different asteroid families. A large fleet of spacecraft must perform the flybys and each spacecraft must accomplish the flyby of several asteroids. Meeting this requirement at affordable cost is a challenge. To overcome the challenge, below we propose a novel mission architecture based by the electric solar wind sail (E-sail).

## 3.2 Instrument requirements

The optical-NIR instrument requirements arise from the science requirements. The observing event is the flyby with an asteroid. We have two options for the overall design of the camera instrument. The more ambitious design would have a hyperspectral camera, i.e., an imaging spectrometer over the wavelengths that we propose, 0.5–3.2 or 4 µm. However, an imaging instrument for the longer wavelengths might need active temperature control components that, in turn, consume both power and space. The other camera design is to combine an optical camera and an integrating spectrometer. This design would also be more

optically sensitive. Our proposed designs can be implemented with a Fabry-Pérot interferometer -based instrument, similar to the ASPECT instrument proposed for the AIM mission and which will also be flight-demonstrated with the Aalto-1 CubeSat (launch: Q4/2016).

The proposed observation setup, some tens of seconds for a flyby with 1,000-km distance from the target in the main belt or further, require a decent sensitivity for the camera so that short integration times can be used. The irradiance $E_{solar}$, the radiant flux received by surface unit area, is 1,360 W/m$^2$ at Earth's distance, but 190 W/m$^2$ at 2.7 au (main belt), 130 W/m$^2$ at 3.25 au (Hildas), and 50 W/m$^2$ at 5.3 au (Trojans). The irradiance is spectrally distributed according to the solar spectrum. Assuming that the (spherical) Bond albedo for an asteroid is a valid estimate of its surface element albedo, for dark C-type asteroids the radiance $L$, the reflected light to solid angle by unit area, is 0.6 W/m$^2$/sr (main belt), 0.4 W/m$^2$/sr (Hildas), or 0.2 W/m$^2$/sr (Trojans). The spectral distribution of radiance is shown in Fig. 3.1 for main-belt C-type asteroid surface element.
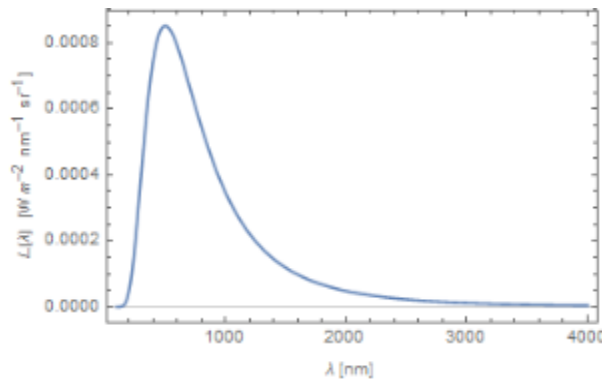


Figure 3.1. Spectral radiance, reflected light to solid angle by unit area at C-type asteroid surface (assuming flat reflectance spectra) at 2.7 au distance from the Sun.

We are proposing to have a telescope with 4 cm aperture on board. That aperture is seen at $5 \times 10^{-15}$ steradians from the asteroid surface, so the radiant flux $\Phi$ received by the aperture from unit surface element on C-type asteroid is 3.3 fW (main-belt), 2.3 fW (Hildas), and 0.8 fW (Trojans). On the other hand, if a single pixel on the camera integrates flux from a 10 m × 10 m area, the radiant flux per pixel is 0.33 pW (main-belt), 0.23 pW (Hildas), and 0.08 pW (Trojans). Finally, moving into photons, Fig. 3.2 sums up the received photons per second per pixel per wavelength, when a camera with 4 cm aperture sees a C-type asteroid from 1,000 km distance, and one pixel corresponds to 100 m$^2$ area on the surface. The imaging instrument needs to be able to have a decent S/N ratio with these photon counts with given integration time. On the other hand, the instrument pointing needs to be stable during the same integration time, so it cannot be extended freely.
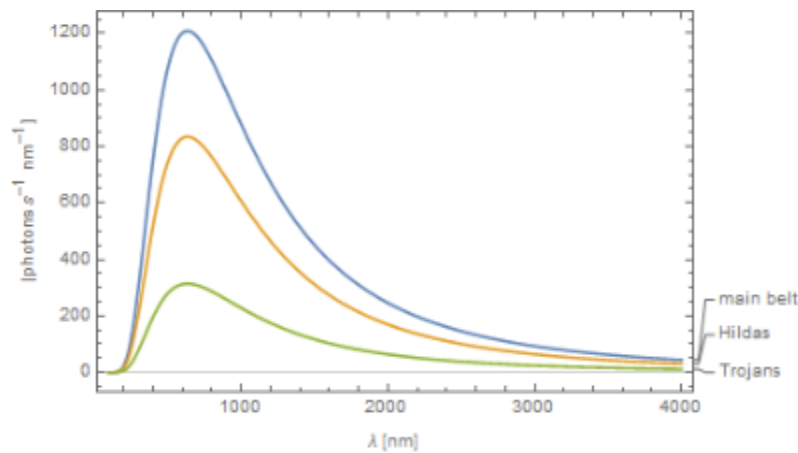
Figure 3.2. Spectral photon counts per camera pixel integrating over 100 m² surface area on a C-type asteroid.

# 3.3 Mission concept

## 3.3.1 Overall mission architecture

We consider a fleet of small spacecraft, each equipped with a single-tether electric solar wind sail propulsion system and a small optical and near infrared (NIR) instrument. The instrument can be, e.g., a derivative of an instrument flown in Aalto-1 cubesat and further developed for the ASPECT cubesat of the AIM mission. Each spacecraft of the fleet makes a flyby of several (typically 6-7) asteroids. The mission is scalable by the size of the fleet. A small launch vehicle such as PSLV can deliver of order 500 kg payload to marginal escape orbit which corresponds to fleet size of about 50, hence enabling an optical+NIR flyby study of 300-350 different asteroids. To keep the telemetry costs down, data are are stored in flash memory during the mission and downloaded at the terminating Earth flyby. Hence, increasing the size of the fleet incurs only extra launch cost but almost no extra telemetry cost: the deep-space network time needed per spacecraft is of order 3 hours only. Thus the mission is easily scalable by the number of spacecraft. Launching is flexible because the only launch requirement is delivery to marginal escape or higher orbit. The launch can be dedicated or piggyback or any combination. Since each spacecraft works independently of the others, simultaneous launching is not mandatory.

The main new technology whose current TRL is below six is the electric solar wind sail (E-sail). We need the E-sail only in its simplest form (single tether). A single-tether E-sail of 100 m length will be launched in LEO in Q4/2016 onboard the Aalto-1 cubesat. Furthermore, NASA Marshall Space Flight Center is studying the E-sail as a vehicle to reach the heliopause boundary in conveniently short time and NASA is also planning a cubesat-based single-tether E-sail test and demonstration mission in the solar wind (Wiegmann, 2016). We also need autonomous optical navigation based on observing nearby asteroids by the telescope. The AutoNav system developed at the Jet Propulsion Laboratory is an example of such a system (Bhaskaran, 2012). AutoNav is mature technology and has been used in several NASA-led missions to asteroids and comets.

## 3.3.2 E-sail cubesat fleet

The electric solar wind sail (E-sail) uses the natural solar wind to produce spacecraft propulsion using a number of centrifugally stretched highly positively biased tethers to gather momentum from the solar wind. For the present application we consider a simple E-sail consisting of only one tether (Fig. 3.3). Large, more complex E-sails consisting of multiple tethers are possible and have been analysed thoroughly (e.g., Janhunen et al., 2010[2]), but are not used in this proposal. Despite being based on the solar wind which is intrinsically variable, the E-sail is accurately navigable (Toivanen and Janhunen, 2009). This feature of the E-sail is due to certain natural feedbacks in the way the E-sail interacts with the solar wind.
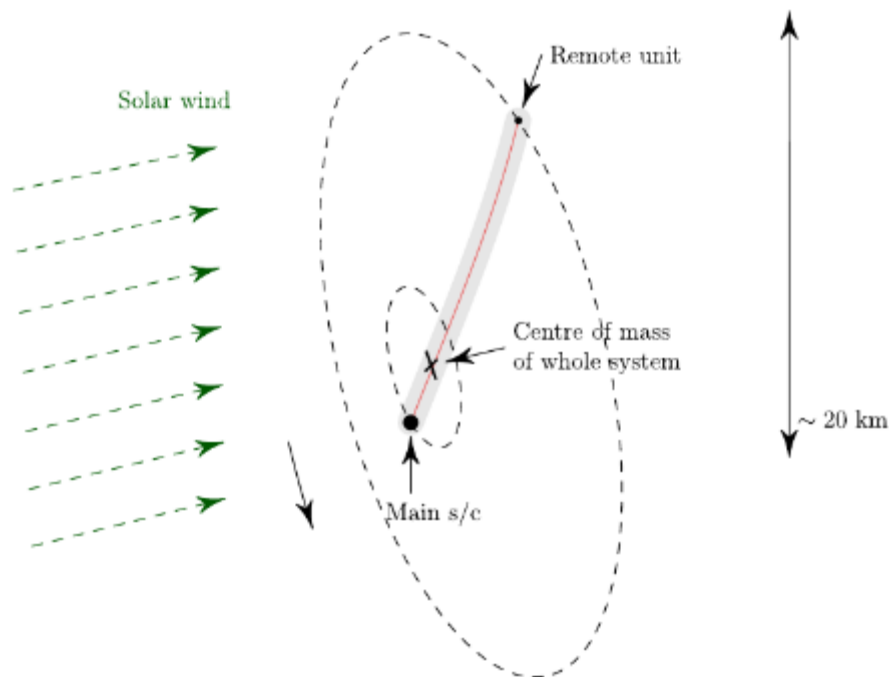


Figure 3.3: Single-tether E-sail.

The flight system depicted in Fig. 3.3 consists of a few-kilogram main spacecraft (main s/c), a ~0.5 kg remote unit which contains a MEMS cold gas thruster for spin initiation and spin-rate management, and a 10-20 km long E-sail tether connecting them. The system is spun slowly (spin period ~30-50 minutes) about the common centre of mass to maintain a suitable ~5 cN (gram) tension of the tether. The tether deployment system (reel) can reside in an auxiliary unit which is jettisoned at the end of the deployment phase so that the mass of the deployment system does not unnecessarily reduce the acceleration delivered by the E-sail (the remote unit still remains connected to the tether's end). The main spacecraft contains a high-voltage source and an electron gun. To keep the power consumption down,

---

[2] For all electric sail publications, see http://www.electric-sailing.fi/publications.html (refereed papers) and http://www.electric-sailing.fi/fp7/fp7docs.html ("ESAIL" EU FP7 project deliverables).

the electron gun can be of a cold cathode type so that no cathode heating power is needed. Such emitters are commercially available e.g. from XinRay Systems.

Figure 3.4 shows the main spacecraft viewed from the direction of the spin axis (i.e., viewed in direction normal to the tether's spin plane). The body of the main spacecraft is a 3-U cubesat (34 cm long, 11x11 cm wide). At one end of the body there is a 4-cm aperture diameter telescope used for viewing the asteroids during the flyby events. The nominal closest flyby distance is 1000 km, which at diffraction limit of the 4-cm telescope would produce a surface resolution of 17 m in visible light.
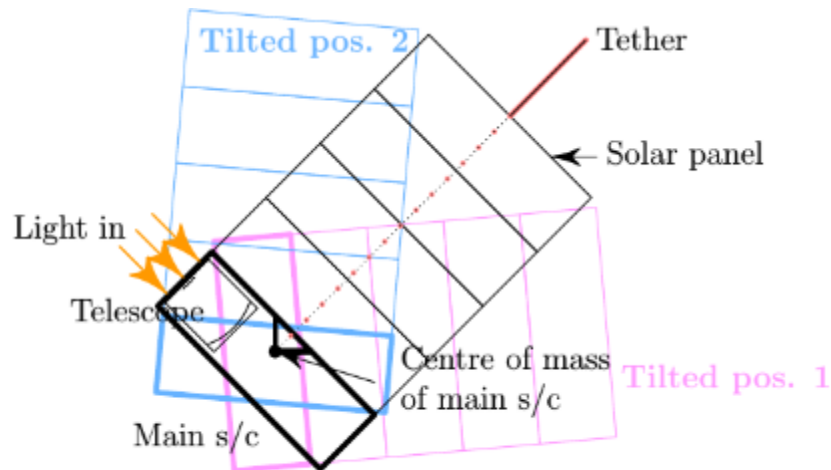


Figure 3.4: Top view of main spacecraft.

The spacecraft and the telescope can be pointed to any target in the following way. The tether is attached near the centre of mass of the main spacecraft so that the spacecraft's attitude is passively stable, but the stability is marginal so that the spacecraft can be easily tilted along the spin axis of the tether (i.e. axis which is perpendicular to the plane of Fig. 3.4 and vertical in Fig. 3.5) by operating internal reaction wheels. Since the spacecraft can also be easily tilted around the tether (Fig. 3.6), we obtain the ability to point the telescope into any target in any phase of the tether's rotation. This ability is used during the flyby to view the asteroid. At 1000 km closest distance and with typical 10 km/s relative speed, the nearest phase of the flyby lasts ~100 s, or 2 minutes.
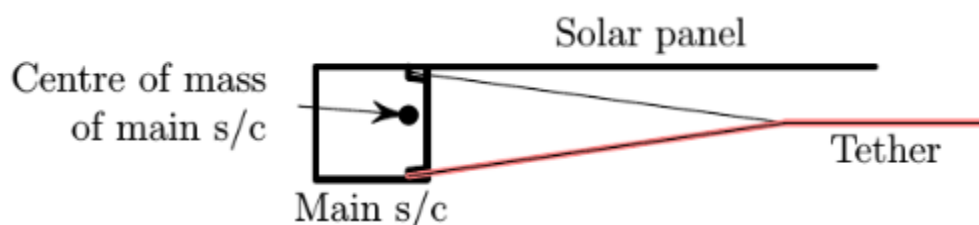


Figure 3.5: Side view of main spacecraft.

15
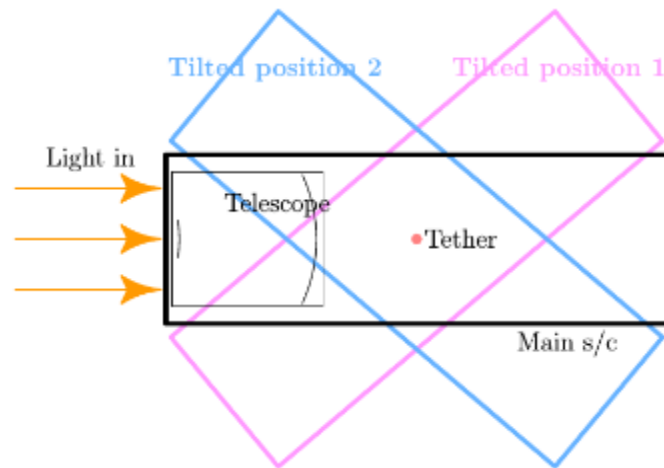
Figure 3.6: Along-tether view of the main s/c.

The roof of the spacecraft has a deployable solar panel (Figs. 3.4 and 3.5). To prevent the backside of the solar panel from touching the high-voltage tether, the final part of the tether can be a several centimetres wide foil or the tether can branch into two as shown in Fig. 3.5. The high-voltage part need be only one branch of the tether (Fig. 3.5, red). The arrangement prevents the main spacecraft from oscillating along an axis which is perpendicular to the plane shown in Fig. 3.5 (the same axis is horizontal in Fig. 3.6).

There are alternative geometric ways of mounting the solar panel(s) to the spacecraft. For example, one can put the solar panel on the left hand side in Fig. 3.5 which corresponds to the southwest side in Fig. 3.4. Then the tether and the solar panel are on opposite sides of the spacecraft so that the two-branch tether shown in Fig. 3.5 is not needed. A slight drawback of this alternative geometric arrangement is that the centre of mass is moved towards southwest in Fig. 3.4 so that the shallow prism-shaped intrusion (Fig. 3.4) which is necessary to connect the tether to the centre of mass of the spacecraft body needs to be deeper. Yet another alternative is to put the solar panel on both sides and use the two-branch tether ending as in Fig. 3.4. The latter alternative would be relevant especially if one wants to extend the mission up to the Jupiter Trojan distance because then the solar panel area must be larger. Even larger variety of geometric options become possible if one makes the spacecraft nonsymmetrical or if one allows a solar panel near the field of view of the telescope. In the latter case, possible stray-light issues would have to be checked.

The telescope is also used as a star tracker for attitude determination and for optical navigation during cruise phases: when flying in the asteroid belt, the position of nearby asteroids against background stars can be used to infer the location of the spacecraft at ~1000 km or better error. When flying in the mainbelt, five or so most nearby numbered asteroids are typically at less than 10 million kilometres from the spacecraft. If the telescope detects the nearby asteroids with angular resolution of $10^{-4}$ rad (20 arcseconds), we thus obtain less than 1000 km in the knowledge of the instantaneous location of the spacecraft. This is a conservative estimate for the error because observing the angular direction of five or so asteroids yields redundant information and improved estimate. Furthermore, at diffraction limit a 4 cm telescope would yield about six times better angular resolution than the 20 arcseconds used in this calculation.

16

### 3.3.3 Exemplary orbits

Figure 3.7 shows an exemplary mainbelt flyby mission using an E-sail that delivers 1 mm/s$^2$ characteristic acceleration to the spacecraft at 1 au. The mission departs from Earth and applies maximal E-sail thrust for 1 year (red trajectory). During the remaining 2.2 years of the mission, the E-sail is used to maximise the number of flybys (green trajectory, science phase). The effect of the science phase to the trajectory was taken into account in Fig. 3.7 in an average sense by assuming that the E-sail's average thrust during the science phase is radial and 40% of the available maximum. The mission ends with a final Earth flyby, during which data gathered in flash memory are returned. After leaving the mainbelt, there is time for orbital corrections to enable a safe Earth flyby (in the plot, also this phase is marked green as the science phase proper). The amount of data is of the order of 10 GB per spacecraft and the maximum data rate needed is 10 MB/s which can be reached by using deep space network antennas at typical 10$^5$ km Earth flyby distance in a ~3 hour long data transfer window. The mission's maximum heliocentric distance is 2.4 au and the mission's science phase spends more than 1.5 years inside the mainbelt (whose approximate lower limit is shown by pink dashed line in Fig. 3.7).

Figures 3.8 and 3.9 show the corresponding trajectories for missions extending up to the inner edge of the Hilda family (Fig. 3.8) and up to the Trojan cloud (Fig. 3.9). Other than taking a longer time and requiring the spacecraft to survive at a larger heliocentric distance (which is mainly a power and thermal design topic), the Hilda and Trojan capable enhanced missions are similar to the baseline mainbelt mission scenario.
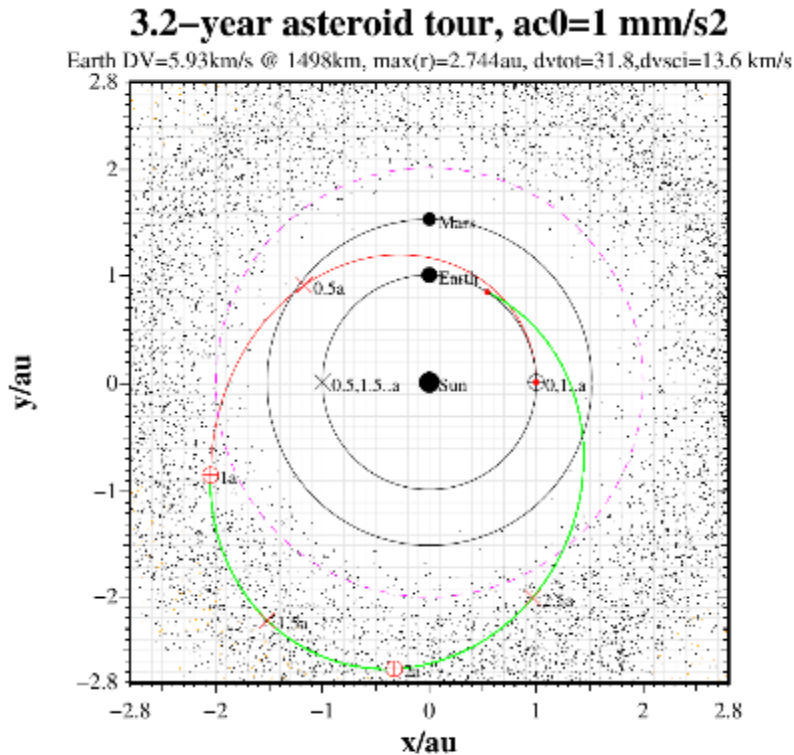


Fig. 3.7: Mainbelt flyby mission. Position of spacecraft and Earth at every 0.5 years is marked. Cruise phase red, science phase green.

## 4.3-year asteroid tour, ac0=1 mm/s2

Earth DV=6.51km/s @ 1879.1km, max(r)=3.248au, dvtot=35,dvsci=14 km/s
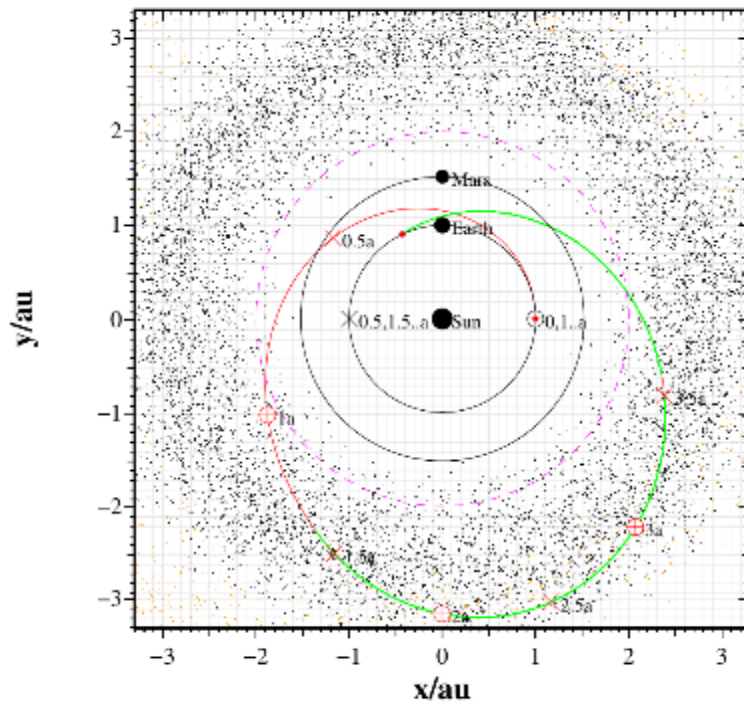


Fig. 3.8: Mainbelt and Hilda asteroid flyby.

## 8.3-year asteroid tour, ac0=0.989 mm/s2

Earth DV=12.4km/s @ 59491km, max(r)=5.332au, dvtot=55.9,dvsci=17.6 km/s
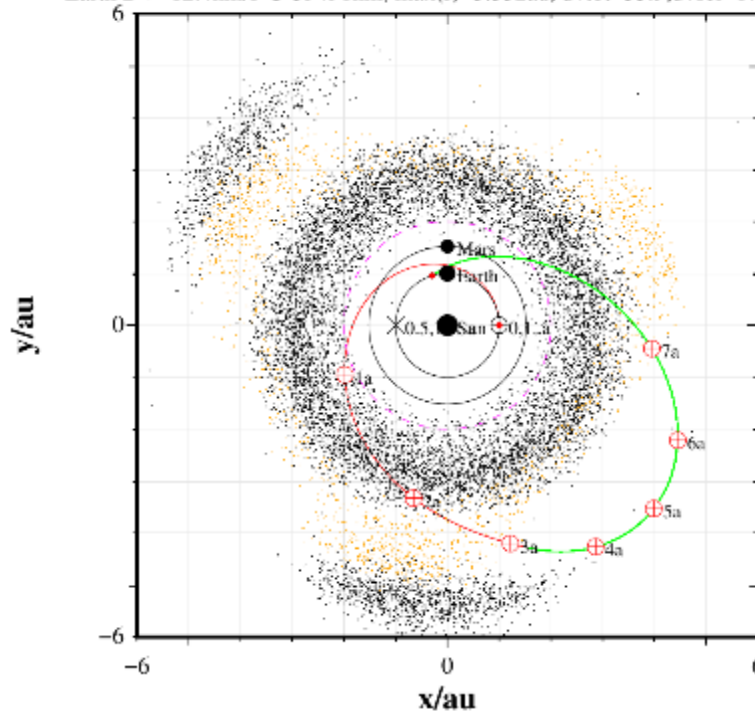


Figure 3.9: Mainbelt, Hilda and Trojan flyby mission. Caveat: since the asteroids are plotted at a fixed moment of time, the Hilda and Trojan clouds do not correspond to what the spacecraft would observe. In practice the spacecraft would encounter Trojans.

18

## 3.3.4 Number of asteroids per spacecraft

We made statistical simulations where the spacecraft is initially placed in an elliptic orbit which traverses the asteroid belt and then its E-sail (with given 1 au characteristic acceleration) is used to accomplish a flyby with any numbered (i.e., well known) asteroid as soon as possible. We repeat the run 100 times varying the initial epoch randomly. When the orbit's aphelion is 1.9 au (i.e., inside the mainbelt) and perihelion is 1.2 au, we find that the mean time between successive flybys is 2.5 months if the characteristic acceleration $a_c$ at 1 au is $a_c$=1 mm/s$^2$. It is easy to show by simple kinematics arguments that the time between flybys is expected to vary as a function of $a_c$ as $a_c^{-2/5}$. Our simulations also confirm this analytic prediction. Thus, for each year that the spacecraft spends inside the mainbelt, 4 or 5 (on average 4.8) asteroid flyby possibilities are expected to arise when the 1 au characteristic acceleration is 1.0 mm/s$^2$.

## 3.3.5 Dedicating some spacecraft for rendezvous

Since we have a fleet, it is possible to dedicate some spacecraft to making rendezvous (slow flyby) observations of some particularly valuable target asteroids. The rendezvoused asteroids should not be very far away, however, or else the mission time is prolonged. If the designed lifetime is 5 years, one can accommodate rendezvous of inner mainbelt asteroids (Fig. 3.10).
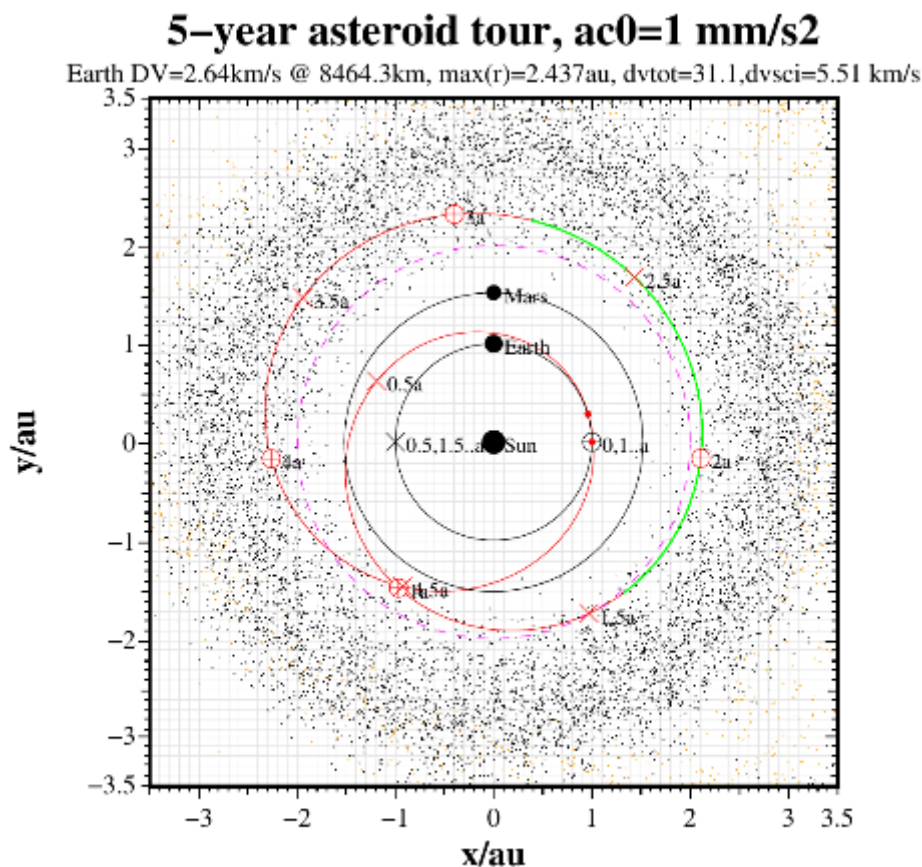


Figure 3.10: Inner mainbelt rendezvous mission.

With 8.4 years maximum mission duration, also the outer mainbelt can be observed in rendezvous mode (Fig. 3.11). The tradeoff is that if a spacecraft in the fleet is programmed to make rendezvous, the number of ordinary flybys that the spacecraft can make is reduced. One rendezvous corresponds to several, perhaps five or so, ordinary flybys in delta-v sense.
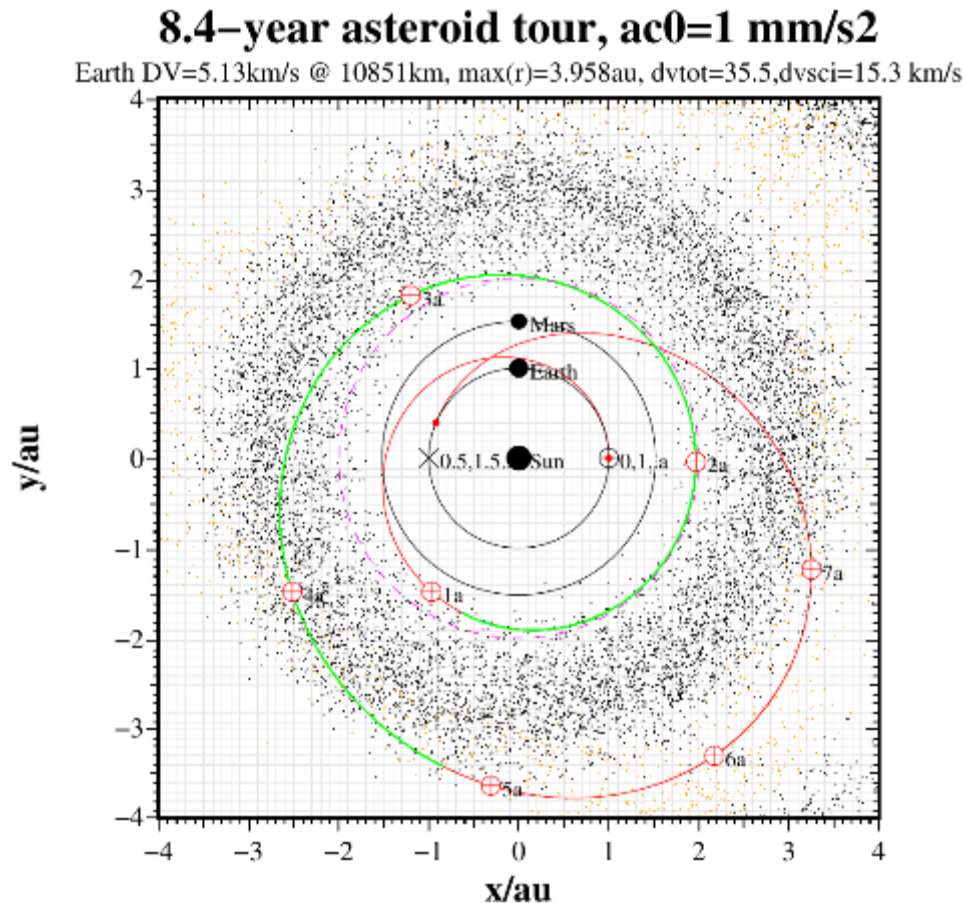


Figure 3.11: Outer mainbelt rendezvous mission.

## 3.3.6 Devoting more than one spacecraft to valuable targets

In addition to the rendezvous (slow flyby), one also has the option of observing a valuable target asteroid by more than one spacecraft. This has the benefit that a single flyby can only observe one side of the asteroid (unless the asteroid is particularly fast rotating), but two flybys made at different times can potentially observe almost the entire surface. Besides completing the geologic mapping of the body, observing the entire surface reduces the uncertainty in the asteroid's volume and consequently reduces the uncertainty in its average mass density if the total mass is also known. The total mass is known if the asteroid has a moon (either known beforehand or discovered during the flyby), because the moon's orbit can be reconstructed from the flyby images. Measuring the mass from deflection of the spacecraft's orbit is probably not realistic except perhaps for the largest asteroids.

Devoting two spacecraft for an asteroid in ordinary flyby mode is cheaper in delta-v sense than making a rendezvous (slow flyby) because a rendezvous is worth several ordinary flybys in the delta-v sense.

## 3.3.7 Mission lifetime and radiation dose

The cumulative high-energy radiation dose may be a lifetime limiting factor for a nanospacecraft. Hence at first hearing, a 8.3-year lifetime required by a Trojan flyby mission raises the question of its feasibility. However, in interplanetary space the high-energy radiation dose is dominated by solar energetic proton flux, which scales approximately as $r^{-1.5}$ where $r$ is the solar distance (Lario et al., 2007). Because the orbit spends most of the time near its aphelion, the accumulated radiation flux for a Trojan mission is not significantly larger than for a normal interplanetary cubesat designed to undergo a mainbelt mission.

After each spacecraft has performed its Earth flyby and downloaded its data, if the equipment still works it can be commanded to a second round through the asteroid belt, to double the number of targets for that spacecraft. This kind of extended mission would incur only minimal extra cost because one only needs to be ready to receive the data when the spacecraft comes again to Earth's vicinity. The second round may also be pre-programmed so that no uploading of new trajectory plan is mandatory.

## 3.3.8 Bonus science: solar wind

When operating, the E-sail produces housekeeping data from which the solar wind plasma density (at high time resolution) as well as an estimate of the solar wind velocity vector (at few minute time resolution) can be deduced. If a magnetometer is added to the payload (such as a derivative of the MAGIC magnetometer of Imperial College which has a cubesat-compatible form factor), also the interplanetary magnetic field (IMF) can be monitored during the cruise phase, yielding information of the solar wind key parameters from many points simultaneously on different sides and different distances from the Sun. Such a dataset can be used afterwards to gain information about the propagation of interplanetary coronal mass ejections (ICMEs), shock fronts and other space weather structures propagating and evolving in the solar wind. Currently such data are routinely available only from one measurement location (Earth-Sun Lagrange L1 point), which leaves the spatio-temporal ambiguities of the solar wind unsolved.

## 3.3.9 Bonus science: size distribution of small mainbelt asteroids

During cruise phases between the asteroids, the telescope is needed for the optical navigation only part of the time. As much as the power budget and other technical constraints allow, the telescope could monitor the surrounding sky to make discoveries of small main-belt asteroids which are too faint to be seen from ground. This yields a measurement of the asteroid number density in the asteroid belt as a function of the absolute brightness. It is well-established that small main-belt asteroids are the source population of NEOs which are short-lived in the geologic timescale. Directly measuring the number density of small asteroids in the asteroid belt sets strong constraints on models describing the evolution of asteroids from the asteroid belt to the near-Earth region. The

number density of small main-belt asteroids is also important knowledge for, e.g., future human and robotic activities in the asteroid belt.

For discovering new small asteroids and for measuring the mainbelt small asteroid number density, a fleet of small telescopes is *a priori* equally efficient as a single large telescope. By structural engineering considerations, a space telescope's mass is proportional to $D^3$ where $D$ is the diameter of the aperture. The light-gathering power is proportional to $D^2$ and hence, by the inverse square distance law of apparent brightness, the maximum range of detection of a certain limit magnitude is proportional to $D$. The volume of detected space is then proportional to $D^3$, i.e. it has the same dependency on $D$ as the telescope mass. Hence, a fleet of small telescopes can detect a volume of space (regarding some fixed limit magnitude of targets) that is equally large as that detected by a big monolithic telescope of the same total mass, if both are flying within the asteroid belt and so are immersed in the cloud of targets to be discovered.

# 5. Bibliography

S. Bhaskaran (2012). *Autonomous navigation for deep space missions.* In Proceedings for SpaceOps 2012 (11-15 June, Stockholm, Sweden), paper #1267135, http://www.spaceops2012.org/proceedings/documents/id1267135-Paper-001.pdf.

F.E. DeMeo, C.M.O'D. Alexander, K.J. Walsh, C.R. Chapman, and R.P. Binzel (2015). *The compositional structure of the asteroid belt.* In: Asteroids IV, P. Michel et al. eds., pp. 13–41, Univ. of Arizona, Tucson.

M.J. Gaffey (2010). *Space weathering and the interpretation of asteroid reflectance spectra.* Icarus 209, 564–574.

A.W. Harris (2015). *A global approach to near-Earth object impact threat mitigation.* Final report for the FP7 project NEOShield (http://elib.dlr.de/98732/1/NEOShield_Final_Report_pub_5Aug15.pdf).

P. Janhunen, P.K. Toivanen, J. Polkko, S. Merikallio, P. Salminen, E. Hæggström, H. Seppänen, R. Kurppa, J. Ukkonen, S. Kiprich, G. Thornell, H. Kratz, L. Richter, O. Krömer, R. Rosta, M. Noorma, J. Envall, S. Lätt, G. Mengali, A.A. Quarta, H. Koivisto, O. Tarvainen, T. Kalvas, J. Kauppinen, A. Nuottajärvi and A. Obraztsov (2010). *Electric solar wind sail: Toward test missions.* Rev. Sci. Instrum., 81, 111301.

R. Jedicke, M. Granvik, M. Micheli, E. Ryan, T. Spahr, and D.K. Yeomans (2015). *Surveys, astrometric follow-up, and population statistics.* In: Asteroids IV, P. Michel et al. eds., pp. 13–41, Univ. of Arizona, Tucson.

D. Jewitt, H, Hsieh, and J. Agarwal (2015). *The active asteroids.* In: Asteroids IV, P. Michel et al. eds., pp. 221–241, Univ. of Arizona, Tucson.

D. Lario, A. Aran, N. Agueda, and B. Sanahuja (2007). *Radial dependence of proton peak intensities and fluences in SEP events: influence of the energetic particle transport parameters.* Adv. Space Res., 40, 289–294.

K. Lehtinen, U. Bach, K. Muinonen, M. Poutanen, and L. Petrov (2016). *Asteroid sizing by radiogalaxy occultation at 5 GHz.* The Astrophysical Journal Letters 822, L21.

J.-L. Margot, P. Pravec, P. Taylor, B. Carry, and S. Jacobson (2015). *Asteroid systems: binaries, triples, and pairs.* In: Asteroids IV, P. Michel et al. eds., pp. 355–374, Univ. of Arizona, Tucson.

J.R. Masiero, F.E. DeMeo, T. Kasuga, and A.H. Parker (2015). *Asteroid family physical properties.* In: Asteroids IV, P. Michel et al. eds., pp. 323–340, Univ. of Arizona, Tucson.

J.R. Masiero, A.K. Mainzer, T. Grav, J.M. Bauer, R.M. Cutri, J. Dailey, P.R.M. Eisenhardt, R.S. McMillan, T.B. Spahr, M.F. Skrutskie, D. Tholen, R.G. Walker, E.L. Wright, E. DeBaun, D. Elsbury, T. Gautier IV, S. Gomillion, and A. Wilkins (2011). *Main belt*

*asteroids with WISE/NEOWISE.* I. Preliminary Albedos And Diameters. The Astrophysical Journal 741(2), 20 pp.

P. Michel, F.E. DeMeo, and W.F. Bottke, eds. (2015). Asteroids IV, Univ. of Arizona, Tucson.

V. Reddy, T.L. Dunn, C.A. Thomas, N.A. Moskovitz, and T.H. Burbine (2015). *Mineralogy and surface composition of asteroids.* In: Asteroids IV, P. Michel et al. eds., pp. 43–63, Univ. of Arizona, Tucson.

A.S. Rivkin, H. Campins, J.P. Emery, E.S. Howell, J. Licandro, D. Takir, and F. Vilas (2015). *Astronomical observations of volatiles on asteroids.* In: Asteroids IV, P. Michel et al. eds., pp. 65–87, Univ. of Arizona, Tucson.

A.S. Rivkin, E.S. Howell, F. Vilas, and L.A. Lebofsky (200). *Hydrated minerals on asteroids: the astronomical record.* In: Asteroids III, W.F. Bottke Jr. et al. eds., pp. 235–253, Univ. of Arizona, Tucson.

P.K. Toivanen and P. Janhunen (2009). *Electric sailing under observed solar wind conditions*. Astrophys. Space Sci. Trans., 5, 61–69.

B.M. Wiegmann (2016). *Electric sail propulsion to enable quick heliopause and beyond missions of scientific discovery.* NASA NIAC symposium, Aug 23, 2016, http://livestream.com/viewnow/NIAC2016/videos/133764483 , http://www.nextbigfuture.com/2016/09/nasa-niac-e-sail-phase-2-heliopause.html

---

For electric sail publications, see also http://www.electric-sailing.fi/publications.html (refereed papers) and http://www.electric-sailing.fi/fp7/fp7docs.html (deliverables of "ESAIL" EU FP7 project which increased electric sail TRL to 4-5).

# Appendix E

# Perigee drag calculation

We have the polar coordinate representation of an ellipse where origin is at focus (wikipedia/Ellipse, 2019):

$$r(\varphi) = \frac{a(1-e)(1+e)}{1+e\cos\varphi} = r_0 \frac{1+e}{1+e\cos\varphi} \tag{E1}$$

where $a$ is the semimajor axis, $e$ is the eccentricity and $r_0 = a(1-e)$ is the perigee distance. For small $\varphi$, $\cos\varphi = 1 - \varphi^2/2 + O(\varphi)^4$ so that

$$r(\varphi) = r_0 \left( 1 + \frac{1}{2}\frac{e}{1+e}\varphi^2 \right) + O(\varphi)^4, \tag{E2}$$

which is the same as equation 1 of Heppenheimer (1971). The square of the line element is

$$ds^2 = dr^2 + r^2 d\varphi^2 = r_0^2 \left( \frac{e}{1+e} \right)^2 \varphi^2 d\varphi^2 + r_0^2 \left( 1 + \frac{e}{1+e}\varphi^2 \right) d\varphi^2$$

$$= \left[ 1 + \frac{e^2 + e(1+e)}{(1+e)^2}\varphi^2 \right] r_0^2 d\varphi^2. \tag{E3}$$

Taking the square root and using the fact that $\varphi$ is small we obtain

$$ds = \left[ 1 + \frac{e(\frac{1}{2}+e)}{(1+e)^2}\varphi^2 \right] r_0 d\varphi. \tag{E4}$$

From this vis-viva equation, the speed is

$$v = \sqrt{GM_E \left( \frac{2}{r} - \frac{1}{a} \right)} \tag{E5}$$

where $a = \frac{r_0}{1-e}$ is the semimajor axis so that

$$v = \sqrt{GM_E \left( \frac{2}{r} - \frac{1-e}{r_0} \right)}$$

$$= \sqrt{\frac{GM_E}{r_0} \left( 1 + e - \frac{e}{1+e}\varphi^2 \right)}$$

$$= \sqrt{\frac{GM_E}{r_0}(1+e) \left[ 1 - \frac{e}{(1+e)^2}\varphi^2 \right]}$$

$$= \sqrt{\frac{GM_E}{r_0}(1+e)} \left[1 - \frac{e}{2(1+e)^2}\varphi^2\right]. \tag{E6}$$

We are systematically dropping terms of order $O(\varphi)^4$. The drag force is

$$F = \frac{1}{2}C_D\rho v^2 A \tag{E7}$$

and the atmospheric density model is

$$\rho = \rho_0 \exp\left(-\frac{r-r_0}{H}\right) \tag{E8}$$

The impulse due to aerobraking during the perigee pass is

$$\begin{aligned}
I = \int F dt &= \int \frac{F}{v} ds \\
&= \frac{1}{2}C_D A \rho_0 \int ds\, v \exp\left(-\frac{r-r_0}{H}\right) \\
&= \frac{1}{2}C_D A \rho_0 r_0 \sqrt{\frac{GM_E}{r_0}(1+e)} \int d\varphi \left[1 + \frac{e(\frac{1}{2}+e)}{(1+e)^2}\varphi^2\right]\left[1 - \frac{e}{2(1+e)^2}\varphi^2\right]\exp(..) \\
&= \frac{1}{2}C_D A \rho_0 r_0 \sqrt{\frac{GM_E}{r_0}(1+e)} \int d\varphi \left[1 + \frac{e(\frac{1}{2}+e)}{(1+e)^2}\varphi^2 - \frac{e}{2(1+e)^2}\varphi^2 + O(\varphi)^4\right]\exp(..) \\
&= \frac{1}{2}C_D A \rho_0 r_0 \sqrt{\frac{GM_E}{r_0}(1+e)} \int d\varphi \left[1 + \left(\frac{e}{1+e}\right)^2\varphi^2\right]\exp\left(-\frac{r-r_0}{H}\right) \\
&= \frac{1}{2}C_D A \rho_0 r_0 \sqrt{\frac{GM_E}{r_0}(1+e)} \int d\varphi \left[1 + \left(\frac{e}{1+e}\right)^2\varphi^2\right]\exp\left(-\frac{1}{2}\frac{r_0}{H}\frac{e}{1+e}\varphi^2\right).
\end{aligned} \tag{E9}$$

The $\varphi$–integration is in principle from $-\pi$ to $\pi$, but since $r_0/H \gg 1$, the limits can be put to $\pm\infty$. Doing the Gaussian integrals [1], we obtain

$$\begin{aligned}
I &= \frac{1}{2}C_D A \rho_0 r_0 \sqrt{\frac{GM_E}{r_0}(1+e)} \frac{\sqrt{2\pi H(1+e)}((e+1)r_0 + He)}{\sqrt{e}(1+e)r_0^{3/2}} \\
&= C_D\sqrt{\frac{\pi}{2e}}\left[1 + e\left(1 + \frac{H}{r_0}\right)\right] A\rho_0\sqrt{GM_E H} \\
&\approx C_D\sqrt{\frac{\pi}{2e}}(1+e) A\rho_0\sqrt{GM_E H},
\end{aligned} \tag{E10}$$

where in the last step we used $H \ll r_0$.

The maximum drag occurs at $r = r_0$ and it is

$$F_{\max} = \frac{1}{2}C_D\rho_0 v(r_0)^2 A = \frac{1}{2}C_D\rho_0 A \frac{GM_E}{r_0}(1+e). \tag{E11}$$

The effective duration $\Delta t_{\mathrm{dur}}$ of the perigee braking is obtained by dividing the impulse $I$ by the maximum drag:

$$\Delta t_{\mathrm{dur}} \equiv \frac{I}{F_{\max}} = \sqrt{\frac{2\pi}{e}}r_0\sqrt{\frac{H}{GM_E}} = \sqrt{\frac{2\pi}{e}}\frac{\sqrt{r_0 H}}{\sqrt{GM_E/r_0}}. \tag{E12}$$

---

[1]For $a > 0$, $\int_{-\infty}^{\infty} d\varphi e^{-a\varphi^2} = \sqrt{\frac{\pi}{a}}$, and $\int_{-\infty}^{\infty} d\varphi \varphi^2 e^{-a\varphi^2} = \frac{1}{2a}\sqrt{\frac{\pi}{a}}$.

It is also instructive to compute the effective path length $\Delta s$ of the atmospheric pass by multiplying $\Delta t_{\mathrm{dur}}$ by the speed at perigee, $v(r_0)$:

$$\Delta s \equiv \Delta t_{\mathrm{dur}} v(r_0) = \sqrt{\frac{2\pi}{e}} \frac{\sqrt{r_0 H}}{\sqrt{GM_E/r_0}} \sqrt{(1+e)GM_E/r_0}$$

$$= \sqrt{2\pi \frac{1+e}{e}} \sqrt{r_0 H}. \tag{E13}$$

Thus the braking path length $\Delta s$ is proportional to the geometric average of the perigee distance $r_0$ and the atmospheric scale height $H$.

# Appendix F

# Rate of apogee lowering due to aerobraking

Consider an elliptic orbit around Earth, with semimajor axis $a$ and perigee radial distance $r_0$.

When a small perigee braking delta-v of $\delta v$ is applied, the semimajor axis decreases from $a$ to $a + \delta a$, where $\delta a$ is negative because the semimajor axis decreases by the braking. Using the vis-viva equation for the initial and final states, one can write the relationship

$$
\begin{aligned}
\delta v &= \sqrt{GM_E \left( \frac{2}{r_0} - \frac{1}{a} \right)} - \sqrt{GM_E \left( \frac{2}{r_0} - \frac{1}{a + \delta a} \right)} \\
&= \sqrt{GM_E \left( \frac{2}{r_0} - \frac{1}{a} \right)} - \sqrt{GM_E \left[ \frac{2}{r_0} - \frac{1}{a} \left( 1 - \frac{\delta a}{a} \right) \right]} \\
&= \sqrt{GM_E \left( \frac{2}{r_0} - \frac{1}{a} \right)} - \sqrt{GM_E \left( \frac{2}{r_0} - \frac{1}{a} + \frac{\delta a}{a^2} \right)}.
\end{aligned}
\tag{F1}
$$

For any $X$ and its small change $\delta X$, one has

$$
\sqrt{X} - \sqrt{X + \delta X} = \sqrt{X} - \sqrt{X \left( 1 + \frac{\delta X}{X} \right)} = \sqrt{X} \left[ 1 - \left( 1 + \frac{1}{2} \frac{\delta X}{X} \right) \right] = \sqrt{X} \left( -\frac{1}{2} \frac{\delta X}{X} \right).
\tag{F2}
$$

Now $X = GM_E \left( 2/r_0 - 1/a \right)$ and $\delta X = GM_E \delta a / a^2$ so that

$$
\begin{aligned}
\delta v &= \sqrt{GM_E \left( \frac{2}{r_0} - \frac{1}{a} \right)} \left( \frac{-1}{2} \right) GM_E \frac{\delta a / a^2}{GM_E \left( \frac{2}{r_0} - \frac{1}{a} \right)} \\
&= -\frac{1}{2} \sqrt{GM_E \left( \frac{2}{r_0} - \frac{1}{a} \right)} \frac{\delta a / a}{\frac{2a}{r_0} - 1}.
\end{aligned}
\tag{F3}
$$

From this equation we can solve $\delta a / a$:

$$
\frac{\delta a}{a} = \frac{-2 \Delta v \left( \frac{2a}{r_0} - 1 \right)}{\sqrt{GM_E \left( \frac{2}{r_0} - \frac{1}{a} \right)}} \; .
\tag{F4}
$$

The orbital period $T$ is given by Kepler's third law as

$$
T = 2\pi \sqrt{\frac{a^3}{GM_E}} \; .
\tag{F5}
$$

The average rate of semimajor axis decay is then obtained as

$$\frac{da}{dt} = \frac{\delta a}{T} = -2a\Delta v \left( \frac{2a}{r_0} - 1 \right) \frac{\sqrt{GM_E}}{2\pi a^{3/2}\sqrt{GM_E \left( \frac{2}{r_0} - \frac{1}{a} \right)}}$$

$$= -\frac{1}{\pi}\Delta v \sqrt{\frac{2a}{r_0} - 1} \ . \tag{F6}$$